

Friction and fracture: richness and complexity in dynamic rupture

Présentée le 9 juin 2023

Faculté de l'environnement naturel, architectural et construit
Laboratoire de simulation en mécanique des solides
Programme doctoral en génie civil et environnement

pour l'obtention du grade de Docteur ès Sciences

par

Thibault Didier ROCH

Acceptée sur proposition du jury

Prof. B. T. A. Lecampion, président du jury
Prof. J.-F. Molinari, directeur de thèse
Dr H. Bhat, rapporteur
Dr D. Bonamy, rapporteur
Prof. J. Kolinski, rapporteur

*La science, mon garçon, est faite d'erreurs
mais d'erreurs qu'il est bon de commettre,
car elles mènent peu à peu à la vérité.*

— Jules Verne

Acknowledgements

The end of a thesis is a great time to look back on this incredible academic adventure and to celebrate by thanking all the people that have made it possible. Words cannot express my gratitude to my advisor Jean-François Molinari for giving me the opportunity to conduct a Ph.D. in his team. Jean-François has always been an inspiration since I first did a project in his laboratory during my undergraduate studies almost ten years ago. His enthusiasm and curiosity in any circumstances have been a great motivation to give my best during this thesis. I am incredibly grateful for his trust and confidence in my ideas and suggestions. It has been such a great pleasure to work under his supervision. I am also incredibly thankful to Eran Bouchbinder for our long collaboration on frictional systems and for hosting me for a few months in his team. I want to thank the members of the jury: Brice Lecampion, Harsha Bhat, Daniel Bonamy, and John Kolinski, for their time and the exciting discussion during the defense. I would also like to thank Marie Violay for her interest in my work and presence at the oral exam.

I was especially lucky to collaborate with numerous people during my thesis. I want to thank Mathias Lebihain for introducing me to the joy of line tension and for the fruitful discussions on heterogeneous fracture. I am also grateful to Fabian Barras and Phillippe Geubelle for the collaboration on *cRacklet*. Thanks to Efim Brener and Michael Aldam for our work on frictional systems, and to Tal Cohen for the remote collaboration and the supervision of the master theses of Evelyne Ringoot and Thibault Ghesquière-Diérickx. These years spent in the laboratory would not have been that productive without an incredible team. I have great memories both on a scientific and a personal level with the entire LSMS family: Guillaume, Nicolas, Roozbeh, Tobias, Fatima, Gianluca, Joaquin, Lucas, Enrico, Mohit, Emil, Son, Manon, Lucas, Yulin, Sacha, Parissa, Raquel, Shad, Roxane, Jacopo, Angelos, Birgitte, Emma, Anne-Françoise. I am grateful that I was consistently able to find someone in the lab to grab a beer at Sat at the end of a long day of work. I also want to thank Yuri, Avraham, Sanhita, Anna, and Vladimir for the great time spent at Weizmann. I want to thank my former Civil Engineering classmates Numa and Alexis who showed me the way toward the thesis. Voglio ringraziare Federica per l'aiuto sul riassunto.

While a thesis is mostly about science, it would not have been possible without escaping from the academic world once in a while. I am particularly lucky to have shared many fantastic moments with my friends in Lausanne or elsewhere. It would require an entire thesis to properly thank everyone. I apologize to anyone I forgot but know that if we

Acknowledgements

have shared a moment together, I am thankful for it and that it contributed to bringing me here today. I want to thank my flatmates Bigo, Thomas (and Mornifle), Tristan and Gian Marco for the great times spent at the legendary *Terreaux 23*. I am particularly thankful to the Shrooms for the many laughs, aperos, and parties that offered a great distraction from the hard work required for a thesis. Patrik, Beni, Matthieu, Elo (and Gigi), Jul, Barbo, Cristi, Bouj, Alex, Elea, Gio, Lyn, Livia, Coco, and Fab: I gathered so many great memories with you and I hope there are many more to come. I want to thank the original team from the other side of the lake: Romain, Momo, Marine, Marie, Cyril, Alice, and Camille. I also want to thank Antoine, Alex, Manu, and Mattia. Thanks to Chuka, Napo, Lulah, Meir, Gal, Neri, Yaron, Ben, and Netaly for all the fun during my short visit to Israel. I am extremely grateful to my friends who hosted me during the last few months of this thesis, to everyone who ever showed up at the *Mardi Mine* celebration, and to everyone I have met on the dancefloor.

Je voudrais finalement remercier l'ensemble de ma famille pour leur soutien et les innombrables repas durant ces longues années de thèse. Je veux en particulier remercier ma soeur Mélanie, ainsi que mes parents Corinne et Dominique sans lesquels rien n'aurait été possible.

Lausanne, March 2023

Thibault Roch

Abstract

Understanding how things break and slide is of paramount importance to describe the dynamics of a broad range of physical systems. This includes day-to-day problems such as the breaking of a glass of wine or the sliding of skis on snow, but also engineering systems with, for example, the braking of a car or the failure of a structural component, up to geophysics and earthquake science. These two topics, fracture, and friction, seem unrelated at first but share similar physical characteristics: they are mediated by the propagation of rupture fronts. In both cases, a ruptured state (a crack, or a slipping patch) invades an intact state (the unbroken material, or a sticking interface). While the questions related to fracture and friction are ubiquitous, our physical understanding of these phenomena is far from complete. The Linear Elastic Fracture Mechanics framework describes accurately the stability of defects in materials and their slow growth but fails at describing the unstable three-dimensional dynamics at play in rapid fracture. Concepts from fracture mechanics have been successfully applied to describe the propagation of frictional rupture fronts, but fundamental differences remain due to the complex behavior of the friction coefficient itself, being dependent on the slipping rate and the state of the microcontacts at the interface between two solids. Hence, dynamic rupture exhibits a richness of behaviors. Amongst other things, the interaction between a front and material heterogeneities, boundary conditions, and finite geometry can significantly alter the dynamics of a rupture.

The objective of this work is to explore this richness in dynamic rupture, taking advantage of efficient computational methods that solve the elastodynamic equations. The use of modern computing methods allows modeling ruptures down to the small dissipation length scale near the tip of a rupture, the process zone size. The two software used in this work are open-source codes that were developed in the Computational Solid Mechanics Laboratory at EPFL.

The first part of this work reveals the interactions occurring at the scale of the process zone between a tensile crack and a heterogeneous material in the context of front deformations, which inform on the effective properties of a microstructure. Then, the physical origin of the analogy between frictional rupture and fracture is investigated, demonstrating that the stress drop emerges from the interaction between interfacial and bulk properties. This work also explores the influence of the boundary conditions on the frictional rupture mode, revealing the emergence of a train of self-healing slip pulses

Abstract

under velocity-driven conditions. The study of frictional interfaces is then upscaled by taking a statistical perspective on slip events, demonstrating the emergence of statistical complexity in finite systems even in the absence of material heterogeneities. The last contribution of this thesis is numerical, with a coupling scheme between the two methods used in this work, aiming at providing a better tool for the simulation of complex dynamic rupture problems.

While being rather fundamental, this Ph.D. work offers novel insights into the dynamics of rupture fronts and has direct implications for various domains, ranging from the design of micro-structured materials and interfaces, to the dynamics of earthquakes.

Keywords: dynamic fracture, friction, rupture front, process zone, heterogeneous microstructure, front deformation, rate and state, self-healing pulses, statistical complexity, high-performance computing

Résumé

Comprendre comment les choses cassent et glissent relève d'une importance vitale pour décrire la dynamique de nombreux systèmes physiques. Cela concerne des problèmes du quotidien, comme la rupture d'un verre de vin ou le glissement des skis sur la neige, mais aussi l'ingénierie, avec les freins d'une voiture ou un élément structural qui se fissure, jusqu'à la géophysique et la science des tremblements de terre. La rupture et la friction, bien que très différentes au premier regard, possède des caractéristiques physiques semblables. Toutes deux sont contrôlées par la propagation de front de rupture : un état cassé (une fissure, ou une zone de glissement) propage dans un état intact (matériau sain, ou une interface à l'arrêt). Bien que ces thématiques soient omniprésentes dans notre environnement, la physique qui les dirige est loin d'être parfaitement comprise. La Mécanique Linéaire Élastique de la Rupture prédit avec succès la stabilité des défauts ainsi que leur croissance à basse vitesse, mais échoue à décrire les instabilités dynamique lorsque les fissures propagent à haute vitesses. Certains concepts de la rupture dynamique sont applicables aux ruptures frictionnelles, mais des différences fondamentales subsistent, relatives principalement à la complexité du coefficient de frottement, qui dépend de la vitesse de glissement et de l'état des microcontacts à l'interface entre deux solides. La rupture dynamique peut ainsi prendre de nombreuses formes. Par exemple, les interactions avec une microstructure, les conditions de bords ou la géométrie du problème impactent la dynamique d'une rupture.

L'objectif de cette thèse est d'explorer cette richesse de comportement en utilisant des méthodes numériques efficaces pour modéliser la rupture jusqu'à l'échelle de grandeur ou la dissipation a lieu en pointe de fissure, la zone d'endommagement. Les codes de calculs utilisés pour ce travail sont des codes ouverts qui ont été développés au Laboratoire de Simulation Numérique des Solides et Structures à l'EPFL.

Tout d'abord, ce travail met en avant les interactions ayant lieu à l'échelle de la zone d'endommagement entre une fissure et des hétérogénéités en ce qui concerne les déformations de fronts, qui informent sur les propriétés effectives d'une microstructure. Ensuite, l'analogie entre friction et rupture est étudiée, et il est démontré que la chute de contrainte en friction résulte de l'interaction entre la physique de l'interface et celle des solides en contacts. L'influence des conditions aux limites sur la sélection des modes de rupture est également étudiée, avec l'émergence d'un train de pulses lorsque la vitesse de glissement est prescrite. L'étude des interfaces frictionnelle prend ensuite une tour-

Résumé

nure statistique, en analysant l'émergence de complexité statistique des événements de glissement dans un système sans désordre en ce qui concerne les paramètres matériaux et la friction. La dernière partie de cette thèse est numérique et consiste à proposer un couplage entre les deux méthodes qui ont été utilisées tout au long de ce travail, avec l'objectif de proposer un outil encore plus performant pour simuler la rupture dynamique.

Bien qu'étant plutôt fondamental, les avancées scientifiques sur la dynamique de la rupture découvertes durant cette thèse ont des applications potentielles dans de nombreux domaines, allant du design d'interfaces et de matériaux architecturés à la physique des tremblements de terre.

Mots clés : rupture dynamique, friction, front de rupture, zone d'endommagement, microstructure hétérogène, déformation de front, loi de frottement rate-and-state, pulse de glissement, complexité statistique, calcul scientifique à haute performance

Riassunto

Comprendere come gli oggetti si rompono o scivolano gli uni su gli altri è di fondamentale importanza per descrivere la dinamica di una vasta gamma di sistemi fisici. Questi includono problemi quotidiani come la rottura di un bicchiere di vino o lo scivolamento degli sci sulla neve, altri di natura ingegneristica come la frenata di un'auto o la rottura di un componente strutturale, e persino alcuni di natura geofisica come la meccanica dei terremoti. La frattura e l'attrito, che controllano i fenomeni sopracitati, sembrano non correlati a prima vista, ma condividono simili caratteristiche fisiche: sono mediati dalla propagazione di fronti di rottura. In entrambi i casi, uno stato perturbato (interessato da una crepa o soggetto a una zona di scivolamento) invade uno stato intatto (imperturbato). Sebbene le domande relative alla frattura e all'attrito siano onnipresenti, la nostra comprensione fisica di questi fenomeni è ancora lontana dalla completezza. Il framework della Meccanica della Frattura Elastica Lineare descrive accuratamente la stabilità dei difetti nei materiali e la loro crescita lenta, ma fallisce nel descrivere la dinamica tridimensionale instabile in gioco nella frattura rapida. I concetti della meccanica della frattura sono fin'ora stati applicati con successo per descrivere la propagazione di fronti di rottura per attrito, ma rimangono differenze fondamentali a causa del comportamento complesso del coefficiente di attrito stesso, che dipende dalla velocità di scivolamento e dallo stato dei microcontatti all'interfaccia tra due solidi. Di conseguenza, la rottura dinamica presenta una ricchezza di comportamenti complessi. Tra gli altri vi sono l'interazione tra un fronte di rottura e le eterogeneità del materiale e l'influenza delle condizioni al contorno e della geometria finita del sistema nella dinamica di una rottura. L'obiettivo di questo lavoro è esplorare questa ricchezza nel comportamento della rottura dinamica, sfruttando efficienti metodi computazionali che risolvono le equazioni elastodinamiche. L'utilizzo di metodi di calcolo moderni consente di modellare una rottura fino alla piccola scala di dissipazione nei pressi della sua estremità (zona di processo), permettendo la descrizione del processo nella più adeguata risoluzione. I due software utilizzati in questo lavoro sono codici open-source sviluppati nel Laboratorio di Meccanica dei Solidi Computazionale presso l'EPFL.

La prima parte di questo lavoro rivela le interazioni che avvengono a livello della zona di processo tra una fessura a trazione e un materiale eterogeneo nel contesto delle deformazioni frontali, che informano sulle proprietà effettive di una microstruttura. Successivamente, viene indagata l'origine fisica dell'analogia tra rottura per attrito e

frattura, dimostrando che la perdita di stress emerge dall'interazione tra le proprietà di interfaccia e quelle di volume. Questo lavoro esplora anche l'influenza delle condizioni al contorno sulla modalità di rottura per attrito, rivelando, per un sistema controllato in velocità di scorrimento, l'emergere di un treno di impulsi auto-rigeneranti che attraversa l'interfaccia. Lo studio delle interfacce di contatto viene quindi ampliato, prendendo in considerazione una prospettiva statistica sugli eventi di rottura per scivolamento, dimostrando l'emergere della complessità statistica in sistemi finiti anche in assenza di eterogeneità del materiale. L'ultima contribuzione di questa tesi è numerica, con lo sviluppo di uno schema di accoppiamento tra i due metodi di calcolo utilizzati in questo lavoro, con l'obiettivo di fornire uno strumento migliore per la simulazione di problemi complessi di rottura dinamica.

Pur essendo piuttosto fondamentale, questo lavoro di dottorato offre nuove prospettive sulla dinamica dei fronti di rottura con implicazioni dirette in vari campi, dalla progettazione di materiali e interfacce microstrutturati allo studio della dinamica dei terremoti.

Parole chiave :

rottura dinamica, attrito, fronti di rottura, zona di processo, microstruttura eterogenea, deformazioni frontali, legge di attrito rate-and-state, impulsi di scorrimento, complessità statistica, calcolo scientifico ad alte prestazioni

Contents

Acknowledgements	i
Abstract (English/Français/Italiano)	iii
List of Figures	xiii
List of Tables	xvii
Symbols	xix
1 Introduction	1
1.1 Motivation	1
1.2 Objectives	3
1.3 Outline	4
2 State of the art	7
2.1 Continuum solid mechanics	8
2.1.1 Kinematics	8
2.1.2 Equilibrium and conservation	9
2.1.3 Constitutive law	10
2.1.4 Boundary conditions	11
2.1.5 Elastodynamics	11
2.2 Fracture mechanics	12
2.2.1 Linear elastic fracture mechanics	13
2.2.2 Dynamic fracture mechanics	16
2.2.3 Heterogeneous fracture mechanics	20
2.3 Friction	22
2.3.1 Models of friction	24
2.3.1.1 A brief history of friction	24
2.3.1.2 The rate and state friction framework	26
2.3.1.3 Beyond friction	29
2.3.2 Rupture modes	30
2.3.3 Analogy with fracture	32
2.3.4 Complexity in frictional systems	32
	ix

3	Numerical framework	35
3.1	Finite element method	35
3.1.1	Bulk elements	35
3.1.2	Modeling discontinuity in finite elements	38
3.2	Spectral boundary integral method	42
4	Crack front deformations in cohesive materials	45
4.1	Introduction	46
4.2	Problem description	47
4.2.1	Material properties	47
4.2.2	Numerical scheme	48
4.3	Time evolution of the crack deformations and crack front waves	49
4.4	Toughness contrast with constant process zone size	50
4.5	Crack propagation velocity	52
4.6	Process zone size and type of heterogeneities	53
4.7	Dynamic cohesive line tension model	54
4.8	Comparison between theory and simulations	56
4.9	Discussion	57
4.10	Supplemental material	58
5	On the dynamics of frictional interfaces described by rate and state friction laws	59
5.1	Emergence of crack-like behavior of frictional rupture	61
5.1.1	Introduction	61
5.1.2	The physical origin of stress drops	62
5.1.3	Simulation support for the emergence of $\Delta\tau$	65
5.1.4	Crack-like behavior of frictional rupture	67
5.1.4.1	Equation of motion	68
5.1.4.2	Stress singularity and energy balance	69
5.1.5	Conclusion	71
5.2	Velocity-driven frictional sliding: coarsening and steady-state pulses	72
5.2.1	Introduction	72
5.2.2	Simulating velocity-driven frictional dynamics	77
5.2.2.1	Bulk and interfacial constitutive relations: Linear elastodynamics and rate-and-state friction	77
5.2.2.2	Mimicking velocity-driven frictional dynamics in infinite systems using the boundary integral method	79
5.2.2.3	Simulating velocity-driven frictional dynamics in finite systems using the finite element method	80
5.2.3	Coarsening dynamics: The selection of pulse train periodicity	81
5.2.4	The small H limit: The competition between coarsening and elastofrictional instabilities	83
5.2.5	Single pulse properties in the large H limit	86

5.2.5.1	Pulse equation of motion: Leading edge singularity, effective fracture energy, and propagation velocity	87
5.2.5.2	The pulse width	89
5.2.6	Summary and discussion	92
5.2.7	Supplemental material	93
5.2.7.1	The interfacial constitutive law	93
5.2.7.2	The elasto-frictional length L_c	94
5.2.7.3	The spectral boundary integral formulation	95
5.2.7.4	Finite element method formulation	96
5.2.7.5	The WS friction law	96
5.2.7.6	The space-independent stick-slip like behavior for $H \simeq W \gg L_c$	97
5.2.7.7	The effective fracture energy	98
5.2.7.8	The SW friction law	99
5.2.7.9	Supplementary data	99
6	Statistical and dynamical complexity in a driven frictional system without disorder	101
6.1	Introduction	103
6.2	Model	104
6.3	The numerical method	106
6.4	Identification of slip events	106
6.5	Time dependence of the statistics	110
6.6	Statistical complexity	111
6.7	Collapse of the probability density functions	112
6.8	Dynamical complexity	115
6.9	Influence of wave reflection	116
6.10	Summary and discussion	119
6.11	Supplemental material	120
6.11.1	Independence of the statistics on the thresholds	120
6.11.2	Nucleation length for finite height system	120
7	Coupling the finite element method and the spectral boundary integral method	123
7.1	Introduction	124
7.2	Coupling method	125
7.2.1	Finite element method	125
7.2.2	Spectral boundary integral method	127
7.2.3	Coupling condition	128
7.2.4	Coupling algorithm	129
7.3	Validation	129
7.3.1	Setup and qualitative analysis	129
7.3.2	Quantitative analysis of the error	132
7.4	Example: spontaneous propagation of a crack loaded in tension	134

Contents

7.5	Conclusion	136
7.6	Supplemental material	137
7.6.1	Additional results for the reference problem	137
8	Conclusion	143
8.1	Summary	143
8.2	Future perspectives	145
A	Derivation of the quasi-static cohesive line tension model	149
B	Contribution to open source software	153
B.1	Summary	154
B.2	Statement of need	154
B.3	Features	155
B.4	Example	155
B.5	Publications	156
C	Scientific communication and Art	159
	Bibliography	183
	Curriculum Vitae	185

List of Figures

2.1	Kinematics of a deformable solid from its original configuration $\Omega(t_0)$ to a deformed state $\Omega(t)$	9
2.2	Stresses acting on one of the surfaces of a small block of size $dx\ dy\ dz$. . .	10
2.3	Stress fields near a sharp crack	14
2.4	The three fracture modes	15
2.5	The different stress regimes near a crack	16
2.6	Hoop stress near a moving tensile crack for various propagation velocity	17
2.7	Appearance of the fracture surface of an Homalite specimen	19
2.8	Appearance of the fracture surface of a brittle polyacrylamide gel	20
2.9	Example of front deformations in fracture experiments	21
2.10	Egyptian wall painting	22
2.11	Sketches on friction by Leonardo Da Vinci	23
2.12	A schematic of a friction system	24
2.13	Example of friction laws	25
2.14	Typical response of the friction coefficient to a change in velocity in the rate and state friction framework	28
2.15	Steady-state frictional strength vs. steady-state slip velocity in the rate and state friction framework	29
2.16	Schematic representation of a crack-like rupture and a self-healing slip pulse	30
2.17	Evidence of a crack-like rupture and a self-healing slip pulse in a friction experiment.	31
2.18	Strain fields near a frictional rupture tip and the corresponding LEFM predictions.	33
3.1	Schematic representation of a boundary value problem and a finite element mesh	36
3.2	Schematic representation of the node to node contact in finite element . .	39
4.1	Schematic representation of the system of interest, with the layout of the heterogeneous interface and the constitutive behavior of the interface, a linear weakening cohesive law.	48
4.2	Evolution of the front deformation amplitude with time	49

List of Figures

4.3	Crack front wave velocity as a function of the front velocity	50
4.4	Front deformation amplitude as a function of the toughness contrast . .	51
4.5	Front deformation amplitude as a function of the crack front propagation velocity	53
4.6	Front deformation amplitude as a function of the dynamic process zone size	54
4.7	Comparison between the front deformation amplitude measured from numerical simulations and the prediction given by the classical line tension model and the newly derived dynamic cohesive line tension model . . .	57
5.1	Schematic representation of a stress-driven friction system	62
5.2	N-shaped rate and state friction law and the possible intersections with a constant driving stress	64
5.3	Rate and state friction law with no minimum at high velocity and the possible intersections with constant driving stress	65
5.4	Typical fields (velocity, stress and state) for a crack-like frictional rupture under constant driving stress	66
5.5	Stress drop in frictional rupture	67
5.6	Generalized equation of motion for frictional rupture front	69
5.7	Stress and velocity singularity in frictional rupture	70
5.8	Breakdown energy as a function of slip	71
5.9	Schematic representation of the class of velocity-driven friction system. Steady-state frictional behavior. Schematic representation of a steady train of pulses.	74
5.10	Space-time plot of a typical velocity-driven simulation for large H . Comparison between the pulse profiles obtained for $H \rightarrow \infty$ and finite H . .	82
5.11	Space-time plot of a typical velocity-driven simulation for a finite geometry in the small H limit. Periodic oscillations in the pulse velocity profile.	84
5.12	Velocity, stress and state fields near the propagating rupture front of a slip pulse	88
5.13	Pulse equation of motion with the fracture toughness estimated based on the mapping of the rate and state friction law on a slip weakening law. .	90
5.14	Pulse width as a function of the normalized driving velocity and the normalized system size	91
5.15	Steady state rate and state friction laws used in the context of the emergence of slip pulses	95
5.16	Comparison between the velocity fields of pulses obtained using the N-shaped friction law and the law without strengthening at low slip velocity	97
5.17	Pulse equation of motion with the fracture toughness estimated from the fit of the singular fields	98

6.1	Schematic representation of the velocity driven frictional system of interest. Steady state friction law used in the corresponding finite element simulations.	105
6.2	Space-time map of the velocity in a typical simulation, and the corresponding space-slip plot of the duration required to slip a given slip threshold.	107
6.3	Space-slip map of the time at which a given cumulative slip has been reached, and the corresponding space-slip map of the independent global slip events. The waiting time between nodal slip events with the time threshold used to distinguish between slip events.	108
6.4	Space-slip map of the time for a given global slip event, with the corresponding space-time map of the slip velocity.	109
6.5	Distribution of the number of clusters per slip event.	109
6.6	Activity A of the system as a function of the time computed using various time intervals.	110
6.7	Probability density functions of the average slip, time, and seismic moment for three different time ranges during a simulation	111
6.8	Probability density function of the average slip, time, and seismic moment, and their split between small/non-propagating and large/propagating slip events.	113
6.9	Scaling relations between duration, average slip, seismic moment and rupture length.	113
6.10	Rescaling of the probability density functions of the average slip, time and rupture length for various systems	114
6.11	Detailed extract of the space-time map of the slip velocity during a simulation. Analysis of a sequence of events with the cumulative slip, stress and state profiles.	117
6.12	Space-time plot of the velocity for a single perturbation and various system heights. Probability density functions of the event duration and average slip for various system heights.	118
6.13	Influence of the arbitrary thresholds on the probability density functions.	120
6.14	Theoretical and observed nucleation lengths in finite systems.	121
7.1	Schematic representation of the coupling between the finite element method and the spectral boundary integral method.	126
7.2	System used for the validation of the FEM/SBIM coupling in two dimensions	130
7.3	Comparison of the displacement fields in the x direction between a finite element simulation and a model using the coupling with the spectral boundary integral method.	131

List of Figures

7.4	Comparison of the displacement fields in the y direction between a finite element simulation and a model using the coupling with the spectral boundary integral method.	132
7.5	Evolution of the error in the displacement fields for a reference problem of elastic wave propagation.	134
7.6	Convergence of the error in the displacement fields with the discretization for the coupling scheme.	135
7.7	Schematic representation of a crack under embedded inside an infinite body, solved with the coupling between FEM and SBIM	136
7.8	Numerical simulation of the spontaneous propagation of a mode I crack using the coupling scheme	136
7.9	Comparison of the velocity fields in the x direction between a finite element simulation and a model using the coupling with the spectral boundary integral method.	138
7.10	Comparison of the velocity fields in the y direction between a finite element simulation and a model using the coupling with the spectral boundary integral method.	139
7.11	Evolution of the error in the velocity fields for a reference problem of elastic wave propagation.	140
7.12	Convergence of the error in the displacement fields with the discretization for the coupling scheme.	141
A.1	Schematic representation of the various front configuration used to compute the cohesive stress intensity factor for a deformed front	149
B.1	Scaling efficiency of <i>cRacklet</i>	156
B.2	Example of a large simulation conducted with <i>cRacklet</i>	157
C.1	Mountains of friction.	160

List of Tables

5.1	Typical values of rate-and-state parameters used in Chapter 5	94
6.1	Typical values of bulk and rate-and-state parameters used in Chapter 6 .	105
7.1	Algorithm for the coupling between finite element method and spectral boundary integral method.	130

Symbols

x	Position
t	Time
u	Displacement
\dot{u}	Velocity
\ddot{u}	Acceleration
$\underline{\epsilon}$	Infinitesimal strain tensor
$\underline{\sigma}$	Cauchy stress tensor
ρ	Volumetric mass density
λ	First Lamé coefficient
μ	Shear modulus (Second Lamé coefficient)
E	Young's Modulus
ν	Poisson's ratio
c_d	Dilatational wave speed
c_s	Shear wave speed
c_r	Rayleigh wave speed
G_c	Fracture toughness
G	Energy release rate
K	Stress intensity factor
σ_c	Peak strength
δ_c	Critical opening / Critical slip distance
f	Friction coefficient
A_r	Real contact area
$\Delta\tau$	Stress drop
v	Slip velocity
ϕ	State variable
D	Characteristic size of the microcontacts
c_R	Rupture front velocity
c_H	Healing front velocity
c_p	Pulse front velocity

Symbols

\underline{K}	Stiffness matrix
\underline{M}	Mass matrix
\mathbf{F}^{ext}	External forces
\mathbf{F}^{int}	Internal forces
ω_0	Process zone size at rest
ω_v	Dynamic process zone size
ΔG_c	Toughness contrast
δa	Front deformations
δG_c	Fluctuation of fracture toughness
$\delta \sigma_c$	Fluctuation of strength
$\delta \omega$	Fluctuation of process zone size
δK	Perturbed stress intensity factor
A	Amplitude of front deformations
L_c	Elasto-frictional length
W_p	Periodicity of the pulse train
w_p	Pulse width
v_p	Average pulse slip velocity

1 Introduction

1.1 Motivation

How do things break? How do things slide? At first glance, these two questions seem unrelated, but in reality, their answers share qualitative and even some quantitative similarities. The first question deals with *fracture*, the study of cracks stability and growth in materials, while the second one is related to *friction*, understanding the sliding between bodies. The mechanism that is common to both topics is the propagation of *rupture fronts*. Conceptually, a rupture front represents the separation between an intact state and a broken one, i.e., between continuous fields and a discontinuity.

Fracture mechanics is a rather young discipline that was motivated by the catastrophic failures of man-made structures in the last century, such as the Liberty ships during the Second World War or the Comet airplanes in the 50s. For the former, the low temperature of the North Atlantic turned the behavior of the steel of the ships from ductile to brittle, allowing the nucleation and propagation of cracks. In the latter, improper design, including dangerous stress concentrations near the square windows, was responsible for the airplanes' failure. Griffith¹ and latter Irwin² proposed what became the pillars of the Linear Elastic Fracture Mechanics (LEFM) framework. First, the strength of materials is mediated by the presence of flaws, which concentrate stresses near them. These flaws grow, merge, and ultimately result in material failure for stresses that are way lower than the strength of atomic bonds. Second, the growth of flaws is described by a thermodynamic criterion: a crack grows if the energy released by the crack advance is sufficient to overcome the cost of creating new surfaces [1]. Third, the energy available for crack growth is entirely controlled by the asymptotic fields near the crack tip, bridging the local and global picture of fracture mechanics [2]. The region over which all the dissipative processes associated with fracture occur is called the *process zone size*. LEFM requires this dissipation scale to be negligibly small in front of the other length scales in the problem. This framework has been successfully applied to assess the stability of defects. However, once a defect is predicted to be unstable, LEFM does not describe

¹Alan Arnold Griffith (1893-1963)

²George Rankin Irwin (1907-1998)

how it will grow. As a consequence, this framework has been extended to dynamic rupture, aiming at describing the dynamics of crack growth. While this theory has proven successful in describing the behavior of slow cracks, there exist significant discrepancies with the experiments for fast ruptures. With increasing propagation velocity, out-of-plane damage starts occurring through the formation of steps and microbranches. These observations reveal the inherent heterogeneous nature of dynamic rupture and motivate the understanding of the interplay between a dynamic crack and material heterogeneities. In addition to gaining insights into the occurrence of these dynamic instabilities, it helps to describe the effective properties of a microstructure. Despite the apparent simplicity of brittle fracture, the interaction between dynamic cracks and disorder results in a richness of behaviors.

Friction is one of the oldest scientific problems due to its prevalence in natural and man-made systems. At large scales, friction mediates the occurrence of earthquakes through slip on crustal faults, which is a major threat to population and infrastructure. At the engineering level, it is estimated that 20% of the energy in the world is dissipated to overcome frictional forces [3]. Understanding and controlling friction could thus result in a significant reduction in the emission of greenhouse gas, which is not only necessary but urgent in the context of accelerating global warming. Yet, frictional sliding is an intrinsically complex phenomenon, emerging from the interaction between the interfacial nonlinearity and dissipation, bulk elastodynamics, driving forces, and geometry. Amontons³ and Coulomb⁴ first observed that the frictional force resisting the motion between two bodies is independent of the surface area, but increases with the normal pressure [4; 5]. The ratio between the shear strength and the normal pressure, called the *friction coefficient*, was then assumed to be constant, and this approximation has been proven useful in many engineering applications. However, describing the complex dynamics of frictional systems such as the succession of stick and slip events requires a weakening mechanism during slip. Several models have since been proposed to describe the evolution of the friction coefficient, such as the slip-weakening model or the rate and state friction framework. In the former, the friction coefficient weakens from a static value to a dynamic one when slipping over a given characteristic distance. In the latter, it is a function of the slip velocity and of the structural state of the interface, carrying memory of its history [6; 7]. The contact between two bodies occurs only over a small portion of the apparent contact area, called microcontacts. The structural state variable represents the maturity of the contacts, which changes with time and slip: under stationary contact, the contact area increases due to creep, while microcontacts are broken when slipping. This introduces a notion of healing for frictional interfaces. Due to their inherent weakening nature, frictional instabilities are prone to develop and result in the propagation of rapid slip along frictional interfaces. These ruptures can resemble a classical crack, with an expanding broken area that continues sliding until the

³Guillaume Amontons (1663-1705)

⁴Charles-Augustin de Coulomb (1736-1806)

propagation stops. However, frictional rupture can also occur through the propagation of slip pulses, in which the rupture front is closely followed by a healing front, resulting in a slipping area that is localized in space. Frictional rupture results in a broad variety of events, with various rupture types, propagation velocities, lengths, and duration. Taken from a statistical perspective, frictional systems feature statistical complexity with broadly distributed events characteristics, which are described by power-law scaling.

As mentioned initially, both fracture and friction feature rupture fronts, which propagate a discontinuity (a crack or a slipping patch) in an intact material or interface. The strength behind the rupture fronts is in both cases smaller than the one ahead: in fracture, cracks cannot sustain stresses and for sliding, the friction coefficient usually features a weakening with either slip or velocity. In addition to these qualitative analogies, some quantitative concepts of fracture mechanics such as singular stresses and local energy balance have been successful to describe the propagation of frictional rupture fronts, motivating the joint study of these two topics.

The numerical study of dynamic fracture is challenging, as it involves modeling discontinuities that are accompanied by strong nonlinearity and dissipation over a small length-scale near the rupture tip. Finely discretized time and space domains are thus required to capture the fast dynamics of rupture propagation. In this work, we rely on two numerical methods, namely the finite element method and the spectral boundary integral method, to model dynamic rupture. We use two efficient open source software developed in the Computational Solid Mechanics Laboratory⁵ (LSMS) at École Polytechnique Fédérale de Lausanne (EPFL), *Akantu* [8] and *cRacklet* [9].

1.2 Objectives

This thesis aims at exploring the richness of dynamic rupture modes in fracture and friction. This richness can emerge from the interfacial constitutive law, long-range elastodynamics, boundary conditions, and interactions with heterogeneities, which can arise from disorder in the material parameters or be self-generated by the evolution of the interface itself. The following questions are explored in this thesis:

- **Heterogeneous fracture:** Which scale controls the interaction between a crack and the microstructure? How do crack fronts deform in the presence of heterogeneities?
- **Analogy between friction and fracture:** What is the physical origin of the analogy between the propagation of frictional rupture front and classical fracture? To what extent one can use fracture mechanics to describe the behavior of frictional rupture?

⁵<https://www.epfl.ch/labs/lsms/>

- **Rupture modes:** How are frictional rupture modes selected? What is the influence of boundary conditions on the rupture modes?
- **Complexity in frictional systems:** What are the minimal physical ingredients for the emergence of complexity in frictional systems? Can it be observed in the absence of material heterogeneities?
- **Efficient numerical modeling:** How to overcome the numerical challenges associated with the modeling of dynamic rupture?

1.3 Outline

The chapters of this manuscript are briefly introduced below:

- **Chapter 2 - State of the art**
This first chapter sets the context for this thesis. Continuum solid mechanics, dynamic fracture, and friction are discussed, with a review of the topics and a discussion about the open challenges in these fields.
- **Chapter 3 - Numerical framework**
Modeling the dynamics of discontinuities is computationally challenging, as it usually involves large spatio-temporal domains that need to be finely discretized in both space and time to resolve the singular stress near rupture tips and fast slip events. In this thesis, two methods are used: (i) the finite element method, which is versatile and allows modeling any kind of geometry and heterogeneities, (ii) the spectral boundary integral method, efficient but limited to the case of an interface lying between two homogeneous linear elastic solids. We recall the main equations of both methods and describe how they are employed through this thesis. Both implementations are open source software that have been developed in the Computational Solid Mechanics Laboratory.
- **Chapter 4 - Crack front deformations in cohesive materials**
Crack fronts deform when interacting with heterogeneities. Studying the deformations reveals the local variations of fracture toughness and helps rationalize the effective properties of a heterogeneous interface. The main method used to study front deformations is the *line tension model*, which describes the front as a line and thus treats all asperity scales indifferently. However, a finite dissipation length scale called the *process zone size* is required to regularize the theoretically infinite stresses near the rupture tip predicted by LEFM. This chapter is dedicated to the study of front deformations when the process zone size is not negligible, and its interaction with the size of the asperities. We first conduct numerical simulations showing that the amplitude of front deformations depends on the process zone size. Depending on the type of heterogeneity that is considered (peak stress or process zone size), the amplitude is increased or decreased compared to the reference model with no process zone. We discuss a model recently derived by

a collaborator, Dr. Mathias Lebihain, to treat the deformations of crack fronts in cohesive materials, and extend it to dynamic. We show that this model, called the *dynamic cohesive line tension model*, predicts accurately the numerical results.

- **Chapter 5 - On the dynamics of frictional interfaces described by rate and state friction laws**

In this chapter, we study the frictional rupture modes emerging at a frictional interface described by the *rate and state friction* framework and study the analogy between frictional rupture and fracture mechanics. In the first part, a stress-driven system is studied. Numerical simulations are conducted and result in the nucleation and propagation of expanding crack-like ruptures. It is shown that the stress drop is not an interfacial quantity, as widely assumed, but rather results from the interaction between the interfacial constitutive behavior and the radiation of elastic waves in the surrounding bulk. The analogy between frictional rupture and fracture mechanics is addressed. In the second part, velocity-driven friction is investigated. Under these conditions, the only steady-state solution is a train of pulses, a rupture mode that does not exist in fracture mechanics. We conduct numerical simulations and demonstrate that independently of the system height, a stable train of pulses emerges after a regime of coarsening dynamics that is saturated at the system length. For sufficiently small systems, the pulse is accompanied by periodic elasto-frictional instabilities. The properties of a single pulse, in the limit of a large system height, are then studied. The periodicity of the train of pulses is given by the system length, and the propagation velocity of the pulse is predicted based on an analogy with fracture mechanics, building on the existence of singular fields at the pulse rupture tip. This work wraps up by showing that the properties of the pulse train are determined by two system parameters: the length, and the driving velocity.

- **Chapter 6 - Statistical and dynamical complexity in a frictional system without disorder**

The statistics of slip events in frictional systems obey various power law distributions, implying scale invariance. Statistical complexity is known to emerge either because of disorder in the material properties or because of sufficiently strong non-linearity in the dynamics of the system. In this chapter, we discuss the emergence of statistical complexity in a velocity-driven frictional system in the absence of material heterogeneities. Broadly distributed slip events occur in this system. They can be classified into two categories, with small non-propagating events and large rupture-like ones. This statistical complexity emerges from self-generated stress and state heterogeneities, which are accompanied by dynamical complexity, with intricate interactions between slip events. Finally, we show that the finite geometry of the problem affects both the statistical and dynamical complexity with a characteristic reflection time scale.

- **Chapter 7 - Coupling domain-based and boundary-based methods to model complex dynamic rupture problems**

This chapter presents the coupling of the finite element method and the spectral boundary integral method, with the objective of proposing an efficient numerical method to model complex dynamic rupture problems in unbounded domains. We present the coupling formulation, based on a strong coupling of the velocities at the interface between the methods. A validation of the coupling is presented with a reference problem of elastic wave propagation, along with a comparison to other similar methods. We then show an example of a dynamic rupture simulation using the coupling.

- **Chapter 8 - Conclusion**

In this last chapter, the main results of this thesis are summarized. The potential future research directions opened up by this work are discussed.

In addition, a few topics are treated in Appendix:

- **Appendix A:** The derivation of the quasi-static cohesive line tension model that was done by Dr. Mathias Lebihain in [10] and which is used in Chapter 4 is recalled.
- **Appendix B:** My contribution to open source software is discussed, with my involvement in releasing *cRacklet*.
- **Appendix C:** In this last appendix, my participation in the Scientific Image Competition from the Swiss National Science Foundation in 2022 is presented.

2 State of the art

The aim of this work is to contribute to answering fundamental but rather basic questions such as “how do things break?”, or “how do things slide?”. The mechanics of interest here deal with processes that occur at various length scales, from the rupture of atomic bonds at the nanoscale to the propagation of cracks and frictional rupture fronts at the macroscale. In this thesis, we study rupture and friction at a continuum scale (i.e., not accounting for the discrete nature of matter). This chapter introduces the various concepts used to conduct this study. We first present *continuum solid mechanics*, followed by the *Linear Elastic Fracture Mechanics* (LEFM) framework and its extension to dynamics. We show evidence of the inherent heterogeneous nature of fracture, along with one of the tools used in the literature to study interactions between cracks and microstructure. Then, an overview of friction is presented, including the various approaches for modeling friction and its similarities with fracture mechanics. We close this chapter with a short discussion on the emergence of statistical complexity in frictional systems.

2.1 Continuum solid mechanics

Continuum solid mechanics describes the deformation and motion of a continuous solid under external solicitations (forces, displacements, accelerations...). Here we recall briefly the main principles upon which solid mechanics is built. For a complete description of the topic, the reader is redirected to reference textbooks [11; 12]. Three main principles are required: the description of the geometric change of a deformable solid (kinematics), the balance of momentum in the solid (equilibrium), and the behavior of a given material that links its stress state and its deformation (constitutive law).

2.1.1 Kinematics

We first introduce the concept of kinematics, describing the motion of matter. Let us consider the initial configuration of a body Ω à t_0 with \mathbf{x} the material coordinates, see Fig. 2.1. The displacement field \mathbf{u} is defined as the difference between the deformed position at a time t and the original one, as

$$\mathbf{u}(\mathbf{x}, t) = \mathbf{x}'(\mathbf{x}, t) - \mathbf{x}. \quad (2.1)$$

Similarly, a small segment $d\mathbf{x}$ in the deformed configuration $d\mathbf{x}'$ becomes:

$$\begin{aligned} d\mathbf{x}' &= d\mathbf{x} + \mathbf{u}(\mathbf{x} + d\mathbf{x}, t) - \mathbf{u}(\mathbf{x}, t), \\ &= d\mathbf{x} + \nabla \mathbf{u} d\mathbf{x}, \\ &= (\mathbf{I} + \nabla \mathbf{u}) d\mathbf{x}, \\ &= \mathbf{F} d\mathbf{x}, \end{aligned} \quad (2.2)$$

with $\nabla \mathbf{u}$ the gradient of the displacement field, \mathbf{I} the identity matrix and \mathbf{F} the deformation gradient tensor, that includes both the rigid body translation and the deformation of the solid. The extension of length of a small segment can be written as:

$$|d\mathbf{x}'|^2 - |d\mathbf{x}|^2 = d\mathbf{x}^T \mathbf{F}^T \mathbf{F} d\mathbf{x} - d\mathbf{x}^T d\mathbf{x} = d\mathbf{x}(\mathbf{F}^T \mathbf{F} - \mathbf{I})d\mathbf{x} = d\mathbf{x}(2\mathbf{E})d\mathbf{x}, \quad (2.3)$$

with $\mathbf{E} = 1/2(\mathbf{F}^T \mathbf{F} - \mathbf{I})$ the Green¹-Lagrange² strain tensor. The superscript T indicates a matrix transpose. This thesis is dedicated to the study of brittle materials for which one can assume small strains. The infinitesimal strain tensor $\mathbf{\epsilon}$ is used in place of the Green-Lagrange one, and the former writes:

$$\mathbf{\epsilon} = \frac{1}{2} (\nabla \mathbf{u} + \nabla \mathbf{u}^T). \quad (2.4)$$

¹George Green (1793-1841)

²Joseph-Louis Lagrange (1736-1813)

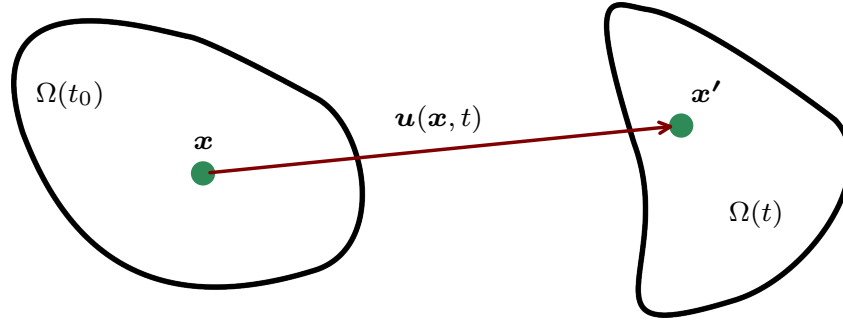


Figure 2.1: Kinematics of a deformable solid from its original configuration $\Omega(t_0)$ to a deformed state $\Omega(t)$.

2.1.2 Equilibrium and conservation

Now that kinematics have been introduced, the next step is to describe stresses in solids. Newton's³ second law states "When a body is acted upon by a force, the time rate of change of its momentum equals the force". For a block of material (see Fig.2.2) one can write the sum of forces ΣF at a time t as:

$$\Sigma \mathbf{F}(t) = \rho \ddot{\mathbf{u}}(t) dx dy dz, \quad (2.5)$$

where $\ddot{\mathbf{u}}(t)$ is the second time derivative of the displacement vector \mathbf{u} , i.e., the acceleration vector, and ρ is the volumetric mass density. dx dy and dz are the respective dimensions of the infinitesimal block that is schematically represented in Fig. 2.2. In the limit of an infinitesimal surface ΔA , the forces transmitted through this surface are called the *stresses* $\boldsymbol{\tau} = \lim_{\Delta A \rightarrow 0} \Delta \mathbf{F} / \Delta A$. The stresses acting on a surface of normal \mathbf{n} are related to the Cauchy⁴ stress tensor $\underline{\boldsymbol{\sigma}}$ as:

$$\boldsymbol{\tau} = \underline{\boldsymbol{\sigma}} \mathbf{n}. \quad (2.6)$$

The component σ_{ij} of the stress tensor corresponds to the stress acting on the surface that is normal to the i component, in the direction of j . An example is shown in Fig. 2.2 where the stresses acting on the face normal to the x axis are represented with green arrows. One can rewrite the equilibrium condition in the absence of body forces:

$$\sigma_{ij,j} = \rho \ddot{u}_i, \quad (2.7)$$

where $,j$ indicates a derivative with respect to j . Eq. (2.7) is called the Cauchy equation of motion and can be written in a compact form as:

$$\nabla \cdot \underline{\boldsymbol{\sigma}} = \rho \ddot{\mathbf{u}}, \quad (2.8)$$

³Isaac Newton (1642-1726)

⁴Augustin Louis Cauchy (1789-1857)

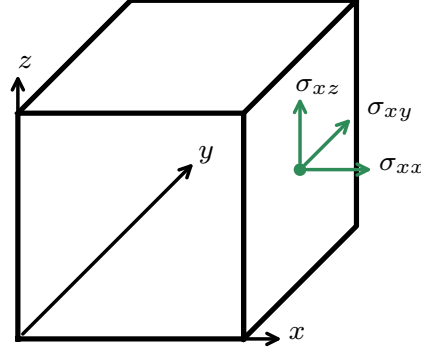


Figure 2.2: Stresses acting on one of the surfaces of a small block of size $dx \, dy \, dz$.

with ∇ the divergence operator.

2.1.3 Constitutive law

The next step consists in relating the strains and the stresses of a deformable body. This is done through a constitutive law, which represents the material behavior. The generic shape of a constitutive law writes:

$$\underline{\sigma} = \mathcal{C}(\underline{\epsilon}, t, T, \dots), \quad (2.9)$$

with \mathcal{C} a function that can depend on the strain $\underline{\epsilon}$, the time t , the temperature T , etc... The most simple constitutive law is the one of linear elasticity, Hooke's law⁵. This law will be employed to describe the behavior of solids in this thesis. The relation between stresses and strains becomes:

$$\underline{\sigma} = \underline{\underline{C}} \underline{\epsilon}, \quad (2.10)$$

with $\underline{\underline{C}}$ a fourth-order tensor. For linear isotropic elasticity, there are only two independent coefficients in $\underline{\underline{C}}$ and the constitutive law can be reduced to:

$$\underline{\sigma} = \lambda \text{Tr}(\underline{\epsilon}) \underline{\underline{I}} + 2\mu \underline{\epsilon}, \quad (2.11)$$

with λ and μ the Lamé⁶ coefficients, and $\text{Tr}(\underline{\epsilon})$ is the trace of the strain tensor. λ is called

⁵Robert Hooke (1635-1703)

⁶Gabriel Lamé (1795-1870)

the first Lamé constant and describes the material response to a change in volume. μ is known as the shear modulus and characterizes the response to shear solicitations. They are connected to the Young's⁷ Modulus of the material E and Poisson's⁸ ratio ν . Taken together, Eqs (2.4), (2.8), (2.11) allow describing the behavior of a linear elastic isotropic.

2.1.4 Boundary conditions

To solve a specific problem, boundary conditions need to be specified on the border $\partial\Omega$ of the domain Ω . These conditions can be classified into two types:

- Dirichlet⁹ boundary conditions: displacements are imposed on the boundaries $\partial\Omega_u$.
- Neumann¹⁰ boundary conditions: surface tractions τ are prescribed on the boundaries $\partial\Omega_\tau$.

The choice of boundary conditions can have a dramatic impact on the behavior of a system. This will be demonstrated in Chapter 5 in the context of a frictional system composed of two elastic bodies sliding against one another.

The *virtual work principle* allows solving such kind of problem. Let us define a virtual displacement field $\delta\mathbf{u}$ that is kinematically admissible (i.e., is continuous, differentiable and satisfies the Dirichlet boundary conditions on the body of interest). Then, the stress field $\underline{\sigma}$ is a solution of the boundary value problem of interest if the following integral is satisfied:

$$\int_{\Omega} \underline{\sigma} \delta\epsilon dV + \int_{\Omega} \rho \ddot{\mathbf{u}} \delta\mathbf{u} dV - \int_{\partial\Omega_\tau} \boldsymbol{\tau} \delta\mathbf{u} dA = 0. \quad (2.12)$$

Eq. (2.12) is known as the weak form of the equilibrium.

2.1.5 Elastodynamics

In this thesis, we are interested in the dynamics occurring during fast fracture or friction. Combining kinematics Eq. (2.4), the Cauchy equation of motion (2.8) and linear elasticity Eq. (2.11), one can write the Navier¹¹ equation:

$$(\lambda + \mu) \nabla (\nabla \cdot \mathbf{u}) + \mu \nabla^2 \mathbf{u} = \rho \ddot{\mathbf{u}}. \quad (2.13)$$

Manipulating Eq. (2.13), and using the Helmholtz¹² decomposition (any vectorial field can be decomposed as a combination of a scalar potential Φ and a vector potential Ψ , $\mathbf{u} = \nabla\Phi + \nabla \times \Psi$), then one can decompose the Navier equation in two wave equations:

⁷Thomas Young (1773-1829)

⁸Siméon Denis Poisson (1781-1840)

⁹Johann Peter Gustav Lejeune Dirichlet (1805-1859)

¹⁰Carl Gottfried Neumann (1832-1925)

¹¹Claude Louis Marie Henri Navier (1785-1836)

¹²Hermann Ludwig Ferdinand von Helmholtz (1821-1894)

$$\begin{aligned}\frac{(\lambda + 2\mu)}{\rho} \nabla^2(\nabla\Phi) &= \frac{\partial^2 \nabla\Phi}{\partial t^2} \\ \frac{\mu}{\rho} \nabla^2(\nabla \times \Psi) &= \frac{\partial^2 \nabla \times \Psi}{\partial t^2}.\end{aligned}\tag{2.14}$$

Eqs. (2.14) describe the types of waves propagating in the solid. First, the longitudinal waves $\nabla\Phi$, which are linked to the volumetric part of the strain tensor and propagate at the *dilatation wave speed* c_d , also referred to as the *pressure wave speed*:

$$c_d = \sqrt{\frac{\lambda + 2\mu}{\rho}}.\tag{2.15}$$

The second part $\nabla \times \Psi$ corresponds to shear waves, propagating at the *shear wave speed* c_s :

$$c_s = \sqrt{\frac{\mu}{\rho}}.\tag{2.16}$$

Waves can also travel at the surface of a solid as Rayleigh waves [13]. In this case, their characteristic propagation speed is c_r the *Rayleigh wave speed* which can be estimated as a fraction of the shear wave speed:

$$c_r \simeq \frac{0.862 + 1.14\nu}{1 + \nu} c_s.\tag{2.17}$$

These wave speeds control the propagation of elastic waves in the bulk, but are also relevant in describing the limiting velocities for the propagation of discontinuities, such as rupture fronts. In the following section, we shortly introduce the main concepts of fracture mechanics.

2.2 Fracture mechanics

Fracture mechanics is the science of how cracks grow in materials. Although inherent to engineering and structural design, this is a rather young thematic of research. Before the possibility of mass production of steel, structures mainly worked in compression and thus prevented spectacular failures related to tensile crack growth. The innovation based on using tensile structural components (mainly steel) brought along the potential occurrence of crack growth and motivated the understanding of fracture mechanics. This section aims at introducing the main principles of the discipline. The reader interested in the topic is referred to the reference textbooks [14; 15].

2.2.1 Linear elastic fracture mechanics

Several centuries ago, Leonardo da Vinci¹³ conducted experiments on iron wires and observed that their strength is inversely proportional to their length, implying that the resistance of materials is controlled by the presence of flaws: the larger the volume, the more likely it is to find a large flaw in the sample that would reduce its strength. In the 1920s, Griffith [1] conducted the first quantitative analysis of the influence of flaws on the fracture strength of materials, which is several orders of magnitude lower than the strength of atomic bonds. Building on the stress analysis of an elliptical hole [16], Griffith proposed an energy-based criterion to predict the growth of flaws, based on the first law of thermodynamics. This allowed overcoming the difficulties of formulating a stress-based fracture criterion related to the *infinite* stress concentration near a sharp crack. Griffith's criterion states that a fracture grows when the change in potential energy dE_{pot} due to an increment of crack size dA is sufficient to compensate for the energy cost of creating new surfaces,

$$-\frac{dE_{\text{pot}}}{dA} = 2\gamma_s, \quad (2.18)$$

with γ_s the surface energy of the material. Eq. (2.18) is known as the *Griffith energy balance*. Note that the factor 2 appears as growing a crack creates two new free surfaces. This approach was successfully applied to glass (a perfectly brittle material) but could not be extended immediately to steel (i.e., to ductile materials), as energy dissipation in the latter is not only related to surface creations but also to plastic deformations. Significant efforts and advances in fracture mechanics resulted from the *Liberty ships* failures, a model of welded boat designed during World War II that experienced significant and serious fractures, with some of the boats breaking in half. After the war, Irwin and Williams independently built on the contribution of Westergaard [17] who derived the stress fields near a crack inside an infinite plate subject to a remote tensile load σ_{yy}^0 . In this case, the tensile stress σ_{yy} in the plane of the crack $y = 0$ writes:

$$\sigma_{yy}(x) = \frac{\sigma_{yy}^0}{\sqrt{1 - (a/x)^2}}, \quad (2.19)$$

with a the half-crack size. For $|x| < a$, the normal stress is equal to zero, as free surfaces cannot sustain tensile stress. Irwin conducted a limit analysis of this solution [2], while Williams [18; 19] derived the asymptotic fields for any crack configurations. They both concluded that the fields near the crack tip are dominated by a singular contribution (the first term in the Williams series [19]). The asymptotic fields can be written as:

$$\lim_{r \rightarrow 0} \sigma_{ij;m}(r, \theta) = \frac{K_m}{\sqrt{2\pi r}} f_{ij;m}(\theta), \quad (2.20)$$

with (r, θ) the coordinates of a polar system whose origin is the crack tip, f_{ij} dimension-

¹³Leonardo di ser Piero da Vinci (1452-1519)

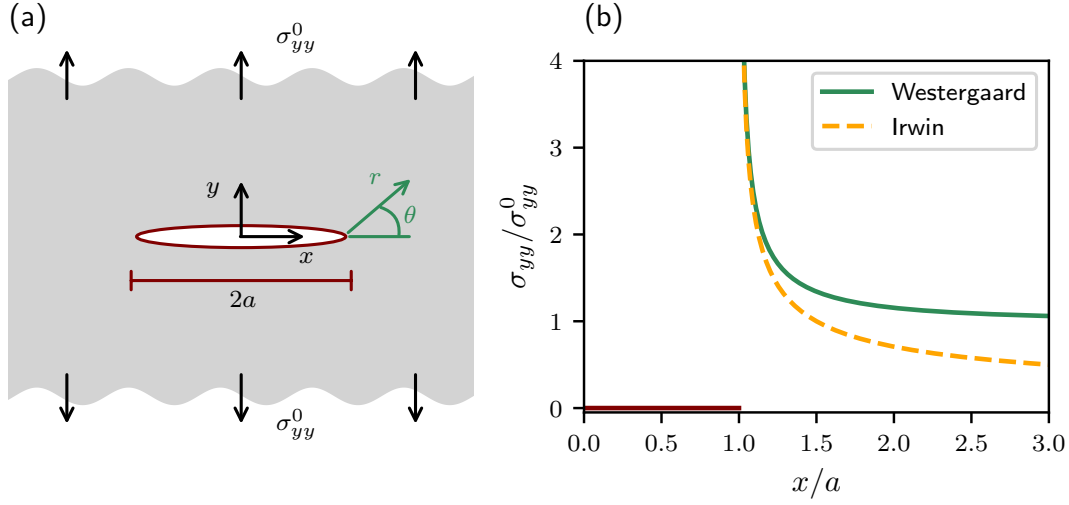


Figure 2.3: (a) Schematic representation of a crack of length $2a$ (in brown) in an infinite body under tensile loading σ_{yy}^0 . Two coordinate systems are shown: a Cartesian system whose origin is the crack center, and a polar one whose origin is the right crack tip. (b) The stress σ_{yy} at $y = 0$ next to the right crack tip. Inside the crack $x/a < 1$, the tensile stress is zero, as shown in brown. The exact solution from Westergaard Eq. (2.19) is shown in green. Close to the tip, the singular approximation of Irwin Eq. (2.20), in dashed orange, describes accurately the full solution.

less functions of the angle, and the subscript m indicating the mode of rupture which can be either tensile fracture (mode I), in-plane shear (mode II) or out-of-plane shear (mode III), see Fig. 2.4. The term K was introduced by Irwin as the *stress intensity factor* which defines the amplitude of the singularity at the crack tip. The stress intensity factor for each rupture mode is controlled by the remote loading and the geometry:

$$\begin{bmatrix} K_I \\ K_{II} \\ K_{III} \end{bmatrix} = Y \sqrt{\pi a} \begin{bmatrix} \sigma_{yy}^0 \\ \sigma_{xy}^0 \\ \sigma_{zy}^0 \end{bmatrix}. \quad (2.21)$$

Y is a dimensionless scalar representing the problem geometry. σ_{yy}^0 , σ_{xy}^0 and σ_{zy}^0 are respectively the remote tensile stress, the in-plane shear stress, and the out-of-plane shear stress. The asymptotic field for σ_{yy} given by Eq. (2.20) is compared to the exact solution of Eq. (2.19) in Fig. 2.3.

By comparing the change of potential energy inside an elastic material between two successive crack configurations of length a and $a + \delta a$, Irwin showed that this change in energy, called the *energy release rate* $G = -dE_{\text{pot}}/dA$ is entirely determined by the near-tip stress field, i.e., by the singular approximation :

$$G = \frac{1 - \nu^2}{E} (K_I^2 + K_{II}^2) + \frac{1}{2\mu} K_{III}^2. \quad (2.22)$$

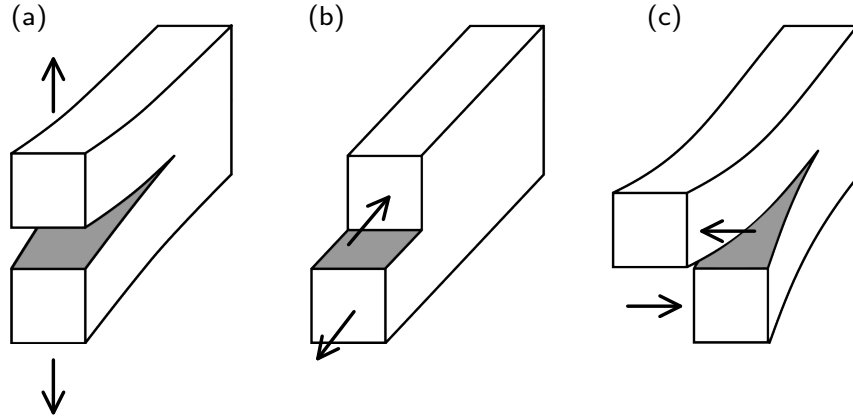


Figure 2.4: Schematic representation of the three fracture modes: (a) Mode I: opening, with the loading applied normally to the crack plane (in gray). (b) Mode II: In-plane shear (c) Mode III: Out-of-plane shear.

Eq. (2.22) makes the link between the local picture of fracture mechanics, with the stress intensity factor K , and the global/energetic approach of Griffith with the energy release rate G .

Irwin extended this framework to ductile materials by adding the dissipation related to local plastic flaws to the surface energy. The fracture energy G_c thus represents all the dissipative processes occurring near the crack tip:

$$G_c = 2(\gamma_s + \gamma_p), \quad (2.23)$$

with γ_p the plastic energy dissipated per unit area of crack created. The criterion for crack propagation given by Eq. (2.18) can be rewritten as:

$$G = G_c. \quad (2.24)$$

Based on the stresses near the crack tip, three regimes can be distinguished, see Fig. 2.5:

1. Close to the crack tip, the stresses diverge, which is impossible as real materials do not have infinite strength. Elasticity thus breaks down over a small length scale called the *process zone size*, where all the dissipative processes embedded in G_c occur.
2. After this length scale, the behavior is still dominated by the singular term scaling with $1/\sqrt{r}$
3. Far from the crack, higher-order terms of the Williams series dominate the behavior and the stress fields converge toward the far-field stresses.

The validity of Eq. (2.22) assumes proper separation of length scales, i.e., that the process

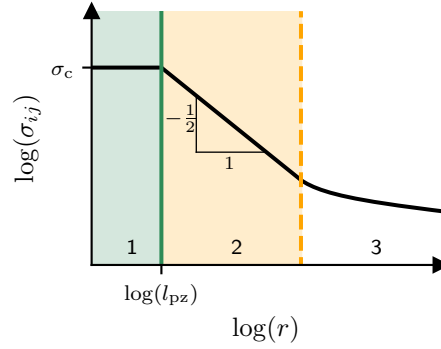


Figure 2.5: 1. Really close to the crack tip, the stresses are limited by the strength of the material, here σ_c . This is the process zone size l_{pz} , in light green. 2. The stresses are then dominated by the singular term $1/\sqrt{r}$, note the slope $-1/2$ in a double logarithmic scale. The singularity-dominated region is filled in orange. 3. Stresses slowly reach the far-field value.

zone size is sufficiently small in front of the other length scales in the problem (e.g., the crack size), and that the singularity-dominated region does exist (the crack is far enough from the boundary conditions). If this is the case, the stability of cracks is controlled entirely by the intensity of the singular fields. This is known as *K-controlled fracture*. An estimation of the process zone size can be found using the strength of the material σ_c and writing $\sigma(r = l_{pz}) = K_c / \sqrt{l_{pz}} = \sigma_c$, where K_c is the critical stress intensity factor of the material. Note that the energy balance criterion of Eq. (2.24) is equivalent to writing $K = K_c$. The process zone size can be estimated as:

$$l_{pz} \sim \left(\frac{K_c}{\sigma_c} \right)^2. \quad (2.25)$$

To describe the behavior of the material in this region where dissipation occurs, Dugdale [20] and Barrenblatt [21] proposed a *cohesive approach of fracture* in which the crack is smeared over some distance, with the stresses being reduced from the peak strength of the material σ_c to zero. This allows regularizing the infinite stresses near the tip without losing the universality of the linear elastic mechanics' framework.

While originally developed for brittle materials, the framework of LEFM has been successfully applied to predict the failure of a large range of materials, including ductile behavior and fatigue solicitations. This theory has been naturally extended toward cracks outside of equilibrium, which is discussed next in section 2.2.2. The influence of material heterogeneities is introduced in section 2.2.3.

2.2.2 Dynamic fracture mechanics

The common approach to studying dynamic fracture is to consider a crack moving at a steady velocity v_c and solve the elastodynamic equations in a moving referential whose

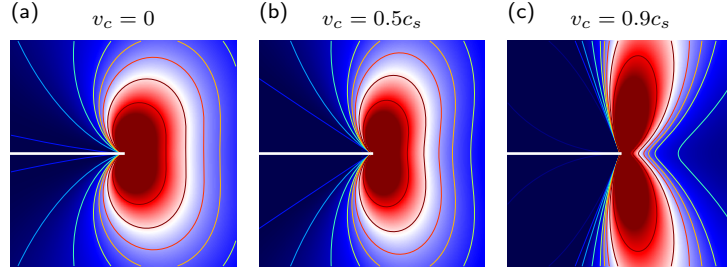


Figure 2.6: Hoop stress field near a steadily moving tensile crack propagating at (a) $v_c = 0$ (b) $v_c = 0.6c_s$ and (c) $v_c = 0.9c_s$.

origin coincides with the crack tip. The reader interested in the derivations of such solutions is referred to the reference textbooks, such as [15]. Similarly to the static case, the asymptotic fields at the tip of a crack moving at a steady velocity inside a continuum elastic body can be written as:

$$\lim_{r \rightarrow 0} \sigma_{ij;m}(r, \theta, v_c) = \frac{K_m(v_c)}{\sqrt{2\pi r}} f_{ij;m}(\theta, v_c), \quad (2.26)$$

where K is now called the *dynamic stress intensity factor* and is a function of the front velocity. Note that the dimensionless functions $f_{ij;m}$ also depend on the velocity. An example of the asymptotic hoop stress near a crack tip propagating at a steady velocity v_c under tensile loading is shown in Fig. 2.6. The shape of the stress field near the crack tip changes with increasing velocity, impacting the shape and size of the process zone. The dynamic stress intensity factors $K_m(v_c)$ are functions of the static stress intensity factors, as $K_m(v_c) = K_m(0)k_m(v_c)$ with $k_m(v_c)$ dimensionless functions of the tip velocity. One can generalize the concept of local energy balance for a dynamic crack. Eq. (2.22) can be written as:

$$G_c = G = \frac{1 - \nu^2}{E} (A_I K_I^2 + A_{II} K_{II}^2) + \frac{1}{2\mu} A_{III} K_{III}^2, \quad (2.27)$$

where A_m are universal functions of the velocity:

$$A_I(v_c) = \frac{\alpha_d v_c^2}{(1 - \nu) D c_s^2}, \quad (2.28)$$

$$A_{II}(v_c) = \frac{\alpha_s v_c^2}{(1 - \nu) D c_s^2}, \quad (2.29)$$

$$A_{III}(v_c) = \frac{1}{\alpha_s}, \quad (2.30)$$

with $\alpha_{s,d} = \sqrt{1 - v_c^2/c_{s,d}^2}$ and $D = 4\alpha_s\alpha_d - (1 + \alpha_s^2)^2$.

It is worth mentioning that with accelerating crack velocity, the size of the process zone (measured on the plane of the crack $y = 0$) shrinks. This is known as the Lorentz¹⁴ contraction [22] of the process zone size, and is directly related to the shape of the stress fields for dynamic cracks, as shown in Fig. 2.6. The dynamic process zone size writes:

$$l_{pz}(v_c) = \frac{l_{pz}(v_c = 0)}{A_m(v_c)}, \quad (2.31)$$

with $l_{pz}(v_c = 0)$ the process zone size at rest. The dynamic change of process zone size with crack velocity is relevant when discussing the interaction of a crack with material heterogeneities [23], which is briefly introduced in section 2.2.3 and then studied in detail in Chapter 4.

The propagation velocity of dynamic cracks is bounded by the celerity of the elastic waves in the surrounding bulk. By looking at the behavior of the functions $A_{I,II}$, one can see that the energy release rate becomes negative for $c_r < v_c < c_s$, thus forbidding propagation at these velocities for tensile and in-plane shear cracks. Supershear propagations $c_s < v_c < c_d$ are however possible in mode II, the partial differential equations being different in this case and resulting in a positive energy release rate. For mode III, the limiting velocity is c_s . Note that the process zone size is expected to vanish when a crack propagates at the limiting velocity.

While LEFM was successfully applied to static fracture problems, its extension to dynamic has proven significantly more difficult. In the following section, we show some dynamic fracture experiments and highlight the discrepancies with the theory.

Dynamic fracture experiments

The first striking observation arising in dynamic fracture experiments is the difficulty to observe propagation velocities that approach the previously discussed theoretical limits. While the theory predicts that under constant loading a crack would accelerate toward its limiting velocity, in practice the propagation velocity of tensile cracks rarely exceeds $\sim 0.6c_r$. The dissipated energy of dynamic cracks is also significantly underestimated by the theory. The fast propagation of cracks is usually accompanied by out-of-plane damage (see Figs. 2.7, 2.8) that occurs through the formation of various structures (steps, microcracks, macrocracks...). This is in sharp contrast with the LEFM representation of fracture, where damage is confined near the crack tip. Note that one notorious exception to this discrepancy is the fracture of weak interfaces, in which a preferential plane of fracture exists in the material. This can be related to the material structure (composites, laminates) or to the problem configuration (frictional cracks between two solids). In this case, the preferential fracture plane is significantly weaker than the bulk material, thus forbidding out-of-plane damage from occurring. Propagations near the limiting velocities have been observed in this context, with both subshear and supershear

¹⁴Hendrik Antoon Lorentz (1853-1928)

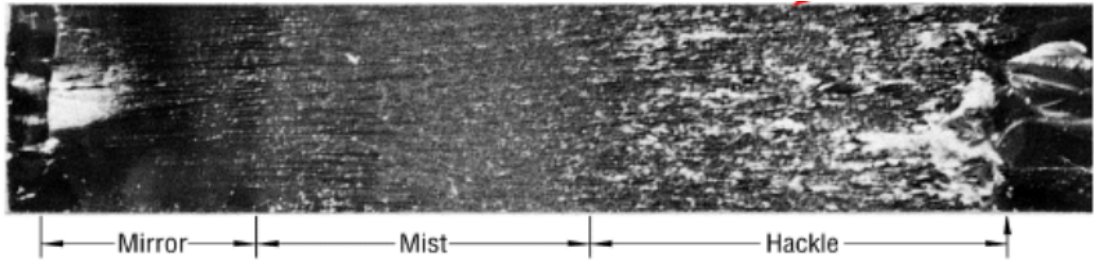


Figure 2.7: Appearance of the fracture surface of an Homalite specimen, taken from [26]. The crack propagates from left to right and accelerates, resulting in an increasingly rougher fracture toward the right of the sample.

ruptures for frictional cracks [24]. Another exception is encountered in thin samples when the thickness is comparable to the dimension of the microbranches. In this case, the microbranching instability is suppressed, and tensile cracks can reach velocities close to $\sim 0.9c_s$, at which a different dynamic instability occurs [25].

Going back to experiments that differ from the theory, it has been observed that the crack surfaces have a different appearance depending on the propagation velocity [26; 27; 28]:

1. For small v_c , a single crack front propagates smoothly and this results in two smooth *mirror-like* crack surfaces.
2. With increasing v_c the crack surface roughens, with the occurrence of some out-of-plane damage through stepping.
3. At large v_c , micro-branching instabilities occur and significant out-of-plane damage takes place.

The change of stress field shape with the crack velocity increases the stresses out of the main crack plane and allows dissipation through the creation of additional surfaces in supplement to the main crack. Taking into account the complex structures created during the fracture process is thus necessary to verify energy balance [29]: the amount of energy dissipated is consistent with the energy required to create these additional surfaces, as observed for example for steps [28]. In the case of microbranches, the energy required for their creation can be an order of magnitude larger than for a smooth crack [30]. The corresponding energy is thus not available to drive the main crack, explaining the lower propagation velocity compared to the theory. This behavior reveals the inherent heterogeneous nature of dynamic rupture, as a result of the complex interaction between dynamic instabilities, the evolution of the elastic fields with the velocity and the presence of material heterogeneities.

Another example of the complex behavior of dynamic fracture is the formation of comet-like patterns at the surface of a polymethyl methacrylate (PMMA) specimen [31]. In these experiments, the main crack propagates through the nucleation and propagation of multiple micro-cracks ahead of the main front, and the macroscopic velocity is directly

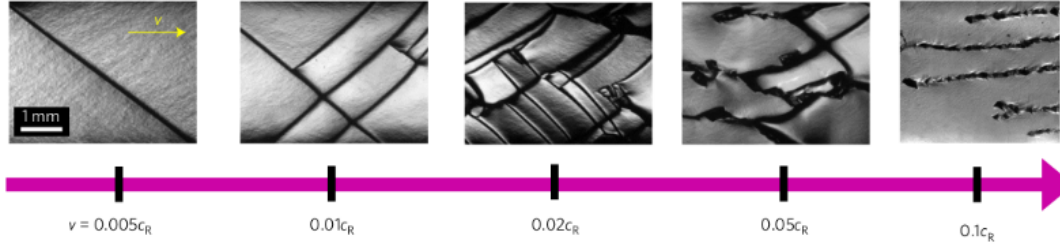


Figure 2.8: Appearance of the fracture surface of a brittle polyacrylamide gel, taken from [28]. For small velocities, the fracture surfaces are either mirror-like or contain a single step line. The number of steps increases with the velocity, up to a point where microbranches start appearing around $v_c = 0.05c_r$. At $v_c = 0.1c_r$, only microbranches remain.

related to the density of nucleated defects, illustrating again the heterogeneous nature of dynamic rupture. In the next section, we shortly introduce heterogeneous fracture mechanics.

2.2.3 Heterogeneous fracture mechanics

Natural (e.g. rocks) and artificial (e.g. composites) heterogeneous materials are ubiquitous. As fracture is essentially controlled by dissipation that occurs over a small length scale near the crack tip, the presence of small-scale material heterogeneities might have a significant effect on the macroscopic response of a material. In this manuscript, we limit ourselves to co-planar crack propagation and thus will only consider heterogeneities in the toughness properties $G_c(\mathbf{x})$ of the interface (with \mathbf{x} the vector position in the fracture plane).

One of the main goals of studying heterogeneous fracture is to assess the effective toughness of a microstructure. The presence of heterogeneities in the fracture toughness results in the roughening and deformation of the crack front (see examples in Fig. 2.9), e.g., parts of the front get pinned by strong heterogeneities. The deformations of the front alter the stress intensity factor locally, which can in turn affect the propagation of the entire rupture front. Crack front deformations are thus reminiscent of the material disorder, and understanding how they occur can tell us about the properties of a given material. The reader interested in the subject is redirected to [34; 35] for reviews on the topic.

Line tension model

Perturbative approaches in fracture mechanics are widely used in the literature to study heterogeneous fracture problems. The *line tension model*, proposed by Rice [36] based on the weight functions theory of Bueckner [37] allows computing local stress intensity factor variations arising from small perturbations of the crack front geometry.

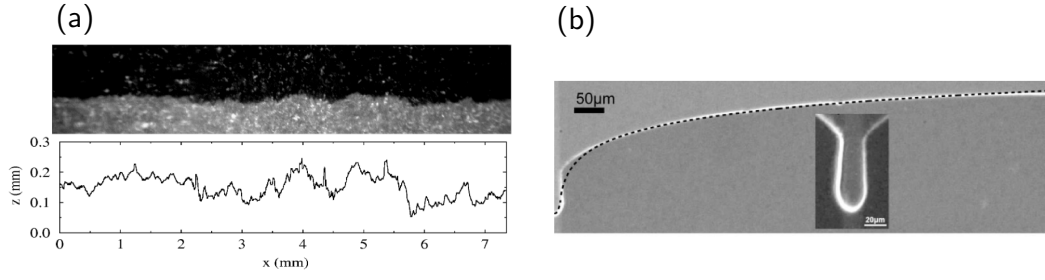


Figure 2.9: (a) Tensile fracture experiment on Plexiglas, taken from [32]. The top shows a raw picture of the specimen, with black being the intact material. Here the crack propagates from the bottom to the top. The location of the crack front is presented at the bottom. (b) Peeling experiments of a silicon elastomer block from a patterned glass substrate, taken from [33]. The deformation of the front is due to the presence of a large toughening obstacle at the center of the specimen. The location of the crack front is shown in white. The inset is a view centered on the tough obstacle, while the main panel shows the front profile of half of the specimen.

When coupled with a local propagation criterion of the type $K(x) = K_c(x)$, one can evaluate crack propagation in heterogeneous fields of toughness. This framework has been successfully applied to the study of front deformations in the presence of various shapes of inclusions [33; 38; 39], to the computation of the effective fracture toughness of heterogeneous materials [40; 41; 42] and to rationalize the intermittent dynamics of front propagation in disordered media [43]. This framework has been extended to dynamics with the works of [44; 45]. However, the *line tension model* is based on the assumption of the LEFM for which the process zone size is negligible. All asperity scales are thus treated in the same way. Yet, as elasticity breaks down at the scale of the process zone, heterogeneities that are smaller than this dissipation length scale are expected to affect the crack behavior differently than larger ones. Indeed, recent studies have shown, for example in the context of the propagation of a shear crack along a one-dimensional interface (thus without front deformations) [46] that heterogeneities in the propagation of the crack direction only alter the crack dynamics if their size is comparable to the process zone. Chapter 4 is dedicated to the study of front deformations in heterogeneous materials when the process zone size is assumed to not be negligible. In this chapter, we compare the *dynamic cohesive line tension model* to numerical simulations. This model is the dynamic version of the *quasi-static cohesive line tension model*, a recent extension of the classical *line tension model* whose derivation is recalled in Appendix A [10].

2.3 Friction

Frictional systems are ubiquitous in natural and man-made systems and are found at all scales, ranging from geological tectonic faults [47] to engineering structures and devices [48]. Understanding how two solids in contact slip relative to each other is of paramount importance in describing the dynamics of such systems. For engineering applications, the objective might be to decrease the frictional resistance to reduce the energy required to overcome friction (*one-fifth* of the energy in the world is dissipated by friction [3]). On the contrary, specific applications aim at maximizing the friction force, for example for car brakes. In addition, understanding how frictional instabilities might develop and lead to catastrophic motion is of great interest to studying earthquake physics, for example. Due to its prevalence in nature and its implications in engineering, friction is one of the oldest scientific problems known to mankind. Evidence of practical solutions employed by man to modify friction is found in Ancient Egypt murals illustrating a man wetting sand to reduce the friction between the ground and a statue being pulled [49], see Fig. 2.10. Another historical example comes from the notebooks of Leonardo Da Vinci who was the first to conduct a systematic study of the force resisting the relative motion between bodies using weights attached by strings and pulleys [50], see Fig. 2.11.



Figure 2.10: A wall painting from 1880 B.C. on the tomb of Djehutihotep [49].

Friction is an inherently complex phenomenon as it couples several length scales and time scales, and involves strongly non-linear behavior. The accumulation of strain energy prior to failure usually occurs over long time scales (e.g., tectonic loading taking years) while slip events are extremely fast in comparison. At small length scales, the contact between two surfaces occurs at the asperity level due to the inherent roughness of surfaces [51] and the mechanics of the micro-contacts are responsible for the highly non-linear response of frictional interfaces: the asperities are loaded under extreme conditions and continuously evolve [52; 53]. In the context of tectonic fault, the contact

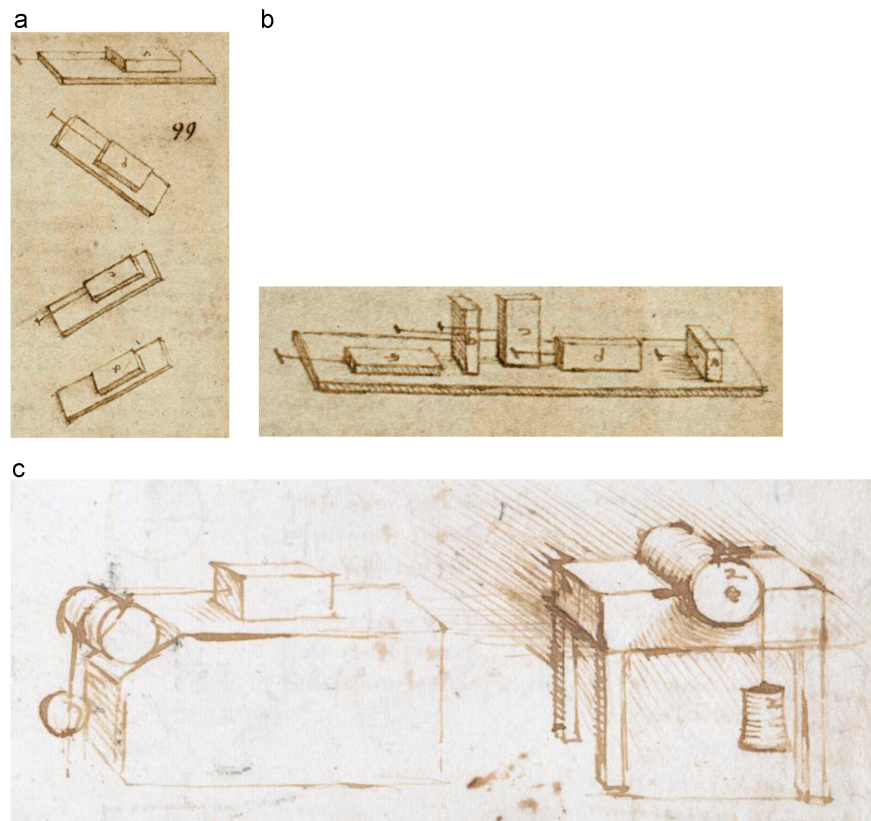


Figure 2.11: Sketches from two different pages in Leonardo's notebooks: (a, b) from Codex Atlanticus, Biblioteca Ambrosiana, Milan (CA folio 532r c. 1506–8), and (c) from Codex Arundel, British Library, London (Arundel folio 41r c. 1500–05), a figure taken from [50].

is not directly between two solid bodies, but rather a third granular body called gouge mediates the frictional behavior. In addition, at large-scale, different parts of the bulk surrounding the frictional interface are coupled through long-range elastodynamics which controls the release of strain energy through slipping. When a slip nucleates somewhere along an interface, it might progressively propagate and invade the contact plane still at rest. The propagation of these *slip fronts* is driven by a balance of energy similar to the propagation of shear cracks. Fig. 2.12 shows a typical frictional system. This section introduces the various models of friction, the rupture modes in frictional rupture and the analogy with fracture mechanics. A discussion on the existence of statistical complexity in frictional systems concludes this section.

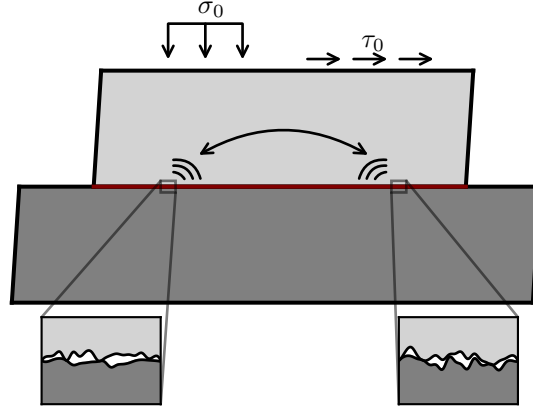


Figure 2.12: A schematic of a frictional system. Two bodies are in contact along an interface (in brown) that is composed of several microcontact junctions (zoom in). The system is loaded with normal and tangential stresses far from the interface (note that it can also be driven by imposed displacement or velocity). The stress state at the interface results from the interaction between the rheology of the microcontacts and the stresses mediated by the elastic bulk surrounding it, including the loading and the long-ranged interaction of various parts of the interface that have slipped differently (shown by the double head arrow).

2.3.1 Models of friction

2.3.1.1 A brief history of friction

Friction, and hence the friction force associated, describe the resistance to the sliding motion of a body on top of another. Our modern understanding of friction starts with the works of Amontons [4] and Coulomb [5] and their observations that the frictional force τ^{str} resisting the motion between two bodies is independent of the surface area but increases with the normal pressure. One can write the frictional force as a function of the pressure σ_0

$$\tau^{str} = f\sigma_0, \quad (2.32)$$

with f being called the friction coefficient. As long as the existing shear stress τ applied on the interface is lower than $f\sigma_0$ there is no relative motion between the two bodies, i.e., the interface is sticking. When the shear strength is exceeded, sliding starts. For Coulomb, the origin of the friction coefficient f emerges from the shear stress required to initiate slip between two corrugated surfaces [54], and its value depends on the topography of the contact surfaces. Several decades later, Bowden and Tabor [55]

showed that the contact between two solid bodies only occurs over a tiny portion of the apparent contact area A and that this real area of contact A_r increases with the normal pressure [52; 53; 56]. Bowden and Tabor [55] reinterpreted the Amontons-Coulomb law with this real contact area. As the bodies are touching only at microcontacts, these contact points are highly stressed and the local pressure reaches the material yield stress, σ_y such that one can write the far field normal pressure as:

$$\sigma_0 = \frac{A_r}{A} \sigma_y. \quad (2.33)$$

The shear stress is also localized at the contact points and can be written

$$\tau = \frac{A_r}{A} \tau_y, \quad (2.34)$$

with τ_y the yield strength of the contact junctions. Hence, the ratio between the macroscopic shear stress and the normal stress is independent of the apparent contact area

$$f = \tau_y / \sigma_y. \quad (2.35)$$

Another rupture mechanism involves the fracture of the microcontacts [57] instead of their plastic deformation. Recently, the transition between the two mechanisms (brittle fracture and plastic shearing of the contact asperities) has been shown to occur at a critical contact size [58; 59].

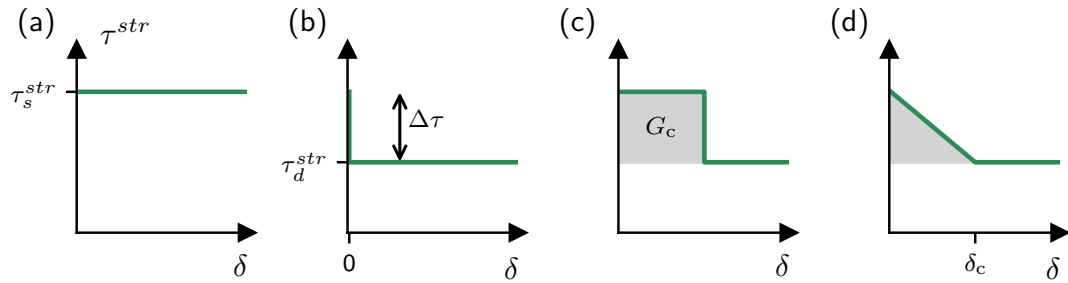


Figure 2.13: Frictional strength $\tau^{str} = f\sigma_0$ for various friction laws: (a) constant Coulomb friction (b) Static/dynamic friction (c) Constant stress cohesive model [20; 21] (d) Linear slip weakening [60; 61; 62]. The area in gray represents the energy G_c that is dissipated during the transition from static to dynamic friction.

Although the constant friction coefficient model of Coulomb (see Fig. 2.13a) is a great approximation that is useful for many engineering applications, it cannot describe the complex dynamics of frictional systems such as stick-slip. Indeed, the succession of stick and slip events arises from the weakening of the interface when slipping. Further models introduce a dynamic friction coefficient f_d which is typically lower than the static one f_s , thus introducing a notion of stress drop $\Delta\tau = (f_s - f_d)\sigma_0$ and allowing slip instabilities. Several different models describe how the transition between these

two coefficients occurs: in the most simple view, the friction coefficient drops to the dynamic value as soon as slip occurs (see Fig. 2.13b). In cohesive models, a given amount of energy G_c has to be dissipated to transition to the dynamic values. These models were initially proposed for regularizing stress concentration in tensile fracture, by Dugdale and Barrenblatt [20; 21]. They first assumed constant cohesive stress (see Fig. 2.13c), and were then modified by Palmer and Rice to include a linear decrease of the stress with the distance [63]. Rabinowicz [64] showed that a characteristic slip distance δ_c controls the transition between static and dynamic friction values, leading to the slip weakening model proposed by Ida [60] and Andrews [61; 62]. The latter is frequently used in the literature for describing the behavior of frictional interfaces. For this slip-weakening law shown in Fig. 2.13d, the frictional strength transition from a peak value τ_s^{str} to a dynamic value τ_d^{str} over a given slip distance δ_c which is associated with the micro-contact evolution or grain rearrangement. These models provide a direct analogy with the cohesive models used in the framework of fracture.

However, it has also been experimentally observed that the dynamic friction coefficient depends on the sliding velocity and the time of contact of the interfaces. These observations motivated the rate and state friction framework initially proposed by Dieterich [65] and Ruina [7], in which the friction coefficient $f_d(v, \phi)$ is function of the slip rate v and a state variable ϕ which represents the maturity of the micro-contacts. This framework is discussed in detail hereafter.

2.3.1.2 The rate and state friction framework

These models were initially introduced as phenomenological laws based on laboratory observations of friction experiments at low slip velocity showing that the dynamic friction coefficient f_d is not a constant value. In what follows, we drop the subscript d for readability. The first observation is a strengthening occurring during stationary contact, with a logarithmic increase of the friction coefficient with time [65; 66]

$$f \propto \log(t). \quad (2.36)$$

Second, the friction coefficient depends on the sliding velocity and decreases with the logarithm of the velocity [67; 68; 69; 70]

$$f \propto -\log(v). \quad (2.37)$$

The reader interested in the details can refer to Marone's review [71]. These observations lead Dieterich [67; 6] and Ruina [7] to propose a generic empirical function for $f(v, \phi)$.

$$f^{\text{DR}}(v, \phi) = f_0 + a \log\left(\frac{v}{v_*}\right) + b \log\left(\frac{v_* \phi}{D}\right). \quad (2.38)$$

In Eq. (2.38), v is the slip velocity and ϕ is an internal state variable that describes the evolution of the interface state (and thus its memory). f_0, a, b, v_*, D are empirical parameters derived from laboratory experiments. Their physical interpretation is discussed

later. In Eq. (2.38), the term with the logarithm of the velocity accounts for the *non-linear viscosity* of the interface while the term with the state variable represents the *evolution effect*. The typical response due to sudden changes in velocity predicted by a generic rate and state friction law is shown in Fig. 2.14. In addition to the relation for the friction coefficient given by Eq. (2.38), an evolution law $\dot{\phi}(v, \phi)$ is also required. Several versions of this evolution law exist. The first two that were proposed are the so-called *aging law* [6]

$$\dot{\phi}(v, \phi) = 1 - \frac{v\phi}{D}, \quad (2.39)$$

and the *slip law* [7]

$$\dot{\phi}(v, \phi) = \frac{v\phi}{D} \log \left(\frac{v\phi}{D} \right), \quad (2.40)$$

One of the usual interpretations of the state variable ϕ is the maturity of the microcontacts, i.e., their average lifetime. The *aging law* hence represents the increase in real contact area for stationary contact due to the creep of microcontacts that was observed by Dieterich and Kilgore [52]. During sliding, the law describes how microcontacts are rejuvenated. For steady-state sliding, the destruction of existing microcontacts and the creation of new ones occur at the same rate such that ϕ reaches a constant value ($\dot{\phi} = 0$):

$$\phi_{ss} = \frac{D}{v_{ss}}, \quad (2.41)$$

with v_{ss} the steady-state sliding velocity. D is the characteristic size of the microcontacts. Slip is required to occur over this length scale in order to bring the interface from one state to another.

Combining Eq. (2.38) and Eq. (2.41), it can be seen that rate and state friction is velocity weakening if

$$\frac{df_{ss}}{d \log(v_{ss})} = a - b < 0. \quad (2.42)$$

This behavior has been extensively observed experimentally [53] but materials can also feature velocity strengthening behavior (e.g. granite at high-temperature [72; 73]). The sign of $a - b$ thus controls the stability: a fault is unstable if the associated friction law is velocity-weakening. Note that this is a necessary but not a sufficient condition for rupture nucleation: the perturbation of a velocity weakening fault will result in the spontaneous propagation of frictional rupture fronts only if the perturbed size is larger than a critical nucleation size L_c . The determination of the latter is extensively discussed in the literature [74; 7; 75; 53; 76; 77; 78; 79; 80]. One implication of the stability of frictional interfaces being governed by $a - b$ in the context of geophysics is that $a - b$ is a non-monotonous function of the depth [81]. Crustal faults are strengthening at low and large depth, with a rate weakening zone in between, determining where earthquakes can potentially be nucleated.

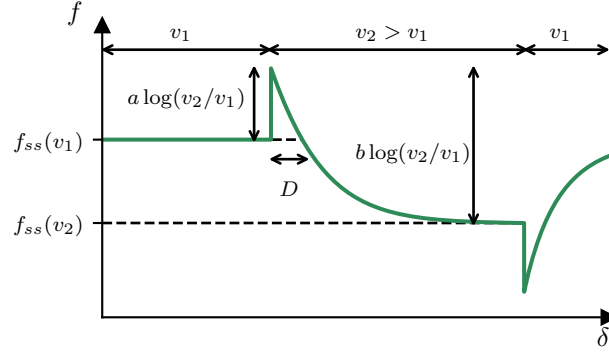


Figure 2.14: Evolution of the friction coefficient f to a sudden change in sliding velocity. The system is initially in steady-state sliding at velocity v_1 with a steady-state friction coefficient $f_{ss}(v_1)$. The velocity is then raised to v_2 and the friction coefficient increases immediately. It is then followed by a slow decrease of the friction coefficient related to the evolution of the state variable. After some time (and slip), the system reaches again a steady-state, characterized by v_2 and $f_{ss}(v_2)$. Bringing back the velocity to v_1 results in an immediate drop in the friction coefficient, followed by a slow increase that is again related to the evolution of the microcontacts.

It is important to note that during fast slip, the rate and state friction framework can be mapped to a slip weakening behavior [80; 82; 83; 84]. It is then possible to define an apparent critical slip distance

$$\delta_c^{eff} \approx D \log \left(\frac{v_r}{v_{bg}} \right), \quad (2.43)$$

with v_r the residual velocity left behind the rupture and v_{bg} the background velocity. From this critical slip distance, one can estimate an equivalent fracture energy [80; 83]

$$G_c \approx \frac{1}{2} D b f_0 \sigma_0 \log^2 \left(\frac{v_r}{v_{bg}} \right). \quad (2.44)$$

Although the original formulations assumed $a - b$ to be independent of the sliding velocity, several works illustrated non-monotonous behavior of the friction law with the velocity [53; 85; 86; 87; 88; 89]. One of the formulations that goes beyond the rate and state formulation originally proposed by Dieterich and Ruina is the *N-shaped* rate and state law that features rate-weakening at intermediate velocities and a strengthening behavior at really low and high sliding velocities. This friction law writes:

$$f^N(|v|, \phi) = \left[1 + b \log \left(1 + \frac{\phi}{\phi_*} \right) \right] \times \left[\frac{f_0}{\sqrt{1 + (v_*/|v|)^2}} + a \log \left(1 + \frac{|v|}{v_*} \right) \right], \quad (2.45)$$

and

$$g(|v|, \phi) = 1 - \frac{|v| \phi}{D} \sqrt{1 + (v_*/v)^2}, \quad (2.46)$$

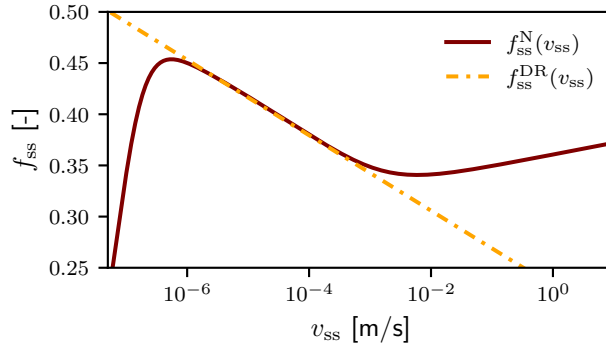


Figure 2.15: The steady-state frictional strength f_{ss} vs. the steady-state slip velocity v_{ss} , presented on a semi-logarithmic scale for two constitutive laws. The first (solid brown curve), which features an N shape and is denoted by $f_{ss}^N(v)$ (see legend), corresponds to Eqs. (2.45)-(2.46). The second constitutive law (dotted-dashed orange curve) corresponds to the original formulation given in Eq. (2.38) with either of Eq. (2.39) or Eq. (2.40) (the steady-state for the aging and the slip law is the same) and is denoted by $f_{ss}^{DR}(v_{ss})$.

with ϕ_* an additional empiric parameter. This formulation differs from the original one in three major aspects: the "+1" term in the logarithm of the velocity and the function $\sqrt{1 + (v_*/|v|)^2}$ ensures that the friction coefficient vanishes for $v = 0$ and that the behavior at very small velocity is rate-strengthening (this regime is related to the creep of microcontacts). The "+1" term in the logarithm of the state leads to the existence of a velocity-strengthening branch at large velocity [86]. Finally, the modification of the evolution law with the term $\sqrt{1 + (v_*/|v|)^2}$ ensures that the state variable saturates after an extremely long time instead of diverging to infinity.

While the rate and state friction framework was originally proposed as an empirical framework, significant efforts have been made to physically motivate this formulation [90; 91]. Baumberger [53] linked it to the microcontacts model that was originally formulated by Bowden and Tabor [55] and related the state field to the real contact area as $A_r \propto 1 + b \log(\phi v_*/D)$. The rate dependence of the friction resistance is usually described using a stress-biased thermal activation process [53; 86].

2.3.1.3 Beyond friction

Even if the friction law discussed in the previous paragraph goes beyond the original formulation of rate and state friction law by including a non-monotonic evolution of the friction coefficient with the sliding velocity, it is at most logarithmically dependent on the velocity. However, experimental evidence of dramatic velocity weakening at high speed shows a relationship stronger than logarithmic with the velocity as $f \propto 1/v$ [92; 93; 94]. Plus, in the absence of a strong weakening mechanism, the temperature rise occurring during earthquakes should result in large-scale melting of the faults, but this is not supported by field observations of exhumed faults. Some thermal weakening should

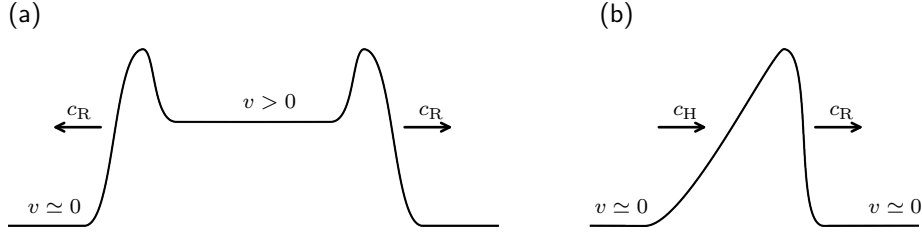


Figure 2.16: Schematic representation of the slip velocity profile of frictional ruptures in the case of: (a) a bilateral crack-like rupture propagation and (b) a slip pulse. For the bilateral crack-like rupture, two frictional rupture fronts propagate at a velocity c_R and invade a stick portion of the interface $v \simeq 0$. A slipping state with large slip velocity $v > 0$ characterizes the interface behind the rupture fronts. For the slip pulse, a rupture front propagates unilaterally at velocity c_R and is followed by a healing front propagating at c_H . The interface is sticking both ahead and behind the slip pulse, resulting in a small localized portion of the interface slipping at a given time. A slip pulse can spatially expand, decay, or remain stable depending on the relation between c_R and c_H .

thus exist in the context of rapid slip to limit the temperature rise. Several mechanisms are thought to be relevant in this context. One of them is the flash heating theory [95; 96], which originated in engineering tribology to describe the dependence on slip rate for dry metal friction [97]. The rapid heating and weakening of frictional asperities in contact between sliding surfaces results in a significant loss of frictional strength. Another mechanism is the thermal pressurization of pore fluids [98; 99; 100; 95]. Faults are often filled with granulated material (gouge) and fluids. With increasing temperature, the increase in pressure of the fluids results then in a drop in the normal pressure acting on the fault and hence significantly reduces the shear strength. These two mechanisms are expected to occur at sliding velocities below the one observed during earthquakes. Their influence on rupture mode dynamics in addition to regular rate and state friction is of significant interest for fast slip. Other chemical mechanisms, such as the decarbonation of rocks, might contribute to the enhanced weakening for high slip velocities [101; 102]. Note that while this thesis only considers interfaces that are driven with far-field stress and velocity, frictional rupture can be driven differently, e.g., in the context of hydraulic fracturing in which the injected fluid drives the propagation [103; 104].

2.3.2 Rupture modes

One fundamental characteristic of the various constitutive models used to characterize the behavior of frictional interfaces, is that they share a weakening response, and thus frictional systems are prone to host frictional instabilities. Their development results

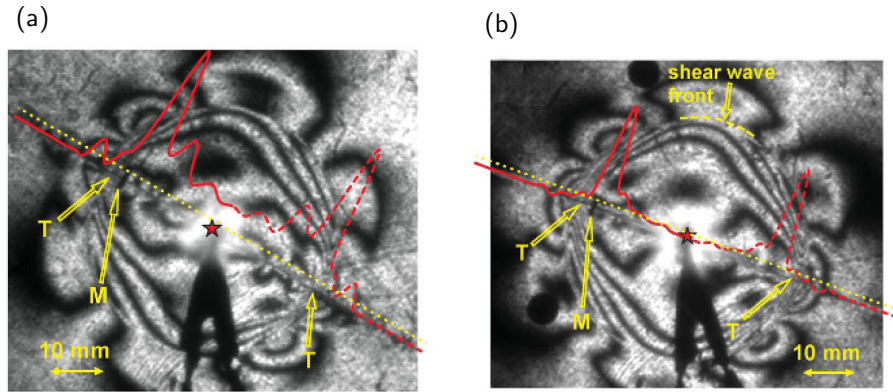


Figure 2.17: Experimental results taken from [109]. Photoelastic pattern of the maximum shear stress contour, with the profile of relative slip velocity at the interface superimposed in red. The letter T indicates the location of a rupture tip, and M is the location of the velocimeter. (a) crack-like rupture (b) slip pulse.

in the propagation of slip along friction interfaces that are mediated by rupture modes. There are two main types of rupture modes: (a) expanding crack-like rupture and (b) compact self-healing slip pulse [105; 106; 107; 108; 109; 110; 111; 112; 113; 114; 115; 116; 117; 118]. In the former (represented in Fig 2.16a), the sliding velocity remains finite behind the rupture front and the entire area that has slipped is still in motion until the entire rupture stops. In the case of slip pulses, the rupture front (Fig 2.16b) is closely followed by a healing front behind which the sliding velocity vanishes, thus only a localized portion of the interface is sliding at a given time. Note that similar behaviors can be found in other systems if a healing mechanism exists, e.g., re-bonding during the peeling of soft-adhesives [119]. A great variety of these rupture modes exist, depending on the propagation velocity of the fronts c_R that can be subshear or supershear. For slip pulses, the velocity of the healing front c_H compared to the rupture front one determines the type of slip pulse: it can spatially expand ($c_R > c_H$), decay ($c_R < c_H$) or propagate steadily ($c_R = c_H$) [120; 121]. The condition under which a frictional system will give rise to a specific rupture mode is not yet entirely clear [122; 114; 113; 123; 116; 82; 124; 117; 125; 120; 126; 127; 128]. Several potential mechanisms have been proposed to explain the emergence of slip pulses: bi-material coupling [115; 129; 112], heterogeneous fault conditions [130] or velocity-weakening friction. For the latter, the level of pre-stress has an influence on the rupture mode [123; 109] as well as the size of the perturbation/nucleation zone [120; 121]. The influence of the type of boundary conditions (stress or velocity controlled) has received much less attention. This issue and the properties of emergent slip pulses under velocity-driven sliding are discussed in Chapter 5.

2.3.3 Analogy with fracture

Rationalizing the behavior of frictional rupture using tools from dynamic fracture mechanics has gained increasing attention in the last few years. Obvious similarities exist between a shear crack and a "crack-like" frictional rupture: rupture fronts propagate into an intact state and let behind them a residual sliding velocity level and a lower stress. The latter is zero for classical tensile fracture, and some residual frictional stress for friction. Cohesive models that have been developed to regularize the infinite stresses near the tip of a crack are similar to the slip-weakening law that describes the evolution of the frictional strength with slip. Taking advantage of the linearity of the bulk surrounding the frictional fault, one can try to map the behavior of frictional interfaces to dynamic fracture mechanics after subtracting the residual level of stress after the passing of the frictional rupture front.

Laboratory earthquake experiments conducted on blocks of PMMA showed that the fields near the rupture tip of a frictional rupture are consistent with the asymptotic fields of fracture mechanics for both sub-Rayleigh [56; 127] and supershear propagation velocities [131]. An example is shown in Fig. 2.18 where the strain fields near the tip of a frictional rupture are compared to the corresponding LEFM prediction. Similar observations were also done on granite [132]. The propagation velocity of frictional cracks is also consistent with the equation of motion of regular cracks [133; 134]. The length and conditions of arrest of frictional ruptures have also been well described by LEFM using the concept of energy balance [135; 136; 137].

However, the cohesive zone model of friction assumes that two quantities are known beforehand: the residual level of stress and the "fracture energy" of the interface. While the first quantity is obvious for tensile rupture (free surfaces cannot hold any tensile stress, thus it is zero), it is not clear what is the residual stress for a frictional crack. LEFM and cohesive zone modeling provide insights into the mechanics of frictional rupture, but understanding the physical origin of the emergence of stress drops and crack-like properties of frictional rupture is still lacking. To what extent the analogy between fracture mechanics and frictional rupture is valid is also an open question: one striking observation from large earthquakes is that the estimated fracture energy is always significantly larger compared to the experimental measurement of fracture toughness, implying that additional dissipation takes place in frictional rupture. These issues are discussed in Chapter 5 using the rate and state friction framework.

2.3.4 Complexity in frictional systems

In this section, we discuss friction from a statistical point of view and no longer deal with single slip events. While friction is an intrinsically complex phenomenon that can result in a variety of slip events, some universal scaling relations do exist for slip events. Taking here the example of earthquakes, numerous power law distributions apply to the description of various quantities of interest in seismology. The most famous is the

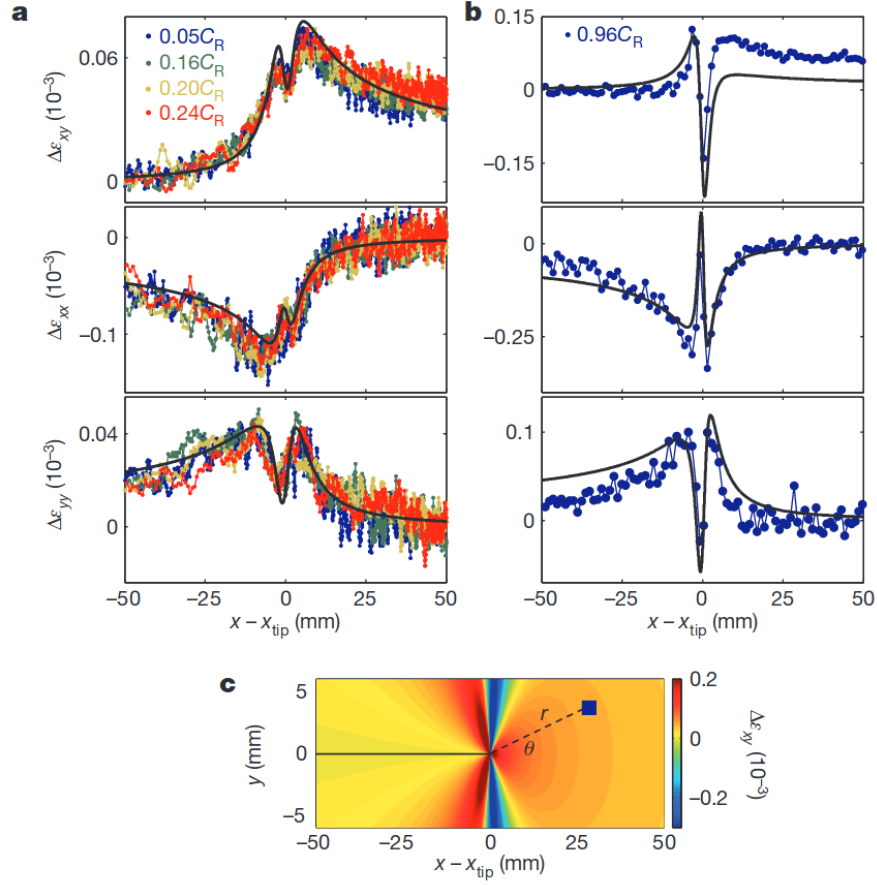


Figure 2.18: Experimental results of friction between PMMA blocks taken from [127]. (a) Strain tensor variations $\Delta\epsilon_{ij}$ near the frictional rupture tip for different front velocities. The black line is the corresponding predictions from LEFM. (b) Average value of the strain tensor variations for a fast rupture, with the corresponding LEFM prediction. (c) A space map of the strain tensor variations near the tip, with the blue square indicating the location of the strain gauge.

*Gutenberg*¹⁵-*Richter*¹⁶ law that describes the frequency-magnitude relation as [138; 139]

$$n(S) \propto S^{-1-\beta}, \quad (2.47)$$

with $n(S)$ the number of earthquakes with magnitude S , and $\beta \simeq 2/3$ a constant. This law implies universal fractal behavior of earthquakes, i.e., scale invariance. Another famous one describes the temporal decay of aftershocks following an earthquake, known as *Omori's*¹⁷ law [140; 141]:

¹⁵Beno Gutenberg (1889-1950)

¹⁶Charles Francis Richter (1900-1985)

¹⁷Fusakichi Omori (1868-1923)

$$\frac{\Delta N}{\Delta t} = t_0(t + t_1)^{-p} \quad (2.48)$$

with N the cumulative number of events with a magnitude larger than a given value, t the time measured from the main earthquake, t_0 and t_1 constants, and $p \simeq 1$. Several other power laws describe the waiting time between events [142], the relation between the slip of an earthquake versus the rupture length [143], between rupture duration and magnitude [144; 145], rupture area and seismic moment [142], etc... Readers interested in this topic are referred to classical textbook [146] or reviews on statistical physics approach of earthquakes [147; 47; 148]. In what follows, *statistical complexity* refers to the existence of these broad distribution laws.

One of the main questions arising from the emergence of complexity in earthquake physics is its physical origin. While it is true that natural faults are rough at all scales [149] and feature heterogeneities in material properties and stress conditions, one can wonder if the non-linearity of the frictional behavior is sufficient for the emergence of complexity or if disorder in the material properties is required. The origin of complexity has gathered significant attention in the literature, with a variety of models and hypotheses. The pioneer works go back to the Burridge-Knopoff slider block model [150]. It consists of several blocks that are driven through springs connected to a slider, interacting with their neighbors with other springs. The friction of each block is described by a constitutive behavior that involves a weakening mechanism to allow for stick-slip. This type of model, discrete by definition, has been widely used with various hypotheses (with or without inertia, different long-range interactions, friction laws...). Complexity in these systems has been observed to emerge even in the absence of material heterogeneities with velocity-weakening friction [151; 152] and rate and state friction [153; 154]. Rice and coworkers however argued that the observed complexity for small events is an artifact of the discreteness of the modeled system and that they do not represent truly homogeneous conditions [129; 77; 155; 156; 157; 158]. For them, complexity is related to the presence of strong material heterogeneities: inertial dynamics on a homogeneous fault is not sufficient to generate a broad class of events by itself, at least *generically*. Other works used a continuum approach and did observe complexity in the absence of material disorder [113; 116; 159; 160] but were conducted either with friction laws that feature strong weakening or the complexity was not generic, i.e., limited to a small parameter range. Complexity can also emerge from the geometry of the fault itself, for example when multiple faults interact [161]. We bring our contribution to this topic in Chapter 6, in which the emergence of complexity in a frictional system of finite dimension in the absence of material heterogeneities is discussed.

3 Numerical framework

The work conducted in this thesis relies on the numerical modeling of dynamic rupture. This is in itself a difficult challenge, as it requires modeling discontinuities. The length-scales and time-scales involved in such problems make it even more difficult: the dissipation occurs on a small length-scale near the crack tip (the process zone) but the dimension of propagation of the rupture might be several orders of magnitude larger. The loading of such systems occurs over long time scales, while the ruptures are comparatively extremely fast. Thus, large and finely discretized time and space domains are required to model dynamic rupture, resulting in complex and computationally expensive modeling. Two types of models are used for fully dynamic simulations in this thesis, the finite element method, and the spectral boundary integral method. This chapter describes the basics of these methods, with their advantages and drawbacks. Both methods consist of solving the partial differential equations of elastodynamics that are described in section 2.1.5.

3.1 Finite element method

The finite element method is a domain-based method that is known for its versatility and adaptability. It relies on the discretization of the full body of interest into small pieces called elements, see Fig. 3.1, over which a discretized version of the weak formulation of the problem is solved. It can be used for any geometry and bulk constitutive behavior. Various approaches to include discontinuities (i.e., cracks) can be employed, such as cohesive elements [162], node-to-node algorithm [163], or the phase field approach [164]. Here we give a brief introduction to the formulation and the usual scheme to model explicit dynamics. The reader interested in the details of the method is directed to reference textbooks [165]. The finite element code used in this thesis is an in-house open source library called *Akantu* [8].

3.1.1 Bulk elements

The displacement field $u(\mathbf{x}, t)$ on an element is written as:

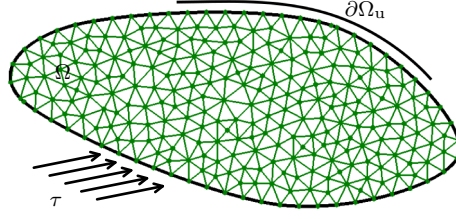


Figure 3.1: Schematic representation of a body Ω in black that is meshed with triangular finite elements, in green. Dirichlet boundary conditions are enforced on part of the boundary $\partial\Omega_u$, and some traction τ (i.e., Neumann BC) on another part of the body. The part where nothing is specified are traction-free conditions.

$$\mathbf{u}(\mathbf{x}, t) = \underline{\mathbf{N}}\mathbf{u}_e, \quad (3.1)$$

where $\underline{\mathbf{N}}$ are known as the *shape functions*, which are piece-wise interpolation functions describing the shape of the displacement field (commonly used shape functions are linear and quadratic) and \mathbf{u}_e the displacements at the nodes of the elements (their number per element depends on the order of the shape functions). The derivatives of the shape functions $\underline{\mathbf{A}}$ give the relation between the displacements and the strains as:

$$\underline{\mathbf{A}}\mathbf{u}_e = \underline{\boldsymbol{\epsilon}}. \quad (3.2)$$

The weak form of the problem, given in Eq. (2.12) is evaluated over each element as:

$$\delta\mathbf{u}_e^T \int_{\Omega_e} \underline{\mathbf{A}}^T \underline{\mathbf{C}} \underline{\mathbf{A}} \mathbf{u}_e dV + \delta\mathbf{u}_e^T \int_{\Omega_e} \rho \underline{\mathbf{N}}^T \underline{\mathbf{N}} \ddot{\mathbf{u}}_e dV - \delta\mathbf{u}_e^T \int_{\partial\Omega_e} \underline{\mathbf{N}}^T \boldsymbol{\tau} dA = 0, \quad (3.3)$$

where $\delta\mathbf{u}_e$ is a virtual nodal displacement field, Ω_e is the volume of the element, $\partial\Omega_e$ its boundary, $\underline{\mathbf{C}}$ the constitutive relationship, $\boldsymbol{\tau}$ the applied boundary stress, and e subscript indicates that the term is for a single element. Evaluating the different integrals allows computing the element stiffness matrix $\underline{\mathbf{K}}_e$, the element mass matrix $\underline{\mathbf{M}}_e$ and the external force vector \mathbf{F}_{ext} as :

$$\begin{aligned} \underline{\mathbf{K}}_e &= \int_{\Omega_e} \underline{\mathbf{A}}^T \underline{\mathbf{C}} \underline{\mathbf{A}} dV \\ \underline{\mathbf{M}}_e &= \int_{\Omega_e} \rho \underline{\mathbf{N}}^T \underline{\mathbf{N}} dV \\ \mathbf{F}_e^{ext} &= \int_{\partial\Omega_e} \underline{\mathbf{N}}^T \boldsymbol{\tau} dA. \end{aligned} \quad (3.4)$$

To assemble the global stiffness $\underline{\mathbf{K}}$ (and mass $\underline{\mathbf{M}}$) matrix for the problem, the connectivity of the mesh is considered. The term in the global stiffness matrix associated to a given

degree of freedom (i.e., a nodal displacement in a given direction) is the sum of the local contributions for each element that are connected to this degree of freedom. The same procedure is done to assemble the global external force vector \mathbf{F}^{ext} . For the entire system, one can write:

$$\underline{\mathbf{K}}\mathbf{u} + \underline{\mathbf{M}}\ddot{\mathbf{u}} = \mathbf{F}^{ext}, \quad (3.5)$$

with \mathbf{u} a vector containing all the nodal displacements of the system. Note that Eq. 3.5 is valid under the assumptions of no velocity damping. If damping would be included, an additional term $\underline{\mathbf{D}}\dot{\mathbf{u}}$ would be added to the left-hand term of the equation, with $\underline{\mathbf{D}}$ the damping matrix of the system.

As we are interested in dynamics behavior, we want to solve the system of equations given by Eq. 3.5 over time. The latter is discretized in small-time steps. Eq. 3.5 can be solved either implicitly or explicitly. In this thesis, we opt for an explicit time integration scheme. We use the Newmark^{1-β} [166] scheme with parameters $\alpha = 0$ and $\beta = 1/2$. This scheme computes the nodal fields at a time step based on the fields at the previous time step. In order to insure the convergence, the time step Δt_F has to be chosen small enough according to the Courant²-Friedrichs³-Lewy⁴ condition [167]. It writes:

$$\Delta t_F = \alpha_F \frac{\Delta x}{c}, \quad (3.6)$$

with Δx the minimum dimension of an element in the mesh and c the maximum characteristic velocity. For linear elasticity, this is c_d , the dilatational wave speed. α_F is a security coefficient smaller than one. For linear elasticity, it can be chosen as large as $\alpha_F \sim 0.8$.

The system of equation for the Newmark- β scheme is expressed as:

$$\begin{aligned} \underline{\mathbf{K}}\mathbf{u}_{n+1} + \underline{\mathbf{M}}\ddot{\mathbf{u}}_{n+1} &= \mathbf{F}_{n+1}^{ext} \\ \mathbf{u}_{n+1} &= \mathbf{u}_n + \Delta t_F \dot{\mathbf{u}}_n + \frac{1}{2}(\Delta t_F)^2 \ddot{\mathbf{u}}_n \\ \dot{\mathbf{u}}_{n+1} &= \dot{\mathbf{u}}_n + \frac{\Delta t_F}{2} (\ddot{\mathbf{u}}_n + \ddot{\mathbf{u}}_{n+1}), \end{aligned} \quad (3.7)$$

with the subscripts n and $n + 1$ indicating the time step. Eqs. 3.7 are solved using a predictor-corrector approach:

1. Predictor: the displacement field at the next time step is computed. One part of

¹Nathan Mortimore Newmark (1910-1981)

²Richard Courant (1888-1972)

³Kurt Otto Friedrichs (1901-1982)

⁴Hans Lewy (1904-1988)

the velocity of the next time step, the predicted velocity $\dot{\mathbf{u}}_{n+1}^P$ is computed:

$$\begin{aligned}\mathbf{u}_{n+1} &= \mathbf{u}_n + \Delta t_F \dot{\mathbf{u}}_n + \frac{1}{2} (\Delta t_F)^2 \ddot{\mathbf{u}}_n \\ \dot{\mathbf{u}}_{n+1}^P &= \dot{\mathbf{u}}_n + \frac{\Delta t_F}{2} \ddot{\mathbf{u}}_n.\end{aligned}\tag{3.8}$$

2. Residual: the acceleration increment is computed based on the difference between the applied external forces and the internal forces which are based on the updated displacement $\mathbf{F}_{n+1}^{int} = \underline{\mathbf{K}}\mathbf{u}_{n+1}$:

$$\delta \ddot{\mathbf{u}}_{n+1} = \underline{\mathbf{M}}^{-1} \left(\mathbf{F}_{n+1}^{ext} - \mathbf{F}_{n+1}^{int} - \underline{\mathbf{M}}\ddot{\mathbf{u}}_n \right).\tag{3.9}$$

3. Corrector: the acceleration at the time step $n + 1$ is computed based on the acceleration increment, and the velocity is corrected accordingly:

$$\begin{aligned}\ddot{\mathbf{u}}_{n+1} &= \ddot{\mathbf{u}}_n + \delta \ddot{\mathbf{u}}_{n+1} \\ \dot{\mathbf{u}}_{n+1} &= \dot{\mathbf{u}}_{n+1}^P + \frac{\Delta t_F}{2} \delta \ddot{\mathbf{u}}_{n+1}.\end{aligned}\tag{3.10}$$

3.1.2 Modeling discontinuity in finite elements

The previous section introduces how the finite element method allows computing the elastodynamics equation for a solid, but lacks the description of discontinuity, like cracks. Various methods have been developed to include them in finite element models. In this thesis, the node-to-node contact algorithm is the principal method used in the context of frictional rupture.

Node to node contact

The node to node contact algorithm allows to couple two independent solids at a planar interface between them, as represented in Fig. 3.2. The two solids need to have conforming mesh at their shared interface (i.e., matching nodes). Two corresponding nodes are coupled together through matching (opposite) normal and tangential forces that depend on the fields at both nodes. First, one needs to rewrite the expression for the acceleration as new forces are to be considered on the interface nodes. Eq. (3.9) in this case can be written as :

$$\ddot{\mathbf{u}}_{n+1} = \delta \ddot{\mathbf{u}}_{n+1} + \ddot{\mathbf{u}}_n = \underline{\mathbf{M}}^{-1} \left(\mathbf{F}_{n+1}^{ext} - \mathbf{F}_{n+1}^{int} + \mathbf{F}_{n+1}^N + \mathbf{F}_{n+1}^T \right),\tag{3.11}$$

with \mathbf{F}_{n+1}^N and \mathbf{F}_{n+1}^T respectively the contact and the frictional forces at the contact interface. Note that they are zero for any nodes that are not on the interface.

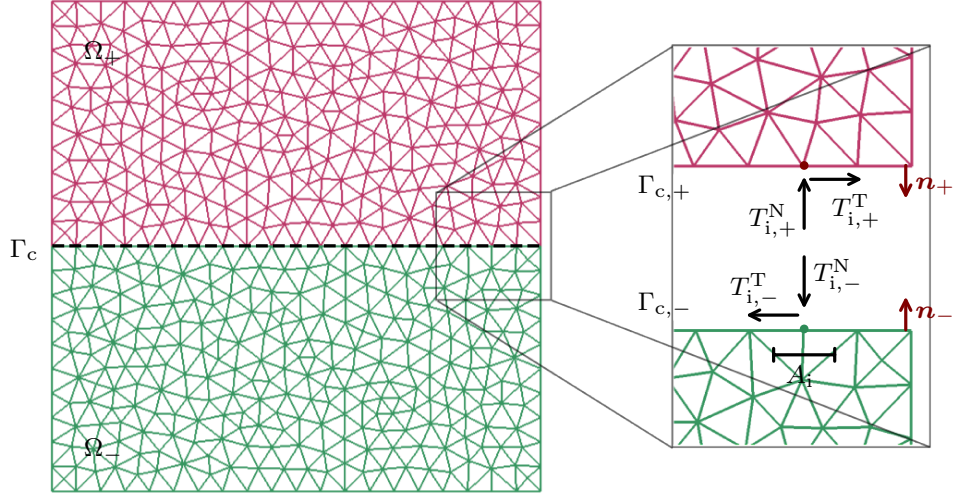


Figure 3.2: Schematic representation of the node to node contact for a finite element mesh. Two bodies Ω_+ and Ω_- that are meshed with triangular finite element (respectively in brown for the top body and green for the bottom one) are in contact at a planar interface Γ_c , in dashed black. The two meshes are conform, i.e., each node has a corresponding node on the other surface. On the right, the forces acting on a pair of nodes i are represented with black arrows. The vector normal to the top n_+ and bottom n_- surfaces are represented with brown arrows.

Contact forces

To compute the contact forces, we start with a non overlapping condition in the normal direction gives:

$$[\![x]\!]_{n+2}^N \geq 0, \quad (3.12)$$

where $[\![x]\!]$ indicates the difference between the jump in fields between the nodal position x of the node in the top body and its matching node in the bottom body, and the superscript N the normal direction. Eq. (3.12) can be expressed as:

$$[\![x]\!]_{n+2}^N = [\![x]\!]_{n+2}^N + [\![u]\!]_{n+2}^N \geq 0, \quad (3.13)$$

Using Eq. (3.8), the gap in displacement $[\![u]\!]_{n+2}^N$ can be expressed as the gap in the fields at the previous time step:

$$[\![x]\!]_{n+2}^N + [\![u]\!]_{n+2}^N + \Delta t_F [\![\dot{u}]\!]_{n+1}^N + \frac{1}{2}(\Delta t_F)^2 [\![\ddot{u}]\!]_{n+1}^N \geq 0. \quad (3.14)$$

Replacing the velocity by its expression based on the predicted velocity and the acceleration increment, one gets

$$\llbracket \mathbf{x} \rrbracket^N + \llbracket \mathbf{u} \rrbracket_{n+1}^N + \Delta t_F \llbracket \dot{\mathbf{u}}^P \rrbracket_{n+1}^N + \frac{1}{2} (\Delta t_F)^2 \left(\llbracket \delta \ddot{\mathbf{u}} \rrbracket_{n+1}^N + \llbracket \ddot{\mathbf{u}} \rrbracket_{n+1}^N \right) \geq 0. \quad (3.15)$$

Replacing $\llbracket \delta \ddot{\mathbf{u}} \rrbracket_{n+1}^N$ by $\llbracket \ddot{\mathbf{u}} \rrbracket_{n+1}^N - \llbracket \ddot{\mathbf{u}} \rrbracket_n^N$, and using Eq. (3.11) results in:

$$\llbracket \mathbf{x} \rrbracket^N + \llbracket \mathbf{u} \rrbracket_{n+1}^N + \Delta t_F \llbracket \dot{\mathbf{u}}^P \rrbracket_{n+1}^N - \frac{1}{2} (\Delta t_F)^2 \llbracket \ddot{\mathbf{u}} \rrbracket_n^N + (\Delta t_F)^2 \underline{\mathbf{M}}^{-1} \left(\llbracket \mathbf{F}^{ext} \rrbracket_{n+1} - \llbracket \mathbf{F}^{int} \rrbracket_{n+1} + \llbracket \mathbf{F} \rrbracket_{n+1}^N \right) \geq 0. \quad (3.16)$$

Let us define $\llbracket \ddot{\mathbf{u}}^{free} \rrbracket_{n+1}^N = \underline{\mathbf{M}}^{-1} (\llbracket \mathbf{F}^{ext} \rrbracket_{n+1} - \llbracket \mathbf{F}^{int} \rrbracket_{n+1})$ the acceleration related to the residual of the bodies that are not related by the node to node algorithm. The contact forces can be written as $\llbracket \mathbf{F} \rrbracket_{n+1}^N = \mathbf{A} \llbracket \mathbf{T} \rrbracket_{n+1}^N$ with \mathbf{A} the area associated to the contact nodes, and \mathbf{T}_{n+1}^N the contact stress. As the stress on the top and bottom matching nodes are equal and opposites, one can replace $\llbracket \mathbf{T} \rrbracket_{n+1}^N$ by $-2\mathbf{T}_{n+1}^N$. Let us introduce the variable \mathbf{Z}

$$\mathbf{Z}^{-1} = \frac{\Delta t_F}{2} \left(\mathbf{M}_+^{-1} \mathbf{A}_+ + \mathbf{M}_-^{-1} \mathbf{A}_- \right). \quad (3.17)$$

We can then simplify Eq. (3.16) as:

$$\llbracket \mathbf{x} \rrbracket^N + \llbracket \mathbf{u} \rrbracket_{n+1}^N + \Delta t_F \llbracket \dot{\mathbf{u}}^P \rrbracket_{n+1}^N - \frac{1}{2} (\Delta t_F)^2 \llbracket \ddot{\mathbf{u}} \rrbracket_n^N + (\Delta t_F)^2 \llbracket \ddot{\mathbf{u}}^{free} \rrbracket_{n+1}^N - 2\Delta t_F \mathbf{Z}^{-1} \mathbf{T}_{n+1}^N \geq 0. \quad (3.18)$$

In Eq. (3.18), all the terms except one are independent of the node to node algorithm. Let us introduce a last variable \mathbf{I}^{free} , that we call here the interpenetration of the free bodies:

$$\mathbf{I}_{n+1}^{free} = \llbracket \mathbf{x} \rrbracket^N + \llbracket \mathbf{u} \rrbracket_{n+1}^N + \Delta t_F \llbracket \dot{\mathbf{u}}^P \rrbracket_{n+1}^N - \frac{1}{2} (\Delta t_F)^2 \llbracket \ddot{\mathbf{u}} \rrbracket_n^N + (\Delta t_F)^2 \llbracket \ddot{\mathbf{u}}^{free} \rrbracket_{n+1}^N. \quad (3.19)$$

Then, if $\mathbf{I}_{n+1}^{free} \geq 0$, it means that there is no need for corrective contact forces to forbid interpenetration, and thus $\mathbf{T}_{n+1}^N = 0$. However, if $\mathbf{I}_{n+1}^{free} \leq 0$, then contact forces need to be computed as:

$$\mathbf{T}_{n+1}^N = \frac{\mathbf{Z} \mathbf{I}_{n+1}^{free}}{2\Delta t_F}, \quad (3.20)$$

and the forces are then applied on the nodes as:

$$\mathbf{F}_{n+1}^N = \mathbf{A} \mathbf{T}_{n+1}^N. \quad (3.21)$$

Friction forces

For the tangential (friction) forces, a similar derivation is done, but this time starting with a condition on the relative velocity in the tangential direction of the matching nodes

at the mid-time step. This first condition assumes that the friction forces are sufficient to hold the body together and thus there is no gap in velocity:

$$\llbracket \dot{\mathbf{u}} \rrbracket_{n+3/2}^T = 0. \quad (3.22)$$

The velocity at the mid-time step is given by $\dot{\mathbf{u}}_{n+3/2}^T = \dot{\mathbf{u}}_{n+1}^T + \ddot{\mathbf{u}}_{n+1}^T \Delta t_F / 2$. Thus, we can write:

$$\llbracket \dot{\mathbf{u}} \rrbracket_{n+1}^T + \frac{\Delta t_F}{2} (\llbracket \delta \ddot{\mathbf{u}} \rrbracket_{n+1}^T + \llbracket \ddot{\mathbf{u}} \rrbracket_{n+1}^T) = 0. \quad (3.23)$$

Defining $\llbracket \mathbf{F} \rrbracket_{n+1}^T = \mathbf{A} \llbracket \mathbf{T} \rrbracket_{n+1}^T$ and using the argument that the frictional forces are equal and opposite $\llbracket \mathbf{T} \rrbracket_{n+1}^T$ by $-2\mathbf{T}_{n+1}^T$, we can write:

$$\llbracket \dot{\mathbf{u}}^P \rrbracket_{n+1}^T - \frac{\Delta t_F}{2} \llbracket \ddot{\mathbf{u}} \rrbracket_n^T + \Delta t_F \llbracket \ddot{\mathbf{u}}^{free} \rrbracket_{n+1}^T - 2\mathbf{Z}^{-1} \mathbf{T}_{n+1}^T. \quad (3.24)$$

Similarly to the contact force, let us introduce \mathbf{R}^{free} as:

$$\mathbf{R}_{n+1}^{free} = \llbracket \dot{\mathbf{u}}^P \rrbracket_{n+1}^T - \frac{\Delta t_F}{2} \llbracket \ddot{\mathbf{u}} \rrbracket_n^T + \Delta t_F \llbracket \ddot{\mathbf{u}}^{free} \rrbracket_{n+1}^T. \quad (3.25)$$

The tangential force that acts in between two matching nodes is then simply given by:

$$\mathbf{T}_{n+1}^T = \frac{\mathbf{Z} \mathbf{R}_{n+1}^{free}}{2}. \quad (3.26)$$

Now that the tangential forces required to forbid any relative movement between the top and bottom nodes have been computed, one needs to compare these forces with the actual strength of the interface. The latter is given by a constitutive law, which in this work is chosen as a rate and state friction law, as introduced in section 2.3.1.2. The strength is given by:

$$\mathbf{S}_{n+1} = \mathbf{F}_{n+1}^N f(v, \phi), \quad (3.27)$$

in which $f(v, \phi)$ is a rate and state friction law and the velocity that is used to evaluate f is chosen as the relative velocity $v = \llbracket \dot{\mathbf{u}}^P \rrbracket_n^T$. Two cases can occur: (1) the strength is larger than the forces required to maintain the bodies together, $\mathbf{S} \geq \mathbf{T}^T$ and in this case the forces applied in the tangential direction are given by Eq. (3.26); (2) the strength is not sufficient to forbid a relative velocity between the two surfaces, then the forces are limited by the strength $\mathbf{T}_{n+1}^T = \mathbf{T}_{n+1}^N f(v, \phi)$.

Note that when using such frictional behavior for the node to node algorithm, the security factor for the time step α_F has to be significantly reduced compared to a simulation involving only bulk elements, see [168]. For the typical simulations described in this thesis, $\alpha_F = \mathcal{O}(0.01)$.

The updated explicit scheme relies on adding both the contact and the frictional forces \mathbf{T}_{n+1}^N and \mathbf{T}_{n+1}^T when the residual is evaluated, by using Eq. (3.11) instead of Eq. (3.9) to compute the acceleration increment. During the corrector step, the velocity and

acceleration will be corrected by a term that accounts for the additional forces at the contact interface.

3.2 Spectral boundary integral method

While the finite element method is a well-established and versatile method to solve elastodynamics problems, it still requires meshing the entire body of interest and thus can be computationally expensive. The boundary-based methods allow for reducing the dimensionality of the problem. These methods are limited to specific geometry and require strong assumptions regarding the behavior of the bulk. The *spectral boundary integral method* allows solving the traction and displacements at the interface between two semi-infinite homogeneous linear elastic bodies. This method has been proposed by Geubelle and Rice [169]. Two variants exist: (i) the *combined formulation* in which both bodies are solved at the same time [169; 170] and (ii) the *independent formulation* which, as suggested by its name, solves each body independently. The latter is more stable and allows describing bi-material interfaces. In this thesis, we use an in-house open source library called *cRacklet* [9] that implements the *independent* formulation. More details about *cRacklet* are given in Appendix B. Here, we recall the main equations of the method.

Let consider an interface between two semi-infinite continua that lies in the plane $y = 0$. The interfacial stress τ acting on the top (+), respectively bottom (−) surface, is given as:

$$\tau^{\pm}(x, z, t) = \tau^{\infty, \pm}(x, z, t) - \underline{V} (\dot{\mathbf{u}}^{\pm}(x, z, t) - \dot{\mathbf{u}}_0) + \mathbf{s}^{\pm}(x, z, t), \quad (3.28)$$

with $\tau^{\infty, \pm}(x, z, t)$ the far field loading. $\underline{V} (\dot{\mathbf{u}}^{\pm}(x, z, t) - \dot{\mathbf{u}}_0)$ is known as the *radiation damping* [155; 122; 123] and represents the instantaneous stress response of the interface due to a change in velocity. It corresponds to waves being radiated in the bulk, thus its name *radiation damping*. \underline{V} depends on the bulk parameters:

$$\underline{V} = \frac{\mu}{c_s} \begin{bmatrix} 1 & 0 & 0 \\ 0 & \eta & 0 \\ 0 & 0 & 1 \end{bmatrix}, \quad (3.29)$$

with $\eta = c_d/c_s$. $\dot{\mathbf{u}}_0$ is a reference velocity, which is usually zero for fracture problems, but can be a finite value for a frictional system that slides at a steady state velocity initially. The last term $\mathbf{s}^{\pm}(x, z, t)$ is a spatio-temporal integral term that accounts for the history of displacement at the interface. The latter is computed in the spectral domain, thus explaining the term *spectral* in the name of the method. There is no close form for the convolution kernels that are used to compute the stress from the displacement in the Fourier⁵ domain, and so they are pre-computed numerically. Their expressions can be found in [171].

In order to solve the problem, the interface is discretized with an evenly spaced grid.

⁵Jean-Baptiste Joseph Fourier (1768-1830)

The problem is integrated in time using an explicit time stepping

$$\mathbf{u}_{n+1} = \mathbf{u}_n + \Delta t_S \dot{\mathbf{u}}_n. \quad (3.30)$$

At each time step n , two quantities are unknown: the interfacial stress (τ_n , left-hand side of Eq. (3.28)) and the velocity $\dot{\mathbf{u}}_n^\pm(x, z)$. The spectral boundary integral method thus needs to be coupled with an interfacial constitutive law that limits the strength of the interface. In this thesis, we use two types of constitutive behavior: (i) a linear-weakening law for studying mode I fracture in Chapter 4 and (ii) rate and state friction laws for studying the behavior of frictional interfaces in Chapter 5.

Linear slip weakening law

In the former, the strength of the interface is a function of the relative displacement between the top and the bottom solid $\delta(x, z, t) = \mathbf{u}^+(x, z, t) - \mathbf{u}^-(x, z, t)$.

$$\tau^{str}(x, z, t) = \sigma_c(x, z) \max [1 - \delta(x, z, t)/\delta_c(x, z), 0], \quad (3.31)$$

with σ_c the maximum strength of the interface, and δ_c the critical opening at which the strength goes to zero. In this case, the resolution consists of the following steps:

1. Update the displacement \mathbf{u}_{n+1} for the new time step based on the fields at the previous time step \mathbf{u}_n and $\dot{\mathbf{u}}_n$.
2. Compute the stress at the interface $\tau_{n+1} = \tau_{n+1}^\infty + \mathbf{s}_{n+1}$, assuming that there is no relative velocity.
3. Evaluate the strength $\tau^{str}(\mathbf{u}_{n+1})$
4. Compare the stress and the strength. There are now two possible cases:
 - $\tau_{n+1} < \tau^{str}$: there is no relative motion, $\dot{\mathbf{u}}_{n+1} = 0$.
 - $\tau_{n+1} > \tau^{str}$: the strength is not sufficient. Solve for $\dot{\mathbf{u}}_{n+1}$. Eq. (3.28) with the left-hand side being equal to the strength.
5. Increment to the next time step.

Rate and state friction law

When studying friction, we employ laws that are dependent on the sliding velocity and an additional state variable, as discussed in section 2.3.1.2. The strength of the interface is given by

$$\tau^{str} = f(\mathbf{v}, \phi) \tau_{yy}, \quad (3.32)$$

with $\mathbf{v} = \dot{\mathbf{u}}^+ - \dot{\mathbf{u}}^-$ the relative slip velocity at the interface. Both the left-hand and the right-hand term of Eq. 3.28 depend on the velocity $\dot{\mathbf{u}}^+$, such that we solve directly for $\dot{\mathbf{u}}$

using a Newton-Raphson⁶ scheme.

The time step is chosen according to the Courant-Friedrichs-Lewy condition [167]

$$\Delta t_S = \alpha_S \frac{\Delta x}{c_s}, \quad (3.33)$$

with $\alpha_S \sim 0.2$ for the linear-slip weakening law and 0.1 for rate and state friction laws. While both methods presented here can be used to simulate dynamic rupture propagation, they are not tailored for the same type of problems. The spectral boundary integral method is extremely efficient but is limited to planar interfaces laying between semi-infinite homogeneous elastic solids, while the finite-element method can handle any geometry and can include bulk heterogeneities or non-linearities but can be costly if one wants to get rid of finite boundary effects. In Chapter 7, we discuss the coupling of the two methods, intending to take advantage of their respective benefits. The objective is to use the spectral boundary method to model boundary conditions that do not reflect waves. This will allow decreasing the computational cost of a finite element simulation by truncating the domain that needs to be discretized.

⁶Joseph Raphson (c.1668–c.1715)

4 Crack front deformations in cohesive materials

When a crack interacts with material heterogeneities, its front distorts due to the disorder in the fracture energy landscape. Understanding how fronts deform allows rationalizing the effective properties of heterogeneous microstructures and helps predict out-of-plane damage. However, the usual model for studying front deformations is based on the linear elastic fracture mechanics framework, which overlooks the influence of the finite dissipation length scale near the crack front, the *process zone*. Neglecting this length scale results in treating all asperities independently of their scale, whereas one would expect asperities that are smaller than this length scale to be treated differently than the larger ones. In this chapter, we study the deformation of crack fronts in heterogeneous cohesive materials by conducting fully dynamic numerical simulations of tensile fracture propagating through a heterogeneous interface described by a cohesive law. We show that a finite process zone size introduces scale effects in the deformation of the crack front, that are mitigated by the dynamics of the crack. The process zone renders the front more compliant to perturbations, but at the same time smooths out the fluctuations of strength and process zone. The dynamic contraction of the process zone diminishes these effects for fast-propagating cracks. Independently, the crack front stiffens with increasing propagation velocity, reducing the overall amplitude of deformations. To rationalize these observations, we extend to dynamics the *quasi-static cohesive line tension model* that was developed by Dr. Mathias Lebihain. We show that the *dynamic cohesive line tension model* predicts accurately the front deformation amplitudes measured in the numerical simulations.

This chapter is an adapted version of the following scientific articles:

M. Lebihain, T. Roch, and J.-F. Molinari, "Quasi-static crack front deformations in cohesive materials," *Journal of the Mechanics and Physics of Solids*, vol. 168, p. 105025, 2022

T. Roch, M. Lebihain, and J.-F. Molinari, "Dynamic crack front deformations in cohesive materials," 2022. arXiv:2206.04588 [cond-mat] *Under review*

4.1 Introduction

The propagation of fronts, defining the border between two distinct phases, occurs in numerous physical contexts such as paper wetting [173], combustion [174], polymerization [175] and fracture mechanics [32]. Fronts usually roughen due to interaction with heterogeneities. In fracture mechanics, a front marks the spatial separation between intact material and crack, and is thereby called a crack front. It deforms as a consequence of the heterogeneous landscape of toughness, the material resistance to crack propagation. Understanding how these deformations occur allow rationalizing the properties of composite materials [34; 35]. In addition, the transition between faceting and micro-branching for fast crack propagation is thought to be related to high in-plane curvature of the front [176]. Studying the dynamics of front deformations is thus key to unraveling the complex dynamics of heterogeneous dynamic rupture. Coplanar crack propagation is usually studied using perturbative approaches, such as the first-order model derived by Rice [177] based on the weight functions theory of Bueckner [37]. This approach has then been extended to dynamic rupture [44; 45] and also to higher orders [178; 38; 176]. This framework has been successfully applied to the deformation of crack front for various shapes of defects [33; 38; 39] as well as predicting the effective toughness of heterogeneous materials [40; 41; 42] and rationalizing the intermittent dynamics of crack front propagation in disordered media [43]. These models are however built on the linear elastic fracture mechanic (LEFM) framework and thereby assume that the dissipation at the crack tip occurs in a finite region, the *process zone*, of negligible size. As a consequence, LEFM-based models are bound to treat each asperity scale indifferently. Yet, elasticity is expected to break down along a finite region at the tip of the crack, and heterogeneities smaller or larger than this length scale are expected to affect the crack dynamics differently [179; 180]. Cohesive zone models of fracture [20; 21] allow considering a finite dissipation length scale through the introduction of stresses resisting the crack opening near the tip over a finite length, the process zone size. Regarding crack distortion, a recent theoretical study [10] shed light on the importance of considering the process zone size for quasi-static cracks. The presence of a finite dissipation length scale (i) controls the stability of crack fronts and (ii) introduces scale effects in the pinning of crack fronts by heterogeneities of fracture energy, and these effects are strongly dependent on how the toughness variations are achieved. For dynamic rupture, the process zone size is known to shrink with increasing propagation velocity, thus increasing the importance of this length scale relatively to the size of the heterogeneities [22; 181; 127]. In this manuscript, we first investigate numerically the dynamic front deformations of co-planar cracks loaded under normal tensile stress (mode-I) conditions and propagating through a heterogeneous toughness field. We solve this problem using our open-source implementation [9] of the spectral boundary integral formulation of the elastodynamic equations [169; 171] and study the influence of toughness heterogeneities arising from heterogeneities of i) peak strength and ii) process zone size. We then extend the theoretical model of [10] to dynamic rupture and compare the numerical results with

the newly derived *dynamic cohesive line tension model* for a broad range of parameters, thus providing a validation of this model. All in all, we provide a comprehensive framework describing dynamic crack front deformations for cohesive materials.

4.2 Problem description

We consider two semi-infinite elastic bodies of section L_x, L_z that are in contact along a planar interface located at $y = 0$ (see Fig. 4.1a). Periodic boundary conditions are imposed in the x and z directions. The bodies are loaded under mode-I conditions that drive a cohesive crack through a planar interface (crack in brown, process zone in orange in Fig. 4.1b) in the positive x direction at a constant velocity v_c . The propagation in the $-x$ direction is prevented. The crack initially propagates inside a homogeneous field of reference toughness G_c^0 . The interface properties are then gradually changed along a distance l_t towards an x invariant field composed of a stripe of larger toughness G_c^s (dark green) of width d embedded in a weaker toughness field G_c^w (light green). The average toughness in the z direction is kept equal to the reference one, $(G_c^s + G_c^w)/2 = G_c^0$, resulting in an effective toughness in the weak pinning regime that is equal to G_c^0 [10]. The gradual transition of properties allows for reducing the oscillations of the crack front deformations, as discussed in section 4.3. In this manuscript, we use $d = L_z/2$, $L_x = 8L_z$. We study the propagation for only $x < 0.75L_x$ to neglect the effect of periodic boundary conditions. We employ a linear cohesive law (see Fig. 4.1c) to describe the cohesive behavior of the interface, for which the stress decays linearly from a peak value σ_c to 0 with the opening δ up to a critical value δ_c :

$$\sigma^{\text{str}}(x, z, t) = \sigma_c(x, z) \max \left[1 - \frac{\delta(x, z, t)}{\delta_c(x, z)}, 0 \right]. \quad (4.1)$$

For the linear slip weakening law, the process zone size at rest ω_0 can be estimated as:

$$\omega_0 \simeq 0.731(1 - \nu)\mu \frac{\delta_c}{\sigma_c}, \quad (4.2)$$

see [182], with ν and μ respectively the Poisson's ratio and the shear modulus of the bulk. The opening is defined as the difference between the displacement fields of the top and bottom solids. In this work, we investigate two types of heterogeneities: (1) heterogeneities of peak strength σ_c with equal process zone size (see Fig. 4.1d) or (2) heterogeneities of varying quasi-static process zone size ω_0 with constant peak strength (see Fig. 4.1e). The toughness contrast is defined as $\Delta G_c = G_c^s - G_c^w$.

4.2.1 Material properties

The simulations reported in this chapter have been conducted using the elastic material properties of Homalite: Young's Modulus $E = 5.3 \times 10^9$ [Pa], Poisson's ratio $\nu = 0.35$ [-] and shear wave speed $c_s = 1263$ [m/s]. For the interface behavior, the fracture toughness $G_c^0 = 90$ [J/m²] is defined by a couple of maximum stress and critical opening values

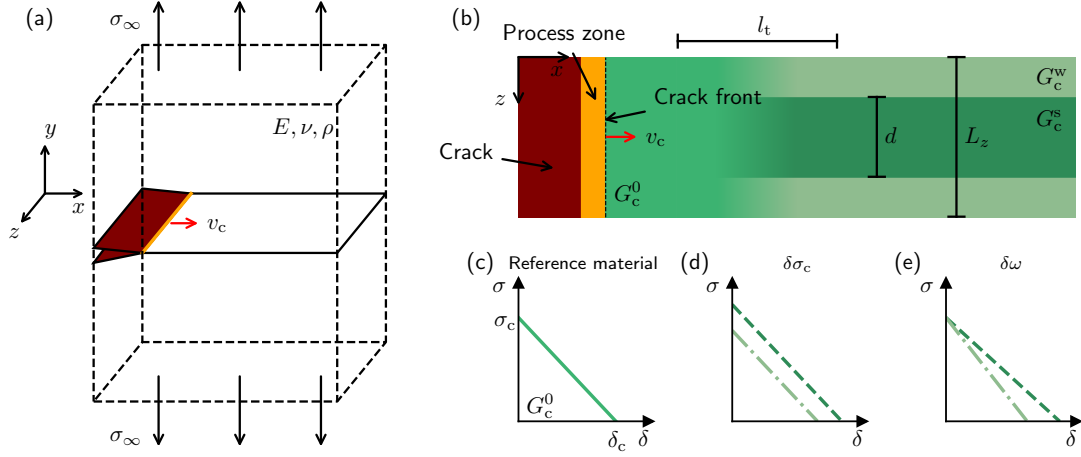


Figure 4.1: (a) Two identical semi-infinite elastic bodies of section L_x, L_z are in contact at a planar interface located at $y = 0$. Periodic boundary conditions are imposed for the x and z axes. The bodies are loaded under normal tensile stress that drives a crack through a heterogeneous toughness field in the positive x direction at a constant velocity v_c . (b) The layout of the interface: the crack is in brown, the finite process zone in orange, and the toughness field is represented by shades of green. The crack front is the separation between the process zone and the intact material and is shown with the dashed black line. The toughness is slowly varied from its reference value G_c^0 to respectively G_c^w and G_c^s along the transition length l_t . (c) Traction-separation law for the reference material. The contrast in toughness can be achieved by (d) changing the peak strength σ_c but keeping the process zone size equal, or (e) changing the quasi-static process zone ω_0 size but keeping the peak strength constant.

between $(\sigma_c^0, \delta_c^0) = (7.79 \times 10^6, 2.31 \times 10^{-5})$ [Pa,m] and $(\sigma_c^0, \delta_c^0) = (2.08 \times 10^6, 8.64 \times 10^{-5})$ [Pa,m]. The process zone at rest associated to these parameters goes from $\omega_0 = 6.54 \times 10^{-3}$ [m] to $\omega_0 = 9.15 \times 10^{-2}$ [m].

4.2.2 Numerical scheme

The problem is solved by conducting full-field dynamic calculations, using an in-house open-source implementation of the spectral boundary integral method [169; 170; 171] called cRacklet [9]. This method relates the displacements u^\pm of the fracture plane to the stresses τ acting on it. The details of the method are available in 3.2. The numerical parameter α_S is chosen to ensure the stability and the convergence of the numerical scheme, and is typically set to 0.2. In our numerical simulations, the interface is initially at rest under homogeneous tensile stresses. A crack is slowly grown until it spontaneously propagates at the targeted velocity. The loading is tailored from a reference simulation in a two-dimensional setup with homogeneous interfacial properties such that the crack velocity is constant during propagation.

4.3 Time evolution of the crack deformations and crack front waves

During a typical simulation, the crack front is initially perfectly straight. It starts deforming when it reaches the heterogeneous field of toughness. The dynamic deformation of the crack front is mediated by the propagation of crack front waves [181; 183; 184], resulting in the front oscillating over an equilibrium configuration. We measure the amplitude A of the front deformations as the distance between the most advanced point in the process zone at the axis of the strong band and at the axis of the weak band, as shown in Fig. 4.4d. If the change in toughness is abrupt, the front deformation amplitude overshoots its final value and then oscillates around it. The amplitude of these oscillations decreases slowly with time $\propto 1/\sqrt{t}$. As we are interested in the value of the equilibrium amplitude, we change progressively the toughness properties along a length l_t to reduce the amplitude of these oscillations, such that the simulated cracks are closer to a permanent regime. We illustrate in Fig. 4.2 the time evolution of the amplitude of the crack front normalized by the heterogeneity size in two cases: one with an abrupt change of toughness, i.e., $l_t = 0$ (yellow diamonds) and a case with $l_t = 5\omega_v$ (brown circles), with ω_v the dynamic process zone size. For these two simulations, $\Delta G_c/G_c^0 = 0.4$, $v_c/c_r = 0.7$ and $\omega_0/d \sim 0.42$. The oscillations of the front amplitude are significantly reduced when the material properties are slowly changed over the transition length l_t . A longer transition length would diminish the oscillations even more, but would require enlarging the length of the system and increase the computational cost.

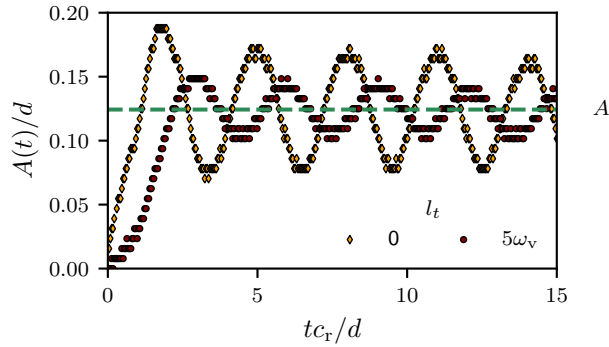


Figure 4.2: Evolution of the amplitude of the front deformations as a function of time for two simulations with $v_c/c_r = 0.7$, $\Delta G_c/G_c^0 = 0.4$ and $\omega_0/d \simeq 0.42$. The yellow diamonds correspond to an interface with an abrupt change of properties $l_t = 0$. The results corresponding to an interface with a gradual change of properties over the transition length $l_t \simeq 5\omega_v$ are shown with brown circles. The green line indicates the steady-state amplitude around which the instantaneous amplitude oscillates.

The period of oscillations is characteristic of the propagation velocity of the crack front waves: the time interval between two local extrema corresponds to the time required for the crack front waves to propagate across a distance d . When possible, we computed the

velocity of the crack front waves and reported them in Fig. 4.3. Note that in some cases the oscillations are almost completely eliminated, and thus it is not possible to measure the velocity of the crack front waves easily. This is mostly the case for simulations with large process zone sizes. The change of properties in the x direction is averaged over the process zone size, leading to an apparent change in toughness that is smoother and results in crack front waves with lower amplitude. The velocities of the crack front waves in our simulations are in agreement with the theoretical prediction given by Ramanathan [185] (in dashed gray in Fig 4.3). The spread around the theoretical prediction for a given crack velocity is related to the difficulty in computing the crack front wave velocity. Contrarily to the case originally explored by Morrissey [181] in mode I or later by Fekak [183] in mode II, in which a single asperity creates a perturbation whose propagation along the front is clearly visible, the heterogeneous pattern investigated in this manuscript results in the front shape changing at every position along z at the same time, leading to a challenging identification of the front wave velocity. The latter is computed as explained previously by identifying the period of oscillations, and thus requires finding local extrema of a discrete set of points. The procedure used here involves smoothing the data, which might alter slightly the precision of the results.

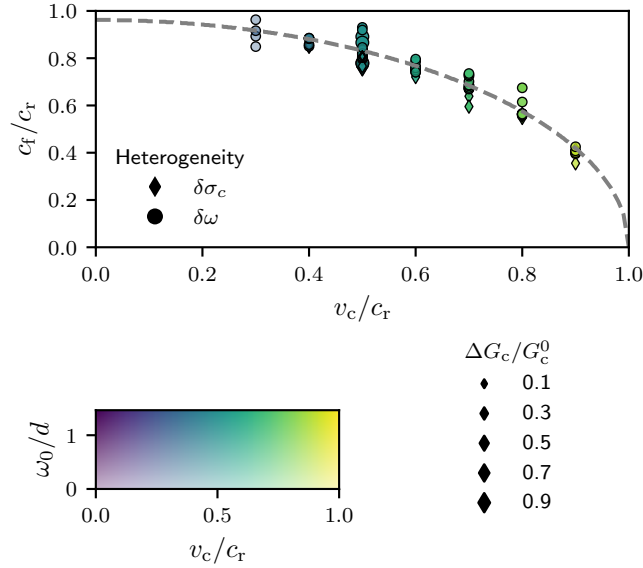


Figure 4.3: Crack front wave velocity c_f as a function of the front velocity v_c . The dashed gray line is the theoretical prediction for mode I [185]. Not all the simulations are shown in this figure, as it is not always possible to determine the crack front wave velocity properly.

4.4 Toughness contrast with constant process zone size

Preliminary to the study of dynamic and process zone effects on the crack deformations, we verified that our numerical model accurately results in a linear increase of front

deformation amplitude with the toughness contrast for a given velocity. The process zone is kept relatively small compared to the heterogeneities size, and the contrast in toughness is achieved by varying the peak strength while keeping the process zone size constant across the interface. The amplitude of the front deformations, normalized by the heterogeneities size, is shown in Fig. 4.4a as a function of the toughness contrast for $\Delta G_c/G_c^0 \in [0.1, 1.4]$. Fig. 4.4b-d are snapshots of the crack front configuration for $\Delta G_c/G_c^0 = 0.3, 0.7, 1.2$. The crack is shown in brown, the process zone size in orange, and the shades of green stand for the toughness of the intact part of the interface. We observed a roughly linear increase of the front deformations with increasing fracture toughness contrast. For brittle materials (i.e., no process zone size), the Fourier transform of the quasi-static front deformations δa is given by, see [10],

$$\widehat{\delta a}(k) = -\frac{1}{|k|} \frac{\widehat{\delta G_c(k)}}{G_c^0}, \quad (4.3)$$

with δG_c the fluctuations of fracture toughness, k the wavenumber and $\hat{\cdot}$ indicates a Fourier transform. Eq. (4.3) predicts a linear dependency of the front amplitude on the toughness contrast, which is consistent with our observations. For large contrasts, the observations deviate from the predictions, which is expected as second-order effects start being relevant.

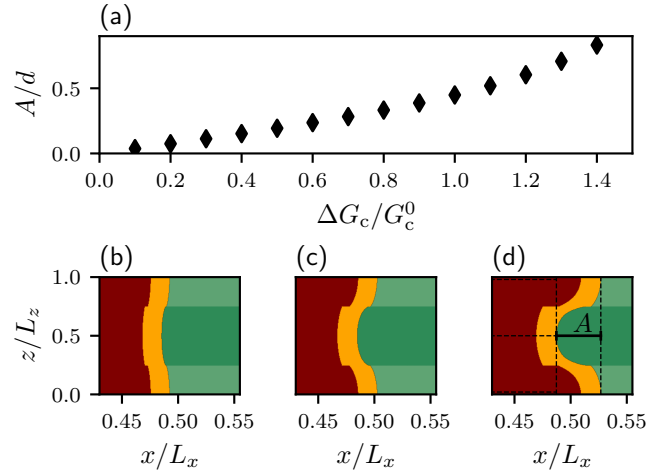


Figure 4.4: (a) Scaling of the amplitude A of the front deformations with the toughness contrast $\Delta G_c/G_c^0$. (b)-(c)-(d): snapshots of the crack front deformation for respectively $\Delta G_c/G_c^0 = 0.3, 0.7, 1.2$. The crack is in brown, the process zone in orange, the strong toughness in dark green and the weak one in light green. The crack velocity in these simulations is $v_c/c_r = 0.5$.

4.5 Crack propagation velocity

We investigate now the effect of the propagation velocity on the dynamic crack front deformations. The process zone size at rest ω_0 is kept relatively small compared to the heterogeneities size, and the contrast in toughness is achieved by varying the peak strength while keeping the process zone size at rest constant across the interface. According to [186], a front dynamically stiffens with increasing propagation velocity and thus diminishes its deformations. We show in Fig. 4.5a the amplitude A of front deformations as a function of the propagation velocity with $v_c/c_r \in [0.3 - 0.9]$ (black diamonds), with c_r the Rayleigh wave speed. The amplitude indeed decreases for faster cracks. The effect of dynamic stiffening on front deformations can be quantified by the function $D_I(v_c)$ which only depends on the propagation velocity and whose derivation is given hereafter. We consider a permanent regime, i.e., a crack that has been propagating at a constant velocity for an infinite amount of time. An expression for the perturbation of the dynamic stress intensity factor for a small deviation from straightness of a crack is provided by [44]. The general structure of the equation relates the perturbed stress intensity factor to the original stress intensity factor and a convolution of the front deformations with a function P , see Eq. (8.10) in [44]:

$$K_I(z, t) = K_I^0(z) + \delta K_I(z, t) = K_I^0(z) + \frac{\delta K_I^0}{\delta a}(z) \delta a(z, t) - \text{PV} \int_{-\infty}^{+\infty} P(z, t) K_I^0(z') [\delta a(z, t) - \delta a(z', t)] dz'. \quad (4.4)$$

For a mode I crack, its perturbed stress intensity factor K_I writes as Eq. (4.4). K_I^0 is the stress intensity factor in the unperturbed configuration, and PV denotes a Cauchy principal value. $P(z, t)$ is a kernel whose expression in the wavenumber-frequency domain ($z \rightarrow k$), ($t \rightarrow \theta$) is given by [185; 186]. We consider only the permanent regime for which there is no time dependency ($\theta = 0$) and in this case $P(z, t)$ reduces to $D_I(v)|k|/2$ with $D_I(v)$ given by Eq. (4.5):

$$D_I(v_c) = 1 / \left(\frac{2}{\sqrt{1 - (v_c/c_r)^2}} - \frac{1}{\sqrt{1 - (v_c/c_d)^2}} - (v_c/c_r)^2 \int_{c_s}^{c_d} \phi(v) dv \right), \quad (4.5)$$

and

$$\phi(v) = \sqrt{\frac{2}{\pi [(v/c_r)^2 - (v_c/c_r)^2]}} \arctan \left(\frac{4\sqrt{1 - (v/c_d)^2} \sqrt{(v/c_s)^2 - 1}}{(2 - (v/c_s)^2)^2} \right). \quad (4.6)$$

It corresponds to the dynamic stiffening term associated with mode I solicitation. The dashed black line in Fig. 4.5a is $D_I(v_c)A_{\text{lefm}}/d$, with A_{lefm} the predicted amplitude of front deformation based on the classical line tension model which is valid for small process zone size. It tends towards 1 for the quasi-static case $v_c = 0$ and towards 0 for cracks approaching the limiting propagation velocity, the Rayleigh wave speed c_r . The predicted amplitude $D_I(v_c)A_{\text{lefm}}/d$ matches the amplitude observed in the simula-

tions. Fig. 4.5b-d are snapshots of the crack front configuration for $v_c/c_r = 0.3, 0.6, 0.9$. The crack is shown in brown, the process zone size in orange, and the shades of green stand for the toughness of the intact part of the interface. In these snapshots, two effects of an increasing crack velocity are visible: (i) a decrease of the deformations and (ii) a decrease of the process zone size. The latter is known as the Lorentz contraction [22] of the process zone and is highly relevant for the following when we assess the effect of this length scale on front deformation. The instantaneous process zone size for a mode I crack is given by $\omega_v = \omega_0/A_I(v_c)$ with A_I a universal function of the crack velocity [15].

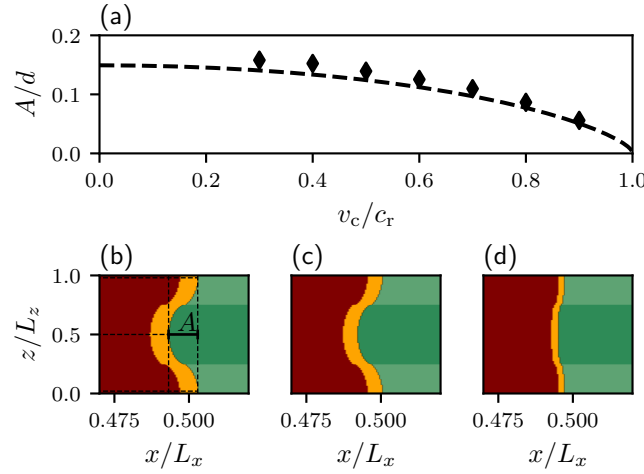


Figure 4.5: (a) Scaling of the amplitude A/d of the front deformations with the propagation velocity v_c/c_r . A is defined as the distance along x between the most advanced points in the process zone size at $z = 0$ and at $z = 0.5L_z$ as shown in panel (b). The dashed black line corresponds to the prediction of the classical line tension model A_{lefm}/d corrected to take into account the dynamic stiffening of the front by the term $D_I(v_c)$, see details in the text. (b)-(c)-(d) : snapshots of the crack front deformation for, respectively $v_c/c_r = 0.3, 0.6, 0.9$. Note that the x -scale and z -scale are different. The crack is in brown, the process zone in orange, the strong toughness in dark green and the weak one in light green. The toughness contrast in these simulations is $\Delta G_c/G_c^0 = 0.4$.

4.6 Process zone size and type of heterogeneities

The influence of the process zone size is investigated. We consider two different cases: heterogeneities of peak strength σ_c (with constant process zone, see Fig 4.1d), and heterogeneities of process zone size at rest ω_0 with constant peak strength, see Fig 4.1e). We vary in both cases the average value ω_0 of the quasi-static process zone size while keeping the toughness contrast and the propagation velocity constant. The amplitude of crack front deformations is shown in Fig. 4.6a, for $v_c/c_r = 0.5$, $\Delta G_c/G_c^0 = 0.4$ and $\omega_v/d \in [0.05 - 1.5]$ for heterogeneities of peak strength (diamonds) and process zone size (circles). For small relative process zone size ω_v/d the front deformation amplitude is similar for both types of heterogeneities. However, they get significantly farther

apart with increasing process zone size. On one hand, the amplitude increases with the dissipation length scale for heterogeneities of peak strength (diamonds in Fig. 4.6a and snapshots in Fig. 4.6b-d). On the other hand, the amplitude diminishes with the process zone size for heterogeneities of process zone (circles in Fig. 4.6a and snapshots in Fig. 4.6e-g). Changes in process zone size are accommodated more easily by a crack front than changes in peak strength. These observations are striking: the deformations of a cohesive crack propagating through a heterogeneous microstructure are strongly dominated by the nature of the heterogeneities. For two interfaces sharing the same fracture toughness contrast, the difference between the two types of heterogeneities investigated in this work reaches up to a factor 4 when the process zone and the heterogeneities have the same size $\omega_v/d \sim 1$. The deformations are not tied directly to the toughness contrast, but rather to the variations of the cohesive parameters. For the slip weakening law used in this manuscript and heterogeneities that are achieved by varying both the peak strength and the process zone size (not presented in this manuscript), we expect the behavior to be bounded by the two limiting cases that were investigated. Note that this difference is expected to vanish for negligibly small relative process zone size, which can occur either with brittle materials or when cracks propagate at a velocity close to the limiting wave speed due to the Lorentz contraction.

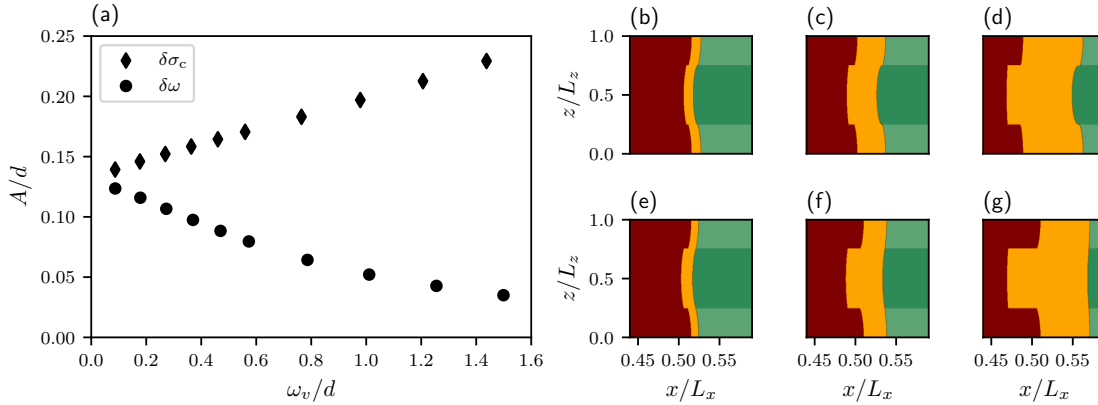


Figure 4.6: (a) Scaling of the amplitude A of the front deformations with the process zone size ω_v for heterogeneities of constant process zone size (diamonds, snapshots shown in (b)-(c)-(d) for $\omega_v/d \sim 0.2, 0.6, 1.25$) and constant peak strength (circles, snapshots shown in (e)-(f)-(g) for $\omega_v/d \sim 0.2, 0.6, 1.25$). For the latter, the value of ω_v is the average of $\omega_v(z)$ over the crack front. The crack velocity in these simulations is $v_c/c_r = 0.5$.

4.7 Dynamic cohesive line tension model

In order to understand these surprising observations, we go back to the *quasi-static cohesive line tension* model [10]. The derivation is recalled in Appendix A for completeness. This model extends Rice [22] first-order theory by including the effect of cohesive stresses that resist the crack opening and is based on the weight functions associated to a

point force located at a given distance from the front (i.e., inside the process zone). Two competing mechanisms arise from the presence of a cohesive zone : (i) the front *stiffness* is reduced and (ii) the fluctuations of strength $\delta\sigma_c$ and process zone $\delta\omega$ are smoothed out. They are extensively discussed in [10]. It is predicted that these competing effects can have two different outcomes in the quasi-static regime: for heterogeneities of strength only, the front deformation amplitude is enhanced, while for heterogeneities of process zone they are diminished. This is in qualitative agreement with the results reported in Fig. 4.6a. However, our simulations correspond to fully dynamic rupture while [10]'s model is limited to quasi-static cracks. Two additional effects are expected to emerge when extending this model to dynamics: (iii) the process zone size changes dynamically with the propagation velocity: it shrinks when a crack accelerates due to the Lorentz contraction [22] and (iv) the front stiffens with increasing crack velocity [186]. For the same interface layout, a faster crack is expected to deform less, and the differences between the type of heterogeneities should be reduced.

In order to validate our observations, we thus derive a *dynamic cohesive line tension model*, building on the quasi-static model of Lebihain et al. [10]. We derive it in the permanent regime (i.e., constant propagation velocity). The difficulty resides in computing the expression of the stress intensity factor k of the deformed front \mathcal{F}^* that is generated at a point $z = z_0$ by a pair of unitary forces that are applied at a given distance x behind the crack front at a point $z = z_1$, see Eq. (A.4). In the permanent dynamic regime, it writes

$$k(\mathcal{F}^*; z_0, z_1, x, v_c) = k(\mathcal{F}; z_0, z_1, x, v_c) + D_I(v_c) \int_{-\infty}^{+\infty} k(\mathcal{F}; z; z_1, x, v_c) \frac{\delta a(z) - \delta a(z_1)}{(z - z_1)^2} dz, \quad (4.7)$$

where $k(\mathcal{F}; z_0, z_1, x, v_c = 0)$ is known analytically for the semi-infinite coplanar crack with a straight crack front \mathcal{F} .

The derivation of the dynamic cohesive line tension model follows then the one presented in Appendix A for the quasi-static case for the crack face weight functions and the cohesive stress intensity factor, with two main differences: the process zone to be considered is the instantaneous cohesive zone size ω_v instead of the rest one ω_0 , and the pre-factor $D_I(v_c)$ multiplies the terms. The complete prediction for the deformation of a front in the dynamic regime due to both heterogeneities of strength and process zone thus corresponds to Eq. (A.17) with the two changes mentioned above, which results in Eq. (4.8):

$$\widehat{\delta a}(k) = -D_I(v_c) \left(\omega_v \frac{\hat{\Sigma}(|k|\omega_v)}{\hat{\mathcal{A}}(|k|\omega_v)} \frac{\widehat{\delta\sigma_c}(k)}{\sigma_c^0} + \omega_v \frac{\hat{\Omega}(|k|\omega_v)}{\hat{\mathcal{A}}(|k|\omega_v)} \frac{\widehat{\delta\omega}(k)}{2\omega_v} \right). \quad (4.8)$$

with k the wavenumber and $\hat{\cdot}$ indicates a Fourier transform. ω_v is the instantaneous process zone size (related to (iii) above) and $D_I(v_c)$ is a function of the velocity and represents the dynamic stiffening of the front (point (iv) above). $\hat{\mathcal{A}}$ and $\hat{\Sigma}$ and $\hat{\Omega}$ are functions of the nature of the weakening, the wavenumber k and the process zone size. The exact formulation for these functions is given in section 4.10. The term $\hat{\mathcal{A}}$ acts as the

loss of stiffness of the front due to the introduction of a finite-size region of dissipation mentioned in point (i), while $\hat{\Sigma}$ and $\hat{\Omega}$ smooth out the fluctuations of material properties mentioned in point (ii). Note that as $D_I(v_c = 0) = 1$, we recover the formulae for the quasi-static front deformation in presence of a process zone. For cracks propagating at the limiting velocity, we have $D_I(v_c = c_r) = 0$, resulting in theoretically undeformable crack front in this limit (in the hypothesis of co-planar crack propagation). In practice, fast cracks will often trigger out-of-plane damage and instabilities before reaching the limiting velocity.

4.8 Comparison between theory and simulations

Crack front deformation simulations have been conducted for a broad range of parameters, including variations of process zone size at rest ω_0 , toughness contrast, type of heterogeneities, and crack front velocity v_c . In Fig. 4.7a the front deformation amplitude measured from the simulations is plotted versus the prediction from the standard line tension model that does not consider the existence of a finite dissipation length scale near the crack tip, but including the dynamic stiffening term from Eq. (4.3). This prediction fails, as we have established previously that a finite process zone size strongly impacts the crack front deformations. For a given prediction based on the LEFM theory (take for example $A_{\text{lefm}}/d = 0.25$) there is a large spread of measured amplitude, which can be either larger or lower than the predicted one (the dashed-gray line has a slope of 1) depending on the type of heterogeneities. It is expected from the observations of Fig. 4.6 that simulations with a small process zone (e.g., for fast ruptures) will result in a significantly smaller difference between the two types of heterogeneities. This is apparent with the data points corresponding to fast cracks (yellow-green in Fig. 4.7a) that are significantly closer than the ones for slower cracks (blue data points). The effect of the front stiffening with increasing velocity is also visible from Fig. 4.7a, with large velocities resulting in small amplitudes. In Fig. 4.7b, the prediction of Eq.(4.8), the *dynamic cohesive line tension model*, is tested: all the data are falling close to a linear master curve, strongly supporting the validity of our model for rationalizing the effect of a finite process zone. While the predictions of Eq. (4.8) are based on the assumption of a semi-infinite crack, finite-size cracks have been considered in the simulations. Plus, the simulated ruptures are not in a steady permanent regime as assumed in the model. Second-order effects might also be required to accurately describe the deformations of cohesive fronts, as the latter can display larger curvatures than the classical line tension fronts. This could potentially explain the small deviation from the predictions. Nonetheless, the proposed model successfully predicts the numerical observations and thereby the non-trivial influence of a finite dissipation length scale for crack front deformations at constant propagation velocity: not only does the process zone influence front deformations, but also its outcome varies strongly depending on the description of the heterogeneities. Note that a comparison with experiments was done in [10] in the quasi-static case. Including the effect of the process zone size on the front deformation helps to improve

the prediction of the crack front profile when encountering a strong heterogeneity. In particular, the *cohesive line tension model* can predict significantly stronger curvature near the defect compared to the classical line tension model.

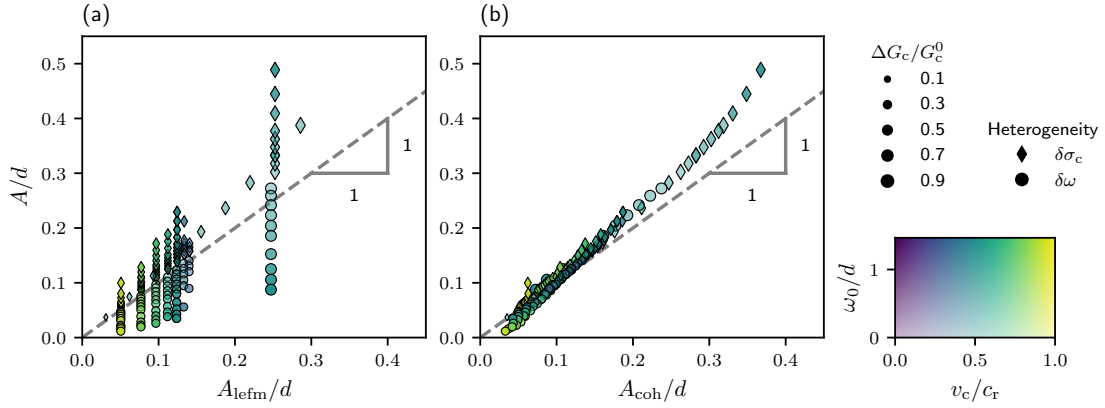


Figure 4.7: The amplitude of the front deformations measured in simulations is compared with: (a) the prediction from the LEFM theory that does not account for a finite process zone, (b) the prediction from our newly derived *dynamic cohesive line tension model*. The simulations shown here explore a broad range of parameters, including variations of the crack propagation velocity v_c , the process zone size at rest ω_0 , the toughness contrast ΔG_c and the type of heterogeneities (constant process zone or constant peak strength).

4.9 Discussion

The deformations of a dynamic cohesive crack propagating through a heterogeneous field of toughness have been investigated numerically using the spectral boundary integral method coupled with a cohesive zone model. While the influence of the toughness contrast on front deformation amplitude is in agreement with the prediction of the classical line tension model (i.e., a linear increase of amplitude with contrast), modifying the process zone size introduces scale effects in the deformation of the crack front that are non-trivial. For the same toughness contrast and average process zone size, the crack front deformation amplitude is enhanced when considering heterogeneities of peak strength and diminished for heterogeneities of process zone. When considering the dynamics of the front, these differences are mitigated by the Lorentz contraction of the process zone size, and the amplitude of front deformations is decreased due to the dynamic stiffening of the front with increasing crack velocity. To rationalize these observations, we extended the *cohesive line tension model* recently proposed in [10] to dynamic rupture. This model predicts accurately the amplitude of the observed deformations, taking into account the instantaneous average process zone size and the propagation velocity. All in all, our model reveals the non-trivial effect of a finite dissipation length scale on the front deformations, and particularly the importance of the nature of the

heterogeneities. Building a complete cohesive model including change in velocity and variations of properties along the front propagation direction remains a challenge. For the latter, the process zone size is expected to be also the relevant length scale, as the properties are averaged over the process zone size [179]. This work provides the necessary ingredients to characterize the front roughness of disordered materials [187; 188], giving access to an estimate of the Larkin length. This directly impacts the prediction of the effective propagation threshold in cohesive composites [189]. Finally, this work might help understand the occurrence of out-of-plane damage as a consequence of high in-plane curvature of the front [176], and more generally the deformations of a three-dimensional crack front for which the process zone size changes with the orientation from the crack tip.

4.10 Supplemental material

For completeness, we recall here the expression for $\hat{\mathcal{A}}$ and $\hat{\Sigma}$ and $\hat{\Omega}$. Note that these expressions slightly differ from the one given by [10] as we consider here the dynamic process zone size ω_v and not the static one ω_0 .

$$\begin{cases} \hat{\mathcal{A}}(|k|\omega_v) &= -\frac{1}{C_w} \int_0^{+\infty} \frac{f'_w(u)}{u^{1/2}} (1 - e^{-|k|\omega_v u}) du \\ \hat{\Sigma}(|k|\omega_v) &= \frac{1}{C_w} \int_0^{+\infty} \frac{f_w(u)}{u^{1/2}} e^{-|k|\omega_v u} du \\ \hat{\Omega}(|k|\omega_v) &= -\frac{2}{C_w} \int_0^{+\infty} f'_w(u) u^{1/2} e^{-|k|\omega_v u} du \end{cases} \quad (4.9)$$

with $C_w = \int_0^{+\infty} f_w(u) u^{-1/2} du$ and $f_w(x/\omega)$ the shape function that relates to the nature of the weakening. For the linear traction separation law considered in this work there is no analytical expression for the shape function as a function of the distance, but it can be computed numerically, see [10] Appendix C.4. for details.

5 On the dynamics of frictional interfaces described by rate and state friction laws

Frictional sliding is an intrinsically complex phenomenon, emerging from the interplay between driving forces, elasto-frictional instabilities, interfacial nonlinearity and dissipation, material inertia, and bulk geometry. Frictional rupture propagation corresponds to a high slip rate state invading a relatively low slip rate area ahead of the frictional rupture front. This picture of frictional rupture is reminiscent of the classical representation of fracture, in which a displacement discontinuity invades the intact material. However, several fundamental differences exist between frictional rupture and classical fracture. First, the residual strength that is left behind the rupture front is not zero for frictional rupture, while broken surfaces in tensile fracture cannot sustain any stress. If the residual stress is well-defined and is smaller than the far-field stress, then an analogy between friction and fracture can be maintained, i.e., edge singularity and energy balance might be applicable. While these assumptions have been consistent with fields and laboratory measurements, there is not yet a basic understanding of the physical mechanism for the emergence of stress drops in frictional rupture. Once the origin of the stress drop is established, one can wonder to what extent frictional rupture might be viewed as an ordinary fracture process in terms of edge singularity and energy balance. I contributed answering to these questions with Dr. Fabian Barras at the end of his thesis [190]. The main results are presented in the first part of this chapter. The second fundamental difference with fracture arises from the rupture modes existing in frictional rupture, crack-like rupture but also compact self-healing slip pulses. The latter consists of a rupture front closely followed by a healing front, such that the slip velocity behind the front goes to zero over some finite length-scale, contrarily to crack-like ruptures where it remains finite. The conditions under which slip pulses are favored in place of crack-like rupture are not yet clear, and the property of such objects have not yet been studied in depth. In the second part of this chapter, the emergence of slip pulses in velocity-driven frictional sliding is presented. The slip pulses are analyzed using the analogy with fracture mechanics to derive their equation of motion.

Chapter 5. On the dynamics of frictional interfaces described by rate and state friction laws

This chapter is an adapted version of the following scientific articles:

F. Barras, M. Aldam, T. Roch, E. A. Brener, E. Bouchbinder, and J.-F. Molinari, "Emergence of cracklike behavior of frictional rupture: The origin of stress drops," *Physical Review X*, vol. 9, p. 041043, 2019

F. Barras, M. Aldam, T. Roch, E. A. Brener, E. Bouchbinder, and J.-F. Molinari, "The emergence of crack-like behavior of frictional rupture: Edge singularity and energy balance," *Earth and Planetary Science Letters*, vol. 531, p. 115978, 2020

T. Roch, E. A. Brener, J.-F. Molinari, and E. Bouchbinder, "Velocity-driven frictional sliding: Coarsening and steady-state pulses," *Journal of the Mechanics and Physics of Solids*, vol. 158, p. 104607, 2022

5.1 Emergence of crack-like behavior of frictional rupture

5.1.1 Introduction

Frictional rupture consists of a state with a large slip rate invading a state of low (stick) slip rate, through the propagation of a rupture front. In this sense, it is analogous to ordinary tensile cracks (mode I fracture), for which a finite displacement discontinuity behind the crack tip invades an intact material with no displacement discontinuity. However, there exists a significant difference between frictional rupture and tensile one. A tensile crack is composed of free surfaces that cannot sustain tensile stress, and thus stress vanishes behind the crack tip. This difference in stress, called stress drop, is compensated by a large concentration of stress near the tip, in the form of a mathematical singularity, and its intensity controls the crack behavior. For frictional rupture, the bodies remain in contact behind the rupture front and stress does not drop to zero. The analogy between fracture and friction can hold if, as widely assumed, the residual stress level is well-defined and smaller than the background stress such that a finite stress drop emerges. It is usually assumed that the residual friction stress is a property of the frictional interface, often linked to the dynamic friction coefficient. Under these conditions, a finite stress drop emerges, and it is expected that the main concepts of fracture mechanics (edge singularity, energy balance) are valid. This has been widely assumed in numerical modelling [60; 63; 61; 194; 179; 195; 115; 196; 197; 198; 199; 200; 201; 202; 203; 204; 135; 205], has been consistent with geophysical observations [206; 205] and confirmed with laboratory earthquakes experiments [207; 208; 209; 127; 136; 210; 211; 133]. However, there is no basic understanding of how and under what conditions the crack-like behavior of frictional rupture emerges from fundamental physics. First, one needs to understand the origin of the finite stress drop $\Delta\tau$ and the conditions required for its emergence. We show in this chapter that the stress drop for rapid frictional rupture is related to waves radiated from the interface to the bulk and thus is not an interfacial parameter, but rather is related to the interaction between the frictional behavior and long-range bulk elastodynamics. Once the existence of a finite stress drop is established for frictional rupture, we show that frictional rupture is quantitatively described by a crack-like energy balance equation. In particular, we show the existence of a square root singularity of the velocity and stress fields near the rupture tip and verify the local energy balance between the related energy release rate and fracture energy. This leads to an adapted equation of motion for frictional rupture fronts that is validated with numerical simulations. We conclude this chapter by showing that there exists additional energy dissipation that is non-edge localized and illustrate deviations from the classical picture of fracture mechanics.

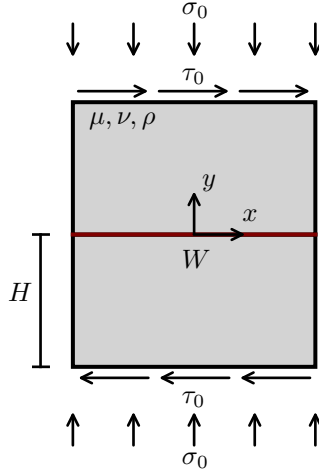


Figure 5.1: A schematic representation of the class of frictional systems under consideration. Two identical elastic bodies of width W and height H are in contact along an interface located at $y=0$ (brown line). The bodies are under constant normal (compressive) stress σ_0 and are driven anti-symmetrically at the upper and lower boundaries with constant shear stress τ_0 . Periodic boundary conditions are imposed in the x direction.

5.1.2 The physical origin of stress drops

The frictional system under consideration for our argument consists of two identical homogeneous bodies in contact at a planar interface located at $y = 0$, see Fig. 5.1. The solids are linear elastic, i.e., are described according to Hooke's law. The behavior of the interface involves three bulk quantities: the slip velocity at the interface $v(x, t) = \dot{u}_x(x, y = 0^+, t) - \dot{u}_x(x, y = 0^-, t)$ where u_x is the displacement field, the dot represents a time derivative, and \pm denote the top and bottom bodies, the interfacial shear stress $\sigma_{xy}(x, y = 0, t)$ that is in equilibrium with the frictional stress $\tau(x, t)$ and the normal stress acting on the interface $\sigma_{yy}(x, y = 0, t)$. The interfacial constitutive law also depends on an internal state variable that describes the structural state of the interface and its history, commonly noted $\phi(x, t)$. The interfacial constitutive law writes as follows:

$$\tau = \sigma_{yy} f(|v|, \phi). \quad (5.1)$$

The complete description of the interface behavior also requires describing the state variable evolution, with a function $\dot{\phi} = g(v\phi/D)$. ϕ is usually interpreted as representing the maturity or age of the microcontacts at the interface, see section 2.3 for more details. Usually, $g(1) = 0$ and D is the characteristic slip displacement that controls the transition from stick conditions to steady sliding at slip velocity v characterized by a state value $\phi_{ss} = D/v$. The exact function of $g(\cdot)$ does not play a role in the following discussion. We first consider a generic frictional behavior $f(|v|, \phi_{ss})$ that is N shaped under steady-

state conditions, i.e., it is rate strengthening at small and really large velocities, and rate weakening at intermediate velocities. This generic behavior has been observed for a large range of slip rates for numerous materials [86] and is shown in Fig. 5.2a in brown. Now consider that the system under consideration is driven at a constant stress τ_0 . Then, what kind of frictional rupture can emerge under these conditions?

As we established before, a frictional rupture is composed of a fast slip state propagating into a sticking state. This can be related to the intersection of the frictional steady-state curve with the driving stress. The left-most intersection is in the rate-strengthening branch for small velocities (marked with a red star) and corresponds to the state of the interface ahead of the rupture edge. The rightmost intersection (also indicated with a red star) features a large slip velocity $v > 0$ and corresponds to the state behind the rupture edge. The transition between these two configurations depends on the evolution law $\dot{\phi}$ and bulk elastodynamics. Note that a third intersection exists, in the rate-weakening branch, but this one is not stable due to the existence of frictional instabilities associated with rate-weakening effects. The important thing to notice here is that the stress ahead and behind the rupture edge is $\tau = \tau_0$ and thus the expected stress drop is zero, $\Delta\tau = 0$. In front of this apparent absence of stress drop and consequently crack-like behavior, one might wonder what would occur with another generic friction law widely used in the literature, that does not feature the rate strengthening branch at high slip velocities, as shown in brown in Fig. 5.3. Here, only a single stable point exists at small slip velocity for a constant driving stress τ_0 . Then, the slip behind the rupture edge is expected to continuously accelerate and no finite stable stress drop can emerge.

The previous theoretical discussion is in sharp contrast with the observations of a stress drop in various frictional systems [212; 207; 208; 127; 210; 136; 133; 213]. Then, how one can reconcile these two apparently incompatible observations?

We write in detail the elastodynamics relations at the interface between two solids that are driven by a constant stress far from the interface, τ_0 . In these conditions (and not specifically at steady-state), the interfacial stress writes $\sigma_{xy} = \tau_0 + \tilde{s}(x, t)$ with \tilde{s} a spatiotemporal integral that describes the long-range stress transfer between two parts of the interface. Under strict homogeneous steady-state before any slip, $\tilde{s}(x, t) \rightarrow 0$ and thus the equilibrium at the interface give the left-most intersection on Fig. 5.2a (and Fig. 5.2b). However, at finite times after rupture, the term $\tilde{s}(x, t)$ makes a contribution that describes the deviation from steady-state. If one considers finite times before the elastic waves have time to reach the system boundaries at $y = \pm H$, the spatiotemporal contribution can be decomposed into two terms: (i) the instantaneous response of the interface due to a change in slip velocity, known as the radiation damping term $\mu/(2c_s)(v - v_0)$ with μ the shear modulus of the bulk, c_s the shear wave velocity, and v_0 the reference sliding velocity, (ii) and a non-local contribution $s(x, t)$ [169; 170; 171]. One can write:

$$\sigma_{xy}(x, t) = \tau_0 - \frac{\mu}{2c_s} [v(x, t) - v_0] + s(x, t). \quad (5.2)$$

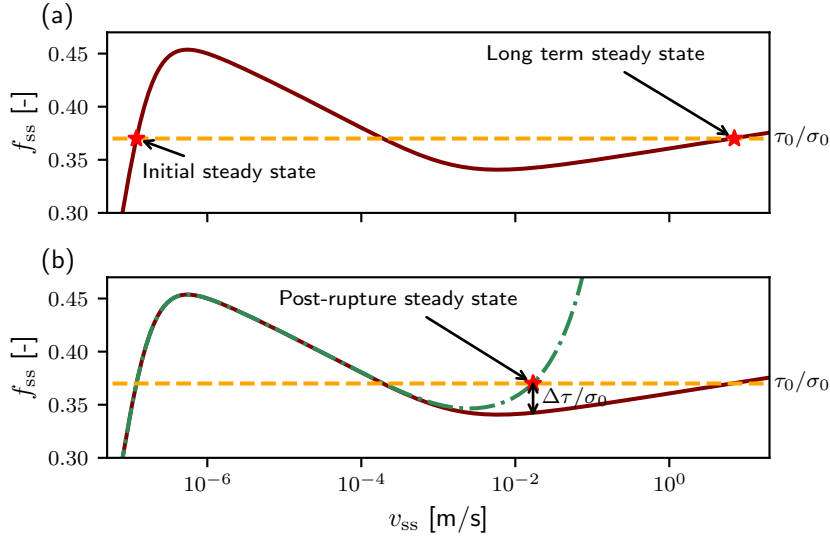


Figure 5.2: (a) The steady-state normalized frictional strength f_{ss} (solid brown line) vs. the steady-state slip velocity v_{ss} on a semilogarithmic scale. The curve has a generic N shape [86], with two rate-strengthening branches ($df_{ss}/dv_{ss} > 0$) separated by a rate-weakening branch ($df_{ss}/dv_{ss} < 0$). The dashed horizontal orange line represents an imposed driving stress $f_0 = \tau_0/\sigma_0$. It intersects the steady-state friction curve at three points: the first one, for small velocity, is stable (on a rate-strengthening branch) and describes the state of the system before perturbation ("Initial steady state"). There is another stable-fixed point at large velocities that describes the state of the interface after rupture to equilibrate the friction coefficient with the driving stress ("Long term steady state"). The last one is unstable and is located on the rate-weakening branch. The latter will be discussed later in this chapter, when we will consider velocity-driven sliding. (b) The effective steady-state friction curve (dotted dashed green line) obtained by adding the radiation damping term ($v_{ss}\mu/2c_s$) to the solid brown line. The driving stress intersects the effective friction curve at a different velocity, marked as the "Post-rupture steady state". The corresponding stress drop $\Delta\tau/\sigma_0$ is indicated by the black double arrow.

The radiation damping term plays an important role in the emergence of a stress drop. Consider a system that is sufficiently large such that the spatiotemporal integral term $s(x, t)$ vanishes far behind the rupture edge, but the radiation damping term is still relevant, i.e., wave reflection at the boundaries and back to the interface has not occurred yet. Then, the equilibrium of stress far from the rupture front can be written as:

$$\tau(v_{\text{res}}) \simeq \tau_0 - \frac{\mu}{2c_s} [v_{\text{res}} - v_0], \quad (5.3)$$

with v_{res} the residual sliding velocity far behind the front. Thus, the residual stress can be written as $\tau_{\text{res}} = \tau_0 - \frac{\mu}{2c_s} v_{\text{res}}$ and the corresponding finite stress drop is the radiation damping term:

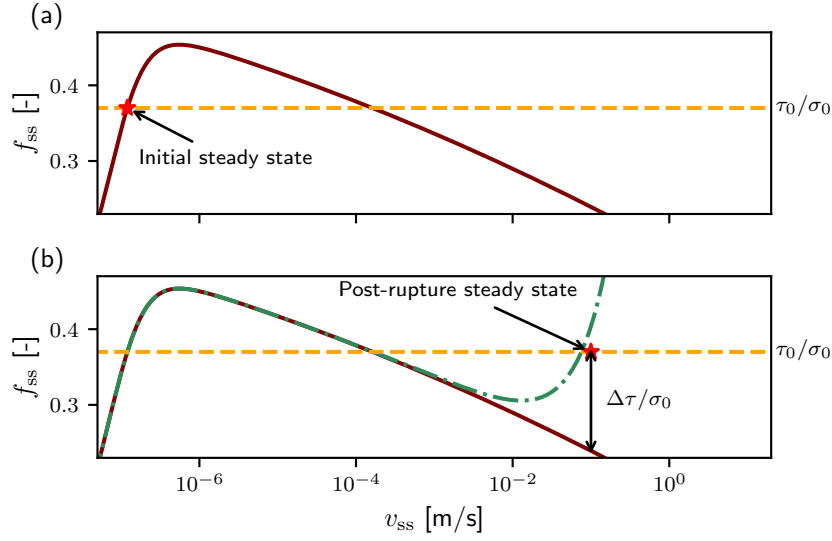


Figure 5.3: The same figure as Fig. 5.2 but for a steady-state friction law that is purely weakening at high velocities. (a) The steady-state normalized frictional strength f_{ss} (solid brown line) vs. the steady-state slip velocity v_{ss} on a semilogarithmic scale. The dashed horizontal orange line represents an imposed driving stress $f_0 = \tau_0/\sigma_0$. Contrarily to the N-shaped law, the driving stress intersects the steady-state friction curve only at two points: at small velocity and in the weakening branch. There is no "Long term steady state" in this case. However, when adding the radiation damping term to obtain the effective steady-state friction curve (b), there is a stable point that again gives the stress drop according to Eq. (5.4).

$$\Delta\tau \simeq \frac{\mu}{2c_s} v_{\text{res}}. \quad (5.4)$$

The previous equation is valid only for timescale $\mathcal{O}(H/c_s)$. This situation is represented in Fig. 5.2b, in which the friction law with the addition of the radiation damping term (left-hand side of Eq. (5.3)) is the dotted dashed green curve. This *effective* steady-state friction intersects the driving stress at a smaller velocity than the initial friction law. For the friction law with no minimum (Fig. 5.3b), this creates a new stable point compared to the initial law, which is only valid at finite times. The corresponding stress drop is indicated with black double arrow in Fig. 5.2b and Fig. 5.3b. Note that this physical picture is limited to timescale before the reflections of shear waves at the boundaries and back to the interface. After that, the stress drop is expected to decrease to zero in discrete steps corresponding to each wave reflection, see [79].

5.1.3 Simulation support for the emergence of $\Delta\tau$

We now aim at verifying the prediction of Eq.(5.4) by conducting numerical simulations of frictional rupture in infinite systems, such that no wave reflection occurs. We use the

Chapter 5. On the dynamics of frictional interfaces described by rate and state friction laws

spectral boundary integral method described in chapter 3.2 to simulate the behavior of two semi-infinite elastic homogeneous bodies in contact along a frictional interface. Periodicity at the extremity of the interface ($x = 0, x = W$) is employed, and we load the system in anti-plane shear (mode III) conditions. Both the N-shaped friction law Eq. (2.45) and the one without minimum at high velocities are tested. The interface is initially at steady-state with a small sliding velocity $v_0 \simeq 0$ and under constant shear stress τ_0 . Rupture is nucleated at the center of the interface by introducing a Gaussian perturbation in the slip velocity field (with an amplitude sufficiently large that the interface behavior in the perturbed area is velocity weakening). The outcome of a typical simulation is shown in Fig. 5.4. The velocity (panel (a), brown curve) and the stress (panel (b), orange curve) profiles reveal two propagating rupture fronts going in opposite directions at a rupture velocity $c_R = 0.84c_s$. As expected, the residual velocity reaches a plateau far behind the rupture edge, with the stress also saturating at a finite value. One can thus measure the observed stress drop (indicated with black double arrow in Fig. 5.4b) and compare it to the prediction of Eq. (5.4).

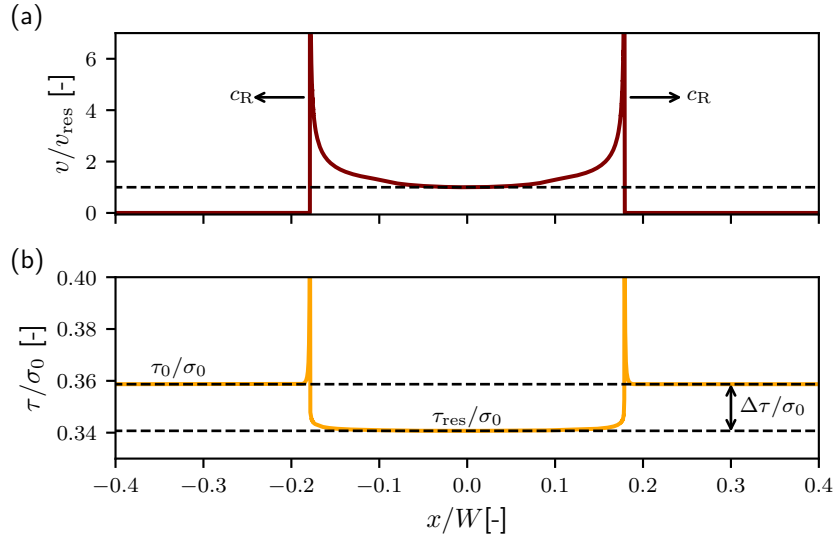


Figure 5.4: (a) A snapshot of the slip velocity $v(x)$ normalized by the residual velocity behind the tip v_{res} . Two fronts are propagating in opposite directions at high velocity (here $c_R = 0.84c_s$). The rupture invades the interface that is currently sticking $v \simeq 0$ and lets behind it some residual velocity. The axe is truncated for visual clarity (b) A snapshot of the shear stress τ normalized by the compressive stress σ_0 . The rupture fronts propagate in regions characterized by the driving stress τ_0 , and let behind them a well-defined residual stress $\tau_{\text{res}} < \tau_0$. Thus, a finite stress drop $\Delta\tau$ emerges.

This comparison is shown in Fig. 5.5. The theoretical predictions are shown in solid brown for the N-shaped law and orange for the no-minimum friction law, while the results of numerical simulations are shown with brown circles (N-shaped) and orange squares (no-minimum), for various driving stress τ_0 . The agreement between prediction

5.1 Emergence of crack-like behavior of frictional rupture

and numerical results is excellent (note that it is better for the N-shaped law). The reader interested in detailed explanation regarding the error for the no-minimum curve is redirected toward [191]. A similar discussion for slow ruptures in which the spatiotemporal term $s(x, t)$ might be dominant is also presented in [191], as well as a comparison with experiments.

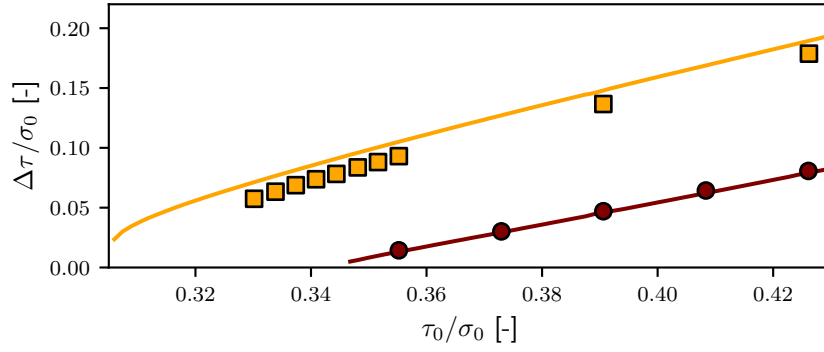


Figure 5.5: Theoretical prediction for the value of the stress drop given by Eq. 5.4 for $\Delta\tau$ for rapid ruptures, for respectively the N-shaped friction law shown in Fig. 5.2 (brown curve) and the no-minimum law shown in Fig. 5.3 (orange curve). The brown circles correspond to the stress drop measured in numerical simulations with the N-shaped law, while the orange squares are for the no-minimum law.

5.1.4 Crack-like behavior of frictional rupture

Once the emergence of a finite stress drop is established, one can explore the implication on the behavior of frictional rupture. First, the existence of a stress drop implies that the region near the rupture tip should carry an increased amount of stress to compensate for this reduction. In the theory of linear elastic fracture mechanics, this amplification of stress is singular near the rupture edges, as:

$$\sigma_{xy} \propto \frac{K(L, c_R)}{\sqrt{x - x_r}}, \quad (5.5)$$

where $K = \Delta\tau\sqrt{L}\mathcal{K}(c_R/c_s)$ is the stress intensity factor, L is the size of the rupture, c_R the velocity of the rupture front (not to be confused with the Rayleigh wave speed c_r), x_r the location of the rupture edge and $\mathcal{K}(c_R/c_s)$ a dimensionless function of the rupture edge's propagation velocity. The slip velocity near the rupture edges follows a similar scaling, as :

$$v \propto \frac{c_R K(L, c_R)}{\mu\sqrt{x - x_r}}. \quad (5.6)$$

Note that Eqs. (5.5,5.6) are valid independently of the rupture mode (for in-plane shear and out-of-plane shear). One of the fundamental principles of fracture mechanics is that

Chapter 5. On the dynamics of frictional interfaces described by rate and state friction laws

the square root singularity at the tip is accompanied by a finite flux of energy at the crack tip, the so-called *energy release rate* G . It is directly related to the stress intensity factor, and writes:

$$G(L, c_R) \propto \mathcal{A}(c_R/c_s) \frac{[K(L, c_R)]^2}{\mu}, \quad (5.7)$$

in which $\mathcal{A}(c_R/c_s)$ is a dimensionless function of the rupture velocity and depends on the rupture mode. If the local energy balance is valid (as expected from fracture mechanics), the energy release rate is equal to the fracture energy $G = G_c$. It is important to note that contrarily to ordinary tensile brittle fracture (mode I) where the dissipation is localized at the tip, in the case of frictional rupture, dissipative processes are in play on the entire interface. Once a stress drop exists, are the fields near a frictional rupture front square root singular, and if so, can one extract the fracture energy from the entire dissipation occurring at the interface? Is the local energy balance valid for frictional rupture? Before addressing all of these questions, that have been partially discussed in the literature already [200; 82; 80; 214; 215; 216; 217], we address the question of the frictional rupture front equation of motion.

5.1.4.1 Equation of motion

Assuming that the previous equations are valid, and combining them, one can obtain the propagation velocity as a function of a length-dependent stress drop quantity, as :

$$\frac{c_R}{c_s} = \mathcal{F}\left(\frac{L}{L_G(\Delta\tau)}\right), \quad (5.8)$$

and

$$L_G(\Delta\tau) = \mu G_c / (\Delta\tau)^2, \quad (5.9)$$

where $L_G(\Delta\tau)$ is a generalized Griffith-like length. The previous equation is valid under the assumption that the fracture energy is constant and independent of the rupture velocity c_R . \mathcal{F} is an increasing monotonous function that depends on the rupture mode. We test this prediction with the simulations that were used to determine the stress drop shown in Fig. 5.5. We compute the local rupture velocity c_R and the frictional rupture length L (as the distance between the two frictional rupture tips) and represent them in Fig. 5.6a. According to Eq. (5.8), all the curves should be collapsing when rescaling by the Griffith-like length $L_G(\Delta\tau)$. This is done in Fig. 5.6b, in which $G_c = 0.65$ [J/m²] and a unit prefactor have been used. All the curves $c_R(L)$ collapse on a master envelope after rescaling. Some deviations are observed at early times for each curve, which is expected, as the crack-like nature of frictional rupture is not valid during the nucleation stage. This first preliminary verification provides strong support to the assumptions of crack-like behavior. We now aim at verifying it directly.

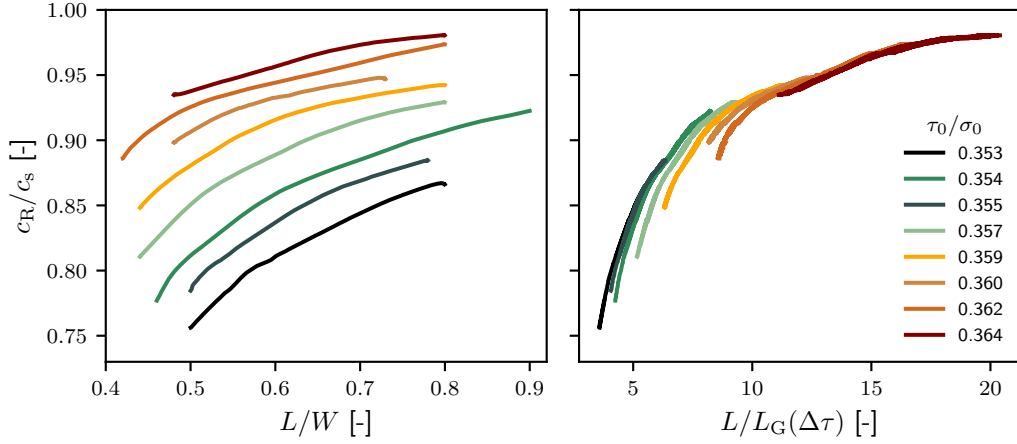


Figure 5.6: (a) The rupture velocity c_R normalized by the shear wave speed c_s as a function of the size of the frictional rupture L , normalized by the system size W for various driving stress value τ_0/σ_0 using the N-shaped friction law shown in Fig. 5.2. (b) The rupture velocity versus the rupture size normalized by a generalized Griffith-like length $L_G(\Delta\tau)$ as given by Eq. 5.9. The curves collapse on a master envelope as predicted by Eq. 5.9.

5.1.4.2 Stress singularity and energy balance

We represent in Fig. 5.7 a zoom on the fields near a rupture tip: the stress in dashed orange $((\tau - \tau_0)/\sigma_0)$ and the slip velocity in solid brown $(v\mu\alpha_s(c_R)/2c_R\sigma_0)$. We then fit the two fields such that they share the same stress intensity factor K and the same rupture tip location x_r (details about the procedure can be found in [192]), and plot the corresponding square root singular fields in dashed black. The latter represent faithfully the velocity and stress fields near the rupture tip, supporting the existence of singular fields for frictional rupture once a stress drop is present. The inset illustrates this match in a double logarithmic scale, with the square root singularity being indicated as a line with slope $-1/2$. The range over which the velocity field is square root singular is significantly larger than its stress counterpart. From this fit, one can extract the value of the stress intensity factor and then compute the energy release rate associated with the rupture front, as was done in [190].

To assess if the concept of local energy balance is valid, we need to compute the fracture toughness independently. This verification was done by Dr. Fabian Barras [190], and we recall it here for completeness. The dissipated energy during frictional rupture at a given location x is given by:

$$E_{BD}(\delta, x) = \int_0^\delta (\tau(\delta') - \tau_{res}) d\delta'. \quad (5.10)$$

The dissipated energy, here called breakdown (and not fracture energy yet) is computed at distinct locations behind the rupture tip (noted $x = l_i$ with $i = 1 - 3$, 1 being the

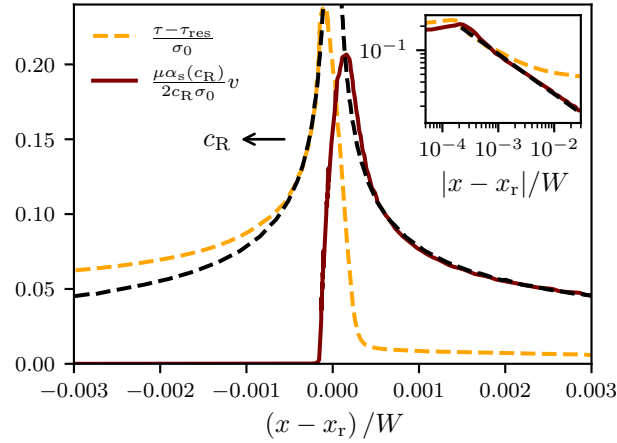


Figure 5.7: The normalized profile of the shear stress $\tau(x, t)$ (orange) and the slip velocity $v(x, t)$ (brown) near a rupture edge, propagating towards the left with a velocity $c_R \simeq 0.94c_s$. The position x is shifted by the position of the rupture edge x_r . The dashed lines are the result of fitting the singular fields of fracture mechanics as described in Eqs. (5.5,5.6). (inset) The same as the main panel, but in a double logarithmic scale, illustrating the quality and the range of the fit for the singular fields.

closest to the nucleation site and 3 the farthest). We plot the breakdown energy in Fig. 5.8 for the three locations. The three curves are perfectly equivalent for small slips, but then show some location dependency for larger slip values. This can be understood as follows: the shear stress features a strong decay close to the tip location, and then a slow decay towards its residual value on a significantly larger length-scale. The latter is related to the rate and state nature of the friction law, with a residual steady-state that is slowly reached. In addition, the rupture front accelerates (as shown in Fig. 5.6), which implies that the function $\tau(\delta)$ is different for each location. The localized edge dissipation should be understood as the effective fracture energy G_c that appears in the equations of fracture mechanics. This value is indicated with a black horizontal line in Fig. 5.8. One possibility to evaluate G_c independently relies on the observations that, around the rupture tip, the function $v\phi/D$ is significantly larger than 1 [190]. We recall here that $v\phi/D$ being larger or smaller than unity determines if the contact area is reduced or increased, as it directly controls the sign of the evolution law $\dot{\phi}$. To estimate G_c , one can thus compute the dissipated energy only in the region where the state value is decreasing (i.e., microcontacts are broken), with:

$$G_c = \frac{1}{c_R(t)} \int_{v\phi/D > 1} (\tau(x, t) - \tau_{\text{res}}) v(x, t) dx. \quad (5.11)$$

The ratio between this quantity and the energy release rate estimated from the singular fields is shown in the inset of Fig. 5.8, with the ratio being close to 1. The breakdown energy, however, can be in significant excess compared to G_c , implying that non-localized friction dissipation is a generic feature of interfaces following a rate and state friction

law.

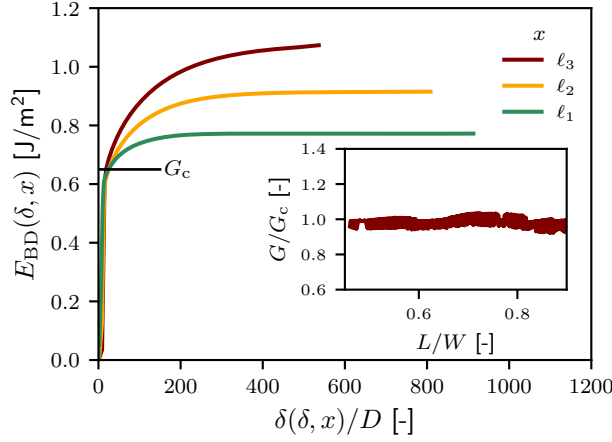


Figure 5.8: Breakdown energy E_{BD} as a function of the slip for three interface locations on the interface with $\ell_1 = 0.15W$, $\ell_1 = 0.2W$ and $\ell_1 = 0.25W$. The three curves are collapse up to $E_{BD} \simeq 0.65 \text{ [J/m}^2\text{]}$ which is identified as G_c . (inset) The ratio between the energy release rate G and the fracture energy G_c computed independently as a function of the position of the rupture tip.

5.1.5 Conclusion

In the first part of this chapter, we show that contrarily to what is usually assumed, the stress drop in frictional rupture is not a characteristic property of the interface, but is rather a quantity that is determined by the bulk elastodynamics (through wave radiations and long-range wave transfer), the friction law and the driving stress. This stress drop (for rapid rupture) is a finite time effect that is limited by the time of travel of waves in the system. We then evaluate if frictional rupture, once a finite stress drop exists, behaves like regular cracks. We show that for the constitutive relations considered here (rate and state friction), the near tips fields are approximately square root singular. The local balance of energy near the tip is satisfied once one has extracted the fracture energy from the total dissipated energy, which also involves frictional dissipation that is non-edge-localized. The effective fracture energy computed here is constant, while the total breakdown energy features position dependency. The analogy between frictional rupture and ordinary fracture is thus not complete. The deviations from the classical picture of fracture mechanics have been discussed in [218; 219; 220], and have significant implications in understanding the total energy budget of earthquakes.

5.2 Velocity-driven frictional sliding: coarsening and steady-state pulses

Frictional sliding is an intrinsically complex phenomenon, emerging from the interplay between driving forces, elasto-frictional instabilities, interfacial nonlinearity and dissipation, material inertia, and bulk geometry. We show that homogeneous rate-and-state dependent frictional systems, driven at a prescribed boundary velocity — as opposed to a prescribed stress — in a range where the frictional interface is rate-weakening, generically host self-healing slip pulses, a sliding mode not yet fully understood. Such velocity-driven frictional systems are then shown to exhibit coarsening dynamics saturated at the system length in the sliding direction, independently of the system's height, leading to steadily propagating pulses. The latter may be viewed as a propagating phase-separated state, where slip and stick characterize the two phases. While the coarsening process is limited by the system's length — leading in the presence of periodic boundary conditions to a pulse train with periodicity identical to the system's length —, the single pulse width, characteristic slip velocity, and propagation speed exhibit rich properties, which are comprehensively understood using theory and extensive numerics. Finally, we show that for sufficiently small system heights, the pulse is accompanied by periodic elasto-frictional instabilities.

5.2.1 Introduction

Frictional systems are composed of two bodies coupled at a contact interface, formed by compressive forces that hold them together. Frictional motion is typically driven in shear (either stress-controlled or velocity-controlled) applied far from the frictional interface. The frictional interface and its spatiotemporal dynamics are generically characterized by strong nonlinearity and dissipation, where the interfacial response depends on the local slip velocity v and on the structural state of the interface, carrying memory of its history [7; 74; 71; 221; 53; 222; 223; 76]. Different parts of the frictional interface are coupled through long-range spatiotemporal interactions mediated by the bodies in contact. The latter corresponds to the bulk elastodynamics of the bodies, dependent on their elastic response functions — which in turn depend also on their geometry — and on material inertia. Consequently, frictional dynamics inherently emerge from the coupled effects of interfacial and bulk physics, as discussed in the previous section and in [191; 79; 192].

The interplay between external driving forces, interfacial nonlinearity and dissipation, material inertia, and bulk geometry gives rise to very rich spatiotemporal dynamics, which characterize a wide variety of natural and man-made frictional systems, ranging from geological earthquake faults to a multitude of engineering structures and devices [47; 224; 48; 225; 226; 227]. Understanding, predicting and controlling frictional dynamics remain major scientific and technological challenges. An inseparable aspect of these challenges is that frictional systems host various spatiotemporal instabilities;

among these, the most well-characterized instability is associated with rate-weakening friction, i.e. with physical situations in which the steady frictional resistance is a decreasing function of the slip velocity v [228; 156; 129; 229; 230; 158; 80; 83; 84; 231; 232; 233; 234; 235; 236; 78; 120]. This interfacial destabilizing process is counteracted by stabilizing bulk elastic interactions, giving rise to a critical elasto-frictional length for the onset of instability (to be accurately defined below). Such instabilities typically result in rapid slip propagation along frictional interfaces, mediated by rupture modes [122; 114; 113; 123; 116; 229; 82; 124; 117; 125; 120; 126; 127; 128].

Spatiotemporal rupture propagation modes can be generally classified into expanding crack-like rupture fronts and compact self-healing slip pulses [105; 122; 114; 113; 123; 116; 229; 237; 121; 238; 118; 239]. In the former, v at an interfacial position behind the propagating mode remains finite as long as propagation persists, while in the latter, v vanishes over a finite time as propagation persists. The emergence of self-healing slip pulses and their properties are not yet fully understood, though it is currently accepted that this mode of frictional rupture propagation is relevant in various frictional systems and physical situations [105; 107; 229; 109; 112; 106; 118; 239]. For example, it is not yet clear how and under what conditions the very same frictional system can feature both crack-like rupture and slip pulses [122; 114; 113; 123; 116; 229; 82; 124; 117; 125; 120; 126; 127; 128; 239]. Moreover, whether steady-state slip pulses exist and if so whether they are stable, how the pulse width and propagation velocity are self-consistently selected in the presence of rate and state dependent friction, and what is the dependence of such rupture modes on the type of external driving are not yet clear.

In this section, we show that there exist generic, and in fact widely used, external driving forces that may lead to the generation of slip pulses. In particular, we show that velocity-driven frictional sliding — as opposed to stress-driven frictional sliding — may give rise to propagating periodic slip pulse trains, whose emerging properties are extensively studied below. It is important to stress that while slip pulses are commonly (but not exclusively) associated with bimaterial frictional interfaces (i.e., interfaces separating bodies made of different materials, see for example [112] and references therein), we show that slip pulses naturally emerge in the absence of a bimaterial contrast under velocity-driven conditions (though our basic reasoning applies to bimaterial frictional interfaces as well).

To understand the qualitative differences between velocity-driven and stress-driven frictional sliding, consider the frictional system illustrated in Fig. 5.9a, composed of two identical bodies of height H and length W , and characterized by elastic constants μ (shear modulus) and ν (Poisson's ratio), and mass density ρ . The bodies are held together by a homogeneous normal (compressive) stress σ_0 and are subjected to some shear-related boundary conditions. In the figure, the boundary conditions at the upper and lower edges are denoted by $v_0/2$, implying that in this case the applied velocity (of overall magnitude v_0) is kept fixed. However, one could also consider a situation in which the applied shear stress τ_0 is kept fixed, as discussed in the previous section.

To explain why these two types of driving forces may lead to qualitatively different

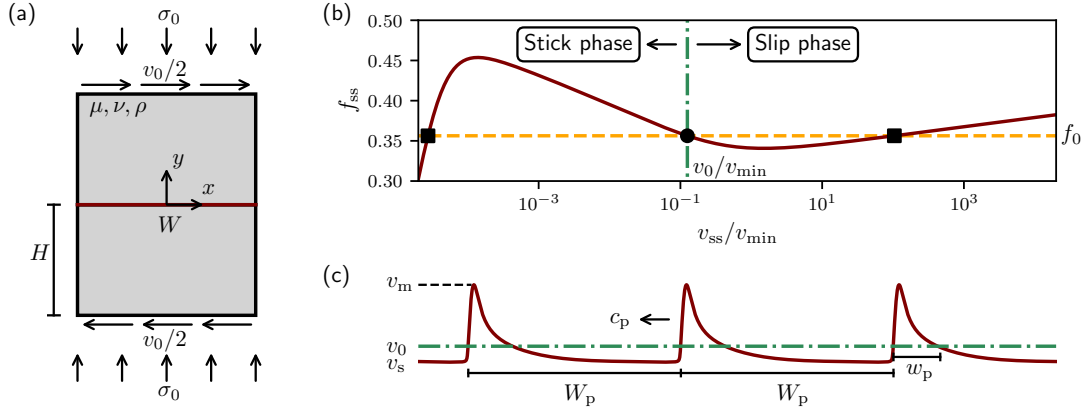


Figure 5.9: (a) A schematic representation of the class of frictional systems under consideration. Two identical elastic bodies of width W and height H are in contact along an interface located at $y=0$ (brown line). The bodies are under constant normal (compressive) stress σ_0 and are driven anti-symmetrically at the upper and lower boundaries with a constant shear velocity $v_0/2$ such that the overall applied slip rate is v_0 . Periodic boundary conditions are imposed in the x direction. (b) The steady-state normalized frictional strength f_{ss} (solid brown line) vs. the steady-state slip velocity v_{ss} (normalized by v_{min} , the minimum of f_{ss}) on a semi-logarithmic scale. The curve has a generic N shape [86], with two rate-strengthening branches ($df_{ss}/dv_{ss} > 0$) separated by a rate-weakening branch ($df_{ss}/dv_{ss} < 0$), see text for additional discussion. The dashed horizontal orange line represents an imposed driving stress $f_0 = \tau_0/\sigma_0$, which intersects the steady-state friction curve at three points. Two are stable fixed-points on the rate-strengthening branches of the friction law (black squares), while the third one is an unstable fixed-point on the rate-weakening branch (black circle). The dashed-dotted vertical green line corresponds to an imposed driving velocity v_0 — as in panel (a) — and intersects the friction law at a single point on a rate-weakening branch. As is extensively discussed in the text, imposing a slip velocity v_0 on the *unstable* rate-weakening branch cannot result in spatially-homogeneous sliding; rather, it leads to a dynamic and spatially-inhomogeneous phase separation between low velocity (‘stick phase’, left-pointing arrow) and high velocity (‘slip phase’, right-pointing arrow) regions. The outcome is a propagating phase-separated state in the form of a pulse train. (c) A generic sketch of a pulse train observed under velocity-controlled frictional sliding. The train travels at a velocity c_p and features periodicity W_p and pulses of width w_p . The pulses feature a maximum slip velocity v_m and propagate into the stick phase of a characteristic stick velocity v_s , which is vanishingly small. The dashed-dotted horizontal green line corresponds to the driving velocity v_0 .

physical consequences, we plot in Fig. 5.9b the steady-state frictional resistance, $f_{ss} = \tau_{ss}/\sigma_0$ (where τ_{ss} is the steady-state frictional strength/stress), as a function of the logarithm of the steady-state slip velocity v_{ss} . By steady-state we mean that we focus on a point along the frictional interface that experiences a slip velocity v_{ss} for a sufficiently long time, and measure the resulting frictional strength/stress τ_{ss} ; the steady-state

friction coefficient, which out of steady-state depends on the instantaneous slip velocity v and on a set of structural (internal) variables (see below), is simply given by $f_{ss} = \tau_{ss}/\sigma_0$, as stated above. The steady-state friction curve $f_{ss}(v_{ss})$ features a generic N shape [86], where friction is rate-strengthening at both low and high slip velocities (the latter occurs above the minimum of the curve, denoted by v_{\min}), and rate-weakening at intermediate velocities (typically spanning a few orders of magnitude, note again the logarithmic v_{ss} -axis).

To highlight the differences between velocity-driven and stress-driven sliding, consider the frictional system illustrated in Fig. 5.9a under the application of a fixed (total) slip velocity v_0 , which resides in the rate-weakening branch of the steady-state friction curve (marked by the dashed-dotted vertical green line in Fig. 5.9b). Consider also the stress-driven counterpart of this system, i.e. the case in which a fixed shear stress τ_0 is applied. The latter corresponds to $f_0 = \tau_0/\sigma_0$ (marked by the dashed horizontal orange line in Fig. 5.9b) and is chosen such that $f_0 = f_{ss}(v_0)$, i.e. the dashed-dotted vertical and dashed horizontal lines intersect the steady-state friction curve at the very same point, marked by a black circle in Fig. 5.9b. The horizontal line, corresponding to stress-driven sliding, intersects the steady-state friction curve also at two other points on the two rate-strengthening branches, marked by black squares. Let us focus first on the stress-driven case and ask whether spatially homogeneous and stable steady sliding can emerge under these conditions. It is clear that steady sliding of the whole system at v_0 is not possible because the rate-weakening branch is unstable (for W larger than the critical elasto-frictional length). On the other hand, homogeneous and stable steady sliding at the velocities corresponding to the black squares is possible, because the latter reside on rate-strengthening branches, which are stable [191].

This situation is in sharp and qualitative contrast to the velocity-driven case, where the sliding velocity v_0 is enforced on the outer boundaries. In this case, spatially homogeneous sliding is *impossible* because v_0 resides on the rate-weakening branch, implying instability, and no other spatially homogeneous velocity solutions are possible either (unlike the stress-driven case). Consequently, either steady sliding does not exist at all or spatially inhomogeneous steady-state $v(x, t)$ emerges (x here denotes the spatial coordinate along the frictional interface and t is the time) such that $W^{-1} \int_0^W v(x, t) dx = v_0$ at any time. In the latter situation, $v(x, t)$ must take the form of a steadily propagating pulse train, illustrated in Fig. 5.9c. The pulse train is characterized by a spatial periodicity W_p and a propagation velocity c_p . Each pulse within the train features a characteristic width w_p (to be accurately defined below), a maximal velocity $v_m > v_0$, and a minimal velocity $v_s < v_0$. Since v_s is typically much smaller than v_0 , it is termed the ‘stick velocity’, corresponding to a nearly non-sliding state, which is termed the ‘stick phase’ (cf. Fig. 5.9b). The parts of a pulse train that feature $v(x, t) > v_0$ can be regarded as ‘slip phases’ (cf. Fig. 5.9b); consequently, a pulse train may be viewed as a propagating mode composed of alternating stick and slip phases.

This physical picture of pulse trains as propagating modes composed of alternating stick and slip phases, emerging under velocity-driven conditions, may suggest an analogy

Chapter 5. On the dynamics of frictional interfaces described by rate and state friction laws

to phase separation (and the associated Maxwell construction) in equilibrium thermodynamics [240]. In the latter, phase separation emerges when the pressure-volume isotherm of a system in equilibrium features a non-monotonic behavior, corresponding to a non-convex free energy [240]. If then the system is enforced to have a volume in the non-monotonic region of the pressure-volume isotherm, where the pressure is an increasing function of the volume (thermodynamic stability requires the pressure to be a decreasing function of the volume), it cannot attain a (single) homogeneous phase; rather, the system undergoes a phase transition that leads to the co-existence of two phases of different densities [240]. While $f_{ss}(v_{ss})$ of Fig. 5.9b is by no means an equilibrium pressure-volume isotherm, rather it corresponds to a strongly dissipative interfacial response function of a driven open system, and while the imposed slip velocity v_0 inside the rate-weakening (unstable) branch is by no means the volume of an equilibrium system, there exists a clear and direct analogy between the two physical situations. In the frictional case, the result is not static phase separation, but rather a periodic and propagating phase-separated state of alternating stick and slip phases, the train of pulses illustrated in Fig. 5.9c.

It is important to stress that in practical terms, velocity-driven frictional sliding is the rule, rather than the exception. That is, velocity is almost always what is actually being controlled; in order to maintain a fixed stress, one needs to employ a feedback loop such that the velocity is precisely varied so as to keep the stress fixed. This procedure depends on the dynamics of the system, which may be fast, and is in general difficult to achieve. In most cases, it is just the velocity that is prescribed.

Our goal in this section is to understand the spatiotemporal dynamics of velocity-driven frictional systems, and in particular the emergence of steadily propagating pulse trains. Moreover, we aim at understanding the selection of the train properties, i.e. its spatial periodicity and propagation velocity, as well as the properties of a single pulse within the train. These goals are achieved using extensive numerical simulations — employing several computational methodologies — and theoretical analysis performed within a generic rate-and-state friction constitutive framework (to be detailed below). In particular, we employ the Boundary Integral Method in the $H \rightarrow \infty$ limit; while this method is formulated for stress-driven sliding in terms of τ_0 [169; 170; 171], we show that it can nevertheless be employed to mimic velocity-driven frictional dynamics. For finite H , we employ the Finite Element Method, as explained below.

We find that frictional systems under velocity-driven conditions, where the imposed velocity v_0 resides on an unstable rate-weakening branch of the steady-state friction curve, feature coarsening dynamics that lead to pulse trains whose periodicity W_p is determined by the system length W (where periodic boundary conditions in the sliding direction are employed, see below), independently of H . That is, surprisingly, periodic “pulse trains” emerge in our calculations due to the employed periodic boundary conditions in the sliding direction, but not due to any other train periodicity selection process. The terms “pulse train” and “train periodicity” are used hereafter in this sense. We also show that in the small H limit, coarsening competes with elasto-frictional in-

stabilities, giving rise to pulse trains with $W_p = W$ that experience repeated/periodic instabilities. Furthermore, we show that the pulse train propagation velocity c_p , the average single pulse slip velocity, and the single pulse width w_p are related through an equation of motion inspired by fracture mechanics [15]. The latter involves the pulse leading edge singularity and the emergence of an effective fracture energy. Finally, we show that the single pulse width w_p reveals non-trivial dependencies on $W_p = W$ and v_0 , featuring properties that are qualitatively different from those of ideal pulse solutions [241; 242; 243]. Taken together, we provide a comprehensive physical picture of velocity-driven frictional sliding in general, and of the properties of the emerging pulse trains in particular.

5.2.2 Simulating velocity-driven frictional dynamics

The rich spatiotemporal dynamics featured by frictional systems, with the multitude of physical factors at play (as discussed above), make purely analytical treatments of this class of problems practically impossible. Consequently, one needs to resort to numerical simulations, at least at the initial stages of investigating a given set of questions. Independently of the approach taken — either analytic, computational, or hybrid — one should first adopt bulk and interfacial constitutive relations, which is done in Sect. 5.2.2.1. To fully define the problem at hand, one should then specify the bulk geometry and external driving forces (boundary conditions) — here following Fig. 5.9a —, and finally one needs to select a solution method for the coupled bulk-interface problem. Focusing first on computational methods, we explain in Sect. 5.2.2.2 how the Boundary Integral Method — conventionally formulated in terms of stress boundary conditions — can be used to mimic velocity-driven frictional dynamics in the $H \rightarrow \infty$ limit. Next, in Sect. 5.2.2.3, we discuss the usage of the Finite Element Method to address the finite H regime.

5.2.2.1 Bulk and interfacial constitutive relations: Linear elastodynamics and rate-and-state friction

The frictional system illustrated in Fig. 5.9a is formed by two symmetric bodies, each satisfying its own continuum momentum balance equation $\rho \ddot{\mathbf{u}}(x, y, t) = \nabla \cdot \boldsymbol{\sigma}(x, y, t)$, where ρ is the mass density, $\mathbf{u}(x, y, t)$ is the displacement vector field, $\boldsymbol{\sigma}(x, y, t)$ is the stress tensor field, (x, y) is a two-dimensional Cartesian coordinate system and t is the time (a superposed dot represents a partial time derivative). $\boldsymbol{\sigma}$ in each body is related to \mathbf{u} through a bulk constitutive relation, which is taken here to be that of linear elasticity, i.e. we adopt Hooke's law [244] of the form $(1 + \nu)\mu [\nabla \mathbf{u} + (\nabla \mathbf{u})^T] = \boldsymbol{\sigma} - \nu(\mathbf{I}\boldsymbol{\sigma} - \boldsymbol{\sigma})$. Here \mathbf{I} is the identity tensor, ν is Poisson's ratio and μ is the shear modulus of each body. Note that body forces are neglected in the momentum balance equation and that the interface resides at $y=0$ (cf. Fig. 5.9a). An interfacial constitutive law is an implicit boundary condition for the two bulk problems defined above, formulated in terms of a functional relation between the interfacial shear stress, the interfacial normal stress, and

Chapter 5. On the dynamics of frictional interfaces described by rate and state friction laws

the slip velocity (and typically also additional interfacial state fields, see below). In the problems considered in this section, the interfacial normal stress is constant (uncoupled to frictional sliding), i.e. $\sigma_{yy}(x, y=0, t) = -\sigma_0$, where σ_0 is the applied compressive stress (cf. Fig. 5.9a).

The slip velocity $v(x, t)$ is the time derivative of the slip displacement $\delta(x, t)$, $v(x, t) = \dot{\delta}(x, t)$. Under in-plane shear (the so-called mode-II) conditions, where $\mathbf{u}(x, y, t) = (u_x(x, y, t), u_y(x, y, t), 0)$ (here the z component of the displacement vector field, $u_z(x, y, t)$, vanishes), one has $\delta(x, t) \equiv u_x(x, y \rightarrow 0^+, t) - u_x(x, y \rightarrow 0^-, t)$, where $+/-$ correspond to the upper/lower bodies, respectively. The relevant interfacial shear stress, in this case, is $\sigma_{xy}(x, y=0, t)$. Under anti-plane shear (the so-called mode-III) conditions, where $\mathbf{u}(x, y, t) = (0, 0, u_z(x, y, t))$ and z is the out-of-plane direction (perpendicular to the $x-y$ plane), one has $\delta(x, t) \equiv u_z(x, y \rightarrow 0^+, t) - u_z(x, y \rightarrow 0^-, t)$, and relevant interfacial shear stress, in this case, is $\sigma_{yz}(x, y=0, t)$. The interfacial shear stress, either $\sigma_{xy}(x, y=0, t)$ (mode-II) or $\sigma_{yz}(x, y=0, t)$ (mode-III), is continuous across the interface and equals the frictional stress/strength $\tau(x, t)$. Below we present results for both mode-II and mode-III, which are qualitatively and even semi-quantitatively similar. Mode-III (corresponding to scalar elastodynamics) is, however, mathematically and computationally simpler. The frictional stress/strength $\tau(x, t)$ is related to $v(x, t)$, $\sigma_{yy}(x, y=0, t)$ (which in our case equals $-\sigma_0$) and additional interfacial state fields through the interfacial constitutive law. The latter, at any position x along the interface and at any time t , is described by the following local relation

$$\tau(\sigma_0, v, \phi) = \sigma_0(v) f(|v|, \phi), \quad (5.12)$$

where $\phi(x, t)$ is a non-equilibrium order parameter, sometimes termed an internal-state field, which represents the structural state of the interface and encodes its history [7; 74; 71; 221; 53; 222; 223; 76]. Extensive evidence indicates that ϕ physically represents contact's age/maturity [74; 71; 221; 53; 222; 223; 76] and that its evolution follows

$$\dot{\phi} = g\left(\frac{\phi|v|}{D}\right), \quad (5.13)$$

with $g(1) = 0$. The characteristic slip displacement D controls the transition from a stick state $v \approx 0$ to a steadily slipping/sliding state $v_{ss} \neq 0$, with $\phi_{ss} = D/v_{ss}$ (the latter corresponds to $\dot{\phi} = g(1) = 0$). Under steady-state sliding conditions and a controlled normal stress σ_0 , the function $f_{ss}(v_{ss}) = f(|v_{ss}|, \phi_{ss} = D/v_{ss}) = \tau_{ss}(v_{ss})/\sigma_0$ has been measured over a broad range of slip rates v for many materials [86]. $f_{ss}(v_{ss})$ is generically N-shaped, as shown in Fig. 5.9b, where the precise functional form of $f(\cdot)$ and $g(\cdot)$ are detailed in section 5.2.7.1.

5.2.2.2 Mimicking velocity-driven frictional dynamics in infinite systems using the boundary integral method

With the bulk and interfacial constitutive relations at hand, the coupled bulk-interface problem is fully defined once the bulk geometry is specified. The system length is taken to be W , as shown in Fig. 5.9a; in order to avoid lateral edge effects, we employ periodic boundary conditions along this direction. The remaining geometric length scale in the problem is H , i.e. the height of each body (cf. Fig. 5.9a). It makes a difference whether H is taken to be arbitrarily large or finite, as is explained below. Here we first discuss the $H \rightarrow \infty$ case.

In the $H \rightarrow \infty$ limit, i.e. when the upper and lower boundaries are located infinitely away from the frictional interface, and no wave reflections from these boundaries take place, one can naturally invoke a Green's function approach. The latter allows eliminating the two bulk problems altogether, reducing the coupled bulk-interface problem to an interfacial integro-differential equation of the form [169; 156; 170; 171; 75]

$$\tau[v(x, t), \phi(x, t)] = \tau_0(t) - \frac{\mu}{2c_s}[v(x, t) - v_0] + s(x, t) . \quad (5.14)$$

where $\phi(x, t)$ satisfies Eq. (5.13) and the right-hand side is the interfacial shear stress. The latter contains three physically distinct contributions, to be discussed next.

The first contribution is the applied (spatially homogeneous) stress $\tau_0(t)$, i.e. this approach is directly applicable to stress-controlled conditions. The second contribution is the so-called radiation damping term [155; 122; 123; 245], where c_s is the shear wave speed and v_0 is set as a reference slip velocity (to be identified with the applied slip velocity v_0 in our velocity-controlled setting, see below). The radiation damping term locally depends on $v(x, t)$ and physically represents plane-waves being radiated away from the interface into the surrounding bulks, serving as effective damping from the perspective of the interface. Finally, the third contribution $s(x, t)$ is non-local in space and time, and physically represents the spatiotemporal interaction of different points on the interface, mediated by bulk elastodynamics. $s(x, t)$ generally does not admit real-space representation, and is related to the gradient of $\delta(x, t)$ in the spectral domain via a convolution integral, which is different for mode-II and mode-III [169; 170; 171]. The spectral nature of the formulation fits the choice of periodic boundary condition in the lateral/sliding direction (with periodicity W), and is reflected in its common name, the spectral Boundary Integral Method (BIM).

As explained above, and as evident in Eq. (5.14), the BIM is most suitable for stress-controlled boundary conditions represented by $\tau_0(t)$. Yet, we propose here an approach in which the BIM formulation can be nevertheless used to mimic velocity-driven frictional dynamics that are of interest here. The idea is the following: as explained above, under velocity-driven conditions *and* once the system reached steady-state, one has

$$\frac{1}{W} \int_0^W v(x, t) dx = v_0 . \quad (5.15)$$

Chapter 5. On the dynamics of frictional interfaces described by rate and state friction laws

Consequently, one can choose $\tau_0(t)$ — an a priori unknown function of time t — such that Eq. (5.15) is satisfied at any time t . That is, we propose to treat $\tau_0(t)$ in Eq. (5.14) as unknown and instead to impose Eq. (5.15) for any t . Thinking about a numerical implementation of the formulated problem, where both the time t and the spatial coordinate x are discretized, it is clear that the above suggestion leads to a well-defined problem; at each discrete time t_i , we added a single unknown $\tau_0(t_i)$ and a single constraint (Eq. (5.15) at t_i). Moreover, as v_0 is the relevant slip velocity in this modified BIM formulation, we used it as a reference velocity in the radiation damping term in Eq. (5.14).

The modified BIM formulation, aimed at mimicking velocity-driven frictional sliding, has both clear advantages and potential limitations. On the one hand, it is a relatively computationally cheap and very robust approach, which is expected to reveal velocity-driven steady-states in the $H \rightarrow \infty$ limit (if these exist). On the other hand, as Eq. (5.15) is strictly valid only in steady-state — i.e. some deviations from it are expected in early-time, out of steady-state dynamics — some dynamical aspects of the full velocity-driven problem may not be accurately captured. We address this potential limitation in two ways; first, we mainly focus on the long-time, steady-state behavior of the system, where our modified BIM formulation is strictly valid. Second, we verify through Finite Element Method (FEM) that the possible deviations of the transient dynamics in the $H \rightarrow \infty$ BIM calculations from the exact transient dynamics have no effect on the obtained steady-state solutions. More importantly, the FEM formulation to be discussed next allows us to understand the roles played by a finite H on the physics of the problem at hand.

5.2.2.3 Simulating velocity-driven frictional dynamics in finite systems using the finite element method

The length scale H may play important roles in velocity-driven frictional sliding. Consequently, it is essential to supplement the $H \rightarrow \infty$ BIM calculations with FEM ones, which allow probing the finite H regime. Moreover, finite H FEM calculations can be used to verify the validity of the modified BIM calculations, as discussed above, for selected test cases in which H is chosen to be large enough (see below). The new physics introduced by a finite H is the wave interaction of the frictional interface with the boundaries at $y = \pm H$, which is absent in the $H \rightarrow \infty$ limit, where waves are being radiated from the interface to $\pm\infty$ without reflections.

FEM simulations of frictional systems, especially when rate-and-state friction is taken into account, are significantly more challenging and computationally demanding than their BIM counterparts [168]. They are also prone to numerical and physical instabilities (associated with the finite H) that are absent in their BIM counterparts. One such physical instability is encountered in our large- H FEM calculations. This issue, along with the full details of our FEM simulations, are addressed in section 5.2.7.4. Agreement between our FEM and BIM calculations for mode-II (simpler mode-III calculations are performed only using BIM) is demonstrated in the next section, where we start discussing the emergent physics of velocity-driven frictional systems, and pulse trains

in particular.

5.2.3 Coarsening dynamics: The selection of pulse train periodicity

The first question we aim at addressing is whether steady-state pulse trains indeed emerge under velocity-driven sliding conditions and if so, what determines the train periodicity W_p . As the latter is of length dimension, one can a priori ask what quantities of length dimension existing in the posed problem could possibly determine W_p . The problem at hand, as formulated above, features 3 length scales: the system height H , the system length W and in addition to these two geometric/extrinsic length scales, we also have the intrinsic interfacial length D . As D is a mesoscopic length that characterizes the interfacial response, it does not appear in itself in the macroscopic coupled bulk-interface problem. Rather, it appears through the elasto-frictional length L_c that characterizes the rate-weakening ($df_{ss}/dv < 0$) elasto-frictional instability [7; 228; 156; 129; 230; 158; 80; 83; 84; 231; 232; 233; 234; 235; 236; 78; 120].

The elasto-frictional length L_c can be determined using a systematic linear stability analysis [78; 79], which is very briefly reviewed in section 5.2.7.2. Here we are mainly interested in the scaling structure of L_c , taking the form

$$L_c(H, D) = H \mathcal{F}\left(\frac{\mu D}{-\sigma_0 H v_0 df_{ss}/dv_0}\right), \quad (5.16)$$

where $\mathcal{F}(\mathcal{X}) \sim \mathcal{X}$ for $\mathcal{X} \ll 1$ and $\mathcal{F}(\mathcal{X}) \sim \sqrt{\mathcal{X}}$ for $\mathcal{X} \gg 1$ [79], with $\mathcal{X} \equiv -\mu D/(\sigma_0 H v_0 df_{ss}/dv_0)$. \mathcal{X} clearly manifests the coupled bulk-interface nature of L_c , incorporating the shear modulus μ of the bodies in contact, their height H (a geometric/extrinsic length), the applied normal stress σ_0 , the mesoscopic interfacial length D and the constitutive interfacial property $v_0 df_{ss}/dv_0 = \frac{df_{ss}(v_0)}{d \log v} < 0$. Note that the limiting behaviors of $\mathcal{F}(\mathcal{X})$, stated above, imply that L_c is independent of H in the limit $H \rightarrow \infty$. The length L_c implies that infinitesimal perturbations of wavelength larger than L_c , on top of homogeneous sliding with slip velocity v_0 , are linearly unstable. That is, for $L_c < W$ the system is linearly unstable as unstable perturbations can fit in (to ensure that this is the case, we use $L_c \ll W$ throughout this work). Moreover, the wavelength of the fastest growing mode of instability features the same scaling properties as L_c in Eq. (5.16).

To address the question of whether W_p exists, i.e whether steady-state pulse trains emerge, and if so how W_p depends on $L_c(H, D)$, H and W , we first explore the $H \rightarrow \infty$ limit using the BIM formulation of Sect. 5.2.2.2. That is, we first consider the case $L_c \ll W \ll H$. A representative result under mode-III conditions is presented in Fig. 5.10a, where a space-time plot of $v(x, t)/v_0$ is shown. It is observed that, as expected, at early times the velocity-driven frictional system experiences instabilities, resulting in multiple interacting slip pulses. As time progresses (increasing vertical direction in the space-time plot), the number of pulses decreases until — in the long-time limit — a single pulse survives. The latter corresponds to a steady-state pulse train of periodicity W , i.e. $W_p = W$ (recall that throughout this work we employ periodic boundary conditions along the

Chapter 5. On the dynamics of frictional interfaces described by rate and state friction laws

sliding direction). That is, the frictional system undergoes coarsening dynamics that are saturated at the system length W . To test the robustness of this observation, we varied W and the interfacial parameters over a wide range (cf. section 5.2.7.1 and 5.2.7.3); independently of these variations, we always observed $W_p = W$ in our $H \rightarrow \infty$ calculations, indicating coarsening dynamics that are truncated at the system length.

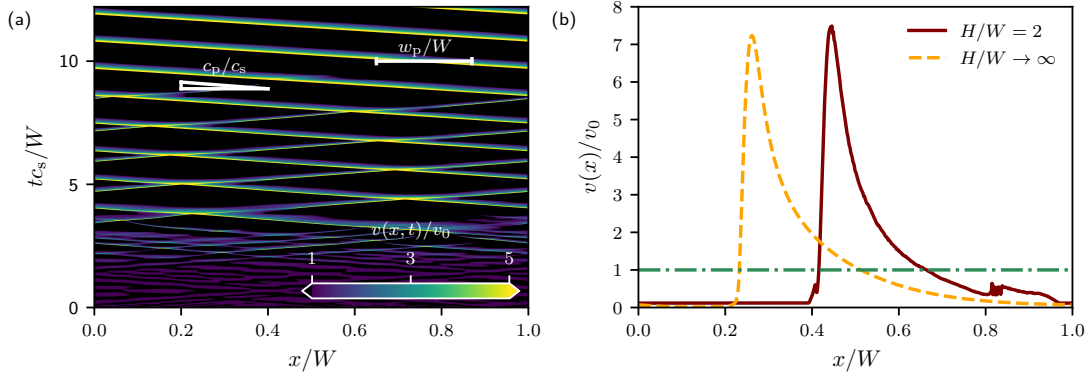


Figure 5.10: (a) A space-time plot of the slip velocity field $v(x, t)$ (normalized by v_0) obtained using a BIM simulation ($H \rightarrow \infty$) with $v_0 = 3 \times 10^{-3} \text{m/s}$, $W = 28.14 \text{m}$ and the N-shaped steady-state friction law of Fig. 5.9b. Black regions correspond to the stick phase, $v(x, t) < v_0$. At early times, the system hosts several instabilities. The interface progressively coarsens with increasing time until a single pulse remains in the periodic domain. The asymptotic pulse propagation velocity c_p/c_s is shown as the slope of the slip phase $v(x, t) > v_0$. The normalized pulse width w_p/W corresponds to the extent of the slip phase along the x axis at a given time t . A movie of this simulation is available in section 5.2.7.9. (b) A snapshot of $v(x, t)$ of a steady-state pulse train, comparing a BIM simulation (dashed orange line) and a FEM simulation (solid brown line) with $v_0 = 1 \times 10^{-3} \text{m/s}$, $W = 6 \text{m}$ and the steady-state friction law of Fig. 5.15. The dashed-dotted horizontal green line corresponds to the driving velocity v_0 . Both pulses are propagating towards the left at the same velocity $c_p \simeq 0.35 c_s$ and their shapes are almost identical.

Next, we aim at understanding whether a finite height H can result in a qualitative change in this physical picture, i.e. whether the pulse train periodicity W_p can be affected/determined by H . To address this question, one clearly needs to resort to FEM calculations. Due to numerical stability considerations, we use a rate-and-state friction law that does not feature the very low velocity rate-strengthening branch, see section 5.2.7.5 for discussion and details. In particular, we focus on the regime where $H \simeq W \gg L_c$ in order to see whether H affects W_p in addition to W (as they are comparable). In this regime, we encountered in addition to the elasto-frictional instability associated with L_c also a system-size instability. In this instability, the slip velocity vanishes throughout the interface for some period of time, and then the interface starts sliding almost *homogeneously*. That is, this instability appears to feature a space-independent stick-slip behavior (see section 5.2.7.6), which is likely to be related to the finite- H

elasto-frictional instabilities discussed in [246]. We have not studied this instability in depth; yet, it is not easy to imagine that an interface separating two deformable bodies would feature such a space-independent stick-slip behavior over increasingly large lengths and time scales. At the same time, FEM calculations with large W performed over long times are very demanding from the computational perspective, hence we cannot explicitly demonstrate the disappearance of the space-independent stick-slip behavior for sufficiently large W and times. Instead, we effectively eliminated this space-independent instability by breaking translational symmetry along the interface using a constraint similar to Eq. (5.15), as explained in section 5.2.7.6.

In Fig. 5.10b, we present a snapshot of the long-time behavior of an FEM simulation (as described above) of a frictional system with $H = 2W$ (solid line), where yet again a steady-state pulse train with $W_p = W$ is observed. This result is further strengthened by additional FEM calculations where the value of H has been varied for a fixed W , still having $H \simeq W \gg L_c$, yielding $W_p = W$ independently of H . The independence of W_p on H also suggests that for a fixed set of frictional parameters and W , the $H = 2W$ FEM calculation and the $H \rightarrow \infty$ BIM calculation should give rise to very similar results. Such a quantitative agreement is possible if the radiation damping term is not too large. This is the case if c_p is not close to the relevant wave speed.

In Fig. 5.10b, we superimposed the $H \rightarrow \infty$ BIM results (dashed line, for mode-II as in the FEM calculation) on top of the $H = 2W$ FEM ones (the two snapshots are shifted along x for visual clarity). It is observed that in both cases $W_p = W$ and that the pulse shape is almost identical (the same applies to the pulse train velocity $c_p \simeq 0.35c_s$, see figure caption). These convergent results demonstrate the robustness and validity of our FEM calculations. More importantly, they show that velocity-driven frictional systems exhibit coarsening dynamics that are saturated at the system length, independently of the system's height H in the regime $L_c \ll W \leq H$, leading to steadily propagating pulse trains with $W_p = W$. In light of the independence of W_p on H , we would like next to understand whether L_c can affect W_p , which requires considering the small H regime.

5.2.4 The small H limit: The competition between coarsening and elasto-frictional instabilities

The results of the previous section strongly suggest that we have $W_p = W$ independently of H for $L_c \ll W \leq H$, where L_c does not seem to play a role in the long-time pulse train as well. To address the possible role of L_c in the selection of the pulse train periodicity W_p , we explore here the small H limit for which $H < L_c \ll W$. Before discussing our FEM calculations in this regime, let us invoke some theoretical considerations regarding their possible outcomes. One possibility is that we find steady-state pulse trains with $W_p \simeq L_c$. While we cannot a priori rule out this possibility, we note that — if true — it implies that coarsening dynamics play no role whatsoever in this regime. It is not easy to imagine this in light of the fact that coarsening dynamics strongly dominate the physics for $L_c \ll W \leq H$. Another possibility is that coarsening dynamics remain dominant,

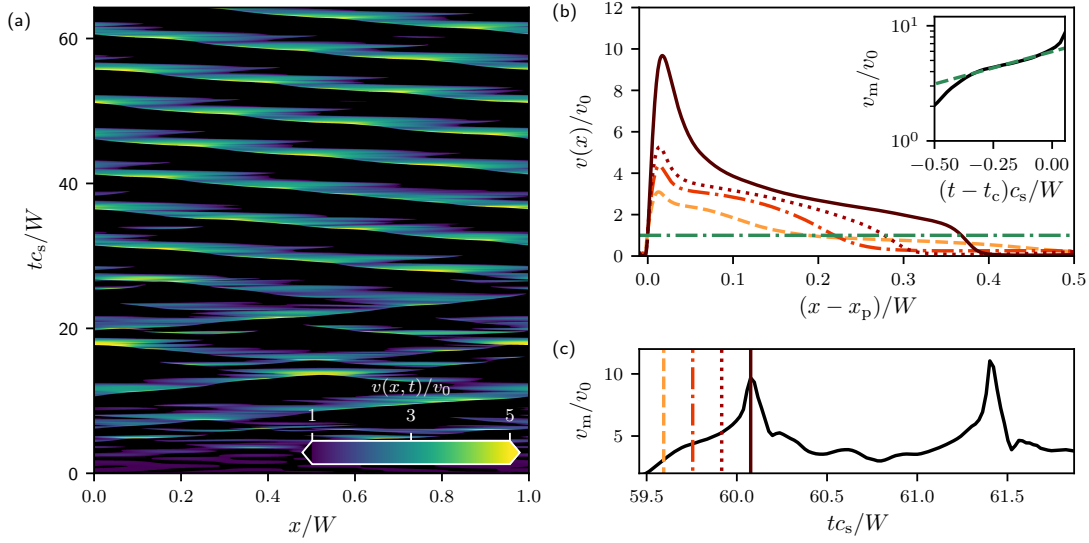


Figure 5.11: (a) A space-time plot as in Fig. 5.10a for a FEM simulation with $v_0 = 2 \times 10^{-3} \text{m/s}$, $W = 4 \text{m}$, $H = 0.2 \text{m}$ and the dashed-dotted orange steady-state friction law of Fig. 5.15. The observed behavior is similar to the BIM example ($H \rightarrow \infty$) of Fig. 5.10a, with the notable difference that the pulse train that remains in the system in the long-time coarsening limit features repeated oscillations (visible from the variation of the width and slip rate of the pulse). A movie of this simulation is available in section 5.2.7.9. (b) Successive snapshots of $v(x)/v_0$ are presented in the co-moving frame of the pulse train (with x_p being the pulse's leading edge). The pulse profiles are ordered in time as follows (line colors): dashed yellow, dashed-dotted orange, dotted brown, and solid dark brown. The dashed-dotted horizontal green line corresponds to the driving velocity v_0 . As time progresses, both the pulse width w_p and the slip velocity increase, indicating an elasto-frictional instability. A movie of the instability in the co-moving frame of the pulse is available in section 5.2.7.9. (inset) The time evolution of the normalized maximum velocity v_m (solid black curve) of the dynamics shown in panel (b), presented on a semi-logarithmic scale. The green dashed line is the best linear fit, corresponding to an exponential growth characterizing a linear instability, with the growth rate being the slope of this line. t_c corresponds to the time at which the growth becomes nonlinear. (c) The time evolution of v_m/v_0 . The vertical lines indicate the time of the snapshots in panel (b), with the same style and color codes. Two events of this repeated behavior (growth and decay of the pulse) are shown.

leading to $W_p = W$ as before. This, however, cannot lead to a strict steady-state.

To understand this statement, let us consider some of the properties of the slip velocity field inside a pulse within a pulse train, for both large and small H . In the former case, the slip velocity inside the pulse is significantly amplified compared to v_0 over a large fraction of the pulse width w_p , such that most of the pulse is characterized by a slip velocity out of the unstable rate-weakening branch of the friction curve. This is demonstrated in the pulse shown in Fig. 5.10b (see Sect. 5.2.5.1 for additional discussion

of the slip velocity amplification). This is qualitatively different from the small H case, $H < L_c \ll W$; here, the slip velocity is amplified over a scale H that is significantly smaller than w_p . This situation is closely related to the finite height strip problem of fracture mechanics [243], where the controlling length scale is the strip height H . This implies that a significant fraction of the pulse/interface is characterized by $v(x, t) \simeq v_0$, and since $w_p \gg L_c$ (see Sect. 5.2.5.2 for additional discussion of the properties of w_p), this extended region is characterized by a slip velocity belonging to the rate-weakening branch of the friction curve and hence is unstable. Consequently, if $W_p = W$ also for $H < L_c \ll W$, then we expect to observe repeated instabilities on top of the pulse train. That is, we expect the competition between coarsening and elasto-frictional instabilities to prevent the system from reaching a strict steady-state.

In Fig. 5.11a we present a space-time plot (in the same format of Fig. 5.10a) obtained using FEM simulations in the $H < L_c \ll W$ regime. It is important to note that in this regime we do not observe the space-independent stick-slip instability discussed in Sect. 5.2.3 and hence no additional constraints that break translational symmetry along the interface are introduced. The results in Fig. 5.11a indicate that coarsening dynamics dominate in this regime as well, leading to a pulse train with $W_p = W$. This pulse train, however, is not in strict steady-state as it is clearly observed to be repeatedly/periodically interrupted by bursts of large slip velocities (compare to Fig. 5.10a, where these bursts are absent and the system reaches a strict steady-state). These observations support the physical picture discussed in the previous paragraph, where coarsening dynamics compete and coexist with repeated elasto-frictional instabilities in the $H < L_c \ll W$ regime.

In order to better understand these complicated spatiotemporal dynamics, we focus in Fig. 5.11b on a sequence of snapshots of $v(x)$ of the pulse within the pulse train observed in the long-time dynamics of Fig. 5.11a, during one of the bursts (the snapshots are shown in the pulse train co-moving frame, see figure caption). The snapshots are ordered in time, where the smallest $v(x)$ corresponds to early time and the largest to late time. The time points in which the snapshots were taken are marked by vertical lines in Fig. 5.11c (same colors and line styles as in the curves of Fig. 5.11b), where the maximal slip velocity v_m is plotted as a function of time. The early time field reveals a long plateau, larger than L_c (recall that here $L_c \ll W$), featuring $v(x) \simeq v_0$, as predicted above. Consequently, an elasto-frictional instability is indeed expected.

As is evident from both Fig. 5.11b and Fig. 5.11c, the slip velocity inside the pulse grows significantly, indicating an elasto-frictional instability. A clear signature of the linear elasto-frictional instability associated with L_c is an exponential growth of the slip velocity at the early stages of the instability development. This is indeed demonstrated in the inset of Fig. 5.11b, supporting the physical picture discussed above. Moreover, the observed exponential growth rate appears to be in the ballpark of the theoretically estimated growth rate (not shown). Finally, the repeated nature of the instability, already observed in Fig. 5.11a, is evident also in Fig. 5.11c. There, the maximal slip velocity v_m is plotted as a function of time, and it is observed that after the instability shown in Fig. 5.11b relaxes, another instability with very similar properties occurs after some

interval of time.

The results of this section and of the previous one suggest that velocity-driven frictional systems, at least the rather generic class of frictional systems considered in this section, are strongly dominated by coarsening dynamics that lead to pulse trains characterized by periodicity determined by system length in the sliding direction. For $H < L_c \ll W$, the train pulse experiences repeated elasto-frictional instabilities, but for larger H 's the pulse train is a stable steady-state solution. It is important to note that in this section we do not study in depth and quantitatively the coarsening dynamics themselves (this will be done elsewhere), but rather focus on their long-time outcome. Next, we shift our focus to other salient features of the observed pulse trains, i.e. their propagation velocity c_p and the properties of single pulses within the train.

5.2.5 Single pulse properties in the large H limit

Self-healing slip pulses, as explained in Sect. 5.2.1, are frictional rupture modes that are believed to be quite prevalent, yet they are not fully understood [105; 123; 107; 120; 106; 121]. Our analysis above established that self-healing slip pulses, as part of pulse trains, generically and robustly emerge in velocity-driven frictional sliding dynamics. These results offer a rather unusual opportunity to better understand the physical properties of single pulses, which is the main goal of this section.

A steady-state pulse train is composed of single pulses that repeat themselves with spatial periodicity W_p , extensively discussed above. Once the train periodicity W_p is known — it was shown above to be coarsening-limited (i.e. equal to the system length, $W_p = W$) —, one is interested in the selection of the train velocity c_p (which is obviously also the single pulse propagation velocity) and in the spatial distributions of slip velocity $v(x)$ and stress $\tau(x)$ within the single pulse. Obtaining closed-form solutions for the field distributions is a difficult challenge not addressed here; instead, we focus below on the behavior of $v(x)$ and $\tau(x)$ near the leading edge of the single pulse, and on some characteristic properties of $v(x)$ and $\tau(x)$. More importantly, as already introduced in Fig. 5.9, we are interested in the single pulse width w_p and in its average slip velocity v_p . The single pulse width w_p , as illustrated in Fig. 5.9c, is defined as the size of the portion of the single pulse for which $v(x) \geq v_0$. Accordingly, the average slip velocity of a single pulse is defined as $v_p \equiv w_p^{-1} \int_0^{w_p} v(\tilde{x}) d\tilde{x}$, where $\tilde{x} = 0$ in this context corresponds to the spatial point on the pulse's leading edge such that $v(\tilde{x} = 0) = v_0$ (the corresponding relation at the trailing edge reads $v(\tilde{x} = w_p) = v_0$). Our goal in this section is to gain physical insight into the single pulse quantities c_p , w_p and v_p as a function of the control parameters W and v_0 for the adopted interfacial constitutive law, in the $H \rightarrow \infty$ limit. Moreover, we would like to understand the interrelations between c_p , w_p and v_p , and clearly three such relations are needed in order to determine these three quantities. One such relation is readily obtained from the steady-state condition of Eq. (5.15). The latter implies

$$W^{-1}[w_p v_p + (W - w_p) v_s] = v_0 \implies w_p v_p \simeq W v_0, \quad (5.17)$$

where the slip velocity in the ‘stick region’, v_s (cf. Fig. 5.9c), has been assumed to be negligibly small (as is indeed the case). Note that Eq. (5.17) does not explicitly include the propagation velocity c_p . In Sect. 5.2.5.1 we show that another relation between c_p , w_p and v_p emerges from the pulse’s leading edge behavior, a relation that may be viewed as a pulse equation of motion. A third relation is discussed in Sect. 5.2.5.2, where we focus on the pulse width w_p .

5.2.5.1 Pulse equation of motion: Leading edge singularity, effective fracture energy, and propagation velocity

A slip pulse, like other rupture fronts, is expected to feature nearly singular fields near its leading edge, where the negligibly small slip velocity ahead of the pulse, v_s , dramatically increases to the peak velocity, v_m (cf. Fig. 5.9c), over a short length scale. It has been recently shown [191; 192; 219; 218] that for the class of rate-and-state friction constitutive laws illustrated in Fig. 5.9b, where the rate dependence of friction is rather weak, the singular leading edge behavior is described by the classical square-root singularity of Linear Elastic Fracture Mechanics (LEFM) [15] to a good approximation.

In the framework of LEFM, the slip velocity behind the leading pulse edge is expected to take the following universal form [15]

$$v(x) \simeq \frac{2 c_p K_{\text{III}}}{\alpha_s(c_p) \mu \sqrt{2\pi(x - x_p)}}, \quad (5.18)$$

where $\alpha_s(c_p) = \sqrt{1 - (c_p/c_s)^2}$, x_p is the leading edge position and K_{III} is the mode-III stress intensity factor, quantifying the amplitude of the universal square root singularity (Eq. (5.18) refers to mode-III conditions, which we focus on in this section, but the same singularity applies to mode-II conditions [15]). In Fig. 5.12 we plot $v(x)$ (properly normalized, see legend) over the entire pulse train period $W_p = W$ (solid brown line, left y -axis). To test whether the observed amplified slip velocity near the leading edge indeed follows the square root singularity of Eq. (5.18), we plot in the inset the same normalized $v(x)$ behind the leading edge against $(x - x_p)/W$ on a double-logarithmic scale. As is indicated by the dashed line of slope $-\frac{1}{2}$, there exists a spatial range near the leading edge, over which $v(x)$ follows the square root singular behavior of Eq. (5.18). The singular slip velocity behavior of Eq. (5.18) behind the pulse’s leading edge is accompanied by a shear/frictional stress field $\tau(x)$ that features the same square root singularity *ahead* of the leading edge and a predominantly constant residual stress behind it [191; 192]. In Fig. 5.12 we present $\tau(x)$ (properly normalized, see legend) again over the entire pulse train period $W_p = W$ (dashed orange line, sharing the *same* left y -axis with the normalized $v(x)$ field). It is observed that indeed $\tau(x)$ features significant amplification ahead of the leading edge (its quantification is not presented here) and that it is approximately constant behind the leading edge inside the pulse. Finally, we present in Fig. 5.12 $v(x)\phi(x)/D$ (dashed-dotted green line, right y -axis), whose deviation from

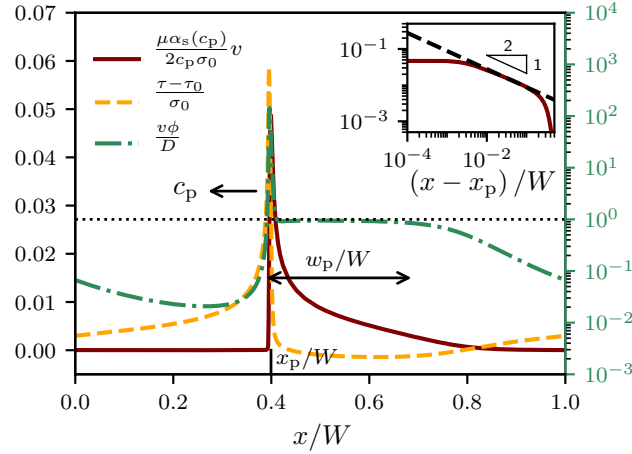


Figure 5.12: The normalized (see legend) profiles of the velocity $v(x)$ (solid brown line, left y -axis), the shear/frictional stress $\tau(x)$ (dashed orange, left y -axis) and $v(x)\phi(x)/D$ (dashed-dotted green line, right y -axis) of a steady-state pulse train propagating to the left at $c_p = 0.85c_s$, as obtained by a BIM simulation ($H \rightarrow \infty$) with $v_0 = 3 \times 10^{-3} \text{m/s}$, $W = 14.07 \text{m}$ and the N-shaped steady-state friction law of Fig. 5.9b. The leading edge is indicated by x_p/W and the pulse width by w_p/W (and a double-arrow). Both the stress and the velocity fields reveal a singular behavior near the pulse leading edge, see text for discussion. (inset) The velocity field $v(x)$ (solid brown line) behind the leading edge, on a double-logarithmic scale, with the x axis being $(x - x_p)/W$. The dashed black line features a slope of $-1/2$, characteristic of the square root singularity of LEFM, see text for additional discussion.

unity provides a measure of the degree by which $\phi(x)$ is out of steady-state with respect to $v(x)$. It is observed that inside the pulse $v(x)\phi(x)/D \simeq 1$ (see horizontal dashed line) almost everywhere. That is, inside the pulse away from the leading edge transition region, $\phi(x)$ is “equilibrated” with $v(x)$.

The approximate validity of Eq. (5.18) has significant implications for the pulse dynamics. Most notably, the square root singular fields are accompanied by a finite (non-singular) flux of energy G into the leading edge region. The latter is dissipated near the leading edge, i.e. it is balanced by an effective fracture energy G_c , which quantifies the dissipation involved in slip pulse propagation (on top of the background frictional dissipation [247; 192]). That is, we expect the following relation [15]

$$G_c \simeq G = \frac{K_{\text{III}}^2}{2\alpha_s(c_p)\mu}, \quad (5.19)$$

to approximately hold. The effective fracture energy G_c can be independently estimated using the interfacial constitutive law, following [80; 83] and as shown in section 5.2.7.7. With G_c at hand, one can eliminate K_{III} between Eqs. (5.18)-(5.19), yielding an expression for the singular part of $v(x)$ near the leading edge of the pulse.

The resulting $v(x)$ allows to derive a relation between c_p , w_p and v_p . It is important to note that the latter two quantities characterize the whole pulse, not just its singular part. To bridge over this gap, we assume that the singular part of $v(x)$ describes reasonably well the entire pulse, up to an overall shift that dominates the trailing edge behavior. The shift can be determined by demanding $v(x_p + w_p) = v_0$, which follows from the definition of w_p , leading to

$$\frac{v(x)}{c_s} \simeq \sqrt{\frac{4G_c}{\pi\mu}} \frac{c_p}{c_s \sqrt{\alpha_s(c_p)}} \left(\frac{1}{\sqrt{x - x_p}} - \frac{1}{\sqrt{w_p}} \right) + \frac{v_0}{c_s}. \quad (5.20)$$

With this approximation at hand, we can then calculate v_p according to its definition $v_p = w_p^{-1} \int_{x_p}^{x_p + w_p} v(\tilde{x}) d\tilde{x}$, leading to

$$\frac{c_p}{c_s \sqrt{\alpha_s(c_p)}} \sim \sqrt{\frac{\pi \mu w_p}{G_c}} \frac{v_p - v_0}{2c_s}. \quad (5.21)$$

The prediction in Eq. (5.21) is a relation between c_p (left-hand side), and w_p and v_p (right-hand side), where the pre-factor is expected to be $\mathcal{O}(1)$. It may be viewed as an equation of motion for the pulse. Moreover, note that Eq. (5.17) (which has been independently verified) can be used to eliminate v_p from the right-hand side of Eq. (5.21), making it a function of w_p alone. Equation (5.21) is tested in Fig. 5.13 over a broad range of W and v_0 values. It is observed that the theoretical prediction is strongly supported by the simulational data, where the pre-factor is indeed $\mathcal{O}(1)$. Consequently, only one additional relation between c_p , w_p and v_p is needed in order to fully determine the single pulse properties. In particular, predicting the pulse width w_p in terms of W and v_0 would be sufficient since Eqs. (5.17) and (5.21) would then allow to calculate v_p and c_p , respectively. Therefore, we next consider $w_p(W, v_0)$.

5.2.5.2 The pulse width

Our goal in this subsection is to discuss the pulse width $w_p(W, v_0)$. It would be useful in this context, as a preparatory step, to consider the “ideal” solution for an isolated pulse. The latter corresponds to an isolated pulse in an infinite medium ($H \rightarrow \infty$) whose slip velocity $v^{(i)}(x)$ (the superscript (i) denotes hereafter “ideal pulse”) vanishes for $x < x_p$ and $x > 2w_p^{(i)} + x_p$, and the frictional strength is constant for $x_p \leq x \leq 2w_p^{(i)} + x_p$. The solution takes the form [241; 242; 243]

$$v^{(i)}(x) = v_0 \sqrt{\frac{2w_p^{(i)} + x_p - x}{x - x_p}} \quad (5.22)$$

for $x_p \leq x \leq 2w_p^{(i)} + x_p$. Note that the solution in Eq. (5.22) features the square root singularity of Eq. (5.18) in the $x \rightarrow x_p^+$ limit and it is consistent with the single pulse

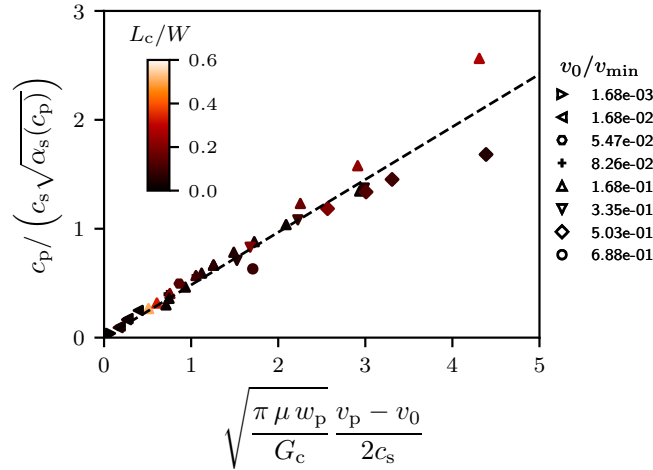


Figure 5.13: Testing the theoretical prediction of Eq. (5.21) for a broad range of parameters, including variations of the system length W , the driving velocity v_0 , the shear modulus μ and the characteristic slip displacement D , see section 5.2.7.1 and 5.2.7.3 for additional details and the exact values used. The data correspond to BIM simulations with the N-shaped friction law of Fig. 5.9b, revealing very good agreement with the prediction, with an $\mathcal{O}(1)$ pre-factor. G_c has been estimated following [80; 83], see section 5.2.7.7 for more details.

width definition adopted throughout this paper. That is, we have $v^{(i)}(x = w_p^{(i)} + x_p) = v_0$ such that $w_p^{(i)}$ retains its meaning as the pulse width.

The physics underlying the ideal pulse solution in Eq. (5.22) differs from the physics underlying the train pulse solutions derived above in three major respects: (i) Our solutions correspond to rate-and-state friction, while Eq. (5.22) corresponds to a *constant* frictional strength inside the pulse. (ii) Eq. (5.22) corresponds to an isolated pulse, i.e. to a single pulse that does not interact with other pulses in the train over the periodicity scale $W_p = W$. (iii) $w_p^{(i)}$ in Eq. (5.22) is not selected, an issue that is obviously related to points (i) and (ii).

An attempt to remedy points (ii) and (iii) above, which is inevitably *superficial*, would be to impose the steady-state pulse train condition of Eq. (5.15) on Eq. (5.22), resulting in $w_p^{(i)}/W = 1/\pi$. That is, we construct an approximate pulse train solution by concatenating/superimposing the ideal pulse solutions of Eq. (5.22) with periodicity $W_p = W$ and a single pulse width $w_p^{(i)}/W = 1/\pi$. Below we show that this artificially constructed pulse train qualitatively fails to describe our rate-and-state friction pulse train solutions, where w_p/W is not a constant, but rather depends on both W and v_0 . Moreover, while both the ideal pulse solution of Eq. (5.22) and our pulses (cf. Figs. 5.10b and 5.12) do not feature a singularity at the trailing edge, the pulse shape $v(x)$ near the trailing edge differs quite significantly. Another difference between the two solutions is that while the ideal pulse solution is truly singular at the leading edge, the singularity in our solutions is self-consistently regularized on small scales near the leading edge.

In light of the discussion of the ideal pulse above, which mainly served to highlight the differences compared to our pulse train solutions, our next goal is to better characterize the function $w_p(W, v_0)/W$. The first question we need to address is how to properly nondimensionalize W and v_0 , i.e. the dimensionless pulse width w_p/W should be expressed in terms of dimensionless quantities. We suggest that the proper way to nondimensionalize W and v_0 is through their relation to the elasto-frictional instability, which is a necessary condition for the emergence of pulse trains.

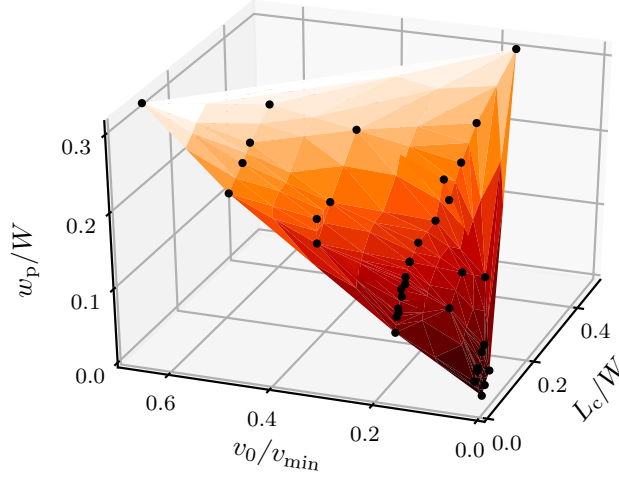


Figure 5.14: The dimensionless pulse width w_p/W as a function of both the normalized driving velocity v_0/v_{\min} and system size L_c/W , see text for additional discussion. Each black circle corresponds to one of the simulations shown in Fig. 5.13, spanning a broad range of system parameters (including variations of the system size W , driving velocity v_0 , shear modulus μ and the characteristic slip displacement D). Variations of μ alter the elasto-frictional length L_c , while variations of D affect both L_c and v_{\min} . The surface is interpolated from the data points, supporting the existence of a smooth and monotonically increasing function $w_p/W = \mathcal{G}(L_c/W, v_0/v_{\min})$, as predicted theoretically (see text for discussion).

The elasto-frictional instability exists if the system is driven at a velocity v_0 that resides on the rate-weakening branch of the steady-state friction curve $f_{ss}(v)$ (cf. Fig. 5.9b), i.e. when v_0 is larger than the slip velocity at which $f_{ss}(v)$ attains its maximum and smaller than v_{\min} . In the limit $v_0 \rightarrow v_{\min}$, the system will approach a stable homogeneous sliding state; that is, as v_0/v_{\min} is increased toward unity, we expect the pulse width to approach W (and obviously its slip velocity to approach v_0). For $v_0 < v_{\min}$, the elasto-frictional instability manifests itself only for $L_c < W$, i.e. when an unstable perturbation can fit into the system. Consequently, in the limit $W \rightarrow L_c^+$ the system will approach a stable homogeneous sliding state; that is, as L_c/W is increased toward unity, we expect the pulse width to approach W .

Taken together, these physical considerations lead us to expect that there exists a smooth function $w_p/W = \mathcal{G}(L_c/W, v_0/v_{\min})$ that monotonically increases with its two arguments.

Chapter 5. On the dynamics of frictional interfaces described by rate and state friction laws

This prediction is tested in Fig. 5.14, where w_p/W is plotted against L_c/W and v_0/v_{\min} . It is observed that a smooth $w_p/W = \mathcal{G}(L_c/W, v_0/v_{\min})$ function seems to exist, and that w_p/W indeed increases with both of its arguments. The theoretical derivation of the precise functional form of $w_p/W = \mathcal{G}(L_c/W, v_0/v_{\min})$ is left as a challenge for future research. With this analysis, we conclude our discussion of the single pulse properties c_p , w_p , and v_p in the large H limit.

5.2.6 Summary and discussion

In this work, we extensively studied velocity-driven frictional systems, using a combination of computational and theoretical approaches. Velocity-driven frictional systems exist in a broad range of engineering and tribological applications, as well as in geophysical contexts. We show that such frictional systems, described within the experimentally motivated rate-and-state friction constitutive framework, give rise to the emergence of pulse trains once driven at a sliding velocity for which the frictional interface is rate-weakening. Such slip pulses do not require the existence of material contrast across the frictional interface. The propagating pulse train is a non-equilibrium dissipative analog of equilibrium phase separation in thermodynamic systems. We find that such velocity-driven frictional systems undergo coarsening dynamics leading to steady-state train periodicity set by the size of the system in the sliding direction, independently of the height of the system. Interestingly, the infinite height rate-and-state friction simulations of [229] (see section 6.4 therein) demonstrated the emergence of transient (i.e., out of steady-state) pulse trains behind crack-like rupture fronts at moderate stress levels, whose periodicity is set by the elasto-frictional length L_c (i.e., by the fastest growing mode of the linear elasto-frictional instability). The properties of single pulses in our simulations are quantitatively and comprehensively analyzed and interpreted. In particular, the pulse propagation velocity, width, and average slip rate are shown to be related through an equation of motion that is associated with the nearly singular fields in the vicinity of the leading pulse edge.

Throughout this work, we employed periodic boundary conditions in the sliding direction. Similar periodic boundary conditions have been employed in the velocity-driven frictional simulations of [118], where instability has been induced by various physical processes leading to a reduction in the effective normal stress, rather than by rate-weakening friction per se (note that the possible emergence of pulse trains under rate-strengthening friction has been discussed in [124]). While coarsening dynamics have not been discussed in [118], the results therein (cf. Fig. 4 in [118]) do indicate similar coarsening dynamics as found here. Such periodic boundary conditions naturally emerge in annular/rotary shear geometry experiments [248; 249], which is also characteristic of many engineering systems. Such an experimental setup offers a natural test bed for our predictions. Moreover, we believe that the coarsening dynamics revealed in this work are physically relevant for sufficiently long systems (large W) that do not feature periodic boundary conditions, as well as for geophysical fault dynamics, issues

that should be addressed in future work.

This work offers a rather robust framework for studying self-healing pulses, which are of importance in many frictional systems. Our results also pose several interesting questions. First, calculating the single pulse shape and consequently its width w_p (cf. Fig. 5.14) remain open challenges. Second, we have not studied in any detail the coarsening dynamics themselves but rather focused on their long-time outcome. Yet, earlier time coarsening (cf. Fig. 5.10a) may be characterized by rather complex spatiotemporal dynamics, possibly chaotic ones. Quantitatively analyzing these dynamics and their acoustic emission signature may be important for understanding the non-steady frictional response of various physical systems. Moreover, in an even broader statistical physics context, such complex dynamics may reveal how anomalous statistical properties (e.g. fat power-law statistical distributions [147; 148]) spontaneously emerge even in the absence of input disorder (quenched or thermal). These interesting issues will be discussed in the following chapter 6.

5.2.7 Supplemental material

5.2.7.1 The interfacial constitutive law

The rate-and-state friction constitutive framework [53; 7; 71; 221] has been formulated in Eqs. (5.12)-(5.13). Here we specify the constitutive functions $f(\cdot)$ and $g(\cdot)$, which appear in these two equations respectively, taking the explicit forms [53; 7; 71; 221; 76; 250; 86; 251; 79; 78; 121; 191]

$$f^N(|v|, \phi) = \left[1 + b \log \left(1 + \frac{\phi}{\phi_*} \right) \right] \times \left[\frac{f_0}{\sqrt{1 + (v_*/|v|)^2}} + a \log \left(1 + \frac{|v|}{v_*} \right) \right] \quad (5.23)$$

and

$$g(|v|, \phi) = 1 - \frac{|v|\phi}{D} \sqrt{1 + (v_*/v)^2}. \quad (5.24)$$

These functions feature 6 parameters: f_0 , a , b , D , v_* and ϕ_* , whose values are specified in Table 5.1. The superscript ‘N’ in Eq. (5.23) denotes the fact that the steady-state friction curve $f_{ss}(v)$ corresponding to Eqs. (5.23)-(5.24) features an N shape, as shown in Fig. 5.9b and again here in Fig. 5.15 (solid brown curve).

The N-shaped steady-state friction curve features rate-strengthening at very low velocities, rate-weakening at intermediate velocities and again rate-strengthening at high velocities, i.e. it follows a strengthening-weakening-strengthening (SWS) sequence with increasing slip velocities. As highlighted in the text, the most crucial branch for the emergence of pulse trains is the rate-weakening one. Consequently, we also considered two variants of SWS-related function $f^N(|v|, \phi)$ of Eq. (5.23). One variant corresponds to

Chapter 5. On the dynamics of frictional interfaces described by rate and state friction laws

replacing Eq. (5.23) with

$$f^{\text{WS}}(|v|, \phi) = f_0 \left[1 + b \log \left(1 + \frac{\phi}{\phi_*} \right) \right] + a \log \left(1 + \frac{|v|}{v_*} \right). \quad (5.25)$$

The resulting steady-state curve is rate-independent at very low velocities, rate-weakening at intermediate velocities, and rate-strengthening at high velocities. Consequently, we use the superscript ‘WS’ for this function and plot the corresponding steady-state curve in Fig. 5.15 (dotted-dashed orange curve).

The second variant corresponds to omitting the ‘+1’ in the logarithm that multiplies b in the first square brackets on the right-hand side of Eq. (5.23). This modification eliminates the high velocities rate-strengthening branch of the steady-state friction curve [86]. Consequently, we term the resulting $f(\cdot)$ that replaces Eq. (5.23) $f^{\text{SW}}(|v|, \phi)$ and plot the corresponding steady-state curve in Fig. 5.15 (dashed green curve). All three steady-state curves, corresponding to $f^{\text{N}}(|v|, \phi)$, $f^{\text{WS}}(|v|, \phi)$ and $f^{\text{SW}}(|v|, \phi)$, essentially share the same rate-weakening behavior at intermediate slip velocities. Results for $f^{\text{WS}}(|v|, \phi)$ and $f^{\text{SW}}(|v|, \phi)$ are presented below.

Parameter	Value	Unit
f_0	0.28	...
a	0.005	...
b	0.075	...
D	5×10^{-7}	m
v_*	1×10^{-7}	m/s
ϕ_*	3.3×10^{-4}	s

Table 5.1: Typical values of rate-and-state parameters used in this work. In addition, D has been varied from 1.25×10^{-7} to 1.5×10^{-6} m in the results appearing in Figs. 5.13, 5.14, 5.17.

5.2.7.2 The elasto-frictional length L_c

The calculation of the elasto-frictional length L_c associated with the rate-weakening instability appears in previous works [74; 7; 75; 53; 76; 78; 79], so here we just very briefly highlight the structure of the calculation. A linear stability analysis of an interface sliding at a constant velocity v_0 is performed; that is, the starting point is a space and time independent solution featuring a steady-state frictional stress $\tau = \sigma_0 f_{\text{ss}}(v_0)$. One then introduces small perturbations to all fields, each assumed to be proportional to a Fourier mode $e^{\Lambda t - i k x}$, where Λ is the complex growth rate and k is the wavenumber. Obtaining expressions for the perturbation of the interfacial shear stress, from the bulk elastodynamic equations corresponding to bodies of height H , and for the perturbation of the frictional strength, one obtains (by equating the two) the linear perturbation spectrum $\Lambda(k)$. The elasto-frictional length is related to the critical wavenumber k_c for

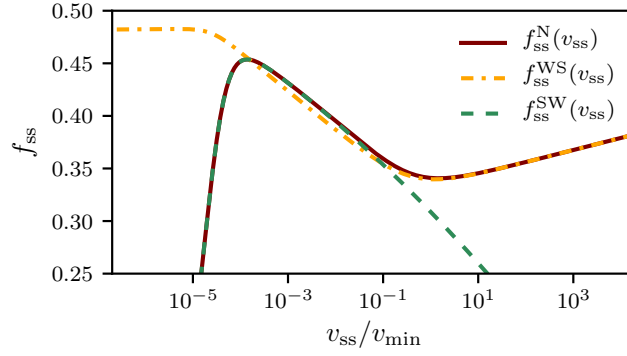


Figure 5.15: The normalized steady-state frictional strength f_{ss} vs. the steady-state normalized slip velocity v_{ss} , presented on a semi-logarithmic scale for three constitutive laws. The first (solid brown curve), which features an N shape and is denoted by $f_{ss}^N(v_{ss})$ (see legend), corresponds to Eqs. (5.23)-(5.24) and has already been presented in Fig. 5.9b. The local minimum of $f_{ss}^N(v_{ss})$, denoted by v_{min} , is used to normalize v_{ss} . The second constitutive law (dotted-dashed orange curve) corresponds to Eqs. (5.24)-(5.25) and is denoted by $f_{ss}^{WS}(v_{ss})$, see text for additional discussion. Finally, the third constitutive law (dashed green curve) features no local minimum (see text for discussion) and is denoted by $f_{ss}^{SW}(v_{ss})$. All three constitutive laws share the same rate-weakening behavior of the steady-state frictional strength at intermediate slip velocities, which plays a major role in this work.

the onset of instability according to $L_c(H) = 2\pi/k_c$, where k_c is determined from the zero crossing of the real part of Λ , i.e. by $\Re[\Lambda(k_c, H)] = 0$. The general structure of $L_c(H)$ appears in Eq. (5.16).

5.2.7.3 The spectral boundary integral formulation

The infinite height ($H \rightarrow \infty$) calculations are performed using an in-house open-source implementation (called cRacklet, see [9]) of the spectral boundary integral formulation of the elastodynamic equations [169; 170; 171]. The basic relation between the interfacial shear stress and the slip displacement in this case is given in Eq. (5.14), where the Fourier representation of the spatiotemporal integral term $s(x, t)$ for both mode-II and mode-III symmetries can be found in [171]. In our numerical calculations, the interface is assumed to be initially at steady-state with $v_{ss} = v_0$ and $\phi_{ss} = D/v_0$. The interface is then perturbed by adding spatial Gaussian noise to the state variable $\phi(x, t)$, and the resulting slip velocity is computed by combining Eq. (5.14) and the rate-and-state friction law $\tau = \sigma_0(v)f(|v|, \phi)$. Note that $\tau_0(t)$ in Eq. (5.14) is treated as unknown and that we impose the constraint of Eq. (5.15). The slip displacement $u(x, t)$ is then integrated in time using an explicit time-stepping scheme $u(x, t + \Delta t) = u(x, t) + \frac{1}{2}v(x, t)\Delta t$, with the time step being $\Delta t = \alpha_{BIM} \Delta x / c_s$, where Δx is the numerical grid spacing. The numerical parameter α_{BIM} is chosen to ensure the stability and the convergence of the numerical

scheme, and is typically set equal to 0.1.

The exact shape of the initial perturbation has no impact on the long-time behavior of the system (i.e. it does not alter the properties of the emergent steady pulse trains). The coarsening dynamics, which are not studied in detail in this work, may depend on the initial perturbation. The bulk parameters in our calculations have been set equal to $\mu = 9 \times 10^9 \text{Pa}$, $\nu = 0.33$ and $\rho = 1200 \text{kg/m}^3$. In addition, μ has been varied from 2.25×10^9 to $9 \times 10^{10} \text{Pa}$ in the results appearing in Figs. 5.13, 5.14, 5.17.

5.2.7.4 Finite element method formulation

The finite height H calculations follow the system configuration sketched in Fig. 5.9a. The top and bottom boundaries are loaded by a horizontal velocity $v_0/2$ (in opposite directions, cf. Fig. 5.9a) and by a constant compressive normal stress of magnitude σ_0 . The bodies are initially moving uniformly in opposite directions at a velocity $v_0/2$, and periodic boundary conditions are enforced at the lateral edges, $x = 0$ and $x = W$. The interface is initially at steady-state with $v_{ss} = v_0$ and $\phi_{ss} = D/v_0$. Perturbations are introduced by adding spatial Gaussian noise to the state variable, as in the BIM case. The bulk parameters used for the FEM simulations and their BIM counterparts (see, for example, Fig. 5.10b) are set equal to $\mu = 3.1 \times 10^9 \text{Pa}$, $\nu = 0.33$ and $\rho = 1200 \text{kg/m}^3$.

The FEM calculations are performed using the explicit dynamic finite element framework, based on an in-house open-source finite element library called Akantu [8]. The domain is discretized into a regular mesh composed of bilinear quadrilateral elements (Q4). The sliding interface between the two elastic bodies is modeled using a node-to-node contact algorithm, whose details can be found in [168]. Time is integrated using the central difference method and the time step is taken small enough to eliminate the numerical instabilities associated with the explicit finite element modeling of rate-and-state friction, as explained in [168]. In our simulations, we set the time step to $\Delta t = \alpha_F \Delta t_{\text{CFL}}$, where Δt_{CFL} is set by the Courant-Friedrichs-Lewy condition and α_F is typically taken to be $\mathcal{O}(0.01)$.

5.2.7.5 The WS friction law

As explained in the main text and in section 5.2.7.1, the most important aspect of the interfacial constitutive relation for our results is the existence of a rate-weakening branch of the steady-state friction curve and that the applied velocity v_0 resides on it. To demonstrate this point, we performed exactly the same BIM simulations except that in one case we used $f^N(|v|, \phi)$ of Eq. (5.23) and in the other $f^{\text{WS}}(|v|, \phi)$ of Eq. (5.25), which are mainly distinguished by the different steady-state behavior at very low velocities, see Fig. 5.15. The long-time behavior of the system in the two cases is presented in Fig. 5.16 (employing the same line type and color scheme of Fig. 5.15). It is observed that the results are quantitatively similar, in terms of the train periodicity ($W_p = W$), single pulse shape, and propagation velocity (see figure legend), substantiating our claim. It turned out that this robustness of our results against changes in the low velocity

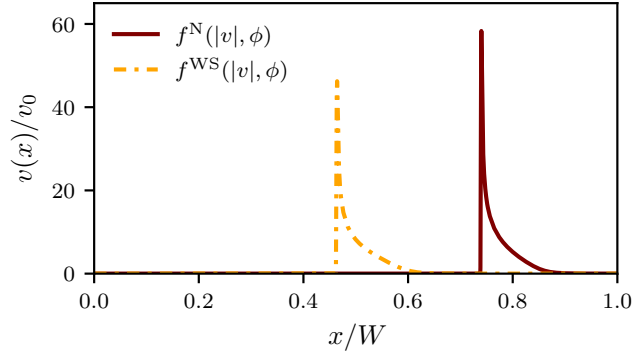


Figure 5.16: Snapshots of the steady-state slip velocity field $v(x)/v_0$ obtained in two BIM simulations, one with the N-shaped friction law (Eq. (5.23), solid brown curve, cf. Fig. 5.15) and the other with the WS friction law (Eq. (5.25), dotted-dashed orange curve, cf. Fig. 5.15). The two simulations are otherwise identical, employing $v_0 = 1 \times 10^{-3} \text{m/s}$ and $W = 40 \text{m}$. In both cases, the resulting pulse train periodicity satisfies $W_p = W$, the single pulse shape is quantitatively similar (note that the two snapshots are shifted along x for visual clarity) and the propagation velocity is also quantitatively similar ($c_p^N \simeq 0.73c_s$ for the N-shaped law and $c_p^{\text{WS}} \simeq 0.70c_s$ for the WS law).

behavior of the friction law (while preserving a very similar rate-weakening behavior) is of technical importance in relation to our FEM calculations. In particular, we found that the FEM calculations suffered from numerical instabilities associated with the low frictional strength featured by the N-shaped interfacial constitutive relation at low velocities. These numerical instabilities can be eliminated by using Eq. (5.25) instead of Eq. (5.23), without affecting the emerging physics. Consequently, in our FEM calculations, we adopted the WS friction law of Eq. (5.25).

5.2.7.6 The space-independent stick-slip like behavior for $H \simeq W \gg L_c$

As explained in the main text, our FEM calculations with $H \simeq W \gg L_c$ featured time periods where the slip velocity almost vanished homogeneously across the interface, followed by nearly homogeneous large slip velocity periods. This space-independent stick-slip like behavior appears to substantially deviate from the steady-average velocity condition of Eq. (5.15), and hence is not expected to persist in the large W and long-time limits. Consequently, we slightly modified our numerical scheme to eliminate this behavior by adding a constraint in the FEM $H \simeq W \gg L_c$ simulations. In particular, at each time step, we computed the average slip rate $\langle v \rangle$ of the interface and compared it to the driving velocity v_0 . We then introduced a small spatially-homogeneous shift $\Delta v = v_0 - \langle v \rangle$ to the velocity field and $\Delta a = 2(v_0 - \langle v \rangle)/\Delta t$ to its acceleration counterpart ($a = \dot{v}$ and Δa is the small shift in a) in computational nodes along the interface (with opposite signs for nodes belonging to the top/bottom body, to preserve the shear symmetry). This amounts to the application of a spatially-homogeneous external stress

on the top/bottom nodes along the interface. This stress is typically very small, less than one percent of the initial frictional stress $\tau_0 = \sigma_0 f_{ss}(v_0)$, yet it nevertheless ensures that the average driving condition of Eq. (5.15) is nearly satisfied at all times.

5.2.7.7 The effective fracture energy

The effective fracture energy G_c of interfaces obeying rate-and-state friction law is self-selected by the interfacial dynamics. In order to test the pulse equation of motion of Eq. (5.21), we computed G_c using two different methods. The first method relies on an approximated mapping of slip-weakening (rather than rate-weakening) friction laws — characterized by a slip-weakening distance — to rate-and-state ones, as discussed in [82]. In [82] it has been shown that an effective slip-weakening distance δ_c^{eff} can be extracted in rate-and-state friction calculations and that it approximately follows the relation $\delta_c^{\text{eff}} \approx D \log(v_r/v_{\text{bg}})$, where v_{bg} is the background slip velocity that a rupture mode propagates into and v_r is the residual slip velocity left behind it. This relation has been later used in [80; 83] to obtain an approximate expression for the effective fracture energy in the form $G_c \approx \frac{1}{2} D b f_0 \sigma_0 \log^2(v_r/v_{\text{bg}})$. We used this estimate for G_c , with $v_{\text{bg}} = v_s$ and $v_r = v_0$, in Fig. 5.13. The results strongly supported the prediction in Eq. (5.21).

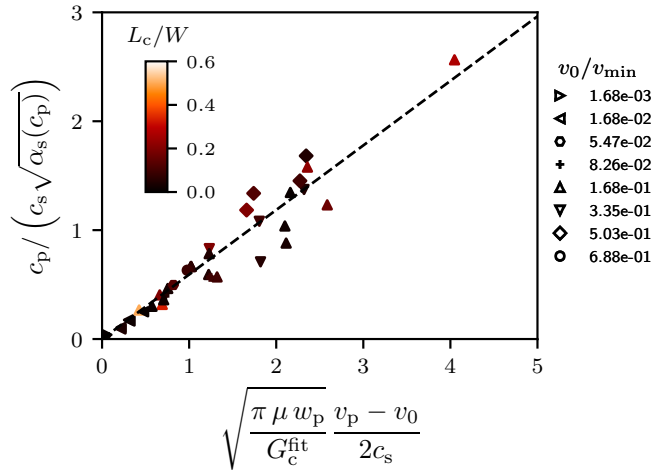


Figure 5.17: Testing the theoretical prediction of Eq. (5.21), using the same data as in Fig. 5.13, but this time with G_c being estimated from the fit of the singular fields near the rupture edge, which is denoted by G_c^{fit} (see text for discussion). The results reveal reasonably good agreement with the prediction, with an $\mathcal{O}(1)$ pre-factor, similarly to the results of Fig. 5.13.

The second method relies on the extraction of the nearly singular fields in the vicinity of the leading edge of the propagating pulse, shown in Fig. 5.12 to be reasonably well approximated by the classical square-root singular fields of LEFM. In particular, such a procedure allows to extract the stress intensity factor K_{III} by fitting simulation data to Eq. (5.18). Invoking then the leading edge energy balance of Eq. (5.19), one can obtain

an estimate of the effective fracture energy, which in this context is denoted by G_c^{fit} . In Fig. 5.17, we present the very same data (and combinations of physical quantities in the x and y axes) as in Fig. 5.13, but this time using G_c^{fit} for G_c , estimated from fitting the singular fields near the pulse leading edge, as just described. The results yet again agree with the prediction in Eq. (5.21) reasonably well, demonstrating the validity of the latter independently of the method used to estimate the effective fracture energy.

5.2.7.8 The SW friction law

Many studies available in the literature employ a rate-and-state friction law that does not feature rate-strengthening at relatively high slip velocities (and hence no local minimum as observed in Fig. 5.9b) [122; 123; 80; 83; 252]. Such behavior is exhibited by the strengthening-weakening (SW) friction law discussed in section 5.2.7.1 (which corresponds to using $f^{\text{SW}}(|v|, \phi)$ in Eq. (5.23)), whose steady-state curve is shown in Fig. 5.15 (dashed green curve). For completeness, we performed mode-III BIM calculations ($H \rightarrow \infty$) with the SW friction law. We find qualitatively similar results to those obtained for the N-shaped law, i.e. coarsening dynamics towards a pulse train with periodicity set by the system length, $W_p = W$. A representative movie of such calculations is available below. We do note that the SW friction law leads to sharper pulses and typically features higher slip and propagation velocities compared to their N-shaped counterparts.

5.2.7.9 Supplementary data

Movies are available as follows:

- M1: Infinite domain with the N-shaped friction law, see Fig. 5.10a.
- M2: $H < L_c < W$ with the WS friction law, corresponding to Fig. 5.11.
- M3: $H < L_c < W$ with the WS friction law, corresponding to Fig. 5.11 in the co-moving frame of the pulse.
- M4: $H \simeq W \gg L_c$ with the WS friction law.
- M5: Infinite domain with the SW friction law, see section 5.2.7.8.

The movies are available at the following link: <https://www.youtube.com/watch?v=UVD4VeJHnRM&list=PLT7c4IN61XQM8dk-hq9ZWtwGCvhT54nt7>

6 Statistical and dynamical complexity in a driven frictional system without disorder

This chapter discusses the emergence of statistical and dynamical complexity in a frictional system that does not feature material heterogeneities or bulk non-linearities. Understanding what are the minimal ingredients that give rise to statistical complexity in frictional systems, i.e., the existence of broad fat-tailed distributions of the slip events characteristics, is a basic problem of interest due to its existence in real frictional systems such as earthquakes. We study this problem in a frictional system of finite size that is velocity driven, where the dissipation and nonlinearity are confined to the contact interface, and the long-range elasto-dynamic interactions are mediated through wave propagation in the elastic bodies. We show that this frictional system features statistical and dynamical complexity even in the absence of material (bulk and frictional) disorder. We use finite element modeling to simulate the behavior of a periodic system (analog to a rotary apparatus) of finite H that embed a homogeneous planar contact interface whose behavior is given by a rate-and-state dependent constitutive law. First, we show that the characteristics of the slip events occurring in this system (duration, average slip, seismic moment) are broadly distributed. In particular, we find that slip events can be classified into two types: small, mainly non-propagating events, which follow a power-law distribution, and large propagating rupture events, which approximately follow a log-normal distribution. The broad distributions emerge from self-generated stress and interfacial (contact area) heterogeneity, which is accompanied by spatiotemporal complexity. The latter reveals intricate interactions between the two types of slip events, between the current state of the interface and its history, and triggering/arrest effects mediated by wave reflections from finite boundaries, which are associated with a travel time $2H/c_s$ (c_s being the shear wave speed). These results demonstrate that complexity might emerge in systems that feature no quenched disorder and bulk nonlinearity.

Chapter 6. Statistical and dynamical complexity in a driven frictional system without disorder

This chapter is an adapted version of the paper:

Statistical and dynamical complexity in a driven frictional system without disorder,
Roch, T., Brener, E. A., Bouchbinder, E., Molinari, J.-F. *In preparation*

6.1 Introduction

The statistical description of slip dynamics in frictional systems, in particular in the context of geophysics and earthquake science, is known to feature broadly distributed event characteristics. For example, the magnitude of earthquakes is power-law distributed [138; 139], as well as the temporal decay of aftershocks after a main event [140; 139], and several scaling laws describing the relation between the characteristics of slip events feature power-laws [144; 145; 142; 143; 146]. The existence of these specific scaling laws implies scale independence and has strong implications on the physical mechanisms driving slip events. How statistical complexity emerges in frictional system is however not yet clear. In a broader physical context, the emergence of complexity can be related to the disorder of the system (e.g., heterogeneities in material properties) or to strong dissipation and nonlinearity. Natural faults are rough at all scales [149] and highly complex in terms of geometry, material and frictional properties, and loading conditions. Heterogeneous interfacial properties are often assumed when studying frictional rupture [179; 253; 254]. However, one can wonder if the apparent complexity in frictional systems originates from the instabilities associated with the inherent weakening of frictional motion or from the complexity of the system itself. This question has been discussed extensively in the literature using various modeling techniques. One of the first models that investigated the emergence of broadly distributed slip events is the Burridge-Knopoff [150] mass and spring model, which has been used with various formulations for the friction law acting on each block [151; 152]. Complexity has been observed to emerge in these systems even in the absence of input disorder in the material properties. However, other authors have argued that the apparent complexity is an artifact of the discreteness of the system, with the model not being representative of a smooth homogeneous fault [77; 155; 157; 156; 129]. For Rice and coworkers, slip event complexity is a consequence of material heterogeneities. Different continuum models demonstrated some kind of statistical complexity in the absence of material disorder but were thought not to be generic as it was limited to specific friction laws with significant weakening or limited to some parameters range [160; 113; 159; 116]. Other origins for statistical complexity, such as geometric complexity (i.e., non-planar or multiple faults) have also been investigated [161]. Despite the abundant literature on the subject, it is not yet clear what is the minimal system in which generic complexity emerges, and in particular if material heterogeneities are mandatory to observe both small and large event complexity. In this chapter, we investigate the possibility that the finiteness of the system, i.e., the interaction between fault and finite boundaries through wave-mediated stress transfers, might bring sufficiently complex interactions for the emergence of complexity in the absence of material heterogeneities. In particular, we expect that the propagation of waves in the bulk will trigger both dynamic slip and arrest, giving rise to a variety of slip events.

We study the frictional behavior of a homogeneous planar fault laying between two

Chapter 6. Statistical and dynamical complexity in a driven frictional system without disorder

elastic bodies of finite height H using finite element simulations. The interface follows a rate and state frictional law. We start by describing the methodology for identifying independent slip events occurring during the simulation and defining the quantities of interest. We show that slip complexity emerges in this system even in the absence of material disorder. First, we investigate the emergent statistical complexity of the main characteristics of the slip events (duration, average slip, and seismic moment). Two types of events are occurring in this frictional system and feature different probability functions: 1) Small non-propagating slip events which are power-law distributed and 2) large propagating rupture events which are log-normal distributed. We show that these distributions are generic and independent of the system parameters, and demonstrate the collapse of these distributions after appropriate rescaling. This broad distribution emerges from self-generated heterogeneity at the sliding interface (in the stress τ and state ϕ fields) and waves traveling in the bulk. This results in spatio-temporal complexity in the system, with intricate interactions between the two types of slip events, the current state of the interface and its history, and the geometry of the system with waves traveling in the bulk and triggering or arresting slip events. We then demonstrate that the characteristic time scale for wave propagation from the interface to the top (or bottom) boundary and back is relevant both for spatio-temporal complexity and for the statistical one, illustrating that interactions with finite boundaries might lead to the emergence of complexity in a system that does not feature material heterogeneities and nonlinearity in the bulk. We conclude this chapter by discussing the possible implications on frictional dynamics.

6.2 Model

The frictional system of interest is composed of two identical elastic bodies of length L , height H and width w that are maintained in contact by a compressive stress σ_0 , as shown in Fig. 6.1a. The system is periodic, i.e., rotary, and is driven at a constant angular velocity v_0/L at $y = \pm H$ such that the (tangential) sliding velocity at the interface is v_0 . The frictional interface behavior is given by a weakening rate and state friction law (see Fig. 6.1b) given by Eq. (6.1) with the state evolution law of Eq. (6.2):

$$f(|v|, \phi) = f_0 \left[1 + b \log \left(\frac{\phi}{\phi_*} \right) \right] + a \log \left(1 + \frac{|v|}{v_*} \right), \quad (6.1)$$

$$g(|v|, \phi) = 1 - \frac{|v|\phi}{D} \sqrt{1 + (v_*/v)^2}. \quad (6.2)$$

The resulting steady-state curve is rate-independent at very low velocities, and rate-weakening at intermediate and high velocities. The driving velocity v_0 is chosen such that it resides in the rate-weakening branch. The system is chosen sufficiently large such that it can host several frictional instabilities ($L \gg L_c$). The constitutive behavior of the bulk is chosen to follow linear elasticity, i.e., Hooke's law [244]. The bulk and frictional parameters of the problem are summarized in Table. 6.1. The top and bottom bodies are

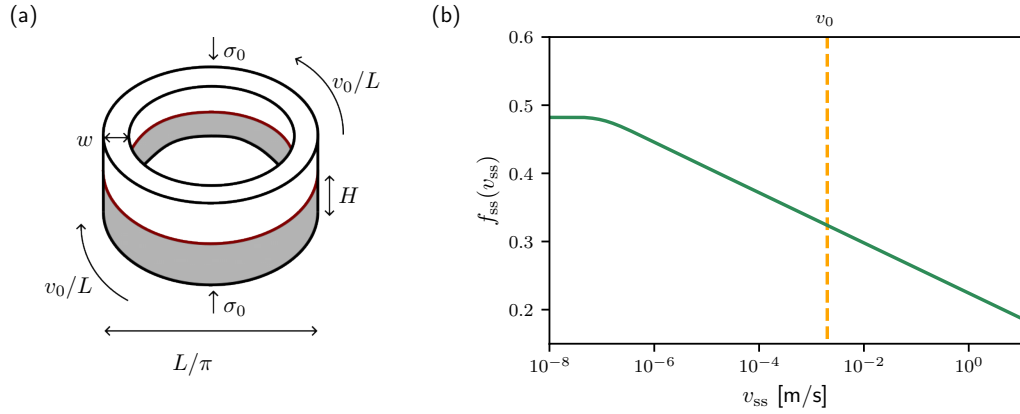


Figure 6.1: (a) A rotary (periodic) frictional system, composed of two identical deformable annuli (white and grey are just used to make a visual distinction) of diameter L/π , height H and thickness w , is sketched. The two annuli are pressed one against the other by a normal stress σ_0 and each is driven by an angular velocity of magnitude v_0/L (anti-symmetrically). The frictional interface (brown) is described by a homogeneous rate-and-state dependent interfacial constitutive law, such that the slip velocity v_0 resides on its velocity-weakening branch (see text for details). (b) The steady-state frictional strength f_{ss} vs. the steady-state slip velocity v_{ss} , presented on a semi-logarithmic scale. The vertical dashed line is the driving velocity v_0 .

initially in equilibrium and moving at a steady (tangential) velocity $v_0/2$ and $-v_0/2$, and the interface is at steady-state with $v_{ss} = v_0$ and $\phi_{ss} = D/v_0$. Perturbations are introduced by adding spatial Gaussian noise to the state field $\phi(x)$, resulting in the destabilization of the entire interface.

Parameter	Value	Unit
ν	0.33	...
μ	9×10^9	Pa
ρ	1200	kg/m ³
f_0	0.28	...
a	0.005	...
b	0.075	...
D	5×10^{-7}	m
v_*	1×10^{-7}	m/s
ϕ_*	3.3×10^{-4}	s

Table 6.1: Typical values of bulk and rate-and-state parameters used in this work. In addition, D has also been varied by a factor 1/3 and 3.

6.3 The numerical method

The calculations are performed using the explicit dynamic finite element framework, based on an in-house open-source finite element library called Akantu [8]. The domain is discretized into a regular mesh composed of bilinear quadrilateral elements (Q4). The sliding interface between the two elastic bodies is modeled using a node to node contact algorithm, whose details are given in section 3.1.2. Time is integrated using the central difference method and the time step is taken small enough to eliminate the numerical instabilities associated with the explicit finite element modeling of rate-and-state friction, as explained in [168]. In our simulations, we set the time step to $\Delta t_F = \alpha_F \Delta t_{CFL}$, where Δt_{CFL} is set by the Courant-Friedrichs-Lewy condition and α_F is typically taken to be $\mathcal{O}(0.01)$.

6.4 Identification of slip events

Here we summarize the procedure that is followed to identify distinct events. The slip activity on the fault is expected to be strongly heterogeneous, both in time and space (fast - spatially localized slip events followed by long waiting periods), see an example in Fig. 6.2a. Most of the time, the interface is sticking. As we are interested in slip events, to sample valuable data, we come up with a slip interval instead of a time interval for data sampling. This method is used in the context of depinning physics. Using slip sample allows us to get detailed information during slip events and reduces the amount of data corresponding to the waiting time between slip events where the velocity of the interface vanished, i.e., almost zero slip. To proceed, we define a slip threshold δ_{th} setting the precision of the measure during the simulation. We record the time that a point along the interface spent to slip from $\delta = 0$ to $\delta = \delta_{th}$, then from $\delta = \delta_{th}$ to $\delta = 2\delta_{th}$ and so on. When the slip accumulated during a single time step is shared between two slip thresholds, the time is allocated based on the relative weight of the two contributions. If a point has slipped more than one slip threshold during a time step, the time spent between the different slip thresholds will be linearly interpolated based on the exact cumulative slip value and its previous value, resulting in duration between thresholds that can be lower than the time step of the numerical scheme itself.

The outcome of this procedure is called a space-slip map of the duration. An example is shown in Fig. 6.2b, with the corresponding space-time plot of the velocity in Fig. 6.2a. The slip is normalized by D , the characteristic asperity size from the rate and state friction framework. In this space-slip map, the dark green/blue colors correspond to short durations Δt required to slip a given δ_{th} , i.e., a large sliding velocity, while the bright blue/white areas correspond to stick conditions. This map contains much more information than the one shown in Fig. 6.2a. Before any quantitative analysis of the slip events, one can notice the highly complex dynamics in play in the system, with events of various sizes and durations happening at the interface.

To identify distinct slip events, we start with time clustering. We convert the space-slip

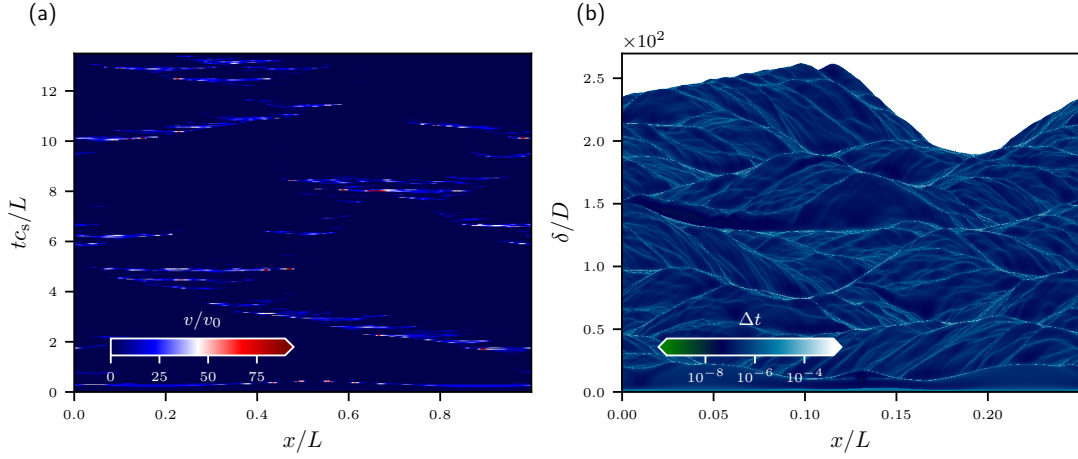


Figure 6.2: (a) Space-time plot of the velocity during a typical simulation. The part of the plot in dark blue corresponds to the interface sticking. (b) Space-slip plot of the time required to slip over a distance δ_{th} . The lower values in dark green/blue indicate a rapid slip while the largest ones in bright white indicate a long waiting period, i.e., sticking condition.

duration map into a space-slip map of the time $t(x, \delta)$ that indicates the time at which a given cumulative slip threshold value has been reached, with

$$t(x, \delta) = \sum_{n=0}^{n=\delta} \Delta t(x, n). \quad (6.3)$$

Fig. 6.3a shows the space-slip time map obtained from Fig. 6.2b. As we are not considering any spatial information yet, the entire data set from the space-slip time map is put into a vector \bar{t}_{NSE} which is sorted by time of occurrence. It contains the information on when a single node has reached a new slip threshold, which we refer to as a nodal slip event (NSE). We then compute the waiting time between two NSE anywhere on the interface, as $\Delta t_{NSE} = \bar{t}_{NSE,i+1} - \bar{t}_{NSE,i}$ where the subscript NSE indicates that we are referring to nodal slip events. If the waiting time is sufficiently large, it means that the interface is entirely sticking and thus indicates the separation between two independent global slip events. An extract of this vector taken at an arbitrary time is illustrated in Fig. 6.3c, where n_{NSE} is the number of NSE. Note that in the entire simulation shown in Fig. 6.3a, there are $\mathcal{O}(10^7)$ NSE. One needs to decide on a waiting time threshold. We choose it in relation to the number of points on the interface, the driving velocity, and the slip threshold.

The system is driven at a given velocity v_0 , such that in average, a node on the interface will slip by an amount δ_{th} every

$$\Delta t_{n=1} = \frac{\delta_{th}}{v_0}. \quad (6.4)$$

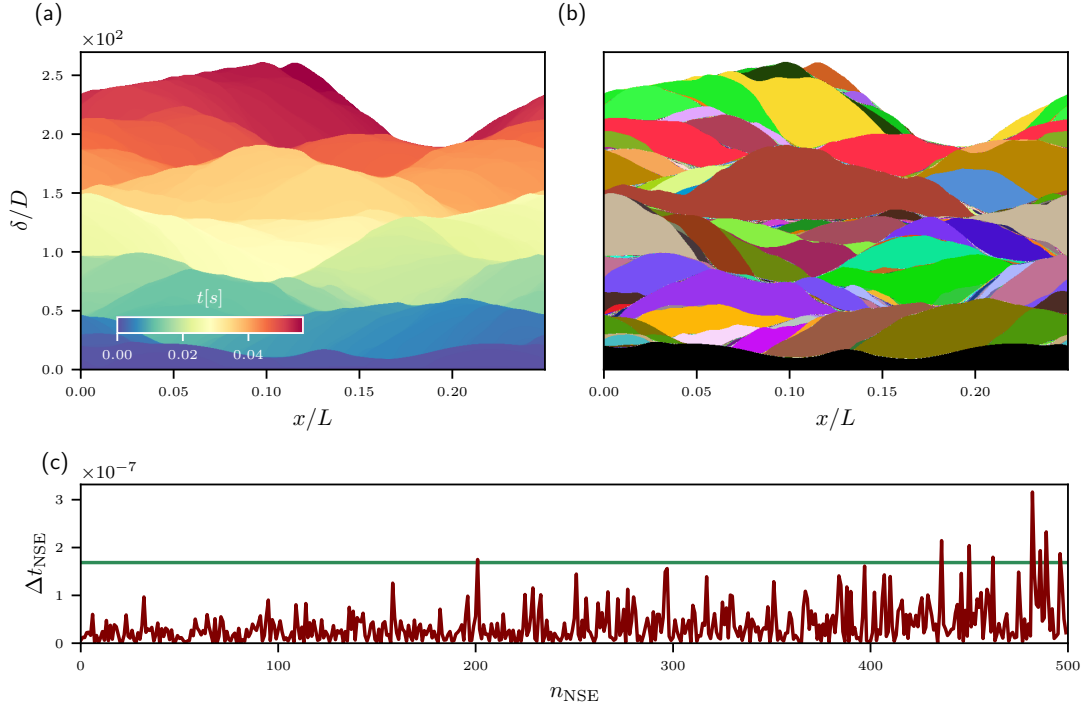


Figure 6.3: (a) Space-slip map of the time t at which a given cumulative slip value δ/D has been reached at a given position on the interface x/L . An area sharing the same color corresponds to a slip that occurred at the same time, while discontinuity in the colors indicates a waiting period. (b) The corresponding space-slip map of the distinct slip events, see text for more details on the procedure.

The interface is discretized with N nodes such that there is in average one NSE every

$$\Delta t_N = \frac{\Delta t_{n=1}}{N} = \frac{\delta_{\text{th}}}{v_0 N}. \quad (6.5)$$

Waiting time significantly below this value means parts of the interface are sliding faster than the imposed driving velocity, while a large waiting time corresponds to the entire interface sticking. The threshold is defined as $\alpha \Delta t_N$ with α an arbitrary constant. The value of α is chosen such that it does not affect the statistical distributions of the slip events, but still allows the method to distinguish between slip events. This threshold is indicated in Fig. 6.3c with the horizontal green line.

All the NSE that falls in between two values exceeding the threshold (for example, from $n_{\text{NSE}} \simeq 200$ to $n_{\text{NSE}} \simeq 430$ in Fig. 6.3c) are grouped inside a single *global slip event*. This information is then digitized back on the space-slip map, and we obtain a visual description of the distinct slip events as shown in Fig. 6.3b in which each color corresponds to a (global) slip event. There are $\mathcal{O}(10^4)$ slip events after applying this procedure in Fig. 6.3b. Note that slip events that are too small, both spatially $\mathcal{O}(dx)$ and in terms of duration $\mathcal{O}(\delta_{\text{th}})$, are removed from the analysis. An example of a single slip

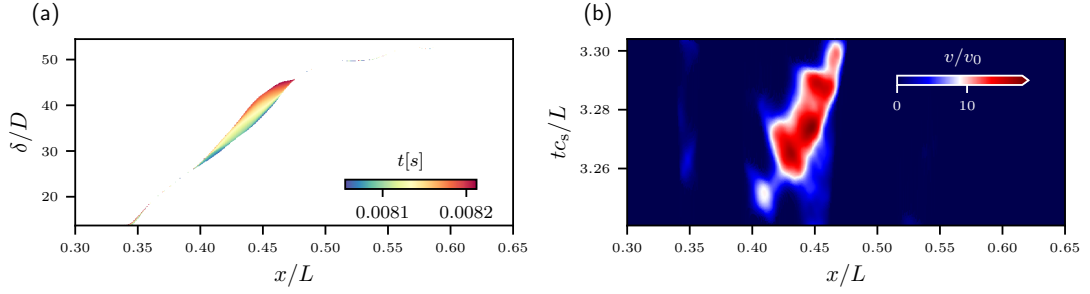


Figure 6.4: (a) Space-slip map of the time t at which a given cumulative slip value δ/D has been reached at a given position on the interface x/L for a single event. Only the colored area is part of the event. (b) The space-time velocity map of this event. It was reconstructed from the information from the space-slip map.

event is shown in Fig. 6.4a in the space-slip map of the time, with the corresponding space-time map of the velocity shown on Fig. 6.4b. The latter has been reconstructed from the information stored in the space-slip map of the duration and is not directly sampled in time. The red patch in Fig. 6.4b, spanning from $x/L = 0.4$ to 0.47 is the main rupture area with a sliding velocity going up to $\mathcal{O}(10v_0)$. This rupture is growing and propagating spatially. Around $x/L = 0.35$, there is some non-sticking velocity (light blue) but these are not propagating events and slip is most likely triggered by wave reflections in the bulk due to past slip events and interactions with finite boundaries. We can investigate the structure of the slip events. One can assess if they are continuous in space or composed of spatially unconnected slipping patches, which we call here *clusters*. Once again, the smallest clusters $\mathcal{O}(\delta_{\text{th}})$ or $\mathcal{O}(dx)$ are filtered out. The distribution of the number of clusters n_c per slip event is shown in Fig. 6.5. Most events are composed of a single cluster. The distribution seems to roughly follow a line in a semi-logarithmic scale, indicating an exponential probability density function.

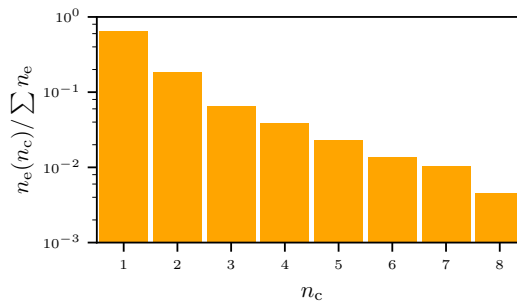


Figure 6.5: Number of slip events $n_e(n_c)$ composed of n_c clusters, normalized by the total number of events.

Now that the slip events are identified, we can compute their characteristics: rupture length L_r , duration T , average slip \bar{u} , seismic moment $L_r \bar{u} \mu$ with μ the shear modulus

of the bulk surrounding the interface, waiting time between events ΔT , average slip velocity $\langle v \rangle$, etc... We can do this for slip events (identified based on the time of occurrence) or for spatially independent clusters. In this section, we report the results for the statistics on the slip events (and not the clusters), but the observations are similar as most of the slip events are composed of a single cluster. Note that the first and last events in each simulation are excluded from this analysis. The first one is always spanning the entire interface and is triggered by the initial noise, while the last one is potentially not complete when we stop the simulation.

6.5 Time dependence of the statistics

Before looking in detail at the statistics themselves, we first want to evaluate if the statistical description of the slip events recorded during our simulations is dependent or independent of the time. We start by computing a measure of the *activity* A on the interface/fault defined as the number of *global* slip events (identified following the procedure presented before) per time interval to assess its evolution during the simulation. In Fig. 6.6, we compare the mean activity (in purple) to the activity computed by dividing the simulation in respectively 20, 50 and 100 evenly sized time intervals. The results shown in Fig. 6.6 correspond to the *richest* simulation at disposal, with $H = 0.1$ [m], $L = 4$ [m] and $v_0 = 2 \times 10^{-3}$ [m/s]. The activity is roughly constant over time, indicating that our system is in a permanent regime.

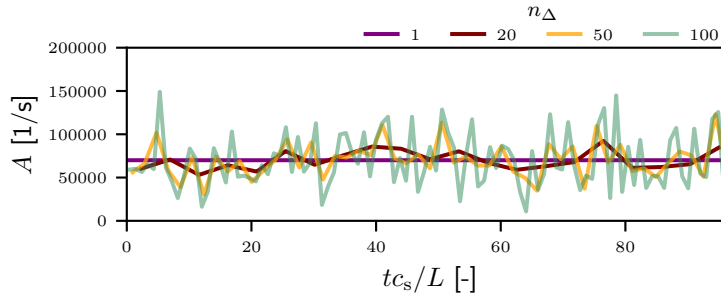


Figure 6.6: Activity A of the system as a function of the time computed using various time intervals.

Then we evaluate if the description of these events changes with time. In Fig. 6.7 we show the probability density functions (PDFs) for the average slip \bar{u} , the duration T , and the seismic moment M_0 for the entire simulation (in orange) and two subsets of events corresponding respectively to the events occurring during the first fifth of the simulation (dotted dashed brown, $t < 0.2t_s$) and the last fifth of the simulation (dashed green, $t > 0.8t_s$). Irrespectively of the time interval, the PDFs are perfectly collapsing with the one computed based on the entire data range, thus the statistics are also time independent (stationary), and we will use the entire data set for each simulation for the

subsequent analysis.

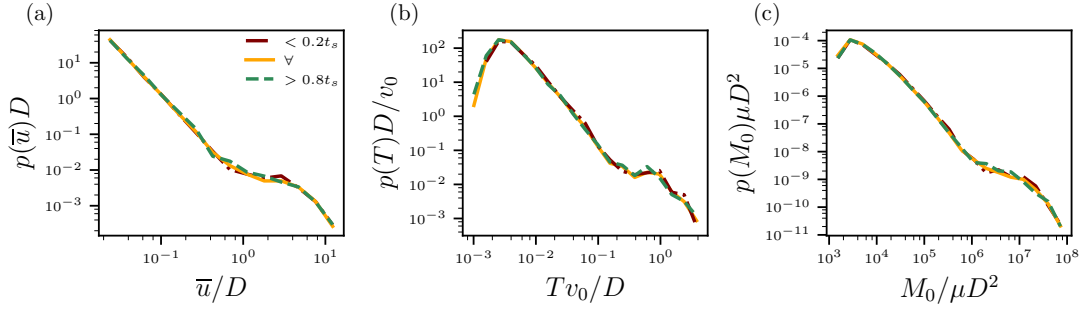


Figure 6.7: Probability density function $p(x)$ (a) of the average slip \bar{u} (normalized by D) (b) the duration T (normalized by D/v_0) and (c) the seismic moment M_0 (normalized by μD^2) for three sets of events: the entire data set (orange), the first fifth of the simulation (dotted dashed brown) and the last fifth (dashed green).

This first result suggests that the system is in a self-organized permanent regime that is likely to be sustained by the various mechanisms in play in the system. This includes the aging of the interface, the dissipative processes through slip events, and bulk mediated wave propagation. The statistics are discussed below.

6.6 Statistical complexity

We now study the statistical distribution of the observable quantities of the slip events recorded during a reference simulation with $H = 0.1$ [m], $L = 4$ [m] and $v_0 = 2 \times 10^3$ [m/s]. We consider three main quantities: the average slip \bar{u} , the duration T and the seismic moment M_0 . The probability density functions (PDFs) of these quantities are presented in Fig. 6.8 (in brown). Note that the characteristics of the PDFs discussed here are not restricted to this specific simulation, but are rather generic to the type of frictional system discussed in this section. The three PDFs have similar characteristics and reveal that the observed slip events are broadly distributed, over several orders of magnitude. We first consider the PDF of the average slip $p(\bar{u})$, see Fig. 6.8a. For small slips, the statistical distribution follows a power law scaling as:

$$p(x) = Cx^{-\beta}. \quad (6.6)$$

This is highlighted by the linear dashed black line in double logarithmic scale, with an exponent $\beta \sim 2.45$. The distribution features a change in behavior for large slips occurring roughly around $\bar{u} = D$ (indicated by the vertical line). The origin of this break in behavior is discussed below.

The PDFs of the duration and the seismic moment share the same characteristics, with a power law scaling for small quantities (with an exponent of respectively $\beta \sim 2.2$ and 2) and a different behavior for large values. The presence of distinct behaviors for small and large events implies that two different types of slip events are occurring at

the interface. On one hand, we have small/non-propagating slip events that feature an average slip lower than D (i.e., the slip accumulated during the event is not large enough to change the state of the interface and nucleate a rupture) and large rupture-like propagating events. The spatio-temporal description of the events validates this distinction between the two typologies of events. The apparent propagation velocity of the events as $c_a = L_r/T$ with L_r the rupture length confirms this as well: the large events have propagating velocity in the range of the elastic wave speeds while the small events have non-physical apparent propagation velocity, several orders of magnitude larger than the theoretical limiting propagation velocity (which is c_d for supershear ruptures). The small events are likely triggered by bulk-mediated stress transfer but do not result in rupture nucleation (and therefore propagation). These events are reminiscent of the events called *breather* in [154]. To distinguish between the two types of events, we use the criterion of the average slip, with slip larger than D corresponding to rupture-like events, as illustrated with the vertical line in Fig. 6.8a. We plot the PDFs of the large propagating events $p(x)[\bar{u}_x > D]$ in dashed green in Fig. 6.8b,c. (Note that we do not plot the $p(\bar{u})[\bar{u}_x > D]$ as it corresponds exactly to $p(\bar{u})$ on the right of D). These distributions follow roughly a log-normal law (orange curve in the insets of Fig. 6.8b,c) that is given by:

$$p(x) = \frac{1}{xs\sqrt{2\pi}} \exp \left[-\frac{(\ln(x) - \bar{x})^2}{2s^2} \right], \quad (6.7)$$

with \bar{x} and s the mean and standard deviation of the variable's natural logarithm. This type of statistical distribution for large propagating events features a somewhat *fat* tail for large events (but is not as broad as a power law distribution).

It is important to note that these features of the statistical distributions of the characteristics quantities of the slip events are generic: changing the geometry (H, L), the characteristics of the friction law (D, α) and the driving velocity v_0 result in similar PDFs. In the next paragraph, we show that with some proper renormalization, the PDFs are quantitatively collapsed. In Fig. 6.9, we also show an example of the interrelation between the observable quantities (\bar{u}, T, M_0 and L_r), which also reveals some apparent non-trivial power law relationships between them, as observed for real earthquakes.

6.7 Collapse of the probability density functions

We explore the parametric space of our system by changing the length L by a factor 2 and $1/2$, the height H again by a factor 2 and $1/2$, and the characteristic slip distance D by a factor 3 and $1/3$. We show in Fig. 6.10a,b,c the (unnormalized) PDFs for the average slip \bar{u} , the duration T and the rupture length L_r . We show the rupture length instead of the seismic moment M_0 as the latter is a combination of both the rupture length and the average slip: collapsing the PDFs for these two quantities should result in the collapse of the seismic moment distribution.

The first striking observation is the immediate collapse of the PDFs for the average slip

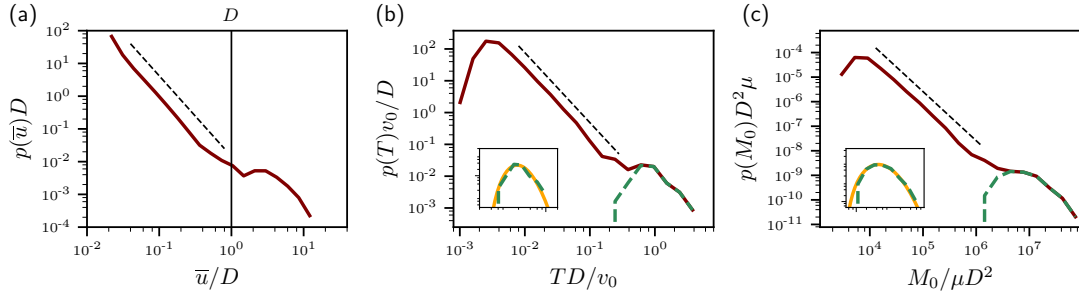


Figure 6.8: (a) The probability distribution function (PDF), $p(\bar{u})$, of the average slip \bar{u} of slip events measured in a long-time simulation of the finite-size velocity-driven frictional system sketched in Fig. 6.1a (for $w \ll L, H$, see text for details). \bar{u} is normalized by the characteristic slip D distance of the rate-and-state friction law (also marked by the vertical line), see text for the precise definition of slip events and D . Events with \bar{u} smaller than D are broadly distributed, following a power-law distribution (the dashed line has a slope ~ -2.45 , and note the double-logarithmic axes used). For $\bar{u} > D$, slip events appear to follow a different distribution. (b) The PDF $p(T)$ of the duration T of slip events (solid brown line), normalized by D/v_0 . Events that feature $\bar{u} < D$, see panel (a), are again power-law distributed (the dashed line has a slope ~ -2.2). The (non-normalized) PDF of events with $\bar{u} > D$ is superposed (dashed green line) and is shown in the inset to follow a log-normal distribution (solid orange line). See text for an extensive discussion of the distinction between events featuring $\bar{u} < D$ and $\bar{u} > D$. (c) The same as in panel (b), but for $p(M_0)$, where $M_0 = \mu \bar{u} L_r$ is the seismic moment, L_r is the event size and μ is the shear modulus. M_0 is normalized by μD^2 (the dashed line has a slope ~ -2).

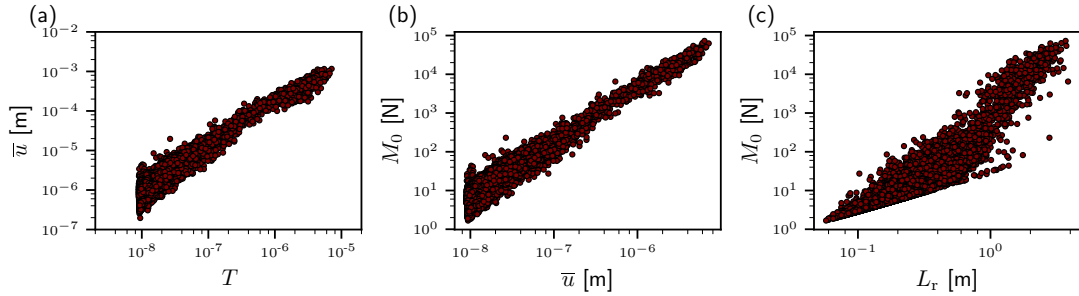


Figure 6.9: Scatter plots of (a) the duration T versus the average slip \bar{u} (b) the average slip \bar{u} versus the seismic moment M_0 and (c) the rupture length L_r versus the seismic moment M_0 .

$p(\bar{u})$ for the power law (small non-propagating events) part, without any normalization parameters. The transition between small and large events changes with variations of D (as expected, as modifying D directly changes the slip value required to transition from one state to another), but more surprisingly also with variations of H . This is an indication that the reflection of waves at the top and bottom boundaries ($y = \pm H$) plays

a role in the statistics and the dynamics, and this will be discussed in detail later on. L does not play a role in any part of the distribution, apart from increasing the cutoff of observable large events. Note that changing the driving velocity v_0 does affect $p(\bar{u})$ and a rescaling by t^*v_0 is required to collapse the small event power law, where t^* is a characteristic time-scale that is not specified here. The impact of v_0 on the statistics is not discussed in detail in this manuscript, but the generic features are not altered when changing the driving velocity. The PDFs of the duration T , see Fig. 6.10b are almost perfectly collapsing except for the variations of D (in brown and pink). Rescaling $p(T)$ by D as shown in the inset leads to a collapse in the small event range. Again, the change of behavior between small and large propagating events is affected by H , and L only affects the cutoff of large durations.

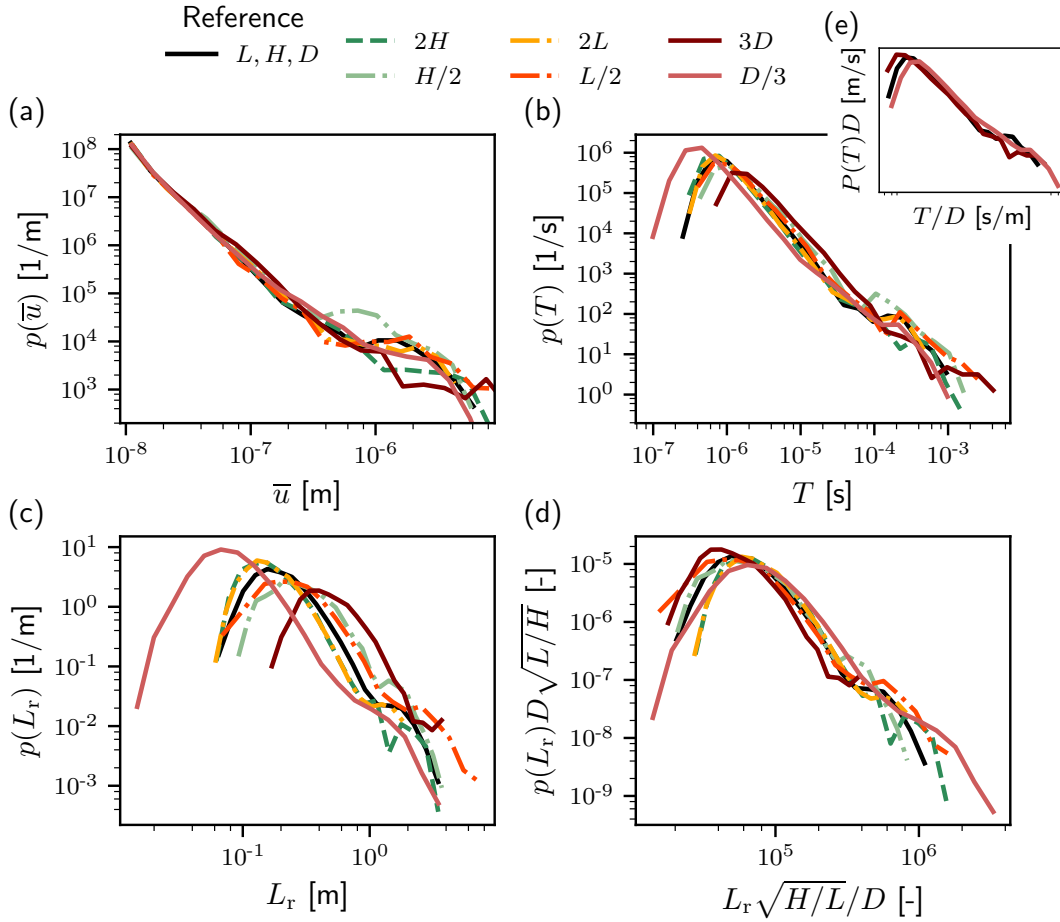


Figure 6.10: PDFs (a) of the average slip \bar{u} (b) the duration T and the rupture length L_r for various system parameters (variations of H, L, D). For the average slip, all the PDFs collapse in the power law regime without rescaling parameters. In the case of the duration, the PDFs collapse after normalization by D , see (e). The rupture length requires a more complex normalization with $\sqrt{H/L}/D$ which is shown in panel (d).

The PDF of the rupture length $p(L_r)$ is slightly different. First, the range of observed rupture length is strictly controlled on the small scale by the spatial discretization and on the large end by the domain size. The tiny event distribution is an increasing function of the rupture length up to a maximum, then the behavior is a power law for intermediate events followed by a change of distribution for large events. The first part is completely absent from $p(\bar{u})$ and significantly less relevant for $p(T)$. Without normalization, all the functions $p(L_r)$ are qualitatively similar but do not collapse. A rescaling involving the three length scales L , H , and D is thus required. Using $\sqrt{H/L}D$ as the rescaling parameter allows collapsing the intermediate (small non-propagating events) part of the distribution, but note that this rescaling is not as good as for the other quantities. We do not provide here a physical explanation of the rescaling by $\sqrt{H/L}$. The PDFs for the seismic moment are also successfully collapsed by rescaling \bar{u} and L_r .

The emergence of broad statistical distributions in the type of frictional system discussed here is thus generic and robust, and the characteristics of the distributions do not depend on the system characteristics for the small non-propagating events. Note that variations of v_0 and of the friction law parameters (namely the weakening rate and the presence or not of a strengthening branch at large velocity) have also been investigated, and the generic features of the PDFs remain unchanged. In the following section, we look at the spatio-temporal organization of these events.

6.8 Dynamical complexity

The slip events at the interface are spatially and temporally related to each other and depend on the history of the interface itself. A detailed sequence of events is shown in Fig. 6.11. In panel (a), a space-time plot of the velocity field $v(x, t)$ normalized by the driving velocity v_0 is shown, for a time interval that is chosen arbitrarily during a simulation (here t ranges from 2 to $4.2c_s/L$). The interface is mostly sticking (in dark blue) and the slip events are shown with colors ranging from bright blue, white, and red for large slip velocities. One large propagating (rupture-like) event is indicated with a green arrow and is called event 1. This event is expanding spatially in time, but eventually arrests. Note that the dynamics that are simulated here are truly two-dimensional, (see section 6.11.2), allowing the propagation of rupture-like events featuring square-root singularities at their tips. The inset of Fig. 6.11a is a zoom on the arrest region of the left edge of rupture 1, after the event. Note that the scale for the velocity in the inset is different (it shows much smaller velocities compared to the main panel) and this reveals some slip patches that were not perceptible with the scale of the main panel. We mark events 2, 3, and 4 with respectively yellow, orange, and brown arrows. The accumulated slip profiles δ relative to the slip before event 1 (called δ_0) are shown in Fig. 6.11b with the corresponding colors. The slip accumulated during event 1 is significantly larger than D which is consistent with a propagating event. The shape of the slip accumulated during this event is similar to the slip of a crack $\delta(x_t) \sim \sqrt{L_r^2 - x_t^2}$ with x_t the position taken from the tip of the rupture and L_r the rupture length (the equivalent of the crack

size). The state $\phi(x)$, see Fig. 6.11c, and the stress $\tau(x)$, in Fig. 6.11c, before (in black) and after (green) event 1 are strongly heterogeneous, even if the absence of material disorder. The heterogeneities are self-generated by the system due to its history. The vertical lines in these two panels indicate the arrest locations of event 1: the state variable is reduced to almost 0 over the rupture length, while it increases over the rest of the interface due to aging, indicated by black arrows (the real contact area increases with time in the absence of sliding while it is reduced during fast slip as microcontacts are broken). The locations of rupture arrest correspond to local minima in the stress profile that existed before the rupture and suggests that arrest of event 1 is related to these low-stressed regions. Other mechanisms can arrest rupture in this system, such as elastic waves unloading the interface locally. Stress concentrations are left at the edges of the rupture.

The subsequent slip events are localized at one of these stress concentrations (we focus on the left one around $x/L = 0.2$, but slipping is also occurring on the right around $x/L = 0.45$). The accumulated slip during events 2, 3, and 4, relative to the slip after event 1 (called δ_1), is shown in the first inset on the top right of Fig. 6.11b. The second inset only shows events 2 and 3 with another y -scale as they are smaller than D and could not be properly resolved by the scale of the main panel and first inset. The shape of the slip accumulated during these small non-propagating events are also of the form $\delta(x_t) \sim \sqrt{L_f^2 - x_t^2}$. A rupture is eventually nucleated (event 4) after this succession of stick/slip in this overstressed area. Note that the velocity goes back to zero in between events.

This spatio-temporal description of successive events is generic during the simulation, as can be seen in Fig. 6.11a : event 4 is followed by several small non-propagating events (in between $tc_s/L = 3 - 3.75$, around $x/L = 0.2$) until a large propagating rupture is nucleated. The small events are thought to be triggered by wave reflections and participate in the build-up of stress concentrations that lead to large propagating ruptures. This small extract from a simulation is another demonstration of the broadly distributed type of slip events at the interface.

6.9 Influence of wave reflection

As the reflection of waves seems to play an important role in the complex dynamics at stake in this frictional system, we study the effect of finite geometry in a system that host a single perturbation (in place of the chaotic system discussed before). We start from an interface sliding at a uniform, steady velocity v_0 (in the rate weakening branch of the rate-and-state friction law) and introduce a Gaussian perturbation in the state field ϕ . The size of the system is chosen such its length L is larger than the critical length for frictional instability L_c . The perturbation is centered at $x/L = 0.5$. A linear frictional instability develops and leads to the nucleation of a frictional rupture. The outcome of this procedure is illustrated with a space-time plot of the slip velocity for two different system heights, $H = 0.1$ [m] and $H = 0.2$ [m] in Fig. 6.12a,b. The velocity (note the logarithmic scale) accelerates at the center of the interface, and this

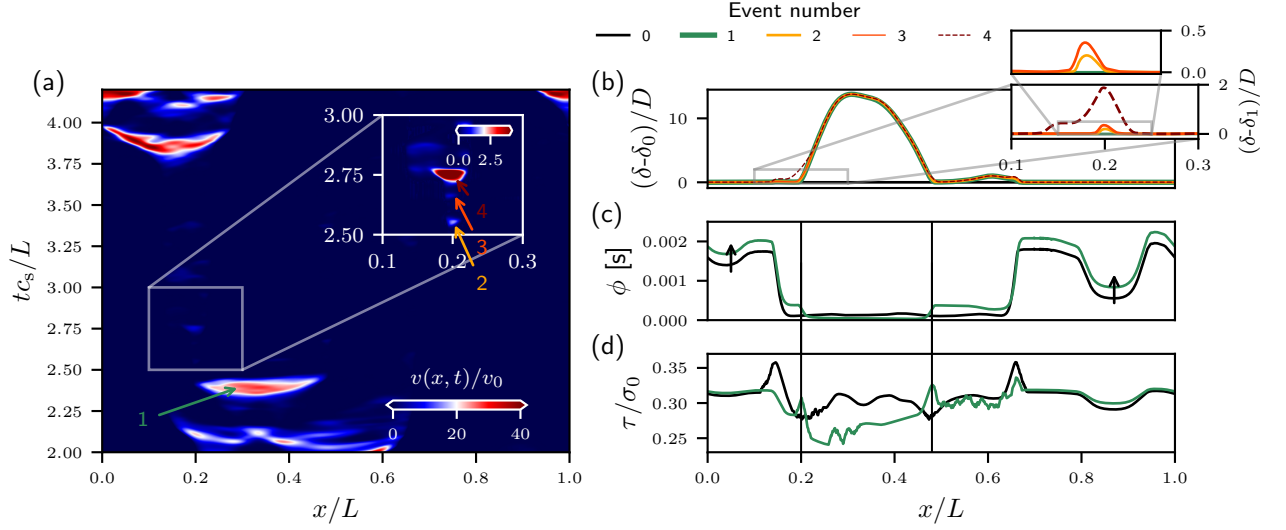


Figure 6.11: (a) A space-time plot of the slip velocity field $v(x, t)$, normalized by v_0 , where x is the coordinate along the interface (normalized by L) and t is the time (normalized by L/c_s , where c_s is the shear wave speed). Dark blue regions correspond to the sticking part of the interface ($v(x, t) < v_0$, see color bar). A zoom in on the space-time interval $x/L = 0.2 - 0.45$ and $tc_s/L = 2.25 - 2.4$ is shown (note the change in scale in the color bar therein). Four events are indicated (different numbers and colors), to be further discussed in subsequent panels. (b) The accumulated slip $\delta(x)$ (in unit of D) of the different slip events marked in panel a (see also upper legend in panel b), relative to the accumulated slip $\delta_0(x)$ prior to event 1 (slip history), denoted as event 0 in the legend. The two insets show a consecutive zoom in (see gray boxes and lines as guides), on smaller spatial scales, of the accumulated slip events 2,3,4, measured relative to the accumulated slip $\delta_1(x)$ of event 1 (see right y-axis). See extensive discussion of the presented spatiotemporal dynamics in the text. (c) The frictional state field $\phi(x)$, which determines the real contact area, both before (black) and after (green) event 1. The arrows indicate contact aging, and the two vertical lines show the interfacial region that slipped during event 1. (d) The interfacial shear stress $\tau(x)$, normalized by σ_0 , before (black line) and after (green line) event 1. See text for extensive discussion of these results.

fast slipping patch (in red) starts expanding spatially. The slip velocity then rapidly drops to zero. The characteristic reflection time-scale for elastic waves caused by slip at the interface is $2H/c_s$ (with c_s the shear wave speed) and is indicated on both panels at $x/L = 0.5$. The time scale over which the interface slides significantly faster than v_0 (in red) matches this characteristic time scale of reflection. It is expected that by doubling the system height, the duration of fast slip at $x/L = 0.5$ will also double. This is verified in Fig. 6.12b. This simple case illustrates that elastic waves can locally alter the dynamics of a slipping patch. It occurs as follows: elastic waves are radiated from the interface when slipping, and then propagate in the bulk up to $y = H$ where they are reflected due

Chapter 6. Statistical and dynamical complexity in a driven frictional system without disorder

to the imposed velocity boundary condition. The waves that travel back to the interface unload the interface and arrest sliding. For $H = 0.1$ [m], this is sufficient to stop the rupture altogether, but for $H = 0.2$ [m], the rupture patch is sufficiently developed such that the two rupture fronts continue their propagation after the return of the elastic waves. In the latter, a crack-like rupture is *split* into two slip pulses by the return of the elastic waves. Note that these pulses are propagating at supershear velocities, as indicated by the slopes representing the elastic wave speeds (c_r , c_s and c_d) in white.

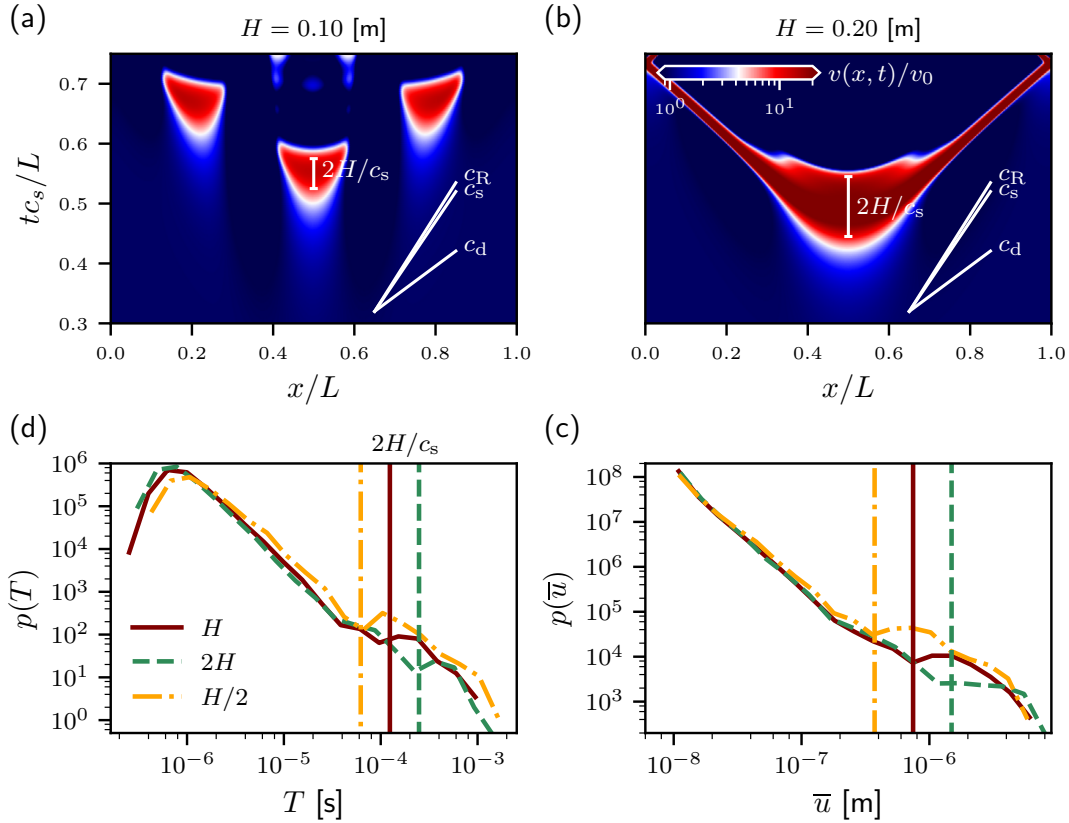


Figure 6.12: (a) A space-time plot of $v(x, t)$ (same format as in Fig. 6.11a) for a system of height $H = 0.10$ m and a perturbation introduced at $t = 0$ at $x/L = 0.5$ (see text for details). The shear wave travel time $2H/c_s$ is marked, as well as the 3 wave speeds: c_R (Rayleigh), c_s (shear) and c_d (dilatational), see white lines. (b) The same as panel (a), but for $H = 0.2$ m. Panels (a) and (b) are extensively discussed in the text. (c) $p(T)$ (normalized as in Fig. 6.8) for 3 values of H , separated by a factor of 2 (see legend and note that $H = 0.1$ m therein). The wave travel time $2H/c_s$ in each case is marked by a vertical line. It is observed that while T of small, non-propagating events are barely affected by H , the large, propagating events distribution is systematically shifted to higher values with increasing $2H/c_s$. (d) The same as panel (c), but for $p(\bar{u})$. Here, the vertical lines correspond to $3v_0 \times 2H/c_s$, see text for discussion.

Interestingly, this time scale is not only related to dynamical complexity, but also to

statistical complexity. The probability density functions of the duration $p(T)$ for systems with various heights ($H/2$ in dotted dashed orange, H in solid brown and $2H$ in dashed green with $H = 0.1$ [m]) are shown in Fig. 6.12c and the reflection time-scale for each system is indicated by vertical lines of the same color and line style. This time scale coincides with the change of behavior observed in the PDFs $p(T)$ between small / non-propagating events and large / rupture-like events. An equivalent observation can be made from the PDFs of the average slip $p(\bar{u})$ in Fig. 6.12: instead of the reflection time-scale $2H/c_s$, the vertical lines indicate a characteristic slip distance associated to this time-scale, as $\gamma v_0 \times 2H/c_s$ where γv_0 is a characteristic slip velocity during slip events, with $\gamma = \mathcal{O}(1)$, and in this plot specifically $\gamma = 3$. This implies that the finite height H plays an important role both for the spatio-temporal description of the slip events and for their statistical descriptions.

6.10 Summary and discussion

In this section, we studied the emergence of statistical and dynamical complexity in a driven frictional system in the absence of disorder. We first show that in a finite system driven at a constant velocity and in which the dissipation only takes place at the interface and does not feature any material heterogeneities (neither in the bulk nor in the frictional properties), broad slip events occur. In particular, the duration, the average slip, and the seismic moment of the recorded slip events span several orders of magnitude. We show that the slip events can be divided into two categories: small/non-propagating events, whose distribution follows a power law, and large/rupture-like events, described by a log-normal probability density function. The small events are characterized by an average slip that is lower than D , the characteristic slip distance of the rate-and-state law that describes the frictional behavior. They are mostly triggered by elastic waves that propagate in the elastic bulk, but these perturbations do not result in a spatial expansion of the slipping area. The emergence of complexity is related to self-generated heterogeneities at the interface level: the complex interactions between weakening during slip, aging, and long-ranged elastic stress transfers through elastic waves propagation lead to highly heterogeneous stress and state (which is a proxy for the contact area) of the interface, in the absence of material heterogeneities. This is a different result compared to the picture of emergent statistical complexity being a manifestation of the material heterogeneities, which has been discussed in [77; 157; 129]. The presence of finite boundaries and the subsequent waves reflections allows for an additional mechanism for rupture triggering and arrest. This is the case with re-nucleation of slip in laboratory-earthquake experiments [255], which is thought to be dynamically triggered by wave-mediated stress transfer. While the wave reflections in this chapter occurred at the solid boundaries, they could also originate from bi-material contrast in the bulk surrounding the interface (e.g., asperities, damage zone near faults). They are expected to be relevant for various frictional systems. To conclude, finite geometry, even in the simplest form employed here (i.e., regular and symmetric geometry), alongside generic

rate and state friction law at the interface, seems sufficient for the emergence of statistical complexity.

6.11 Supplemental material

6.11.1 Independence of the statistics on the thresholds

To illustrate the independence of the statistical descriptions of the slip events on the time threshold Δt_{th} , we show in Fig. 6.13 the probability density function of the average slip, duration and seismic moment for the same simulation computed using $\Delta t_{\text{th}} = 15, 30, 60$. For values significantly larger than that, numerous slip events are grouped together up to a point where the entire interface is considered as a single slip event. The main characteristics of the PDFs do not depend on the threshold: (i) the power law scaling for small events, (ii) the change in scaling law occurs around the same value, and (iii) the large propagating events are roughly log-normal distributed. The behaviors near the cut-offs are however different (as expected): modifying the threshold directly affects the minimal event size. Plus, increasing Δt_{th} result in grouping large event together and thus increase the maximum observed event size.

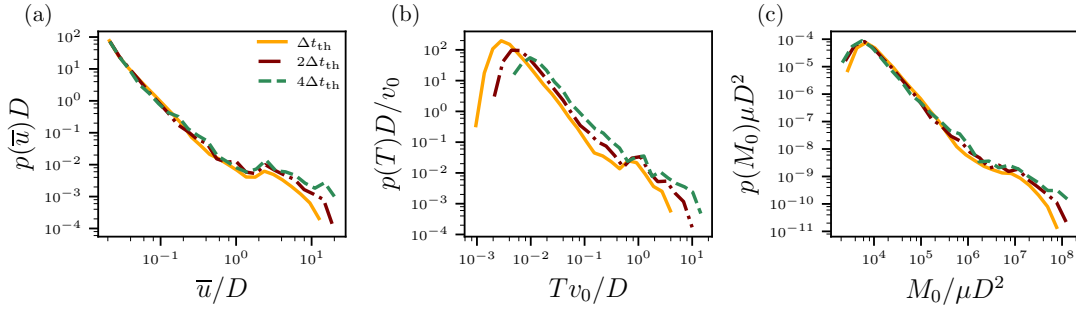


Figure 6.13: Probability density function $p(x)$ (a) of the average slip \bar{u} (normalized by D) (b) the duration T (normalized by D/v_0) and (c) the seismic moment M_0 (normalized by μD^2) for three value of time threshold used to identify events, with $\Delta t_{\text{th}} = 30$.

6.11.2 Nucleation length for finite height system

To verify that the system studied is fully resolving two-dimensional dynamics (i.e., is not in the quasi-one-dimensional limit), we compute the theoretical nucleation length for two homogeneous elastic bodies of height H in contact along a planar interface by conducting a linear stability analysis (LSA), see [78] for details on the procedure. The resulting function $L_c(H)$ is shown with the solid brown line in Fig. 6.14. The theoretical nucleation length of the largest system studied $H = 0.2$ [m] is almost equal to the one for an infinite system (vertical green line). In contrast, for the other heights ($H = 0.05$ and $H = 0.1$ [m]), the nucleation length corresponds to roughly 65% and 80% of $L_c(H \rightarrow \infty)$,

supporting the hypothesis of a two-dimensional system.

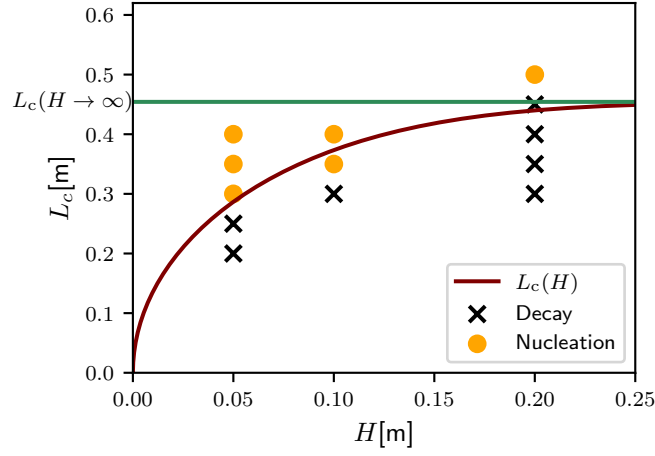


Figure 6.14: Nucleation length L_c as a function of the system height H . In brown, the theoretical nucleation length is based on a linear stability analysis following [78]. The horizontal green line indicates the theoretical nucleation length in the limit of $H \rightarrow \infty$. Results of numerical simulations (see text for details) that lead to the development of a frictional linear instability are indicated with orange dots, while dying perturbations are shown with black crosses.

To assess the validity of the theoretical estimation for L_c , we conduct finite element simulations of the frictional system discussed here and introduce a single perturbation of length L_p . We report in Fig. 6.14 the outcome of this perturbation. It either decays and dies (black crosses) or grows and leads to rupture nucleation (orange circles). The numerical results are in good agreement with the theoretical prediction, validating the two-dimensional nature of the system studied. This implies that singular rupture fronts can develop in this system, which is impossible if we were in the quasi-one-dimensional limit. Note that the typical mesh size is $\Delta x = 2.5 \times 10^{-3}$ [m] such that the nucleation length is discretized with $L_c/\Delta x = \mathcal{O}(100)$ elements. The process zone size can be estimated as $\omega = \mathcal{O}(\mu D/b\sigma[1 - \nu]) = 9.5 \times 10^{-2}$ [m], see [256], resulting in roughly 40 elements in the process zone.

7 Coupling the finite element method and the spectral boundary integral method

This chapter presents the coupling between the two numerical methods used thus far in this thesis: the finite element method, and the spectral boundary integral method. Modeling dynamic rupture problems is computationally challenging, as it involves complex physics and requires resolving length and time scales that can span orders of magnitude. The finite element method is versatile and can be adapted to any geometry, material heterogeneity, and behavior, allowing to model dynamic rupture problems. However, the entire domain has to be discretized, which can be costly if one wants to get rid of the interactions with the boundaries. The spectral boundary integral method, however, is an efficient tool that describes the response of the free surface of a semi-finite homogeneous elastic body. Here, we use the latter as a boundary condition to truncate the simulation domain of a finite element model that encompasses all the non-linearities and dissipation of the problem of interest. We first present the coupling algorithm, based on a strict continuity of velocities at the coupling interface. The validity of the coupling scheme is assessed with a simple example of elastic wave propagations, and its accuracy is compared with another coupling formulation based on a staggered scheme. We show an example of spontaneous crack propagation using extrinsic cohesive elements.

This chapter is an adapted version of the paper:

Coupling the finite element method and the spectral boundary integral method for dynamic rupture simulations, Roch, T., Molinari, J.-F. *In preparation*

7.1 Introduction

The numerical modeling of dynamic rupture is usually challenging, as it involves discontinuities, non-linearities, and dissipation. In addition, the nucleation and propagation of rupture fronts involve a broad range of length and time scales. The dissipation at the tip of a dynamic rupture front occurs over a short distance called the process zone, which can be several orders of magnitude lower than the dimension of the interface over which it propagates. The ruptures themselves are often fast, propagating at velocities close to the elastic wave speeds, while the loading of such systems can be comparatively extremely slow (e.g., tectonic loading can take hundreds of years before triggering a consequent earthquake). Thus, modeling such problems requires large but finely discretized time and spatial domains, and proves to be a technical challenge.

The numerical modeling techniques for simulating elastodynamic problems can usually be classified into two categories. On one hand, domain-based methods, such as the finite difference method and the finite element method (FEM), in which the entire body of interest needs to be discretized. These methods are flexible and allow for considering various bulk constitutive behavior, heterogeneities, and non-linearities. Several techniques to model discontinuities in domain-based methods are commonly used, such as cohesive elements [162], the node-to-node discretization of an interface, and also mesh-independent techniques like phase-field approach of brittle fracture [164]. Any rupture geometry can thus be modelled, including complex faults networks or even cases in which the path of the rupture is not known beforehand (e.g., the growth of microbranches [257]). The main drawback of domain-based methods is the necessity to model a sufficiently large domain such that the dynamics of the problem are not altered by the interaction with boundaries, which can result in simulated domains significantly larger than the area of interest. On the other hand, boundary-based methods are comparatively computationally cheaper as they allow for reducing the dimensionality of the problem. In these methods, the partial differential equations are solved only on the boundaries of the body with the help of Green's functions. The spectral boundary integral method (SBIM) presented in section 3.2 describes the stresses and velocities at the free surface of a semi-infinite elastic body [169; 170; 171]. This method however requires the bulk to be homogeneous linear elastic, limiting its applicability to specific rupture problems. The difficulty to derive closed forms for the Green's functions for other configurations seriously hinders the possibility to extend this method.

A natural solution for solving the main limitation of the domain-based method is to truncate the simulation domain using boundary conditions that do not reflect waves in the domain of interest. This has been achieved with various numerical methods, including infinite elements [258; 259], absorbing boundary conditions [260; 261], absorbing layer methods [262; 263], and perfectly matching layers [264; 265; 266]. These methods, however, suffer to some degree from artificial reflections at the interface and need to be taken sufficiently far from the area hosting the dynamic rupture for good accuracy. Using the SBIM to radiate waves inside a semi-infinite elastic continuum is a promising

alternative, as the propagation of waves is solved exactly with this method. The coupling between SBIM and domain based-method has gained increased attention in the last few years, with a coupling between FD and SBIM [267] and coupling between FEM and SBIM [268; 269; 270; 271]. The latter used a staggered approach, with the response of the semi-infinite elastic body being applied either as Dirichlet [268] or Neumann [271] boundary conditions on the finite element domain.

Building on this idea of truncating a finite element domain using the SBIM to simulate interfaces with semi-infinite elastic bodies, we propose a novel formulation for the hybrid FEM/SBIM method relying on a strong coupling of the velocities at the interface, instead of a staggered approach. The principle of the method is schematized in Fig. 7.1. A dynamic rupture problem is embedded inside an infinite body Ω^∞ (or sufficiently large that the interactions with the finite boundaries are not relevant for the problem). Modeling this problem with SBIM is not possible, as the non-planar interface and the heterogeneities can not be considered with this method. One could use FEM, but this requires simulating a large domain. Interfaces with SBIM are thus introduced around the area where dynamic rupture occurs (see Fig. 7.1b) to reduce the size of the domain that needs to be discretized.

First, we present the formulation of the coupling algorithm. A validation of the scheme is presented with a simple elastic problem of elastic wave radiations. We compare the accuracy of the proposed coupling algorithm with an existing staggered scheme. Then, we show an example using extrinsic cohesive elements, in which a crack loaded in tension spontaneously propagates. We conclude this chapter with a summary of the method and its potential applications.

7.2 Coupling method

We couple two in-house open source software called *Akantu*¹ [8] and *cRacklet*² [9], respectively, for the finite element method and the spectral boundary integral method. First, we recall the main steps of the time integration scheme in both methods.

7.2.1 Finite element method

In what follows, the subscript stands for the time step, and the superscript F indicates that the field is related to the finite element method. As presented in section 3.1, the time integration scheme that we use is based on a Newmark- β [166] scheme with $\beta = 0.5$ and $\alpha = 0$:

¹<https://akantu.ch/>

²<https://gitlab.com/cracklet/cracklet>

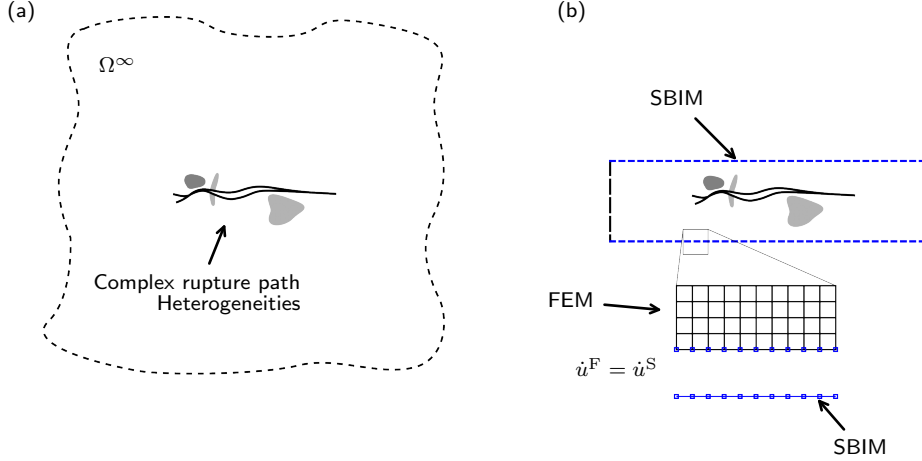


Figure 7.1: Schematic representation of the coupling between the finite element method and the spectral boundary integral method. (a) A complex dynamic rupture problem involving tortuous rupture path and heterogeneities is embedded inside a homogenous elastic body Ω^∞ . (b) The numerical representation of this problem using the coupling scheme. A thin stripe of finite element is used to model the region of interest with the rupture and the heterogeneities. The top and bottom boundaries of this finite element mesh are coupled with the free surface from the spectral boundary integral method (in blue). Nodes are matching in between the FEM mesh and the SBIM surface. The continuity is enforced at the coupling interface by imposing equality between the velocities at the coupling nodes from the finite element mesh \dot{u}^F and the velocities at the surface of the SBIM \dot{u}^S .

$$\begin{aligned} \mathbf{u}_{n+1}^F &= \mathbf{u}_n^F + \Delta t \dot{\mathbf{u}}_n^F + \frac{(\Delta t)^2}{2} \ddot{\mathbf{u}}_n^F \\ \dot{\mathbf{u}}_{n+1}^F &= \dot{\mathbf{u}}_n^F + \frac{\Delta t}{2} [\ddot{\mathbf{u}}_{n+1}^F + \ddot{\mathbf{u}}_n^F], \end{aligned} \tag{7.1}$$

with \mathbf{u}^F the displacement vector-field. A superposed dot represents a partial derivative with time, such that $\dot{\mathbf{u}}^F$ is the velocity vector field and $\ddot{\mathbf{u}}^F$ is the acceleration vector field. All these fields are functions of the position $\mathbf{x} = (x, y, z)$ in a three-dimensional Cartesian coordinate system, but we drop the argument for the sake of readability. Δt is the time step, chosen according to the Courant-Friedrichs-Lewy condition [167].

The system is solved with a predictor-corrector approach:

1. Predictor:

$$\begin{aligned} \mathbf{u}_{n+1}^F &= \mathbf{u}_n^F + \Delta t \dot{\mathbf{u}}_n^F + \frac{1}{2} (\Delta t)^2 \ddot{\mathbf{u}}_n^F, \\ \dot{\mathbf{u}}_{n+1}^{P,F} &= \dot{\mathbf{u}}_n^F + \Delta t \ddot{\mathbf{u}}_n^F, \end{aligned} \quad (7.2)$$

2. Solve:

$$\delta \ddot{\mathbf{u}}_{n+1}^F = \underline{\mathbf{M}}^{-1} \left(\mathbf{F}_{n+1}^{ext} - \mathbf{F}_{n+1}^{int} - \underline{\mathbf{M}} \ddot{\mathbf{u}}_n^F \right), \quad (7.3)$$

3. Corrector:

$$\begin{aligned} \ddot{\mathbf{u}}_{n+1}^F &= \ddot{\mathbf{u}}_n^F + \delta \ddot{\mathbf{u}}_{n+1}^F, \\ \dot{\mathbf{u}}_{n+1}^F &= \dot{\mathbf{u}}_{n+1}^{P,F} + \frac{\Delta t}{2} \delta \ddot{\mathbf{u}}_{n+1}^F. \end{aligned} \quad (7.4)$$

The internal forces in Eq. (7.3) are computed as $\mathbf{F}_{n+1}^{int} = \underline{\mathbf{K}} \mathbf{u}_{n+1}^F$. $\underline{\mathbf{K}}$ and $\underline{\mathbf{M}}$ are respectively the stiffness and the mass matrix. Note that there might be additional terms in the residual Eq.(7.3) (for example, if one part of the problem includes an interface modeled with a node-to-node algorithm), but they are relevant only for the part of the finite element mesh that is not directly coupled to the spectral boundary integral method, so we exclude them for simplicity.

7.2.2 Spectral boundary integral method

The scheme used for the spectral boundary integral method [169; 170; 171] is an explicit time stepping algorithm, but is different from the one of the FEM as the acceleration is never computed but rather the velocity at each time step is solved directly. In what follows, the superscript S indicates that the field is related to the spectral boundary integral method:

$$\mathbf{u}_{n+1}^S = \mathbf{u}_n^S + \Delta t \dot{\mathbf{u}}_n^S, \quad (7.5)$$

with the velocity $\dot{\mathbf{u}}_n^S$ given by the stress condition at the interface:

$$\boldsymbol{\tau}_n^S = \boldsymbol{\tau}_n^\infty - \underline{\mathbf{V}} \left(\dot{\mathbf{u}}_n^S - \dot{\mathbf{u}}_0^S \right) + \mathbf{f}_n^S, \quad (7.6)$$

with

$$\underline{\mathbf{V}} = \frac{\mu}{c_s} \begin{bmatrix} 1 & 0 & 0 \\ 0 & \eta & 0 \\ 0 & 0 & 1 \end{bmatrix}, \quad (7.7)$$

and $\eta = c_d/c_s$ the ratio between the dilatational wave speed and the shear wave speed. The last term \mathbf{f}^S is non-local in space and time and represents the spatio-temporal

Chapter 7. Coupling the finite element method and the spectral boundary integral method

interaction of different points on the interface mediated by bulk elastodynamics. It is computed via a convolution integral in the spectral model of the displacement history $\mathbf{u}^S(n, n-1, \dots)$. The kernels used to compute \mathbf{f}^S are given in [171]. For readability, we assume that there is no reference velocity, $\dot{\mathbf{u}}_0^S = (0, 0, 0)$.

7.2.3 Coupling condition

The velocities at the interface between FEM and SBIM have to be equal at every time step. As the two schemes are different (there is no acceleration in the SBIM), the coupling condition writes:

$$\dot{\mathbf{u}}_{n+1}^F + \frac{\Delta t}{2} \ddot{\mathbf{u}}_{n+1}^F = \dot{\mathbf{u}}_{n+1}^S, \quad (7.8)$$

with Eq. (7.8) valid for any nodes on the coupling interface. This condition ensures that the displacements at each time step are also equal at the coupling interface:

$$\mathbf{u}_{n+1}^S = \mathbf{u}_{n+1}^F. \quad (7.9)$$

Using Eq. (7.4), the coupling condition at the step $n+1$ writes:

$$\dot{\mathbf{u}}_{n+1}^{P,F} + \frac{\Delta t}{2} \delta \ddot{\mathbf{u}}_{n+1}^F + \frac{\Delta t}{2} [\ddot{\mathbf{u}}_n^F + \delta \ddot{\mathbf{u}}_{n+1}^F] = \dot{\mathbf{u}}_{n+1}^S, \quad (7.10)$$

and introducing the expression for the predicted velocity $\dot{\mathbf{u}}_{n+1}^{P,F}$ from Eq. (7.2):

$$\dot{\mathbf{u}}_n^F + \frac{3\Delta t}{2} \ddot{\mathbf{u}}_n^F + \Delta t \delta \ddot{\mathbf{u}}_{n+1}^F = \dot{\mathbf{u}}_{n+1}^S. \quad (7.11)$$

Using the expression for the acceleration increment $\delta \ddot{\mathbf{u}}_{n+1}^F$ of Eq. (7.3) gives:

$$\dot{\mathbf{u}}_n^F + \frac{3\Delta t}{2} \ddot{\mathbf{u}}_n^F + \Delta t \left[\underline{\mathbf{M}}^{-1} \left(-\underline{\mathbf{K}} \mathbf{u}_{n+1}^F + \mathbf{F}_{n+1}^{cF} \right) - \ddot{\mathbf{u}}_n^F \right] = \dot{\mathbf{u}}_{n+1}^S, \quad (7.12)$$

with \mathbf{F}_{n+1}^{cF} the coupling forces that will be specified below. The stresses at the surface of the SBIM are given by $\boldsymbol{\tau}_{n+1}^{cS}$, allowing to compute the velocity in the SBIM as:

$$\dot{\mathbf{u}}_{n+1}^S = \underline{\mathbf{V}}^{-1} \left(\boldsymbol{\tau}_{n+1}^\infty + \mathbf{f}_{n+1}^S - \boldsymbol{\tau}_{n+1}^{cS} \right). \quad (7.13)$$

The coupling interface is required to be at equilibrium, i.e., the forces from the FEM should compensate for the forces in the SBIM. This additional condition writes:

$$\mathbf{F}_{n+1}^{cF} = \boldsymbol{\tau}_{n+1}^{cS} \mathbf{A} \mathbf{n}, \quad (7.14)$$

with \mathbf{A} the surface of influence of the nodes at the coupling interface, and \mathbf{n} the vector normal to the surface of the coupling interface.

Combining Eqs. (7.12), (7.13) and (7.14) leads to:

$$\dot{\mathbf{u}}_n^F + \frac{\Delta t}{2} \ddot{\mathbf{u}}_n^F + \Delta t \underline{\mathbf{M}}^{-1} \left(-\underline{\mathbf{K}} \mathbf{u}_{n+1}^F + \mathbf{F}_{n+1}^{\text{cF}} \right) = \underline{\mathbf{V}}^{-1} \left(\boldsymbol{\tau}_{n+1}^\infty + \mathbf{f}_{n+1}^S - \mathbf{F}_{n+1}^{\text{cF}} \mathbf{A}^{-1} \mathbf{n}^{-1} \right). \quad (7.15)$$

The only unknown in Eq. (7.15) is the vector of coupling forces $\mathbf{F}_{n+1}^{\text{cF}}$. One can reorganize Eq. (7.15) and write:

$$\mathbf{F}_{n+1}^{\text{cF}} = \mathbf{H}^{-1} \left[\underline{\mathbf{V}}^{-1} \left(\boldsymbol{\tau}_{n+1}^\infty + \mathbf{f}_{n+1}^S \right) - \dot{\mathbf{u}}_n^F - \frac{\Delta t}{2} \ddot{\mathbf{u}}_n^F + \Delta t \underline{\mathbf{M}}^{-1} \underline{\mathbf{K}} \mathbf{u}_{n+1}^F \right], \quad (7.16)$$

with \mathbf{H} a condensation operator that only depends on the system geometry and material parameters:

$$\mathbf{H} = \Delta t \underline{\mathbf{M}}^{-1} + \underline{\mathbf{V}}^{-1} \mathbf{A}^{-1} \mathbf{n}^{-1}. \quad (7.17)$$

It can be pre-computed (assuming no change in area and density). The term inside square brackets in the right-hand side of Eq. (7.16) only depends on fields at the previous time step (recall that $\ddot{\mathbf{u}}_{n+1}^F$ and $\ddot{\mathbf{u}}_{n+1}^S$ are computed from the fields at the previous time step, see Eqs. (7.2) and (7.5)). One can solve for the coupling forces $\mathbf{F}_{n+1}^{\text{cF}}$ and the corresponding coupling stress for the SBIM, see Eq. (7.14). These forces ensure continuity through the models.

7.2.4 Coupling algorithm

We detail in Table. 7.1 the exact steps followed during the coupling scheme for both the FEM and SBIM parts.

7.3 Validation

7.3.1 Setup and qualitative analysis

To validate the coupling scheme, we simulate the travel of elastic waves through the interface between the two methods. The system under consideration is shown in Fig. 7.2. We consider a body occupying a half-plane $y > 0$ in a two-dimensional Cartesian system. Displacements are imposed on a small part of the free surface $y = 0$ as a function of time, resulting in elastic waves being radiated in the bulk. We test the FEM/SBIM coupling by comparing two systems: one where a large finite element mesh is used such that there is no reflection occurring in the simulation timeframe, and one with a coupled FEM/SBIM where waves propagate through the coupling interface Γ^c . The expected intended behavior is that no waves should be reflected at the coupling interface.

The imposed displacement at the center of the free surface is given by:

$$u_y^d(t) = \begin{cases} \sin\left(\frac{2\pi t}{T}\right) & \text{if } t < T/2 \\ 0 & \text{otherwise.} \end{cases} \quad (7.18)$$

Chapter 7. Coupling the finite element method and the spectral boundary integral method

	FEM	SBIM
Initialization	Init \underline{K} , \underline{M} , $\underline{u}_0^F, \dot{\underline{u}}_0^F, \ddot{\underline{u}}_0^F, \underline{F}_0^F$	Init \underline{V} , $\underline{u}_0^S, \dot{\underline{u}}_0^S, \tau_0^\infty$
	Match nodes on coupling interface, compute \underline{A} , \underline{H}	
1.	$\underline{u}_{n+1}^F = \underline{u}_n^F + \Delta t \dot{\underline{u}}_n^F + (\Delta t)^2 \ddot{\underline{u}}_n^F / 2$ $\dot{\underline{u}}_{n+1}^{P,F} = \dot{\underline{u}}_n^F + \Delta t \ddot{\underline{u}}_n^F$	$\underline{u}_{n+1}^S = \underline{u}_n^S + \Delta t \dot{\underline{u}}_n^S$
2.	$\ddot{\underline{u}}_{n+1}^{P,F} = \left(-\underline{K} \underline{u}_{n+1}^F + \underline{F}^{ext,F}_{n+1} \right) \underline{M}^{-1}$	Compute \underline{f}_{n+1}^S
3.	$\underline{F}_{n+1}^{cF} = \underline{H}^{-1} \left[\underline{V}^{-1} \left(\tau_{n+1}^\infty + \underline{f}_{n+1}^S \right) - \dot{\underline{u}}_n^F - \Delta t \ddot{\underline{u}}_n^F / 2 + \Delta t \underline{M}^{-1} \underline{K} \underline{u}_{n+1}^F \right]$ $\tau_{n+1}^{cS} = \underline{F}_{n+1}^{cF} \underline{A}^{-1} \underline{n}^{-1}$	
4.	$\delta \ddot{\underline{u}}_{n+1}^F = \ddot{\underline{u}}_{n+1}^{P,F} - \ddot{\underline{u}}_n^F + \underline{F}^F \underline{M}^{-1}$ $\dot{\underline{u}}_{n+1}^F = \dot{\underline{u}}_{n+1}^{P,F} + \Delta t \delta \ddot{\underline{u}}_{n+1}^F / 2$ $\ddot{\underline{u}}_{n+1}^F = \ddot{\underline{u}}_n^F + \delta \ddot{\underline{u}}_{n+1}^F$	$\dot{\underline{u}}_{n+1}^S = \left(\tau_{n+1}^\infty + \underline{f}_{n+1}^S - \tau_{n+1}^{cS} \right) \underline{V}^{-1}$

Table 7.1: Algorithm for the coupling between finite element method and spectral boundary integral method.

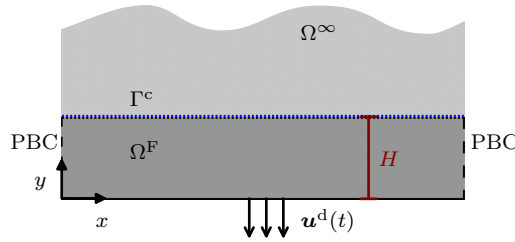


Figure 7.2: System used for the validation of the FEM/SBIM coupling in two dimensions. Dirichlet boundary conditions are imposed on a small part of the free surface at $y = 0$ of a solid laying on the half plane $y > 0$, i.e., a displacement field $\underline{u}^d(t)$. Periodic boundary conditions are enforced on the x direction. Only the body Ω^F of height H is discretized with a finite element mesh, and a coupling interface Γ^c with the semi-infinite body Ω^∞ represented by a spectral boundary integral method interface is achieved using the coupling method presented in the previous section.

The evolution of the displacement fields u_x, u_y is presented in Figs. 7.3, 7.4. In each of these figures, the fields from a reference simulation (from a finite element simulation

with a domain of height $2H$) are shown on the left, with the corresponding fields from a simulation where a coupling interface is located at $y/H = 1$ on the right. Elastic waves are radiated due to the imposed boundary conditions at the free surface, starting at $t = 0$. They reach the coupling interface around $tc_d/H = 1$, which corresponds to the travel time of dilatational waves. At this point, they start interacting with the coupling boundary and thus propagate in the semi-finite elastic, represented by the spectral boundary integral method. There is no apparent reflection from the qualitative results shown in Figs. 7.3, 7.4. The same figures are shown in section 7.6.1 for the velocity fields, which are similar. Subsequently, the same is true for the strain and stress fields, not shown here.

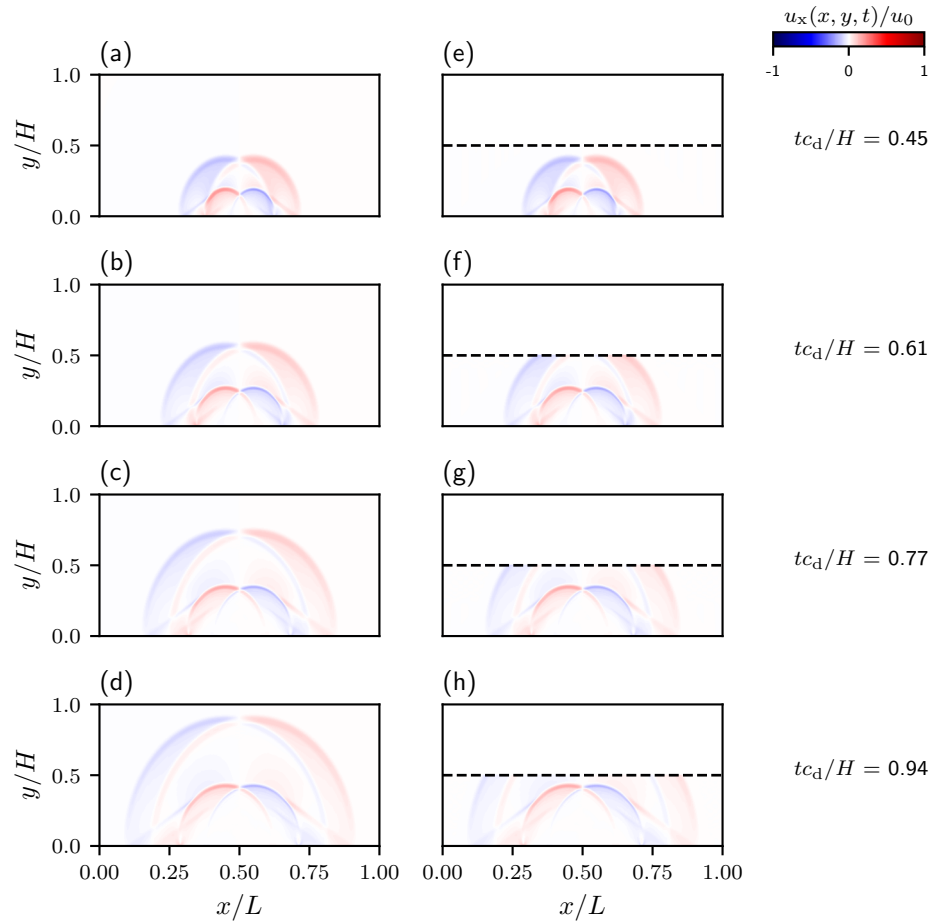


Figure 7.3: Displacement field $u_x(x, y, t)$ for the problem schematized in Fig. 7.2, (a-d) in a simulation where the entire system is modeled with finite elements, (e-g) in a simulation using a coupling interface with an infinite half-body, at $y/H = 0.5$, represented in dashed black lines. Each row corresponds to a given time step. The displacement fields are the same in both systems, without any visible reflections from the boundary with the spectral integral boundary method.

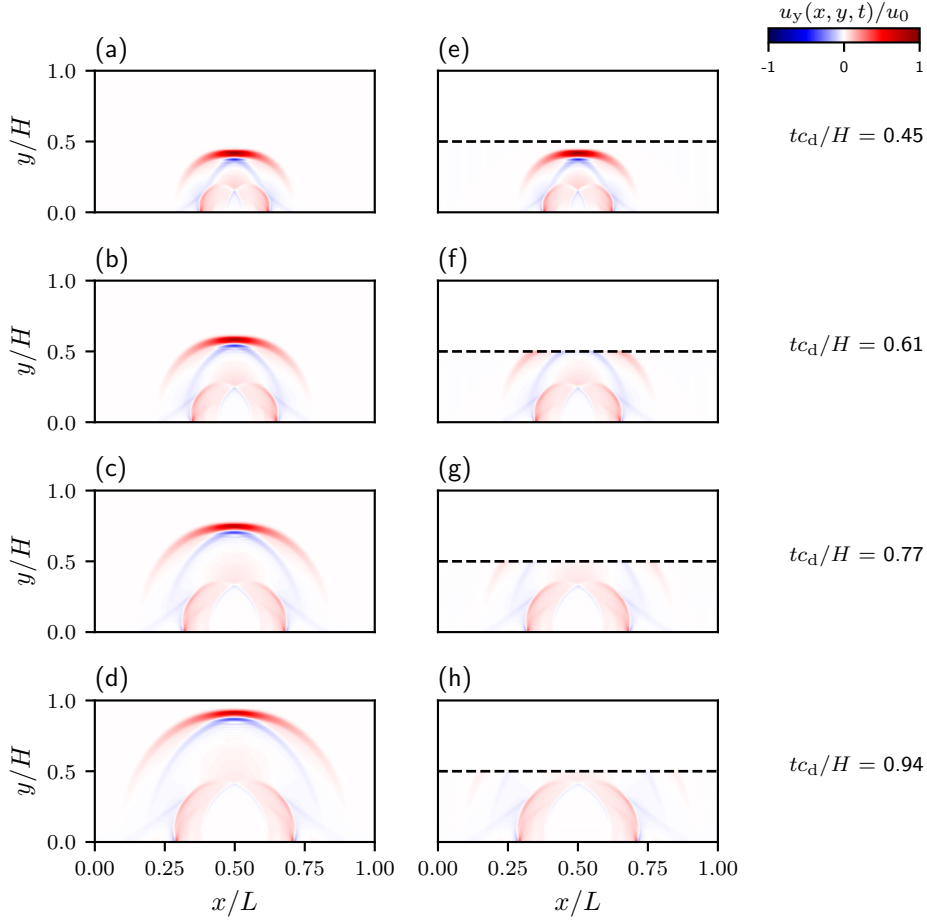


Figure 7.4: Displacement field $u_y(x, y, t)$ for the problem schematized in Fig. 7.2, (a-d) in a simulation where the entire system is modeled with finite elements, (e-g) in a simulation using a coupling interface with an infinite half-body, at $y/H = 0.5$, represented in dashed black lines. Each row corresponds to a given time step. The displacement fields are the same in both systems, without any visible reflections from the boundary with the spectral integral boundary method.

7.3.2 Quantitative analysis of the error

We quantify the error between the reference case and the coupling one by computing the ℓ^2 -norm of each field, defined as:

$$E(\Delta \mathbf{x}) = \sqrt{\sum_{k=1}^n \Delta x_k^2}, \quad (7.19)$$

with $\Delta \mathbf{x}$ the difference between the field from the reference simulation and the simulation done with the coupling. We evaluate the norm over the entire domain that is simulated with finite elements in the coupling algorithm. As we aim at comparing errors

computed based on vectors of different sizes to assess the convergence of the method, we compare the weighted error based on the size of the vector:

$$\overline{E}(\Delta x) = \frac{E(\Delta x)}{\sqrt{n}}, \quad (7.20)$$

with n the size of the vector. Note that this is not an error relative to an analytical solution, but rather a comparison with a reference numerical method. Using the coupling might even improve the error relative to the exact solution: the SBIM is more accurate than FEM as the latter features artificial dispersion. We plot on Figs. 7.5 and 7.11 the evolution of the error as a function of time for respectively the displacement and the velocity fields. The results corresponding to the coupling algorithm presented in this section are shown in solid lines. The dashed lines will be discussed below. Up to $tc_d/H \simeq 1$, there is no error, as the elastic waves have not yet interacted with the coupling interface. Then, when the waves are transmitted through the coupling interface. At this point, the error starts increasing but then eventually stabilizes toward a constant value after the main part of the input signal has been transmitted inside the semi-infinite elastic half-space. The error decreases with the discretization of the interface (n_x is the number of nodes of the coupling interface). With better discretization, the oscillations in the error vanish, illustrating that the coupling scheme is not constantly adding noise to the system.

In Figs. 7.5 and 7.11, the dashed curves correspond to another coupling scheme between FEM and SBIM [271]. This method relies on a staggered Neumann approach. It consists in solving Eq. (7.6) that gives the stresses in the SBIM using the displacements and the velocities that have been computed from the FEM problem and applying these stresses as a Neumann boundary condition to correct for the response of the semi-infinite elastic half-space. The typical scheme is available in [271]. Note that a similar staggered method relying on using Dirichlet boundary conditions has also been proposed [268]. It is expected that the strong coupling presented in this chapter results in a lower error when compared to the staggered scheme, as our formulation ensures that both the velocity and the stress are coupled at each time step. This is indeed the case, with the error being larger for the staggered scheme compared to our coupling, for the same discretization, as can be seen in Figs. 7.5 and 7.11.

The convergence of the coupling algorithm is illustrated in Fig 7.6, showing the maximum error during our test case, alongside a comparison with the Neumann staggered scheme of [271]. Both algorithms seem to have the same convergence rate, but for fine discretization, the strong coupling results in roughly half of the error compared to the staggered scheme. Note that the additional computational costs of solving the strong coupling are small compared to the total cost of the problem. Indeed, the computation of the coupling forces is fully explicit and does not require any iterative scheme. Plus, it is done only over a dimension $N - 1$, where N is the dimension of the finite element problem. The strong coupling is thus a more efficient alternative to the staggered scheme, at a comparable computational cost.

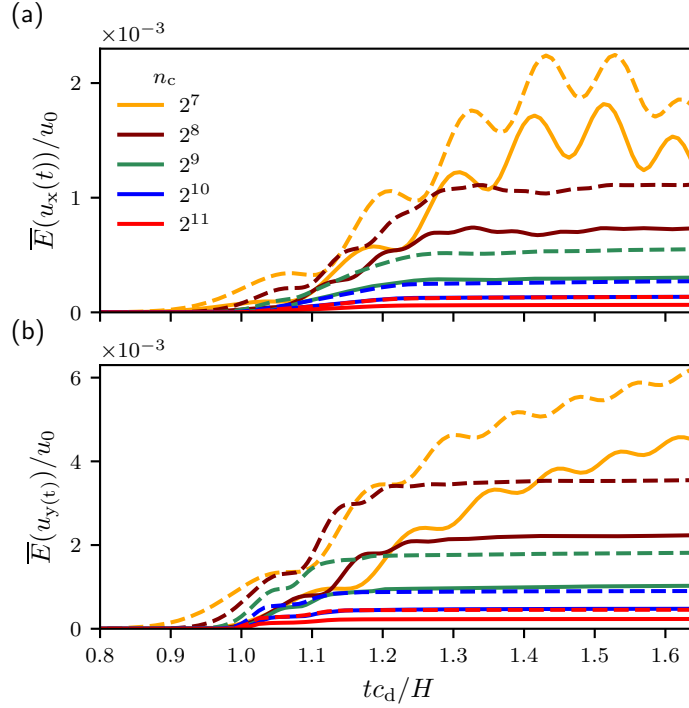


Figure 7.5: Time evolution of the error for (a) u_x and (b) u_y . The solid curves correspond to the coupling presented in this section, for different discretizations, n_c being the number of nodes at the coupling interface. The dashed curves correspond to a staggered coupling scheme as introduced by [271].

7.4 Example: spontaneous propagation of a crack loaded in tension

The previous validation does not feature any dissipation or non-linearity inside the finite element stripe. We present here the basic problem of spontaneous crack propagation in pure mode I. The system is shown in Fig. 7.7. Only a small stripe of the problem is modeled using finite elements Ω^F , and two interfaces with semi-infinite homogeneous elastic continua $\Gamma^{c,+}$ and $\Gamma^{c,-}$ are modeled using the SBIM. This allows for reducing significantly the size of the problem. The crack size a is taken larger than the Griffith crack length (the critical size for stability) L_G such that it starts propagating once the dynamic simulation is initiated. The first step consists in computing the static equilibrium of the body under the far field loads. At this point, the loading is applied as external forces directly on the finite element model. Note that damage is not allowed at this stage. Then, the finite element model is coupled to the two SBIM interfaces and the far field load is moved to the term τ^∞ in the SBIM scheme. To model the propagation of the crack, we use extrinsic cohesive elements [272]. During the simulation, cohesive elements are dynamically inserted in between two bulk elements if the stress

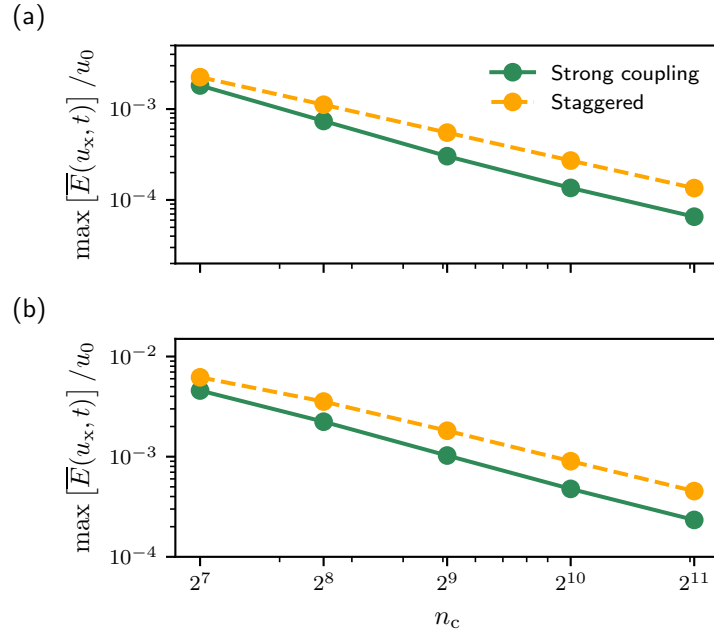


Figure 7.6: Convergence rate of the error of the displacement field for the (a) x component and the (b) y component. The average error is normalized by the amplitude of the input displacement field. The results from the coupling presented in this section are in green, and the errors using a Neumann staggered scheme in orange.

reaches a critical value. The cohesive elements follow a linear cohesive law of the type $\tau = \sigma_c \max(1 - \delta/\delta_c; 0)$ with σ_c and δ_c respectively the maximum stress and the critical opening of the cohesive law. With this approach, the crack path is not prescribed (but still needs to follow the mesh) and the stiffness of the model is not artificially altered by the presence of cohesive elements from the start. The dynamic part of the simulation is solved with the coupling scheme.

The cohesive elements are inserted at the tip of the original crack, on the plane $y = 0$ due to the loading mode. Several snapshots of the velocity field during crack propagation are shown in Fig. 7.8. The elastic waves radiated by the crack are transmitted to the semi-infinite continua without reflection. Some energy is released initially when the simulation transitions from the static equilibrium to inserting cohesive elements in the over-stressed area, resulting in a bit of noise ahead of the rupture front. The mesh near the crack is unstructured, resulting in a crack path that is not perfectly straight. However, due to the location of the stress concentration at the crack tip, the crack path stays around $y/H = 0$.

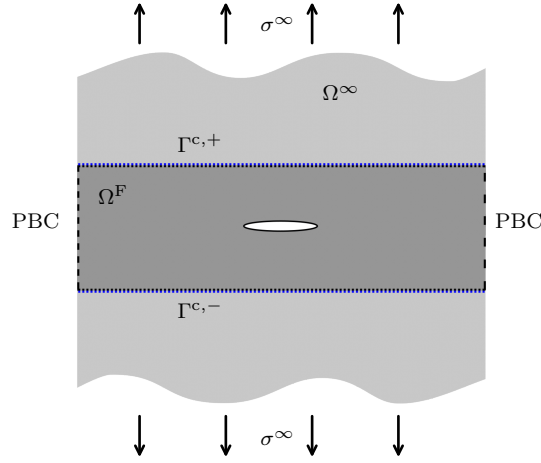


Figure 7.7: A crack of length a is embedded inside an infinite body Ω^∞ and loaded in tension with far field stress σ_∞ .

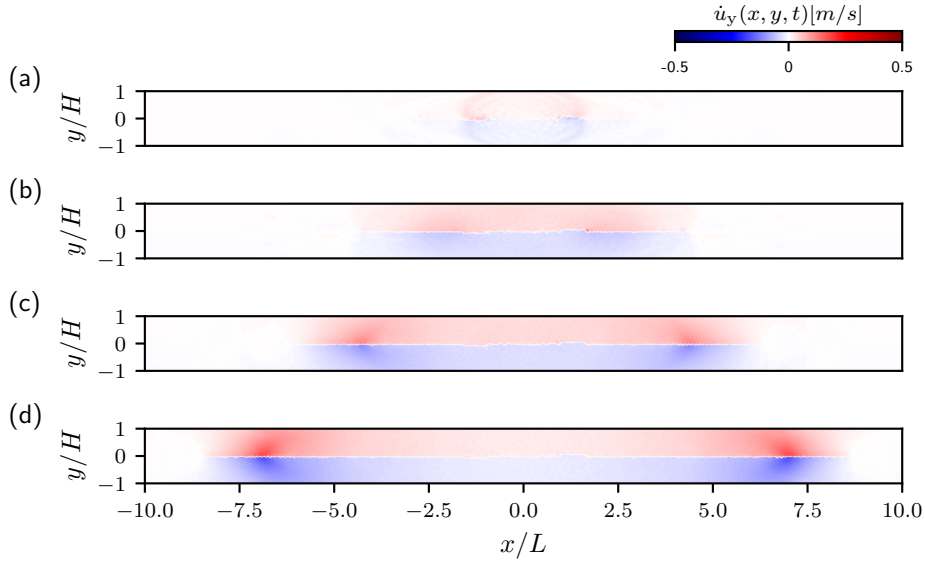


Figure 7.8: Snapshots of the velocity field in the problem presented in Fig. 7.7. Two SBIM interfaces are located at $y/H \pm 1$. The initial crack of length L is centered in $x = 0$ and is on the plane $y = 0$. Cohesive elements are inserted around $y = 0$, note the discontinuity between the velocity fields.

7.5 Conclusion

In this chapter, we proposed a novel coupling scheme between the finite element method and the boundary integral method. The latter is used to simulate infinite boundary

conditions and radiate waves out of the domain of interest that is simulated using the former. This coupling is based on a strict continuity of the velocities at the interface between the methods. We demonstrated the validity of the coupling scheme with a simple problem of wave propagations and highlighted its better accuracy compared to a staggered coupling scheme. The coupling method was used to simulate the spontaneous propagation of a mode I crack using extrinsic cohesive elements. While the examples presented in this chapter are rather simple, this method provides an efficient tool to model dynamic rupture problems in large domains for which the interactions with finite boundaries are not relevant. Studying the occurrence of out-of-plane damage (e.g, microbranches) during fast dynamic rupture or the dynamics of earthquakes nucleation and propagation on complex fault networks are amongst the many potential problems that could be investigated with this new method.

7.6 Supplemental material

7.6.1 Additional results for the reference problem

Here, we show snapshots of the velocity fields Figs. 7.9 and 7.10, alongside the evolution of the error on the velocity in Fig. 7.11 and the convergence rate for the error on the velocity in Fig. 7.12. Note that the error here is normalized by T/u_0 which we define as the characteristic velocity from the loading function given by Eq. (7.18).

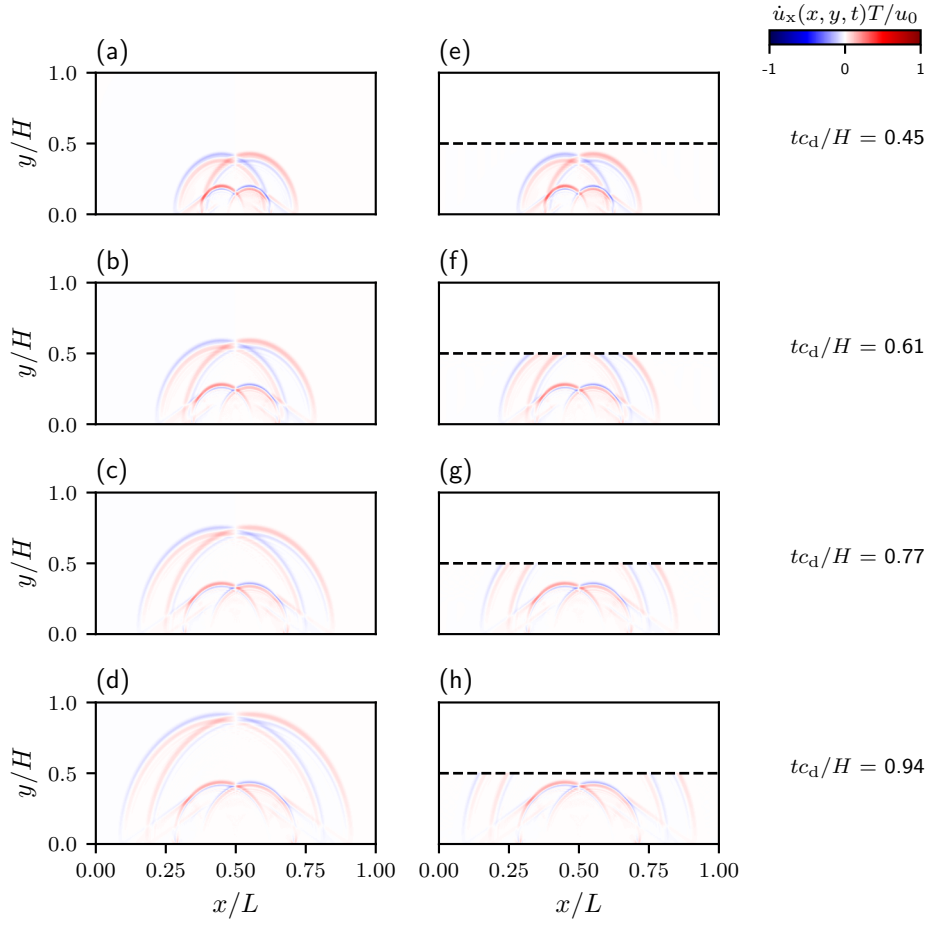


Figure 7.9: Velocity field $\dot{u}_x(x, y, t)$ for the problem schematized in Fig. 7.2(a-d) in a simulation where the entire system is modeled with finite elements, (e-g) in a simulation using a coupling interface with an infinite half-body, at $y/H = 0.5$, represented in dashed black lines. Each row corresponds to a given time step. The velocity fields are the same in both systems, without any visible reflections from the boundary with the spectral integral boundary method at $y/H = 0.5$.

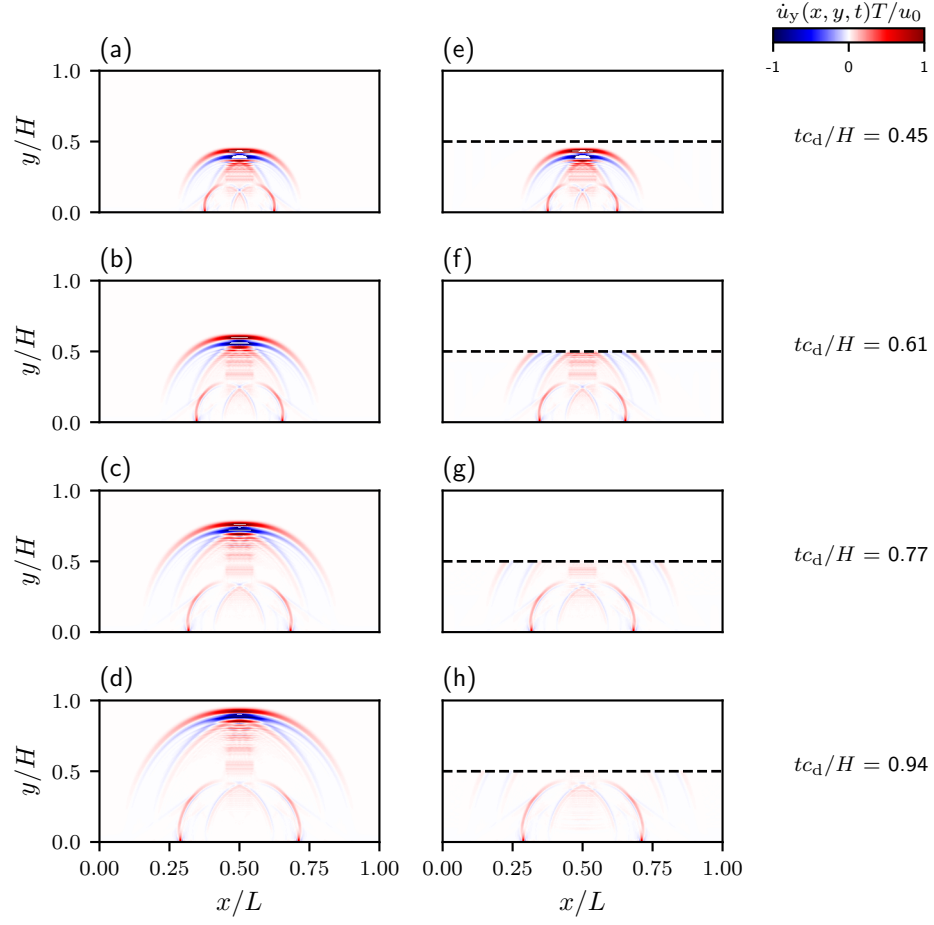


Figure 7.10: Velocity field $\dot{u}_y(x, y, t)$ for the problem schematized in Fig. 7.2, (a-d) in a simulation where the entire system is modeled with finite elements, (e-g) in a simulation using a coupling interface with an infinite half-body, at $y/H = 0.5$, represented in dashed black lines. Each row corresponds to a given time step. The velocity fields are the same in both systems, without any visible reflections from the boundary with the spectral integral boundary method at $y/H = 0.5$.

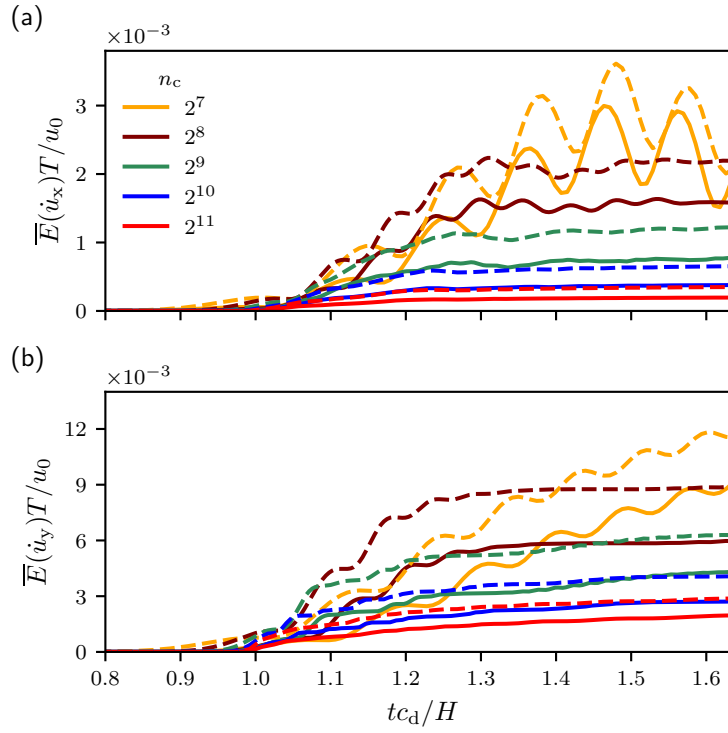


Figure 7.11: Time evolution of the error for (a) \dot{u}_x and (b) \dot{u}_y . The solid curves correspond to the coupling presented in this section, for different discretizations, n_c being the number of nodes at the coupling interface. The dashed curves correspond to a staggered coupling scheme as introduced by [271].

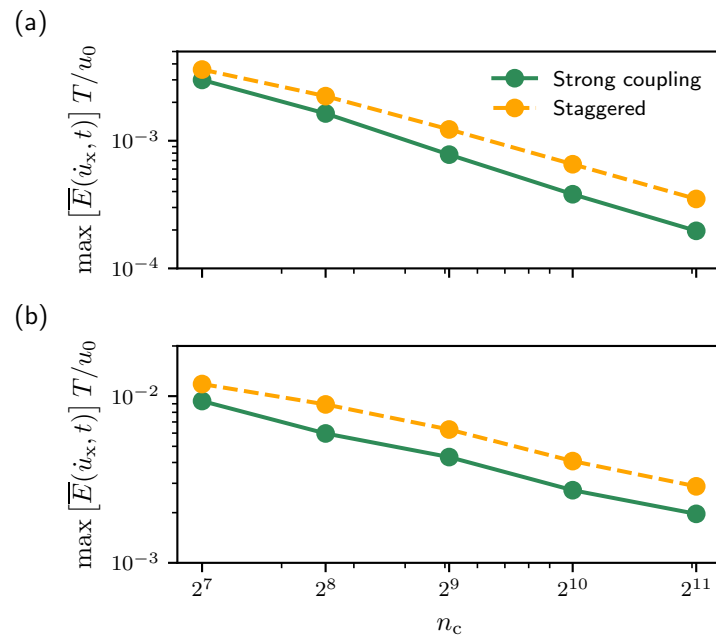


Figure 7.12: Convergence rate of the error of the velocity field for the (a) x component and the (b) y component. The average error is normalized by the ratio of the period over the amplitude of the input displacement field. The results from the coupling presented in this section are in green, and the errors using a Neumann staggered scheme in orange.

8 Conclusion

8.1 Summary

This thesis explored the richness and complexity of dynamic rupture arising from friction and fracture. We investigated the dynamics of planar interfaces lying between homogeneous elastic symmetric bodies. Despite the apparent simplicity of these systems, they host a large variety of behaviors. Among other things, modifying the boundary conditions affect the rupture modes in frictional rupture. The interactions with the disorder also affect the behavior at different levels. In tensile fracture, heterogeneities at the interface deform crack fronts. For frictional interfaces, self-generated heterogeneities related to the evolution and history of the interface give rise to complex slip events of all sizes. We summarize here the main observations and conclusions of this research.

The dynamics of fast-propagating cracks are intrinsically heterogeneous and result from the interactions of the crack fronts with the microstructure. In particular, fronts distort when encountering variations in the fracture toughness field. Therefore, these deformations are reminiscent of the material disorder and can tell us about the effective properties of a heterogeneous material. However, the usual tool used in this context, the *line tension model*, overlooks the influence of the dissipation length scale, called the *process zone size*. This results in treating all asperity scales indifferently. We used a cohesive zone model to introduce this length scale and study tensile cracks interacting with a regular microstructure. The presence of a process zone alters how the crack fronts interact with heterogeneities. In particular, it results in scale effects for front deformations, with a decrease of the front stiffness that increases their amplitude, and a smoothing of the disorder experienced by the crack, which oppositely diminishes them. Depending on the nature of the heterogeneities, these competing effects can lead to either larger or smaller front deformations, stressing the importance of this length scale for heterogeneous rupture. For fast cracks, the contraction of the process zone mitigates these effects. Independently, the dynamic stiffening of the front reduces the overall amplitude of deformations. This study paved the way for a better understanding of the front roughness in disordered materials, impacting the prediction of the effective properties of cohesive composites. It might also help predict the occurrence of out-of-

plane damage subsequently to high in-plane front curvature.

The dynamics of frictional interfaces share similarities with classical tensile fracture, with the propagation of rupture fronts, i.e., the propagation of a discontinuity in a continuous field. However, several important differences exist between fracture and friction. First, the residual stress level behind the rupture front in frictional rupture is, contrary to tensile fracture, not zero, but rather depends on the evolution of the friction coefficient with slip rate. The dynamics of a stress-driven frictional interface obeying a rate and state friction law revealed how the stress drop is selected from the interactions between the interfacial frictional behavior and bulk elastodynamics through the radiation of elastic waves. Once this stress drop is present, the analogy between frictional rupture and classical fracture holds for the presence of the square root singularity near the rupture front, which allowed us to derive an equivalent equation of motion for frictional crack-like rupture. However, this analogy is limited to the time scale before the return of waves, and even during that time, an excess of energy is dissipated in frictional rupture compared to its fracture equivalent. Second, slip pulse is a rupture mode that can emerge in frictional rupture due to the healing mechanism related to the evolution of the real contact area, but is absent from tensile fracture. The conditions under which slip pulses are favored were investigated by studying numerically a velocity-driven frictional system. We showed that under these conditions and the hypothesis of a steady state, a train of pulses emerges as an analog to phase separation in equilibrium thermodynamics, with alternating stick and slip phases propagating at a steady velocity. Coarsening dynamics saturated at the system width preceded the emergence of the pulse train, setting its periodicity, independently of the system height. For small heights, these coarsening dynamics compete with linear elasto-frictional instabilities on top of the pulse train. The properties of a single pulse were intensively studied, as this framework offered a robust way to generate stable pulses, which is not trivial. Despite the fundamental differences between a slip pulse and the classical representation of a crack, the presence of singular fields at its rupture front allows using the analogy with fracture to provide an equivalent pulse equation of motion that relates the pulse width, velocity, and average slip rate. This work offers a rather robust framework to study self-healing slip pulses, which are relevant in many frictional systems.

Friction is an intrinsically complex phenomenon involving physics occurring at various scales, ranging from the micromechanics of the contacting asperities to the long-range stress transfers coupling various parts of an interface together. Despite this complexity, the statistical distributions of slip events in frictional systems are mostly given by power laws, implying scale independence. The emergence of statistical complexity can be related either to the interfacial strongly nonlinear dynamics or to the presence of material disorder. We studied a finite-size velocity-driven frictional system following a generic rate and state friction law that does not feature bulk or frictional heterogeneities. Complexity emerges in these conditions; in the sense of broadly distributed slip event

characteristics. Two main types of events occur: small/mainly non-propagating slip events that follow a power-law distribution and large/rupture-like slip events whose distribution is log-normal. This statistical complexity emerges from self-generated heterogeneity of stress and state (a proxy for the real contact area) at the interface. These heterogeneous conditions are due to the complex interactions between interfacial non-linearity and dissipation, history effects, and elastic waves travel and reflection in the bulk. The statistical complexity is accompanied by dynamical complexity, with intricate spatio-temporal relations between slip events. Wave reflections can dynamically arrest or modify a slip event. The characteristic reflection time scale also affects the statistical distributions of the events. This study illustrated how complexity might emerge in systems that do not feature bulk and frictional heterogeneities.

The last chapter of this thesis is dedicated to overcoming the difficulties in modeling complex dynamic rupture problems. As it usually requires large but finely discretized time and space domains, modeling these problems can be costly. In this thesis, two methods were used: the spectral boundary integral method, which is powerful but limited to interfacial ruptures between two semi-infinite homogeneous elastic solids, and the finite element method, which is versatile and can be used to model complex geometry and include bulk heterogeneities and dissipation but at an increased computational price. Using the spectral boundary integral method to truncate the domain that needs to be discretized by the finite element method is thus a natural solution to improve the efficiency of dynamic rupture modeling for problems in unbounded domains. We presented a coupling algorithm based on a strict continuity of velocities at the coupling interface and demonstrated its validity with some basic examples. This method is an important tool for pushing the study of dynamic rupture toward the third dimension, by including the possibility of out-of-plane damage or complex interface geometry.

8.2 Future perspectives

The numerical studies conducted during this thesis described a variety of behavior in dynamic rupture, both for fracture and friction. The insights gained in both topics open several interesting research directions. Some of these directions are discussed below.

First, understanding the impact of the process zone size in the deformations of crack fronts is a promising step in rationalizing the properties of heterogeneous microstructures. While it has been studied here for a regular microstructure, this analysis can be extended to describe the development of front roughness in disordered materials and characterize the propagation threshold in composite materials. The numerical framework used in this work, i.e., the spectral boundary integral method coupled with a cohesive zone model, could also be applied to studying the intricate dynamics in play in tensile rupture for fast crack propagation. An example is the formation of comet

like-pattern on the fracture surfaces of PMMA specimen [31], in which the propagation of the main crack occurs through the nucleation of multiple micro-cracks. Studying how small defects can be nucleated ahead of a tensile crack is a promising direction for understanding microcracking dynamics. Furthermore, the development of the coupling between the finite element method and spectral boundary integral method allows for studying three-dimensional crack dynamics and the occurrence of out-of-plane damage. With increasing crack velocity, the shape of the stress fields ahead of the crack tip evolves and the maximum hoop stress is deviated out of the crack plane, even for a crack loaded purely in mode I. The interactions between a crack and out-of-plane material heterogeneities might trigger and control the occurrence of dynamic instabilities such as microbranching. Ideally, the phase-field method [164] should be employed, as it is mesh-independent and allows for complex crack geometry and branching.

Despite the apparent simplicity of the systems studied in the context of frictional rupture, i.e., planar homogeneous interface between two symmetric homogeneous elastic bulks, this thesis shed light on the richness and complexity of slip events at friction interfaces. Again, it opens several directions for future investigations. First, conducting rotary velocity-driven friction experiments to test the predictions for the emergence of stable trains of pulses might shed light on their existence and stability in real systems. Then, expanding the numerical and theoretical studies to different frictional behavior might be of interest. In this thesis, we used various rate and state friction laws: one characterized by an N-shape (rate-strengthening at low and large slip velocity, and rate-weakening in between), and a variant without the rate-strengthening behavior at large slip rates. While going beyond the original rate and state formulation that was purely velocity-weakening [6; 7], they do not include the increased weakening mechanism at high slip rates that could be related to flash heating or thermal pressurization of pore fluids. Rate and state law thus might rather be generically M-shaped, with a stronger than logarithmic weakening for fast slip rates. The influence of such constitutive laws on the selection of rupture modes and the behavior of rupture fronts should be investigated. Indeed, the singular fields near the rupture tip of frictional rupture are expected to deviate from the square-root singularity of linear elastic fracture mechanics if the interfacial behavior exhibits strong rate dependency [218; 219], which might have strong implications on their dynamics.

Taking advantage of the coupling method again, one might move from the rather simplified systems that were considered in this thesis toward more realistic geophysical systems. This can be achieved in several ways: by considering geometric asymmetry, bulk heterogeneity, subduction zone geometry and loading, non-planar or branched network of faults, or by allowing for off-fault damage and plasticity, etc... This last point offers endless possibilities to probe the results obtained in simple systems to more complex ones. One interesting point would be to study how the statistical description of slip events is affected when incorporating additional complexity in the system and

comparing it to the minimal case presented in this thesis. This could shed new light on how the various physical ingredients interact and give rise to broad event distributions.

To conclude, this thesis explored the richness and complexity existing in dynamic rupture. In the case of dynamic fracture, this richness arises from the interaction between a dynamic crack and microscopic heterogeneities. In frictional systems, the constitutive behavior itself gives rise to various rupture modes. The complex interactions between the self-generated heterogeneities resulting from the history of the interface, the aging of the microcontacts, and the interactions with the finite geometry and boundary conditions are sufficient for statistical complexity to emerge. This thesis gave an enlightening viewpoint on the variety in dynamic rupture, using efficient numerical methods. The last development with the coupling should offer an efficient tool to progressively complexify the systems of interest, slowly moving towards more realistic engineering and geophysical setups.

A Derivation of the quasi-static cohesive line tension model

We recall here the derivation of the *quasi-static cohesive line tension model* that was derived by Dr. Mathias Lebihain in [10]. This model extended Rice [22] first-order theory by including the effect of cohesive stresses that resist the crack opening and is based on the weight functions associated to a point force located at a given distance from the front (i.e. inside the process zone). We recall here the main steps of the derivation so that we can explain in the Chapter 4 how the *dynamic cohesive line tension model* is derived. The goal is to compute the contribution of the cohesive stress to the stress intensity factor.

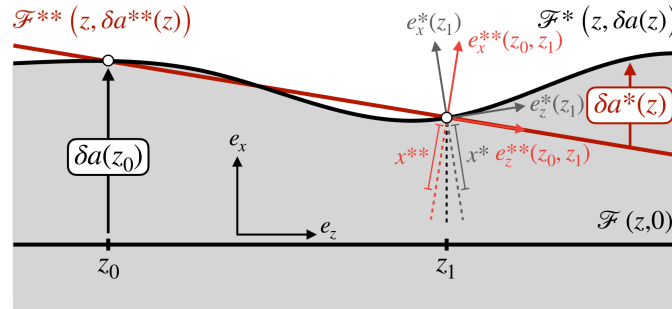


Figure A.1: The mode I stress intensity factor $k(F^*; z_0; z_1, x^*)$ generated at $z = z_0$ by a pair of unitary forces applied along e_y at a distance x^* behind the point z_1 of the perturbed crack front F^* (in black) in the direction of the vector $e_x^*(z_1)$ can be inferred from that generated by a pair of unitary forces applied along e_y at a distance x^{**} behind the point z_1 of the auxiliary front F^{**} (in red) in the direction of the vector $e_x^{**}(z_1)$. Figure taken from [10]

According to Bueckner-Rice's weight function theory [37; 36], the stress intensity factor related to cohesive stress K_{czm} can be expressed as:

$$K_{czm}(z) = \int_{\Gamma^*} k^*(\Gamma^*; z, z', x) \sigma(\mathbf{x}) dz' dx \quad (\text{A.1})$$

where $k^*(\Gamma^*; z, z', x)$ is the mode I crack face weight function (CFWF). It corresponds to the stress intensity factor generated at point z by a pair of unitary tensile forces applied at a point (z', x) located on the faces of Γ^* . The main difficulty consists in computing

Appendix A. Derivation of the quasi-static cohesive line tension model

the expression of this CFWF. Let us start by defining two distinct crack face weight functions:

- $k^*(\mathcal{F}^*; z_0; z_1, x^*)$, which corresponds to the stress intensity factor generated at $z = z_0$ by a pair of unitary forces applied along e_y at a distance x^* behind the point z_1 of the perturbed crack front \mathcal{F}^* in the direction of the vector $e_x^*(z_1)$;
- $k(\mathcal{F}^*; z_0; z_1, x)$, which corresponds to the stress intensity factor generated at $z = z_0$ by a pair of unitary forces applied along e_y at a distance x behind the point z_1 of the perturbed crack front \mathcal{F}^* in the direction e_x .

At first order in the perturbation, one has:

$$k^*(\mathcal{F}^*; z_0; z_1, x^*) = k(\mathcal{F}^*; z_0; z_1, x) \quad (\text{A.2})$$

as the error introduced on the position of the point of application of the forces is of second order in δa [273]. Rice [36] showed that if the crack advance $\delta a(z)$ satisfies the condition:

$$\delta a(z_0) = 0 \text{ and } \delta a(z_1) = 0, \quad (\text{A.3})$$

then $k(\mathcal{F}^*; z_0; z_1, x)$ can be expressed from the CFWF $k(\mathcal{F}; z_0; z_1, x)$ of the reference straight front following:

$$k(\mathcal{F}^*; z_0; z_1, x) = k(\mathcal{F}; z_0; z_1, x) + \frac{1}{2\pi} \int_{-\infty}^{+\infty} k(\mathcal{F}; z; z_1, x) \frac{\delta a(z)}{(z - z_0)^2} dz. \quad (\text{A.4})$$

where $k(\mathcal{F}; z_0; z_1, x)$ is known analytically for the semi-infinite coplanar crack with a straight crack front Γ :

$$k(\mathcal{F}; z_0; z_1, x) = \frac{\sqrt{2}}{\pi^{3/2}} \frac{\sqrt{x}}{(z_0 - z_1)^2 + x^2}. \quad (\text{A.5})$$

The condition given by (A.3) is however not satisfied for an arbitrary perturbation δa . We rely on the ideas of [274] and compute the perturbed CFWF associated to Γ^* based on those a reference crack Γ^{**} that results from a combination of a translation and a rotation δa^{**} making $\delta a^*(z) = \delta a(z) - \delta a^{**}(z)$ vanish in z_0 and z_1 :

$$\delta a^{**}(z) = \delta a(z_0) + \frac{\delta a(z_1) - \delta a(z_0)}{z_1 - z_0}(z - z_0) = \delta a(z_1) + \frac{\delta a(z_1) - \delta a(z_0)}{z_1 - z_0}(z - z_1) \quad (\text{A.6})$$

$(e_z^{**}(z_0, z_1), e_x^{**}(z_0, z_1), e_y)$ denotes the natural basis of vectors associated to the straight crack front \mathcal{F}^{**} of Γ^{**} , and (z^{**}, x^{**}, y) the point coordinates in this basis (see Fig. A.1). One may then define:

- $k^{**}(\Gamma^*; z_0^{**}, z_1^{**}, x^{**})$, which corresponds to the stress intensity factor generated at $z^{**} = z_0^{**}$ by a pair of unitary forces applied along e_y at a distance x^{**} behind the

point z_1^{**} of the perturbed crack front \mathcal{F}^{**} in the direction $e_x^{**}(z_0, z_1)$. Since Γ^{**} is a semi-infinite coplanar crack with a straight crack front, $k^{**}(\Gamma^*; z_0^{**}, z_1^{**}, x^{**})$ reads:

$$k^{**}(\mathcal{F}; z_0^{**}, z_1^{**}, x^{**}) = \frac{\sqrt{2}}{\pi^{3/2}} \frac{\sqrt{x^{**}}}{(z_0^{**} - z_1^{**})^2 + x^{**2}} \quad (\text{A.7})$$

- $k^*(\Gamma^*; z_0^{**}, z_1^{**}, x^{**})$, which corresponds to the stress intensity factor generated at $z^{**} = z_0^{**}$ by a pair of unitary forces applied along e_y at a distance x^{**} behind the point z_1^{**} of the perturbed crack front \mathcal{F}^* in the direction $e_x^{**}(z_0, z_1)$. Applying Eq. (A.4) to Γ^{**} and Γ^* yields:

$$k^{**}(\Gamma^*; z_0^{**}, z_1^{**}, x^{**}) = k^{**}(\Gamma^{**}; z_0^{**}, z_1^{**}, x^{**}) + \frac{1}{2\pi} \text{PV} \int_{-\infty}^{+\infty} k^{**}(\mathcal{F}^{**}; z^{**}; z_1^{**}, x^{**}) \frac{\delta a(z^{**}) - \delta a^{**}(z^{**})}{(z^{**} - z_0^{**})^2} dz^{**} \quad (\text{A.8})$$

Again, the error on the position (z^{**}, x^{**}) with respect to (z, x) is of second order in δa . In the (e_z, e_x, e_y) basis, Eq. (A.8) writes as:

$$k(\Gamma^*; z_0; z_1, x) = \frac{\sqrt{2}}{\pi^{3/2}} \frac{\sqrt{x}}{(z_0 - z_1)^2 + x^2} + \frac{1}{2\pi} \text{PV} \int_{-\infty}^{+\infty} \frac{\sqrt{2}}{\pi^{3/2}} \frac{\sqrt{x}}{(z - z_1)^2 + x^2} \frac{\delta a(z) - \delta a^{**}(z)}{(z - z_0)^2} dz \quad (\text{A.9})$$

Combined with Eq. (A.6), Eq. (A.9) provides a direct way to evaluate Eq. (A.1) numerically. Readers interested in the complete formulation of $k(\Gamma^*; z_0; z_1, x)$ and its derivation are redirected to Eq.(15) of [10] and its Appendix A.

Using Eq. (A.9), it is now possible to compute at first order in δa the stress intensity factor K_{czm} of Eq. (A.1) generated by the cohesive stress acting in the wake of the perturbed crack front \mathcal{F}^* . We take the simplified case of a *translationally invariant* material in the propagation direction (Ox). One can write the cohesive stress as:

$$\sigma(z, x) = \sigma_c(z) f_w(x/\omega(z)) \quad (\text{A.10})$$

where $\sigma_c(z)$ and $\omega(z)$ are the local *strength* and *process zone size* at position z , x is the distance to the crack tip located at $(z, \delta a(z))$, and f_w is a shape function that relates to the nature of weakening.

In the classical line tension approach, perturbation of the crack front δa arises from fluctuation of fracture toughness G_c . With the cohesive description adopted here, the perturbations of the front may be related to spatial variations of strength σ_c and process zone size ω . The latter is related to variations of both strength σ_c and critical crack opening δ_c . We decompose σ_c and ω in uniform contributions σ_c^0 and ω_0 associated to a reference homogeneous material, and spatial fluctuations $\delta\sigma_c$ and $\delta\omega$:

$$\begin{cases} \sigma_c(z) = \sigma_c^0 + \delta\sigma_c(z) \\ \omega(z) = \omega_0 + \delta\omega(z) \end{cases} \quad (\text{A.11})$$

Appendix A. Derivation of the quasi-static cohesive line tension model

where σ_c^0 and ω_0 correspond to the spatial averages of σ_c and ω respectively. We can now insert Eqs. (A.2), (A.9), (A.10), and (A.11) into Eq. (A.1) that gives the cohesive stress intensity factor $K_{\text{czm}}(z)$ acting along the perturbed crack front \mathcal{F}^* . It yields:

$$\begin{aligned} K_{\text{czm}}(z) &= \int_0^{+\infty} \int_{-\infty}^{+\infty} \sigma(z', x) k^*(\Gamma^*; z; z', x) dz' dx \\ &= \int_0^{+\infty} \int_{-\infty}^{+\infty} \sigma_c(z') f_w(x/\omega(z')) [k(\Gamma; z; z', x) + \delta k(\Gamma^*; z; z', x)] dz' dx \end{aligned} \quad (\text{A.12})$$

The cohesive SIF $K_{\text{czm}}(z)$ can be expressed as the sum of a zero-order term K_{czm}^0 , and first-order variations $\delta K_{\text{czm}}(z)$ that relates to the perturbations δa , $\delta \sigma_c$ and $\delta \omega$. Following Irwin's criterion [2], K_{czm}^0 corresponds to the mode I toughness K_{Ic}^0 of the reference material when the crack propagates.

The expression of the first-order variations of cohesive stress intensity factor $\delta \hat{K}_{\text{czm}}(z)$ in the Fourier space is given by (see details in the Appendix B of [10]):

$$\frac{\widehat{\delta K_{\text{czm}}}(k)}{K_{\text{Ic}}^0} = \left(\frac{\hat{\mathcal{A}}(|k|\omega_0)}{\omega_0} - \frac{|k|}{2} \right) \widehat{\delta a}(k) + \hat{\Sigma}(|k|\omega_0) \frac{\widehat{\delta \sigma_c}(k)}{\sigma_c^0} + \hat{\Omega}(|k|\omega_0) \frac{\widehat{\delta \omega}(k)}{2\omega_0} \quad (\text{A.13})$$

with:

$$\begin{cases} \hat{\mathcal{A}}(|k|\omega_0) &= -\frac{1}{C_w} \int_0^{+\infty} \frac{f'_w(u)}{u^{1/2}} (1 - e^{-|k|\omega_0 u}) du \\ \hat{\Sigma}(|k|\omega_0) &= \frac{1}{C_w} \int_0^{+\infty} \frac{f_w(u)}{u^{1/2}} e^{-|k|\omega_0 u} du \\ \hat{\Omega}(|k|\omega_0) &= -\frac{2}{C_w} \int_0^{+\infty} f'_w(u) u^{1/2} e^{-|k|\omega_0 u} du \end{cases} \quad (\text{A.14})$$

We recall here the expression of the perturbed stress intensity factor K_{Iefm} written in Fourier space [177]:

$$\frac{\widehat{\delta K_{\text{Iefm}}}(k)}{K_{\text{I}}^0} = \left(\frac{1}{K_{\text{I}}^0} \frac{\partial K_{\text{I}}^0}{\partial a} - \frac{|k|}{2} \right) \widehat{\delta a}(k) \quad (\text{A.15})$$

Combining Eq. (A.13) and Eq. (A.15), one finds the equation ruling quasi-static crack propagation in heterogeneous cohesive materials:

$$K_{\text{I}}^0 \left[1 + \left(\frac{1}{K_{\text{I}}^0} \frac{\partial K_{\text{I}}^0}{\partial a} - \frac{|k|}{2} \right) \widehat{\delta a}(k) \right] = K_{\text{Ic}}^0 \left[1 + \left(\frac{\hat{\mathcal{A}}(|k|\omega_0)}{\omega_0} - \frac{|k|}{2} \right) \widehat{\delta a}(k) + \hat{\Sigma}(|k|\omega_0) \frac{\widehat{\delta \sigma_c}(k)}{\sigma_c^0} + \hat{\Omega}(|k|\omega_0) \frac{\widehat{\delta \omega}(k)}{2\omega_0} \right] \quad (\text{A.16})$$

At first order in the perturbation, the propagation criterion Eq. (A.16) yields for heterogeneities of strength and process zone size:

$$\widehat{\delta a}(k) = -\omega_0 \frac{\hat{\Sigma}(|k|\omega_0)}{\hat{\mathcal{A}}(|k|\omega_0)} \frac{\widehat{\delta \sigma_c}(k)}{\sigma_c^0} - \omega_0 \frac{\hat{\Omega}(|k|\omega_0)}{\hat{\mathcal{A}}(|k|\omega_0)} \frac{\widehat{\delta \omega}(k)}{2\omega_0} \quad (\text{A.17})$$

B Contribution to open source software

During this thesis, I have been involved in the development and maintenance of several open source Software. The open source philosophy is an integral part of the Computational Solid Mechanics Laboratory mindset at École Polytechnique Fédérale de Lausanne, as a way to guarantee reproducibility in research. I have contributed to the Finite Element library *Akantu* as an active developer and community manager. I also worked on the Spectral Boundary Integral Method library *cRacklet*. During my PhD, we improved the accessibility of the latter by implementing a python interface, documenting the code, and writing tutorials for new users, with the goal of providing an efficient tool for interfacial rupture simulation to the community.

This chapter is an adapted version of the following scientific article that describe the features of *cRacklet*:

T. Roch, F. Barras, P. H. Geubelle, and J.-F. Molinari, “cRacklet: a spectral boundary integral method library for interfacial rupture simulation,” *Journal of Open Source Software*, vol. 7, no. 69, p. 3724, 2022

B.1 Summary

The study of dynamically propagating rupture along interfaces is of prime importance in various fields and system sizes, including tribology (nm to μm), engineering (mm to m) and geophysics (m to km) [224; 47; 48]. Numerical simulations of these phenomena are computationally costly and challenging, as they usually require the coupling of two different spatio-temporal scales. A fine spatial discretization is needed to represent accurately the singular fields associated with the rupture edges. Besides, the problems of interest usually involve a larger length scale along which rupture will propagate, driven by long-range traveling elastic waves. The physical phenomena at play also occur at different timescales, from the slow process of rupture nucleation to the fast propagation of crack front close to the elastic wave speeds. Large and finely discretized spatio-temporal domains are required, which are computationally costly. In addition, the behavior of such interfaces can be highly non-linear, thus increasing the problem complexity. The use of boundary integral methods reduces the dimensionality of the problem. This enables to focus the computational efforts on the fracture plane and allows for a detailed description of the interfacial failure processes.

B.2 Statement of need

cRacklet is a C++ library with a Python interface [275] initiated as a collaboration between the Computational Solid Mechanics Laboratory at EPFL and the Department of Aerospace Engineering of the University of Illinois at Urbana-Champaign. *cRacklet* implements a spectral formulation of the elastodynamics boundary integral relations between the displacements and the corresponding traction stress acting at a planar interface between two homogeneous elastic solids [169; 171]. The formulation implemented is the *independent* one, which considers the top and bottom solids separately [171]. The stresses acting at the interface are related to the history of interfacial displacements via a time convolution evaluated in the Fourier domain. The convolutions are efficiently computed within a shared-memory parallel framework using FFTW3/OpenMP. The prescription of an interfacial behavior allows for solving the continuity of tractions and displacements through the interface. Time integration is achieved using an explicit time-stepping scheme. *cRacklet* is aimed at researchers interested in interfacial dynamics, ranging from nucleation problems to dynamic propagation of rupture fronts. While the spectral boundary integral formulation is a well-established method that has been extensively referenced in the literature [276; 277], we believe that *cRacklet* will be a useful addition to the community by gathering in the same framework various kinds of interfacial problems and constitutive laws, and by offering an easy to handle software thanks to its python interface. *cRacklet* is efficient, accessible (C++ or Python), and suited to study a broad class of problems (fracture and friction). We wish that *cRacklet* will become a link between model developers and users by providing both adaptability and usability.

B.3 Features

1. *cRacklet* is versatile and can be used to study a broad class of problems focused on the behavior of an interface between two semi-infinite solids. The code is particularly suited to study planar dynamic fracture and friction. The interface can be either between two or three-dimensional solids. It can be loaded in any combination of normal traction, in-plane, and out-of-plane shear solicitations. *cRacklet* handles the simulation of interfaces bonded between dissimilar elastic solids. Any stress or material heterogeneity along the fracture plane can be resolved. Several interfacial behaviors are included in the library, such as:
 - Cohesive fracture law [20; 21]: the cohesive strength is a linearly decreasing function of the opening gap. This law can be coupled with a friction law to handle surface interactions in the case of post-failure contact between the solids. Two implementations are available, the classical Coulomb friction law and a regularized one [278].
 - Rate and state dependent friction laws: the frictional resistance is a function of the slip velocity and the history of the interface (the state variable). Several formulations are implemented, including the original ones by [6; 7]. More novel formulations such as rate and state friction with velocity-strengthening behaviors (i.e., N-shaped) are also available, see [86].
2. *cRacklet* is accessible and adaptable. It provides access through both its C++ and Python API to several options to design the various kind of problems mentioned before. *cRacklet* is adaptable due to its object-oriented implementation: it is simple to implement additional behavior for the interface without having to deal with the technical core of the code that handles the computation of the stresses in the Fourier domain. *cRacklet* can also be loaded as an external library to easily interact with other existing computational software. *cRacklet* also has tutorials available on Binder [279] which allows for a quick and easy introduction to its functionality.
3. *cRacklet* is efficient: the Fourier transforms and the convolutions are computed within a shared-memory parallel framework using FFTW3/OpenMP. We illustrate in B.2 the scaling capability of *cRacklet* and compare it to Amdahl's law [280]. The scaling study shows that approximately 85% to 90% of the program is parallelized: this includes the computation of the Fourier transform of the displacements, the convolution, and the invert transform of the stresses back to the real domain.

B.4 Example

The onset of sliding between two rough surfaces in frictional contact is an illustrative example of a multiscale rupture problem. Macroscopic shearing is resisted by the micro-

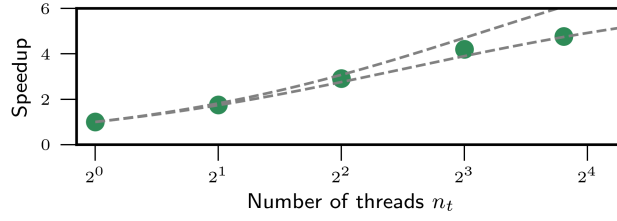


Figure B.1: Time required to solve 10^5 time steps with 2^{12} discretization points, as a function of the number of threads. The code uses *cRacklet* 1.0.0-pre and FFTW 3.3.8, is compiled using GCC [281] and runs on the computational facilities of EPFL, here on a node (2 Intel Broadwell processors running at 2.6 GHz with 14 cores each and 128 GB RAM) of the computing cluster *Fidis*. The dashed gray lines correspond to Amdahl’s law for the theoretical speedup, respectively with 90% (upper bound) and 85% (lower bound) of the program parallelized.

contacts, i.e., by the sparse contacting junctions existing between the asperities of the two surfaces. The successive panels of Fig. B.2 illustrate the nucleation and propagation of a frictional rupture at the interface between two solids, from the individual failure of the microcontacts in panel (b) to the propagation of a macroscopic circular rupture in panel (d). The spatially heterogeneous strength used in this example is a representation of the heterogeneous map of contact between two rough surfaces. In Fig. B.2 (a), the initial configuration of the system is shown. The areas in white are sticking (i.e. no velocity) and correspond to asperities in contact. Colored areas are sliding (blue is for low slip velocity and red for larger ones). The shear load is increased with time in the following panels. The slip velocities increase and previously sticking parts of the interface start sliding (micro-contacts are broken). The inset of Fig. B.2 (b) is a zoomed view of the interface where rupture starts at the asperity scale. In Fig. B.2 (d), frictional cracks have expanded over almost the entire interface.

B.5 Publications

The following publications have been made possible with *cRacklet*:

- F. Barras, D. S. Kammer, P. H. Geubelle, and J.-F. Molinari, “A study of frictional contact in dynamic fracture along bimaterial interfaces,” *International Journal of Fracture*, vol. 189, no. 2, pp. 149–162, 2014
- F. Barras, P. H. Geubelle, and J.-F. Molinari, “Interplay between Process Zone and Material Heterogeneities for Dynamic Cracks,” *Physical Review Letters*, vol. 119, no. 14, p. 144101, 2017
- F. Barras, R. Carpaïj, P. H. Geubelle, and J.-F. Molinari, “Supershear bursts in the propagation of a tensile crack in linear elastic material,” *Physical Review E*, vol. 98, no. 6, p. 063002, 2018

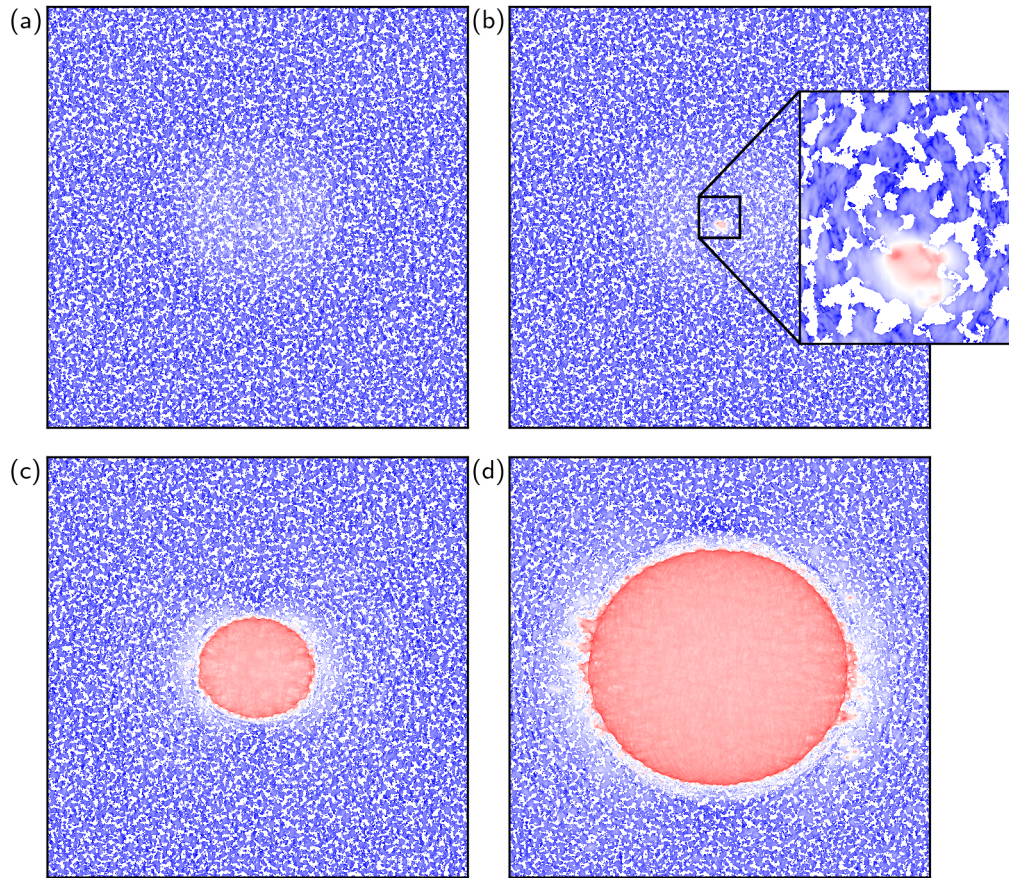


Figure B.2: Snapshot of the slip velocity at the interface between two elastic solids under shear loading. The initial strength is highly heterogeneous. Loading and time have increased between the snapshots, starting from (a) to (d). White areas correspond to sticking conditions (no velocity) while colored ones are sliding. Low velocities are in blue and large ones in red. The code is compiled using [282]. This simulation involves 2^{24} points and was run on one node (with two 16-core Intel E5-2683v4 2.1 GHz and 512 GiB RAM) of the computing cluster *Fram* from the Norwegian e-infrastructure for research and education.

- E. A. Brener, M. Aldam, F. Barras, J.-F. Molinari, and E. Bouchbinder, “Unstable Slip Pulses and Earthquake Nucleation as a Nonequilibrium First-Order Phase Transition,” *Physical Review Letters*, vol. 121, no. 23, p. 234302, 2018
- F. Barras, M. Aldam, T. Roch, E. A. Brener, E. Bouchbinder, and J.-F. Molinari, “Emergence of cracklike behavior of frictional rupture: The origin of stress drops,” *Physical Review X*, vol. 9, p. 041043, 2019
- F. Barras, M. Aldam, T. Roch, E. A. Brener, E. Bouchbinder, and J.-F. Molinari, “The emergence of crack-like behavior of frictional rupture: Edge singularity and energy balance,” *Earth and Planetary Science Letters*, vol. 531, p. 115978, 2020

Appendix B. Contribution to open source software

- F. Fekak, F. Barras, A. Dubois, D. Spielmann, D. Bonamy, P. H. Geubelle, and J. F. Molinari, "Crack front waves: A 3D dynamic response to a local perturbation of tensile and shear cracks," *Journal of the Mechanics and Physics of Solids*, vol. 135, p. 103806, 2020
- R. Rezakhani, F. Barras, M. Brun, and J.-F. Molinari, "Finite element modeling of dynamic frictional rupture with rate and state friction," *Journal of the Mechanics and Physics of Solids*, vol. 141, p. 103967, 2020
- E. A. Brener and E. Bouchbinder, "Unconventional singularities and energy balance in frictional rupture," *Nature Communications*, vol. 12, no. 1, p. 2585, 2021
- M. Lebihain, T. Roch, M. Violay, and J.-F. Molinari, "Earthquake Nucleation Along Faults With Heterogeneous Weakening Rate," *Geophysical Research Letters*, vol. 48, no. 21, p. e2021GL094901, 2021
- T. Roch, E. A. Brener, J.-F. Molinari, and E. Bouchbinder, "Velocity-driven frictional sliding: Coarsening and steady-state pulses," *Journal of the Mechanics and Physics of Solids*, vol. 158, p. 104607, 2022

C Scientific communication and Art

Communicating scientific results and raising interest outside its own scientific community is both a duty, as science is mostly founded on public money, which implies that the public should be aware of the scientific advances, and a challenge, as it involves discussing with a public that is not expert. One way to disseminate scientific question and results is to do it through Art. I participated in the SNSF Scientific Image Competition 2022 contest with the goal of sharing my scientific interests. I submitted the image “Mountains of friction” that is shown in Fig. C.1, and have been awarded a Jury distinction in the category “Object of Study”. This image is the result of a computer simulation of earthquakes, whose apparent complexity is reminiscent of a mountainous landscape. Earthquakes’ dynamics are characterized by anomalous statistical properties, notably fat-tailed power-law distributions. We investigate them by simulating the evolution of a fault for thousands of successive slip events. The shades of blue represent the slip velocity in an abstract map: continuous patches of dark blue correspond to slip events, separated by waiting periods in white. This simulation generates complex statistics, featuring events spread across orders of magnitude in size, duration and waiting times.

Here is the comment of the jury:

“An abstract image quite unlike any other, demonstrating that computer calculations can accidentally produce something beautiful. Aesthetically appealing, but also mysterious, it has the viewer wondering what it is they’re looking at. It is a playful and self-referential image, as plate tectonics lie at the origin of both the earthquakes studied here and of the mountains the picture reminds us of.”

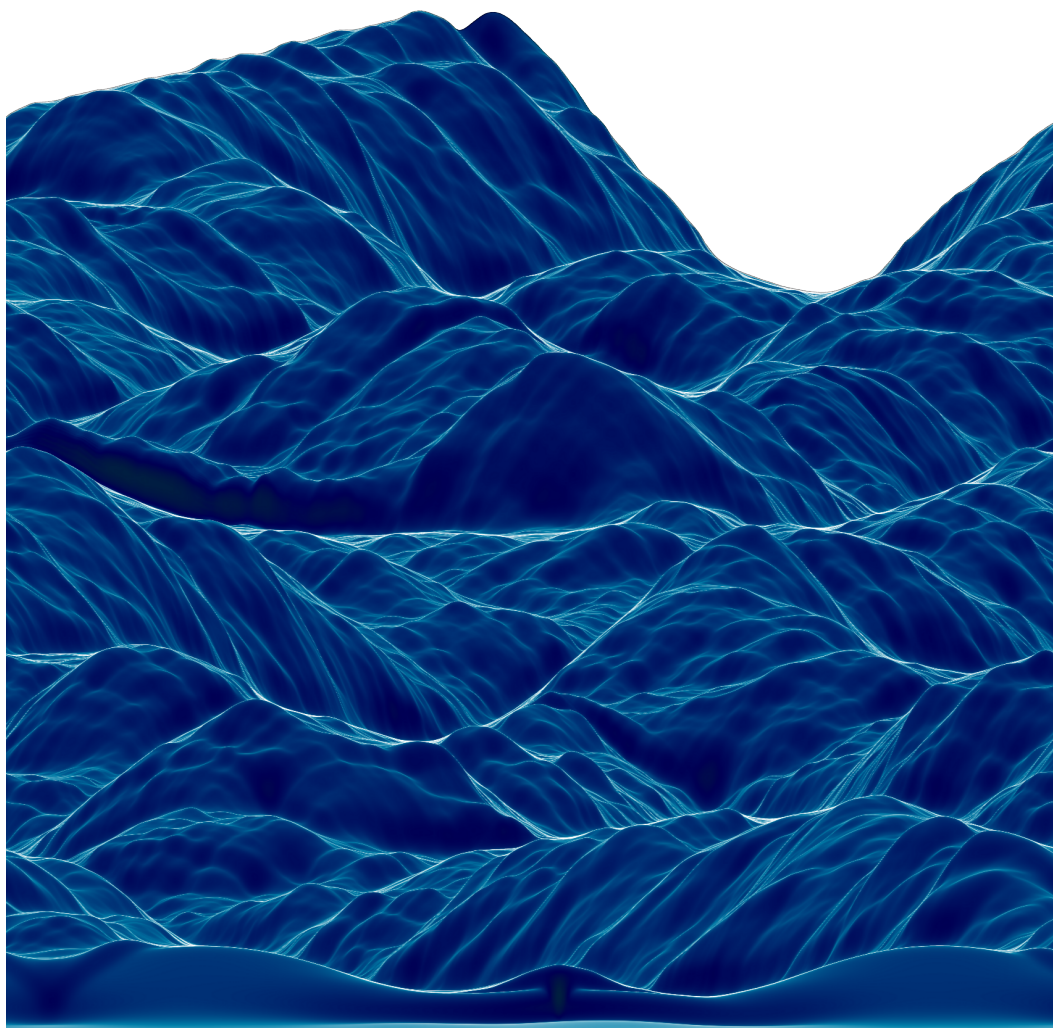


Figure C.1: Mountains of friction.

Bibliography

- [1] A. A. Griffith, "The Phenomena of Rupture and Flow in Solids," *Philosophical Transactions of the Royal Society of London. Series A, Mathematical, Physical and Engineering Sciences*, vol. 221, pp. 163–198, 1921.
- [2] G. R. Irwin, "Analysis of Stresses and Strains Near the End of a Crack Traversing a Plate," *Journal of Applied Mechanics*, vol. 24, pp. 361–364, 1957.
- [3] K. Holmberg and A. Erdemir, "Global impact of friction on energy consumption, economy and environment," *FME Transactions*, vol. 43, no. 3, pp. 181–185, 2015.
- [4] G. Amontons, "De la resistance causée dans les machines," *Mémoires de l'Académie Royale A*, pp. 257–282, 1699.
- [5] C. A. Coulomb, *Théorie des machines simples en ayant égard au frottement de leurs parties et à la roideur des cordages*. Bachelier, 1821.
- [6] J. H. Dieterich, "Modeling of rock friction: 1. Experimental results and constitutive equations," *Journal of Geophysical Research: Solid Earth*, vol. 84, no. B5, pp. 2161–2168, 1979.
- [7] A. L. Ruina, "Slip instability and state variable friction laws," *Journal of Geophysical Research: Solid Earth*, vol. 88, no. B12, pp. 10359–10370, 1983.
- [8] N. Richart and J. F. Molinari, "Implementation of a parallel finite-element library: Test case on a non-local continuum damage model," *Finite Elements in Analysis and Design*, vol. 100, pp. 41–46, 2015.
- [9] T. Roch, F. Barras, P. H. Geubelle, and J.-F. Molinari, "cRacklet: a spectral boundary integral method library for interfacial rupture simulation," *Journal of Open Source Software*, vol. 7, no. 69, p. 3724, 2022.
- [10] M. Lebihain, T. Roch, and J.-F. Molinari, "Quasi-static crack front deformations in cohesive materials," *Journal of the Mechanics and Physics of Solids*, vol. 168, p. 105025, 2022.
- [11] I.-S. Liu, *Continuum Mechanics*. Advanced Texts in Physics, Berlin, Heidelberg: Springer, 2002.

Bibliography

- [12] W. M. Lai, D. Rubin, and E. Krempf, *Introduction to Continuum Mechanics*. Amsterdam ; Boston: Elsevier, 4th edition ed., 2009.
- [13] L. Rayleigh, "On Waves Propagated along the Plane Surface of an Elastic Solid," *Proceedings of the London Mathematical Society*, vol. s1-17, no. 1, pp. 4–11, 1885.
- [14] T. L. Anderson, : *Fundamentals and Applications, Fourth Edition*. Boca Raton: CRC Press, 4 ed., 2017.
- [15] L. B. Freund, *Dynamic Fracture Mechanics*. Cambridge university press, 1998.
- [16] C. E. Inglis, "Stresses in a plate due to the presence of cracks and sharp corners," *Transactions of the institute of naval architects*, vol. 55, no. 219-241, pp. 193–198, 1913.
- [17] H. M. Westergaard, "Bearing pressures and cracks," *Journal of Applied Mechanics*, vol. 6, no. 2, pp. A49–A53, 1939.
- [18] M. L. Williams, "Stress Singularities Resulting From Various Boundary Conditions in Angular Corners of Plates in Extension," *Journal of Applied Mechanics*, vol. 19, pp. 526–528, 1952.
- [19] M. L. Williams, "On the Stress Distribution at the Base of a Stationary Crack," *Journal of Applied Mechanics*, vol. 24, pp. 109–114, 1956.
- [20] D. S. Dugdale, "Yielding of steel sheets containing slits," *Journal of the Mechanics and Physics of Solids*, vol. 8, no. 2, pp. 100–104, 1960.
- [21] G. I. Barenblatt, "The mathematical theory of equilibrium cracks in brittle fracture," in *Advances in Applied Mechanics*, vol. 7, pp. 55–129, Elsevier, 1962.
- [22] J. R. Rice, "The mechanics of earthquake rupture," in *Physics of the Earth's Interior*, pp. 555–649, 1980.
- [23] F. Barras, R. Carpaïj, P. H. Geubelle, and J.-F. Molinari, "Supershear bursts in the propagation of a tensile crack in linear elastic material," *Physical Review E*, vol. 98, no. 6, p. 063002, 2018.
- [24] A. J. Rosakis, "Intersonic shear cracks and fault ruptures," *Advances in Physics*, vol. 51, no. 4, pp. 1189–1257, 2002.
- [25] A. Livne, O. Ben-David, and J. Fineberg, "Oscillations in Rapid Fracture," *Physical Review Letters*, vol. 98, no. 12, p. 124301, 2007.
- [26] K. Ravi-Chandar and W. G. Knauss, "An experimental investigation into dynamic fracture: II. Microstructural aspects," *International Journal of Fracture*, vol. 26, no. 1, pp. 65–80, 1984.

-
- [27] J. Scheibert, C. Guerra, F. Célarié, D. Dalmas, and D. Bonamy, "Brittle-Quasibrittle Transition in Dynamic Fracture: An Energetic Signature," *Physical Review Letters*, vol. 104, no. 4, 2010.
- [28] I. Kolvin, G. Cohen, and J. Fineberg, "Topological defects govern crack front motion and facet formation on broken surfaces," *Nature Materials*, vol. 17, no. 2, pp. 140–144, 2018.
- [29] M. Wang, M. Adda-Bedia, J. M. Kolinski, and J. Fineberg, "How hidden 3D structure within crack fronts reveals energy balance," *Journal of the Mechanics and Physics of Solids*, vol. 161, p. 104795, Apr. 2022.
- [30] E. Sharon, S. P. Gross, and J. Fineberg, "Energy Dissipation in Dynamic Fracture," *Physical Review Letters*, vol. 76, no. 12, pp. 2117–2120, 1996.
- [31] C. Guerra, J. Scheibert, D. Bonamy, and D. Dalmas, "Understanding fast macroscale fracture from microcrack post mortem patterns," *Proceedings of the National Academy of Sciences*, vol. 109, no. 2, pp. 390–394, 2012.
- [32] J. Schmittbuhl and K. J. Maloy, "Direct Observation of a Self-Affine Crack Propagation," *Physical Review Letters*, vol. 78, no. 20, pp. 3888–3891, 1997.
- [33] J. Chopin, A. Prevost, A. Boudaoud, and M. Adda-Bedia, "Crack front dynamics across a single heterogeneity," *Physical Review Letters*, vol. 107, no. 14, p. 144301, 2011.
- [34] V. Lazarus, "Perturbation approaches of a planar crack in linear elastic fracture mechanics: A review," *Journal of the Mechanics and Physics of Solids*, vol. 59, no. 2, pp. 121–144, 2011.
- [35] D. Bonamy and E. Bouchaud, "Failure of heterogeneous materials: A dynamic phase transition?," *Physics Reports*, vol. 498, no. 1, pp. 1–44, 2011.
- [36] J. R. Rice, "Weight function theory for three-dimensional elastic crack analysis," *Fracture Mechanics: Perspectives and Directions (Twentieth Symposium)*, 1989.
- [37] H. Bueckner, "Weight functions and fundamental fields for the penny-shaped and the half-plane crack in three-space," *International Journal of Solids and Structures*, vol. 23, no. 1, pp. 57–93, 1987.
- [38] M. Vasoya, J.-B. Leblond, and L. Ponson, "A geometrically nonlinear analysis of coplanar crack propagation in some heterogeneous medium," *International Journal of Solids and Structures*, vol. 50, no. 2, pp. 371–378, 2013.
- [39] S. Xia, L. Ponson, G. Ravichandran, and K. Bhattacharya, "Toughening and asymmetry in peeling of heterogeneous adhesives," *Physical Review Letters*, vol. 108, no. 19, p. 196101, 2012.

Bibliography

- [40] S. Patinet, D. Vandembroucq, and S. Roux, "Quantitative prediction of effective toughness at random heterogeneous interfaces," *Physical Review Letters*, vol. 110, no. 16, p. 165507, 2013.
- [41] S. M. Xia, L. Ponson, G. Ravichandran, and K. Bhattacharya, "Adhesion of heterogeneous thin films - ii: Adhesive heterogeneity," *Journal of the Mechanics and Physics of Solids*, vol. 83, pp. 88–103, 2015.
- [42] M. Lebihain, "Towards brittle materials with tailored fracture properties: the decisive influence of the material disorder and its microstructure," *International Journal of Fracture.*, vol. 230, no. 1, pp. 99–114, 2021.
- [43] J. Barés, A. Dubois, L. Hattali, D. Dalmas, and D. Bonamy, "Aftershock sequences and seismic-like organization of acoustic events produced by a single propagating crack," *Nature Communications*, vol. 9, no. 1, p. 1253, 2018.
- [44] J. R. Willis and A. B. Movchan, "Dynamic weight functions for a moving crack. i. mode i loading," *Journal of the Mechanics and Physics of Solids*, vol. 43, no. 3, pp. 319–341, 1995.
- [45] A. B. Movchan and J. R. Willis, "Dynamic weight functions for a moving crack. II. Shear loading," *Journal of the Mechanics and Physics of Solids*, vol. 43, no. 9, pp. 1369–1383, 1995.
- [46] F. Barras, D. S. Kammer, P. H. Geubelle, and J.-F. Molinari, "A study of frictional contact in dynamic fracture along bimaterial interfaces," *International Journal of Fracture*, vol. 189, no. 2, pp. 149–162, 2014.
- [47] Y. Ben-Zion, "Collective behavior of earthquakes and faults: Continuum-discrete transitions, progressive evolutionary changes, and different dynamic regimes," *Reviews of Geophysics*, vol. 46, no. 4, p. RG4006, 2008.
- [48] B. Armstrong-Hélouvry, P. Dupont, and C. C. De Wit, "A survey of models, analysis tools and compensation methods for the control of machines with friction," *Automatica*, vol. 30, no. 7, pp. 1083–1138, 1994.
- [49] D. Dowson, *History of tribology*. Addison-Wesley Longman Limited, 1978.
- [50] I. M. Hutchings, "Leonardo da Vincis studies of friction," *Wear*, vol. 360-361, pp. 51–66, 2016.
- [51] F. P. Bowden and D. Tabor, *The Friction and Lubrication of Solids*. Clarendon Press, 2001.
- [52] J. H. Dieterich and B. D. Kilgore, "Direct observation of frictional contacts: New insights for state-dependent properties," *Pure and Applied Geophysics*, vol. 143, no. 1, pp. 283–302, 1994.

-
- [53] T. Baumberger and C. Caroli, "Solid friction from stick-slip down to pinning and aging," *Advances in Physics*, vol. 55, no. 3-4, pp. 279–348, 2006.
- [54] V. L. Popov, *Contact mechanics and friction*. Springer, 2010.
- [55] F. P. Bowden, D. Tabor, and G. I. Taylor, "The area of contact between stationary and moving surfaces," *Proceedings of the Royal Society of London. Series A. Mathematical and Physical Sciences*, vol. 169, no. 938, pp. 391–413, 1939.
- [56] S. M. Rubinstein, G. Cohen, and J. Fineberg, "Detachment fronts and the onset of dynamic friction," *Nature*, vol. 430, no. 7003, pp. 1005–1009, 2004.
- [57] J. D. Byerlee, "Theory of Friction Based on Brittle Fracture," *Journal of Applied Physics*, vol. 38, no. 7, pp. 2928–2934, 1967.
- [58] R. Aghababaei, D. H. Warner, and J.-F. Molinari, "Critical length scale controls adhesive wear mechanisms," *Nature Communications*, vol. 7, no. 1, p. 11816, 2016.
- [59] R. Aghababaei, D. H. Warner, and J.-F. Molinari, "On the debris-level origins of adhesive wear," *Proceedings of the National Academy of Sciences*, vol. 114, no. 30, pp. 7935–7940, 2017.
- [60] Y. Ida, "Cohesive force across the tip of a longitudinal-shear crack and Griffith's specific surface energy," *Journal of Geophysical Research*, vol. 77, no. 20, pp. 3796–3805, 1972.
- [61] D. J. Andrews, "Rupture propagation with finite stress in antiplane strain," *Journal of Geophysical Research*, vol. 81, no. 20, pp. 3575–3582, 1976.
- [62] D. J. Andrews, "Rupture velocity of plane strain shear cracks," *Journal of Geophysical Research*, vol. 81, no. 32, pp. 5679–5687, 1976.
- [63] A. C. Palmer, J. R. Rice, and R. Hill, "The growth of slip surfaces in the progressive failure of over-consolidated clay," *Proceedings of the Royal Society of London. A. Mathematical and Physical Sciences*, vol. 332, no. 1591, pp. 527–548, 1973.
- [64] E. Rabinowicz, "The Nature of the Static and Kinetic Coefficients of Friction," *Journal of Applied Physics*, vol. 22, no. 11, pp. 1373–1379, 1951.
- [65] J. H. Dieterich, "Time-dependent friction as a possible mechanism for aftershocks," *Journal of Geophysical Research*, vol. 77, no. 20, pp. 3771–3781, 1972.
- [66] N. M. Beeler, T. E. Tullis, and J. D. Weeks, "The roles of time and displacement in the evolution effect in rock friction," *Geophysical Research Letters*, vol. 21, no. 18, pp. 1987–1990, 1994.
- [67] J. H. Dieterich, "Time-dependent friction and the mechanics of stick-slip," *Pure and Applied Geophysics*, vol. 116, no. 4, pp. 790–806, 1978.

Bibliography

- [68] C. H. Scholz and J. T. Engelder, "The role of asperity indentation and ploughing in rock friction — I: Asperity creep and stick-slip," *International Journal of Rock Mechanics and Mining Sciences & Geomechanics Abstracts*, vol. 13, no. 5, pp. 149–154, 1976.
- [69] T. E. Tullis and J. D. Weeks, "Constitutive behavior and stability of frictional sliding of granite," *Pure and Applied Geophysics*, vol. 124, no. 3, pp. 383–414, 1986.
- [70] B. D. Kilgore, M. L. Blanpied, and J. H. Dieterich, "Velocity dependent friction of granite over a wide range of conditions," *Geophysical Research Letters*, vol. 20, no. 10, pp. 903–906, 1993.
- [71] C. Marone, "Laboratory-derived friction laws and their application to seismic faulting," *Annual Review of Earth and Planetary Sciences*, vol. 26, no. 1, pp. 643–696, 1998.
- [72] M. L. Blanpied, D. A. Lockner, and J. D. Byerlee, "Fault stability inferred from granite sliding experiments at hydrothermal conditions," *Geophysical Research Letters*, vol. 18, no. 4, pp. 609–612, 1991.
- [73] R. M. Stesky, W. F. Brace, D. K. Riley, and P. Y. F. Robin, "Friction in faulted rock at high temperature and pressure," *Tectonophysics*, vol. 23, no. 1, pp. 177–203, 1974.
- [74] J. R. Rice and A. L. Ruina, "Stability of Steady Frictional Slipping," *Journal of Applied Mechanics*, vol. 50, no. 2, pp. 343–349, 1983.
- [75] N. Lapusta, J. R. Rice, Y. Ben-Zion, and G. Zheng, "Elastodynamic analysis for slow tectonic loading with spontaneous rupture episodes on faults with rate- and state-dependent friction," *Journal of Geophysical Research: Solid Earth*, vol. 105, no. B10, pp. 23765–23789, 2000.
- [76] P. Bhattacharya and A. M. Rubin, "Frictional response to velocity steps and 1-D fault nucleation under a state evolution law with stressing-rate dependence," *Journal of Geophysical Research: Solid Earth*, vol. 119, no. 3, pp. 2272–2304, 2014.
- [77] J. R. Rice, "Spatio-temporal complexity of slip on a fault," *Journal of Geophysical Research: Solid Earth*, vol. 98, no. B6, pp. 9885–9907, 1993.
- [78] M. Aldam, M. Weikamp, R. Spatschek, E. A. Brener, and E. Bouchbinder, "Critical Nucleation Length for Accelerating Frictional Slip," *Geophysical Research Letters*, vol. 44, no. 22, pp. 11,390–11,398, 2017.
- [79] Y. Bar-Sinai, M. Aldam, R. Spatschek, E. A. Brener, and E. Bouchbinder, "Spatiotemporal Dynamics of Frictional Systems: The Interplay of Interfacial Friction and Bulk Elasticity," *Lubricants*, vol. 7, no. 10, p. 91, 2019.

-
- [80] A. M. Rubin and J.-P. Ampuero, "Earthquake nucleation on (aging) rate and state faults," *Journal of Geophysical Research: Solid Earth*, vol. 110, no. B11, p. B11312, 2005.
- [81] C. H. Scholz, "Earthquakes and friction laws," *Nature*, vol. 391, no. 6662, pp. 37–42, 1998.
- [82] A. Bizzarri and M. Cocco, "Slip-weakening behavior during the propagation of dynamic ruptures obeying rate- and state-dependent friction laws," *Journal of Geophysical Research: Solid Earth*, vol. 108, no. B8, p. 2373, 2003.
- [83] J.-P. Ampuero and A. M. Rubin, "Earthquake nucleation on rate and state faults – Aging and slip laws," *Journal of Geophysical Research: Solid Earth*, vol. 113, no. B1, p. B01302, 2008.
- [84] Y. Kaneko and N. Lapusta, "Variability of earthquake nucleation in continuum models of rate-and-state faults and implications for aftershock rates," *Journal of Geophysical Research: Solid Earth*, vol. 113, no. B12, p. B12312, 2008.
- [85] Y. Estrin and Y. Bréchet, "On a model of frictional sliding," *Pure and Applied Geophysics*, vol. 147, no. 4, pp. 745–762, 1996.
- [86] Y. Bar-Sinai, R. Spatschek, E. A. Brener, and E. Bouchbinder, "On the velocity-strengthening behavior of dry friction," *Journal of Geophysical Research: Solid Earth*, vol. 119, no. 3, pp. 1738–1748, 2014.
- [87] A. R. Niemeijer and C. J. Spiers, "Velocity dependence of strength and healing behaviour in simulated phyllosilicate-bearing fault gouge," *Tectonophysics*, vol. 427, no. 1, pp. 231–253, 2006.
- [88] M. Takahashi, M. P. A. van den Ende, A. R. Niemeijer, and C. J. Spiers, "Shear localization in a mature mylonitic rock analog during fast slip," *Geochemistry, Geophysics, Geosystems*, vol. 18, no. 2, pp. 513–530, 2017.
- [89] L. Buijze, A. R. Niemeijer, R. Han, T. Shimamoto, and C. J. Spiers, "Friction properties and deformation mechanisms of halite(-mica) gouges from low to high sliding velocities," *Earth and Planetary Science Letters*, vol. 458, pp. 107–119, 2017.
- [90] H. Perfettini and A. Molinari, "A micromechanical model of rate and state friction: 1. Static and dynamic sliding," *Journal of Geophysical Research: Solid Earth*, vol. 122, no. 4, pp. 2590–2637, 2017.
- [91] A. Molinari and H. Perfettini, "A micromechanical model of rate and state friction: 2. Effect of shear and normal stress changes," *Journal of Geophysical Research: Solid Earth*, vol. 122, no. 4, pp. 2638–2652, 2017.

Bibliography

- [92] G. Di Toro, T. Hirose, S. Nielsen, G. Pennacchioni, and T. Shimamoto, "Natural and Experimental Evidence of Melt Lubrication of Faults During Earthquakes," *Science*, vol. 311, no. 5761, pp. 647–649, 2006.
- [93] G. Sutter and N. Ranc, "Flash temperature measurement during dry friction process at high sliding speed," *Wear*, vol. 268, no. 11-12, pp. 1237–1242, 2010.
- [94] D. L. Goldsby and T. E. Tullis, "Flash Heating Leads to Low Frictional Strength of Crustal Rocks at Earthquake Slip Rates," *Science*, vol. 334, no. 6053, pp. 216–218, 2011.
- [95] J. R. Rice, "Heating and weakening of faults during earthquake slip," *Journal of Geophysical Research: Solid Earth*, vol. 111, no. B5, 2006.
- [96] J. R. Rice, "Heating, weakening and shear localization in earthquake rupture," *Philosophical Transactions of the Royal Society A: Mathematical, Physical and Engineering Sciences*, vol. 375, no. 2103, p. 20160015, 2017.
- [97] A. Molinari, Y. Estrin, and S. Mercier, "Dependence of the Coefficient of Friction on the Sliding Conditions in the High Velocity Range," *Journal of Tribology*, vol. 121, no. 1, pp. 35–41, 1999.
- [98] R. H. Sibson, "Thickness of the Seismic Slip Zone," *Bulletin of the Seismological Society of America*, vol. 93, no. 3, pp. 1169–1178, 2003.
- [99] A. Bizzarri and M. Cocco, "A thermal pressurization model for the spontaneous dynamic rupture propagation on a three-dimensional fault: 1. Methodological approach," *Journal of Geophysical Research: Solid Earth*, vol. 111, no. B5, 2006.
- [100] A. Bizzarri and M. Cocco, "A thermal pressurization model for the spontaneous dynamic rupture propagation on a three-dimensional fault: 2. Traction evolution and dynamic parameters," *Journal of Geophysical Research: Solid Earth*, vol. 111, no. B5, 2006.
- [101] J. Sulem and V. Famin, "Thermal decomposition of carbonates in fault zones: Slip-weakening and temperature-limiting effects," *Journal of Geophysical Research: Solid Earth*, vol. 114, no. B3, 2009.
- [102] S. Aretusini, A. Núñez-Cascajero, E. Spagnuolo, A. Tapetado, C. Vázquez, and G. Di Toro, "Fast and Localized Temperature Measurements During Simulated Earthquakes in Carbonate Rocks," *Geophysical Research Letters*, vol. 48, no. 9, p. e2020GL091856, 2021.
- [103] B. Lecampion and J. Desroches, "Simultaneous initiation and growth of multiple radial hydraulic fractures from a horizontal wellbore," *Journal of the Mechanics and Physics of Solids*, vol. 82, pp. 235–258, Sept. 2015.

-
- [104] B. Lecampion, J. Desroches, R. G. Jeffrey, and A. P. Bunger, "Experiments versus theory for the initiation and propagation of radial hydraulic fractures in low-permeability materials," *Journal of Geophysical Research: Solid Earth*, vol. 122, no. 2, pp. 1239–1263, 2017.
- [105] T. H. Heaton, "Evidence for and implications of self-healing pulses of slip in earthquake rupture," *Physics of the Earth and Planetary Interiors*, vol. 64, no. 1, pp. 1–20, 1990.
- [106] D. Melgar and G. P. Hayes, "Systematic Observations of the Slip Pulse Properties of Large Earthquake Ruptures," *Geophysical Research Letters*, vol. 44, no. 19, pp. 9691–9698, 2017.
- [107] P. Somerville, K. Irikura, R. Graves, S. Sawada, D. Wald, N. Abrahamson, Y. Iwasaki, T. Kagawa, N. Smith, and A. Kowada, "Characterizing Crustal Earthquake Slip Models for the Prediction of Strong Ground Motion," *Seismological Research Letters*, vol. 70, no. 1, pp. 59–80, 1999.
- [108] D. Coker, G. Lykotrafitis, A. Needleman, and A. J. Rosakis, "Frictional sliding modes along an interface between identical elastic plates subject to shear impact loading," *Journal of the Mechanics and Physics of Solids*, vol. 53, no. 4, pp. 884–922, 2005.
- [109] X. Lu, N. Lapusta, and A. J. Rosakis, "Pulse-like and crack-like ruptures in experiments mimicking crustal earthquakes," *Proceedings of the National Academy of Sciences*, vol. 104, no. 48, pp. 18931–18936, 2007.
- [110] S. Nielsen, J. Taddeucci, and S. Vinciguerra, "Experimental observation of stick-slip instability fronts," *Geophysical Journal International*, vol. 180, no. 2, pp. 697–702, 2010.
- [111] G. C. McLaskey, B. D. Kilgore, and N. M. Beeler, "Slip-pulse rupture behavior on a 2 m granite fault," *Geophysical Research Letters*, vol. 42, no. 17, pp. 7039–7045, 2015.
- [112] H. Shlomaï and J. Fineberg, "The structure of slip-pulses and supershear ruptures driving slip in bimaterial friction," *Nature Communications*, vol. 7, p. 11787, 2016.
- [113] A. Cochard and R. Madariaga, "Complexity of seismicity due to highly rate-dependent friction," *Journal of Geophysical Research: Solid Earth*, vol. 101, no. B11, pp. 25321–25336, 1996.
- [114] N. M. Beeler and T. E. Tullis, "Self-healing slip pulses in dynamic rupture models due to velocity-dependent strength," *Bulletin of the Seismological Society of America*, vol. 86, no. 4, pp. 1130–1148, 1996.
- [115] A. Cochard and J. R. Rice, "Fault rupture between dissimilar materials: Ill-posedness, regularization, and slip-pulse response," *Journal of Geophysical Research: Solid Earth*, vol. 105, no. B11, pp. 25891–25907, 2000.

Bibliography

- [116] S. B. Nielsen, J. M. Carlson, and K. B. Olsen, "Influence of friction and fault geometry on earthquake rupture," *Journal of Geophysical Research: Solid Earth*, vol. 105, no. B3, pp. 6069–6088, 2000.
- [117] A. M. Rubin and J.-P. Ampuero, "Self-similar slip pulses during rate-and-state earthquake nucleation," *Journal of Geophysical Research: Solid Earth*, vol. 114, no. B11, p. B11305, 2009.
- [118] E. R. Heimsisson, E. M. Dunham, and M. Almquist, "Poroelastic effects destabilize mildly rate-strengthening friction to generate stable slow slip pulses," *Journal of the Mechanics and Physics of Solids*, vol. 130, pp. 262–279, 2019.
- [119] E. Ringoot, T. Roch, J.-F. Molinari, T. J. Massart, and T. Cohen, "Stick-slip phenomena and Schallamach waves captured using reversible cohesive elements," *Journal of the Mechanics and Physics of Solids*, vol. 155, p. 104528, Oct. 2021.
- [120] A.-A. Gabriel, J.-P. Ampuero, L. A. Dalguer, and P. M. Mai, "The transition of dynamic rupture styles in elastic media under velocity-weakening friction," *Journal of Geophysical Research: Solid Earth*, vol. 117, no. B9, p. B09311, 2012.
- [121] E. A. Brener, M. Aldam, F. Barras, J.-F. Molinari, and E. Bouchbinder, "Unstable Slip Pulses and Earthquake Nucleation as a Nonequilibrium First-Order Phase Transition," *Physical Review Letters*, vol. 121, no. 23, p. 234302, 2018.
- [122] G. Perrin, J. R. Rice, and G. Zheng, "Self-healing slip pulse on a frictional surface," *Journal of the Mechanics and Physics of Solids*, vol. 43, no. 9, pp. 1461–1495, 1995.
- [123] G. Zheng and J. R. Rice, "Conditions under which velocity-weakening friction allows a self-healing versus a cracklike mode of rupture," *Bulletin of the Seismological Society of America*, vol. 88, no. 6, pp. 1466–1483, 1998.
- [124] E. A. Brener, S. V. Malinin, and V. I. Marchenko, "Fracture and friction: Stick-slip motion," *European Physical Journal E*, vol. 17, no. 1, pp. 101–113, 2005.
- [125] O. Ben-David, G. Cohen, and J. Fineberg, "The dynamics of the onset of frictional slip," *Science*, vol. 330, no. 6001, pp. 211–4, 2010.
- [126] Y. Bar-Sinai, R. Spatschek, E. A. Brener, and E. Bouchbinder, "Instabilities at frictional interfaces: Creep patches, nucleation, and rupture fronts," *Physical Review E*, vol. 88, no. 6, p. 060403, 2013.
- [127] I. Svetlizky and J. Fineberg, "Classical shear cracks drive the onset of dry frictional motion," *Nature*, vol. 509, no. 7499, pp. 205–208, 2014.
- [128] T. Putelat, J. H. Dawes, and A. R. Champneys, "A phase-plane analysis of localized frictional waves," *Proceedings of the Royal Society A: Mathematical, Physical and Engineering Sciences*, vol. 473, no. 2203, p. 20160606, 2017.

-
- [129] Y. Ben-Zion, "Dynamic ruptures in recent models of earthquake faults," *Journal of the Mechanics and Physics of Solids*, vol. 49, no. 9, pp. 2209–2244, 2001.
- [130] D. D. Oglesby and S. M. Day, "Stochastic Fault Stress: Implications for Fault Dynamics and Ground Motion," *Bulletin of the Seismological Society of America*, vol. 92, no. 8, pp. 3006–3021, 2002.
- [131] I. Svetlizky, G. Albertini, G. Cohen, D. S. Kammer, and J. Fineberg, "Dynamic fields at the tip of sub-Rayleigh and supershear frictional rupture fronts," *Journal of the Mechanics and Physics of Solids*, vol. 137, p. 103826, 2020.
- [132] D. S. Kammer and G. C. McLaskey, "Fracture energy estimates from large-scale laboratory earthquakes," *Earth and Planetary Science Letters*, vol. 511, pp. 36–43, 2019.
- [133] I. Svetlizky, D. S. Kammer, E. Bayart, G. Cohen, and J. Fineberg, "Brittle Fracture Theory Predicts the Equation of Motion of Frictional Rupture Fronts," *Physical Review Letters*, vol. 118, no. 12, p. 125501, 2017.
- [134] D. S. Kammer, I. Svetlizky, G. Cohen, and J. Fineberg, "The equation of motion for supershear frictional rupture fronts," *Science Advances*, vol. 4, no. 7, p. eaat5622, 2018.
- [135] D. S. Kammer, M. Radiguet, J.-P. Ampuero, and J.-F. Molinari, "Linear Elastic Fracture Mechanics Predicts the Propagation Distance of Frictional Slip," *Tribology Letters*, vol. 57, no. 3, p. 23, 2015.
- [136] E. Bayart, I. Svetlizky, and J. Fineberg, "Fracture mechanics determine the lengths of interface ruptures that mediate frictional motion," *Nature Physics*, vol. 12, no. 2, pp. 166–170, 2016.
- [137] C.-Y. Ke, G. C. McLaskey, and D. S. Kammer, "Rupture Termination in Laboratory-Generated Earthquakes," *Geophysical Research Letters*, vol. 45, no. 23, pp. 12,784–12,792, 2018.
- [138] R. Gutenberg and C. Richter, "Frequency of earthquakes in California," *Bulltin of the Seismological Society of America*, vol. 34, pp. 185–188, 1944.
- [139] T. Utsu, "Representation and Analysis of the Earthquake Size Distribution: A Historical Review and Some New Approaches," *Pure and Applied Geophysics*, vol. 155, no. 2, pp. 509–535, 1999.
- [140] F. Omori, "On the aftershocks of earthquakes," *Journal of the College of Science*, vol. 7, pp. 111–120, 1894.
- [141] T. Utsu, Y. Ogata, R. S, and Matsu'ura, "The Centenary of the Omori Formula for a Decay Law of Aftershock Activity," *Journal of Physics of the Earth*, vol. 43, no. 1, pp. 1–33, 1995.

Bibliography

- [142] J. Davidsen and C. Goltz, "Are seismic waiting time distributions universal?," *Geophysical Research Letters*, vol. 31, no. 21, 2004.
- [143] D. L. Wells and K. J. Coppersmith, "New empirical relationships among magnitude, rupture length, rupture width, rupture area, and surface displacement," *Bulletin of the Seismological Society of America*, vol. 84, no. 4, pp. 974–1002, 1994.
- [144] H. Kanamori and D. L. Anderson, "Theoretical basis of some empirical relations in seismology," *Bulletin of the Seismological Society of America*, vol. 65, no. 5, pp. 1073–1095, 1975.
- [145] M. A. Denolle and P. M. Shearer, "New perspectives on self-similarity for shallow thrust earthquakes," *Journal of Geophysical Research: Solid Earth*, vol. 121, no. 9, pp. 6533–6565, 2016.
- [146] C. H. Scholz, *The Mechanics of Earthquakes and Faulting*. Cambridge: Cambridge University Press, 3 ed., 2019.
- [147] J. B. Rundle, D. L. Turcotte, R. Shcherbakov, W. Klein, and C. Sammis, "Statistical physics approach to understanding the multiscale dynamics of earthquake fault systems," *Reviews of Geophysics*, vol. 41, no. 4, 2003.
- [148] H. Kawamura, T. Hatano, N. Kato, S. Biswas, and B. K. Chakrabarti, "Statistical physics of fracture, friction, and earthquakes," *Reviews of Modern Physics*, vol. 84, no. 2, pp. 839–884, 2012.
- [149] F. Renard, T. Candela, and E. Bouchaud, "Constant dimensionality of fault roughness from the scale of micro-fractures to the scale of continents," *Geophysical Research Letters*, vol. 40, no. 1, pp. 83–87, 2013.
- [150] R. Burridge and L. Knopoff, "Model and theoretical seismicity," *Bulletin of the Seismological Society of America*, vol. 57, no. 3, pp. 341–371, 1967.
- [151] J. M. Carlson and J. S. Langer, "Properties of earthquakes generated by fault dynamics," *Physical Review Letters*, vol. 62, no. 22, pp. 2632–2635, 1989.
- [152] J. S. Langer, J. M. Carlson, C. R. Myers, and B. E. Shaw, "Slip complexity in dynamic models of earthquake faults," *Proceedings of the National Academy of Sciences*, vol. 93, no. 9, pp. 3825–3829, 1996.
- [153] B. Erickson, B. Birnir, and D. Lavallée, "A model for aperiodicity in earthquakes," *Nonlinear Processes in Geophysics*, vol. 15, no. 1, pp. 1–12, 2008.
- [154] B. A. Erickson, B. Birnir, and D. Lavallée, "Periodicity, chaos and localization in a Burridge–Knopoff model of an earthquake with rate-and-state friction," *Geophysical Journal International*, vol. 187, no. 1, pp. 178–198, 2011.

-
- [155] Y. Ben-Zion and J. R. Rice, "Slip patterns and earthquake populations along different classes of faults in elastic solids," *Journal of Geophysical Research: Solid Earth*, vol. 100, no. B7, pp. 12959–12983, 1995.
- [156] Y. Ben-Zion and J. R. Rice, "Dynamic simulations of slip on a smooth fault in an elastic solid," *Journal of Geophysical Research: Solid Earth*, vol. 102, no. B8, pp. 17771–17784, 1997.
- [157] J. R. Rice and Y. Ben-Zion, "Slip complexity in earthquake fault models.," *Proceedings of the National Academy of Sciences*, vol. 93, no. 9, pp. 3811–3818, 1996.
- [158] N. Lapusta and J. R. Rice, "Nucleation and early seismic propagation of small and large events in a crustal earthquake model," *Journal of Geophysical Research: Solid Earth*, vol. 108, no. B4, p. 2205, 2003.
- [159] C. R. Myers, B. E. Shaw, and J. S. Langer, "Slip Complexity in a Crustal-Plane Model of an Earthquake Fault," *Physical Review Letters*, vol. 77, no. 5, pp. 972–975, 1996.
- [160] B. E. Shaw and J. R. Rice, "Existence of continuum complexity in the elastodynamics of repeated fault ruptures," *Journal of Geophysical Research: Solid Earth*, vol. 105, no. B10, pp. 23791–23810, 2000.
- [161] P. Romanet, H. S. Bhat, R. Jolivet, and R. Madariaga, "Fast and Slow Slip Events Emerge Due to Fault Geometrical Complexity," *Geophysical Research Letters*, vol. 45, no. 10, pp. 4809–4819, 2018.
- [162] M. Ortiz and A. Pandolfi, "Finite-deformation irreversible cohesive elements for three-dimensional crack-propagation analysis," *International Journal for Numerical Methods in Engineering*, vol. 44, no. 9, pp. 1267–1282, 1999.
- [163] D. J. Andrews, "Test of two methods for faulting in finite-difference calculations," *Bulletin of the Seismological Society of America*, vol. 89, no. 4, pp. 931–937, 1999.
- [164] G. A. Francfort and J. J. Marigo, "Revisiting brittle fracture as an energy minimization problem," *Journal of the Mechanics and Physics of Solids*, vol. 46, no. 8, pp. 1319–1342, 1998.
- [165] D. L. Logan, *A First Course in the Finite Element Method*. Stamford, CT: CL Engineering, 5th edition ed., 2011.
- [166] N. M. Newmark, "A Method of Computation for Structural Dynamics," *Journal of the Engineering Mechanics Division*, vol. 85, no. 3, pp. 67–94, 1959.
- [167] R. Courant, K. Friedrichs, and H. Lewy, "Über die partiellen Differenzengleichungen der mathematischen Physik," *Mathematische Annalen*, vol. 100, no. 1, pp. 32–74, 1928.

Bibliography

- [168] R. Rezakhani, F. Barras, M. Brun, and J.-F. Molinari, "Finite element modeling of dynamic frictional rupture with rate and state friction," *Journal of the Mechanics and Physics of Solids*, vol. 141, p. 103967, 2020.
- [169] P. H. Geubelle and J. R. Rice, "A spectral method for three-dimensional elastodynamic fracture problems," *Journal of the Mechanics and Physics of Solids*, vol. 43, no. 11, pp. 1791–1824, 1995.
- [170] J. W. Morrissey and P. H. Geubelle, "A numerical scheme for mode III dynamic fracture problems," *International Journal for Numerical Methods in Engineering*, vol. 40, no. 7, pp. 1181–1196, 1997.
- [171] M. S. Breitenfeld and P. H. Geubelle, "Numerical analysis of dynamic debonding under 2D in-plane and 3D loading," *International Journal of Fracture*, vol. 93, no. 1-4, pp. 13–38, 1998.
- [172] T. Roch, M. Lebihain, and J.-F. Molinari, "Dynamic crack front deformations in cohesive materials," 2022. arXiv:2206.04588 [cond-mat].
- [173] A. S. Balankin, R. G. Paredes, O. Susarrey, D. Morales, and F. C. Vacio, "Kinetic Roughening and Pinning of Two Coupled Interfaces in Disordered Media," *Physical Review Letters*, vol. 96, no. 5, p. 056101, 2006.
- [174] J. Maunuksela, M. Myllys, O.-P. Kähkönen, J. Timonen, N. Provatas, M. J. Alava, and T. Ala-Nissila, "Kinetic Roughening in Slow Combustion of Paper," *Physical Review Letters*, vol. 79, no. 8, pp. 1515–1518, 1997.
- [175] E. M. Lloyd, E. C. Feinberg, Y. Gao, S. R. Peterson, B. Soman, J. Hemmer, L. M. Dean, Q. Wu, P. H. Geubelle, N. R. Sottos, and J. S. Moore, "Spontaneous Patterning during Frontal Polymerization," *ACS Central Science*, vol. 7, no. 4, pp. 603–612, 2021.
- [176] I. Kolvin, J. Fineberg, and M. Adda-Bedia, "Nonlinear focusing in dynamic crack fronts and the microbranching transition," *Physical Review Letters*, vol. 119, no. 21, p. 215505, 2017.
- [177] J. Rice, "First-order variation in elastic fields due to variation in location of a planar crack front," *Journal of Applied Mechanics*, vol. 52, no. 3, pp. 571–579, 1985.
- [178] J.-B. Leblond, S. Patinet, J. Frelat, and V. Lazarus, "Second-order coplanar perturbation of a semi-infinite crack in an infinite body," *Engineering Fracture Mechanics*, vol. 90, pp. 129–142, 2012.
- [179] F. Barras, P. H. Geubelle, and J.-F. Molinari, "Interplay between Process Zone and Material Heterogeneities for Dynamic Cracks," *Physical Review Letters*, vol. 119, no. 14, p. 144101, 2017.

-
- [180] D. S. Kammer, D. Pino Muñoz, and J. F. Molinari, "Length scale of interface heterogeneities selects propagation mechanism of frictional slip fronts," *Journal of the Mechanics and Physics of Solids*, vol. 88, pp. 23–34, 2016.
- [181] J. W. Morrissey and J. R. Rice, "Crack front waves," *Journal of the Mechanics and Physics of Solids*, vol. 46, no. 3, pp. 467–487, 1998.
- [182] R. C. Viesca and D. I. Garagash, "Numerical methods for coupled fracture problems," *Journal of the Mechanics and Physics of Solids*, vol. 113, pp. 13–34, 2018.
- [183] F. Fekak, F. Barras, A. Dubois, D. Spielmann, D. Bonamy, P. H. Geubelle, and J. F. Molinari, "Crack front waves: A 3D dynamic response to a local perturbation of tensile and shear cracks," *Journal of the Mechanics and Physics of Solids*, vol. 135, p. 103806, 2020.
- [184] A. Dubois and D. Bonamy, "Dynamic crack growth along heterogeneous planar interfaces: Interaction with unidimensional strips," *Physical Review E*, vol. 103, no. 1, p. 013004, 2021.
- [185] S. Ramanathan and D. S. Fisher, "Dynamics and Instabilities of Planar Tensile Cracks in Heterogeneous Media," *Physical Review Letters*, vol. 79, no. 5, pp. 877–880, 1997.
- [186] J. W. Morrissey and J. R. Rice, "Perturbative simulations of crack front waves," *Journal of the Mechanics and Physics of Solids*, vol. 48, no. 6, pp. 1229–1251, 2000.
- [187] P. Daguer, B. Nghiem, E. Bouchaud, and F. Creuzet, "Pinning and Depinning of Crack Fronts in Heterogeneous Materials," *Physical Review Letters*, vol. 78, no. 6, pp. 1062–1065, 1997.
- [188] A. Delaplace, J. Schmittbuhl, and K. J. Måløy, "High resolution description of a crack front in a heterogeneous Plexiglas block," *Physical Review E*, vol. 60, no. 2, pp. 1337–1343, 1999.
- [189] V. Démery, A. Rosso, and L. Ponson, "From microstructural features to effective toughness in disordered brittle solids," *Europhysics Letters*, vol. 105, no. 3, p. 34003, 2014.
- [190] F. Barras, *When dynamic cracks meet disorder: A journey along the fracture process zone*. PhD thesis, EPFL, Lausanne, 2018.
- [191] F. Barras, M. Aldam, T. Roch, E. A. Brener, E. Bouchbinder, and J.-F. Molinari, "Emergence of cracklike behavior of frictional rupture: The origin of stress drops," *Physical Review X*, vol. 9, p. 041043, 2019.
- [192] F. Barras, M. Aldam, T. Roch, E. A. Brener, E. Bouchbinder, and J.-F. Molinari, "The emergence of crack-like behavior of frictional rupture: Edge singularity and energy balance," *Earth and Planetary Science Letters*, vol. 531, p. 115978, 2020.

Bibliography

- [193] T. Roch, E. A. Brener, J.-F. Molinari, and E. Bouchbinder, "Velocity-driven frictional sliding: Coarsening and steady-state pulses," *Journal of the Mechanics and Physics of Solids*, vol. 158, p. 104607, 2022.
- [194] K. Uenishi and J. R. Rice, "Universal nucleation length for slip-weakening rupture instability under nonuniform fault loading," *Journal of Geophysical Research: Solid Earth*, vol. 108, no. B1, p. 2042, 2003.
- [195] R. Madariaga, "High-frequency radiation from crack (stress drop) models of earthquake faulting," *Geophysical Journal International*, vol. 51, no. 3, pp. 625–651, 1977.
- [196] A. Bizzarri, M. Cocco, D. J. Andrews, and E. Boschi, "Solving the dynamic rupture problem with different numerical approaches and constitutive laws," *Geophysical Journal International*, vol. 144, no. 3, pp. 656–678, 2001.
- [197] J. R. Rice, C. G. Sammis, and R. Parsons, "Off-Fault Secondary Failure Induced by a Dynamic Slip Pulse," *Bulletin of the Seismological Society of America*, vol. 95, no. 1, pp. 109–134, 2005.
- [198] H. S. Bhat, R. Dmowska, G. C. P. King, Y. Klinger, and J. R. Rice, "Off-fault damage patterns due to supershear ruptures with application to the 2001 Mw 8.1 Kokoxili (Kunlun) Tibet earthquake," *Journal of Geophysical Research: Solid Earth*, vol. 112, no. B6, 2007.
- [199] E. M. Dunham and H. S. Bhat, "Attenuation of radiated ground motion and stresses from three-dimensional supershear ruptures," *Journal of Geophysical Research: Solid Earth*, vol. 113, no. B8, 2008.
- [200] A. Bizzarri, "On the relations between fracture energy and physical observables in dynamic earthquake models," *Journal of Geophysical Research: Solid Earth*, vol. 115, no. B10, 2010.
- [201] A. Bizzarri, "How to Promote Earthquake Ruptures: Different Nucleation Strategies in a Dynamic Model with Slip-Weakening Friction," *Bulletin of the Seismological Society of America*, vol. 100, no. 3, pp. 923–940, 2010.
- [202] R. C. Viesca and J. R. Rice, "Nucleation of slip-weakening rupture instability in landslides by localized increase of pore pressure," *Journal of Geophysical Research: Solid Earth*, vol. 117, no. B3, 2012.
- [203] D. S. Kammer, V. A. Yastrebov, P. Spijker, and J.-F. Molinari, "On the Propagation of Slip Fronts at Frictional Interfaces," *Tribology Letters*, vol. 48, no. 1, pp. 27–32, 2012.
- [204] C. Liu, A. Bizzarri, and S. Das, "Progression of spontaneous in-plane shear faults from sub-Rayleigh to compressional wave rupture speeds," *Journal of Geophysical Research: Solid Earth*, vol. 119, no. 11, pp. 8331–8345, 2014.

- [205] A. Bizzarri and C. Liu, "Near-field radiated wave field may help to understand the style of the supershear transition of dynamic ruptures," *Physics of the Earth and Planetary Interiors*, vol. 261, pp. 133–140, 2016.
- [206] R. E. Abercrombie and J. R. Rice, "Can observations of earthquake scaling constrain slip weakening?," *Geophysical Journal International*, vol. 162, no. 2, pp. 406–424, 2005.
- [207] X. Lu, N. Lapusta, and A. J. Rosakis, "Pulse-like and crack-like dynamic shear ruptures on frictional interfaces: experimental evidence, numerical modeling, and implications," *International Journal of Fracture*, vol. 163, no. 1, pp. 27–39, 2010.
- [208] X. Lu, A. J. Rosakis, and N. Lapusta, "Rupture modes in laboratory earthquakes: Effect of fault prestress and nucleation conditions," *Journal of Geophysical Research: Solid Earth*, vol. 115, no. B12, 2010.
- [209] H. Noda, N. Lapusta, and H. Kanamori, "Comparison of average stress drop measures for ruptures with heterogeneous stress change and implications for earthquake physics," *Geophysical Journal International*, vol. 193, no. 3, pp. 1691–1712, 2013.
- [210] I. Svetlizky, D. Pino Muñoz, M. Radiguet, D. S. Kammer, J.-F. Molinari, and J. Fineberg, "Properties of the shear stress peak radiated ahead of rapidly accelerating rupture fronts that mediate frictional slip," *Proceedings of the National Academy of Sciences*, vol. 113, no. 3, pp. 542–547, 2016.
- [211] V. Rubino, A. J. Rosakis, and N. Lapusta, "Understanding dynamic friction through spontaneously evolving laboratory earthquakes," *Nature Communications*, vol. 8, no. 1, p. 15991, 2017.
- [212] I. Svetlizky, E. Bayart, and J. Fineberg, "Brittle Fracture Theory Describes the Onset of Frictional Motion," *Annual Review of Condensed Matter Physics*, vol. 10, no. 1, pp. 253–273, 2019.
- [213] E. Bayart, "Slippery but Tough: The Rapid Fracture of Lubricated Frictional Interfaces," *Physical Review Letters*, vol. 116, no. 19, 2016.
- [214] M. Cocco and A. Bizzarri, "On the slip-weakening behavior of rate- and state dependent constitutive laws," *Geophysical Research Letters*, vol. 29, no. 11, pp. 11–11–4, 2002.
- [215] S. Das, "Dynamic fracture mechanics in the study of the earthquake rupturing process: theory and observation," *Journal of the Mechanics and Physics of Solids*, vol. 51, no. 11, pp. 1939–1955, 2003.
- [216] E. Tinti, P. Spudich, and M. Cocco, "Earthquake fracture energy inferred from kinematic rupture models on extended faults," *Journal of Geophysical Research: Solid Earth*, vol. 110, no. B12, 2005.

Bibliography

- [217] J. S. Chester, F. M. Chester, and A. K. Kronenberg, "Fracture surface energy of the Punchbowl fault, San Andreas system," *Nature*, vol. 437, no. 7055, pp. 133–136, 2005.
- [218] E. A. Brener and E. Bouchbinder, "Theory of unconventional singularities of frictional shear cracks," *Journal of the Mechanics and Physics of Solids*, vol. 153, p. 104466, 2021.
- [219] E. A. Brener and E. Bouchbinder, "Unconventional singularities and energy balance in frictional rupture," *Nature Communications*, vol. 12, no. 1, p. 2585, 2021.
- [220] F. Paglialonga, F. X. Passelègue, N. Brantut, F. Barras, M. Lebihain, and M. Violay, "On the scale dependence in the dynamics of frictional rupture: Constant fracture energy versus size-dependent breakdown work," *Earth and Planetary Science Letters*, vol. 584, p. 117442, Apr. 2022.
- [221] M. Nakatani, "Conceptual and physical clarification of rate and state friction: Frictional sliding as a thermally activated rheology," *Journal of Geophysical Research: Solid Earth*, vol. 106, no. B7, pp. 13347–13380, 2001.
- [222] J. H. Dieterich, "Applications of rate-and state-dependent friction to models of fault slip and earthquake occurrence," *Treatise Geophys.*, vol. 4, pp. 107–129, 2007.
- [223] K. Nagata, M. Nakatani, and S. Yoshida, "A revised rate- and state-dependent friction law obtained by constraining constitutive and evolution laws separately with laboratory data," *Journal of Geophysical Research: Solid Earth*, vol. 117, no. B2, p. B02314, 2012.
- [224] A. Vanossi, N. Manini, M. Urbakh, S. Zapperi, and E. Tosatti, "Colloquium: Modeling friction: From nanoscale to mesoscale," *Rev. Mod. Phys.*, vol. 85, pp. 529–552, 2013.
- [225] J. Wojewoda, A. Stefański, M. Wiercigroch, and T. Kapitaniak, "Hysteretic effects of dry friction: modelling and experimental studies," *Philosophical Transactions of the Royal Society A: Mathematical, Physical and Engineering Sciences*, vol. 366, no. 1866, pp. 747–765, 2008.
- [226] F. Massi, L. Baillet, O. Giannini, and A. Sestieri, "Brake squeal: Linear and nonlinear numerical approaches," *Mechanical Systems and Signal Processing*, vol. 21, no. 6, pp. 2374–2393, 2007.
- [227] D. Tonazzi, F. Massi, A. Culla, L. Baillet, A. Fregolent, and Y. Berthier, "Instability scenarios between elastic media under frictional contact," *Mechanical Systems and Signal Processing*, vol. 40, no. 2, pp. 754–766, 2013.
- [228] T. Yamashita and M. Ohnaka, "Nucleation process of unstable rupture in the brittle regime: A theoretical approach based on experimentally inferred relations," *Journal of Geophysical Research: Solid Earth*, vol. 96, no. B5, p. 8351, 1991.

-
- [229] N. Lapusta, *Elastodynamic analyses of sliding with rate and state friction*. PhD thesis, Harvard University, 2001.
- [230] J.-P. Ampuero, J.-P. Vilotte, and F. J. Sánchez-Sesma, "Nucleation of rupture under slip dependent friction law: Simple models of fault zone," *Journal of Geophysical Research: Solid Earth*, vol. 107, no. B12, p. 2324, 2002.
- [231] G. C. McLaskey and B. D. Kilgore, "Foreshocks during the nucleation of stick-slip instability," *Journal of Geophysical Research: Solid Earth*, vol. 118, no. 6, pp. 2982–2997, 2013.
- [232] S. Latour, A. Schubnel, S. B. Nielsen, R. Madariaga, and S. Vinciguerra, "Characterization of nucleation during laboratory earthquakes," *Geophysical Research Letters*, vol. 40, no. 19, pp. 5064–5069, 2013.
- [233] R. C. Viesca, "Stable and unstable development of an interfacial sliding instability," *Physical Review E*, vol. 93, no. 6, p. 060202, 2016.
- [234] R. C. Viesca, "Self-similar slip instability on interfaces with rate- and state-dependent friction," *Proceedings of the Royal Society A: Mathematical, Physical and Engineering Sciences*, vol. 472, no. 2192, p. 20160254, 2016.
- [235] Y. Kaneko, S. B. Nielsen, and B. M. Carpenter, "The onset of laboratory earthquakes explained by nucleating rupture on a rate-and-state fault," *Journal of Geophysical Research: Solid Earth*, vol. 121, no. 8, pp. 6071–6091, 2016.
- [236] Y. Kaneko, B. M. Carpenter, and S. B. Nielsen, "Nucleation process of magnitude 2 repeating earthquakes on the San Andreas Fault predicted by rate-and-state fault models with SAFOD drill core data," *Geophysical Research Letters*, vol. 44, no. 1, pp. 162–173, 2017.
- [237] S. Nielsen and R. Madariaga, "On the Self-Healing Fracture Mode," *Bulletin of the Seismological Society of America*, vol. 93, no. 6, pp. 2375–2388, 2003.
- [238] N. Brantut, D. I. Garagash, and H. Noda, "Stability of Pulse-Like Earthquake Ruptures," *Journal of Geophysical Research: Solid Earth*, vol. 124, no. 8, pp. 8998–9020, 2019.
- [239] V. Lambert, N. Lapusta, and S. Perry, "Propagation of large earthquakes as self-healing pulses or mild cracks," *Nature*, vol. 591, no. 7849, pp. 252–258, 2021.
- [240] M. Baus and C. F. Tejeri, *Equilibrium Statistical Physics: Phases of Matter and Phase Transitions*. Springer Berlin, Heidelberg, 1999.
- [241] B. V. Kostrov, "Selfsimilar problems of propagation of shear cracks," *J. Appl. Math. Mech*, vol. 28, no. 5, pp. 1077–1087, 1964.

Bibliography

- [242] L. B. Freund, "The mechanics of dynamic shear crack propagation," *Journal of Geophysical Research: Solid Earth*, vol. 84, no. B5, pp. 2199–2209, 1979.
- [243] K. B. Broberg, *Cracks and fracture*. Elsevier, 1999.
- [244] L. Landau and E. Lifshitz, *Theory of Elasticity, Third Edition: Volume 7 (Course of Theoretical Physics)*. Butterworth-Heinemann, 1986.
- [245] P. Crupi and A. Bizzarri, "The role of radiation damping in the modeling of repeated earthquake events," *Annals of Geophysics*, vol. 56, no. 1, p. R0111, 2013.
- [246] E. A. Brener, M. Weikamp, R. Spatschek, Y. Bar-Sinai, and E. Bouchbinder, "Dynamic instabilities of frictional sliding at a bimaterial interface," *Journal of the Mechanics and Physics of Solids*, vol. 89, pp. 149–173, 2016.
- [247] H. Kanamori and T. H. Heaton, "Microscopic and Macroscopic Physics of Earthquakes," in *Geocomplexity and the Physics of Earthquakes*, pp. 147–163, American Geophysical Union (AGU), 2000.
- [248] J. Galeano, P. Español, and M. A. Rubio, "Experimental and theoretical results of stress relaxations in a model of earthquake dynamics," *Europhysics Letters*, vol. 49, no. 4, p. 410, 2000.
- [249] S. Ma, T. Shimamoto, L. Yao, T. Togo, and H. Kitajima, "A rotary-shear low to high-velocity friction apparatus in Beijing to study rock friction at plate to seismic slip rates," *Earthquake Science*, vol. 27, no. 5, pp. 469–497, 2014.
- [250] Y. Bar-Sinai, E. a. Brener, and E. Bouchbinder, "Slow rupture of frictional interfaces," *Geophysical Research Letters*, vol. 39, no. 3, p. L03308, 2012.
- [251] Y. Bar-Sinai, R. Spatschek, E. a. Brener, and E. Bouchbinder, "Velocity-strengthening friction significantly affects interfacial dynamics, strength and dissipation," *Scientific Reports*, vol. 5, no. 1, p. 7841, 2015.
- [252] S. B. Nielsen, "From slow to fast faulting: recent challenges in earthquake fault mechanics," *Philosophical Transactions of the Royal Society A: Mathematical, Physical and Engineering Sciences*, vol. 375, no. 2103, p. 20160016, 2017.
- [253] M. Lebihain, T. Roch, M. Violay, and J.-F. Molinari, "Earthquake Nucleation Along Faults With Heterogeneous Weakening Rate," *Geophysical Research Letters*, vol. 48, no. 21, p. e2021GL094901, 2021.
- [254] G. Albertini, S. Karrer, M. D. Grigoriu, and D. S. Kammer, "Stochastic properties of static friction," *Journal of the Mechanics and Physics of Solids*, vol. 147, p. 104242, 2021.
- [255] V. Rubino, N. Lapusta, and A. J. Rosakis, "Intermittent lab earthquakes in dynamically weakening fault gouge," *Nature*, vol. 606, pp. 922–929, June 2022.

-
- [256] N. Lapusta and Y. Liu, "Three-dimensional boundary integral modeling of spontaneous earthquake sequences and aseismic slip," *Journal of Geophysical Research: Solid Earth*, vol. 114, no. B9, 2009.
- [257] J. Bleyer and J.-F. Molinari, "Microbranching instability in phase-field modelling of dynamic brittle fracture," *Applied Physics Letters*, vol. 110, p. 151903, Apr. 2017.
- [258] P. Bettess, "Infinite elements," *International Journal for Numerical Methods in Engineering*, vol. 11, no. 1, pp. 53–64, 1977.
- [259] H. R. Yerli, B. Temel, and E. Kiral, "Transient Infinite Elements for 2D Soil-Structure Interaction Analysis," *Journal of Geotechnical and Geoenvironmental Engineering*, vol. 124, pp. 976–988, Oct. 1998.
- [260] J. Lysmer and R. L. Kuhlemeyer, "Finite Dynamic Model for Infinite Media," *Journal of the Engineering Mechanics Division*, vol. 95, pp. 859–877, Aug. 1969.
- [261] B. Engquist and A. Majda, "Absorbing Boundary Conditions for the Numerical Simulation of Waves," *Mathematics of Computation*, vol. 31, no. 139, pp. 629–651, 1977.
- [262] R. Kosloff and D. Kosloff, "Absorbing boundaries for wave propagation problems," *Journal of Computational Physics*, vol. 63, pp. 363–376, Apr. 1986.
- [263] J.-F. Semblat, L. Lenti, and A. Gandomzadeh, "A Simple Multi-Directional Absorbing Layer Method to Simulate Elastic Wave Propagation in Unbounded Domains," *International Journal for Numerical Methods in Engineering*, vol. 85, no. 12, p. 1543, 2011.
- [264] J.-P. Berenger, "A perfectly matched layer for the absorption of electromagnetic waves," *Journal of Computational Physics*, vol. 114, pp. 185–200, Oct. 1994.
- [265] W. Chew and Q. Liu, "Perfectly matched layers for elastodynamics: a new absorbing boundary condition," *Journal of Computational Acoustics*, vol. 04, pp. 341–359, Dec. 1996.
- [266] M. Brun, E. Zafati, I. Djeran-Maigre, and F. Prunier, "Hybrid Asynchronous Perfectly Matched Layer for seismic wave propagation in unbounded domains," *Finite Elements in Analysis and Design*, vol. 122, pp. 1–15, Dec. 2016.
- [267] S. Hajarolasvadi and A. Elbanna, "A new hybrid numerical scheme for modelling elastodynamics in unbounded media with near-source heterogeneities," *Geophysical Journal International*, vol. 211, no. 2, pp. 851–864, 2017.
- [268] X. Ma, S. Hajarolasvadi, G. Albertini, D. S. Kammer, and A. E. Elbanna, "A hybrid finite element-spectral boundary integral approach: Applications to dynamic rupture modeling in unbounded domains," *International Journal for Numerical and Analytical Methods in Geomechanics*, vol. 43, no. 1, pp. 317–338, 2019.

Bibliography

- [269] X. Ma and A. Elbanna, "Dynamic rupture propagation on fault planes with explicit representation of short branches," *Earth and Planetary Science Letters*, vol. 523, p. 115702, 2019.
- [270] M. Abdelmeguid, X. Ma, and A. Elbanna, "A Novel Hybrid Finite Element-Spectral Boundary Integral Scheme for Modeling Earthquake Cycles: Application to Rate and State Faults With Low-Velocity Zones," *Journal of Geophysical Research: Solid Earth*, vol. 124, no. 12, pp. 12854–12881, 2019.
- [271] G. Albertini, A. E. Elbanna, and D. S. Kammer, "A three-dimensional hybrid finite element — spectral boundary integral method for modeling earthquakes in complex unbounded domains," *International Journal for Numerical Methods in Engineering*, vol. 122, no. 23, pp. 6905–6923, 2021.
- [272] M. Vocialta, N. Richart, and J.-F. Molinari, "3D dynamic fragmentation with parallel dynamic insertion of cohesive elements," *International Journal for Numerical Methods in Engineering*, vol. 109, no. 12, pp. 1655–1678, 2017.
- [273] E. Favier, V. Lazarus, and J. Leblond, "Coplanar propagation paths of 3d cracks in infinite bodies loaded in shear," *International Journal of Solids and Structures*, vol. 43, no. 7, pp. 2091–2109, 2006.
- [274] J. Leblond, S. Patinet, J. Frelat, and V. Lazarus, "Second-order coplanar perturbation of a semi-infinite crack in an infinite body," *Engineering Fracture Mechanics*, vol. 90, pp. 129–142, 2012.
- [275] W. Jakob, J. Rhineland, and D. Moldovan, "pybind11 – seamless operability between c++11 and python," 2017.
- [276] E. M. Dunham, "Multi-dimensional spectral boundary integral code," 2008.
- [277] D. S. Kammer, G. Albertini, and C.-Y. Ke, "UGUCA: A spectral-boundary-integral method for modeling fracture and friction," *SoftwareX*, 2021.
- [278] V. Prakash, "Frictional Response of Sliding Interfaces Subjected to Time Varying Normal Pressures," *Journal of Tribology*, vol. 120, no. 1, pp. 97–102, 1998.
- [279] Project Jupyter, M. Bussonier, J. Forde, J. Freeman, B. Granger, T. Head, C. Holdgraf, K. Kelley, G. Nalvarte, A. Osheroff, M. Pacer, Y. Panda, F. Perez, B. Ragan-Kelley, and C. Willing, "Binder 2.0 - reproducible, interactive, sharable environments for science at scale.," *Proceedings of the 17th Python in Science Conference*, 2018.
- [280] G. M. Amdahl, "Validity of the single processor approach to achieving large scale computing capabilities," in *Proceedings of the April 18-20, 1967, spring joint computer conference, AFIPS '67 (Spring)*, (New York, NY, USA), pp. 483–485, Association for Computing Machinery, 1967.

- [281] "Gnu compiler collection - 8.4," 2020.
- [282] "Intel® oneapi dpc++/c++ compiler - 2021.4," 2021.



Thibault Roch

Contact

Address Computational Solid Mechanics Laboratory
School of Architecture, Civil and Environmental Engineering
École Polytechnique Fédérale de Lausanne
CH - 1015 Lausanne, Switzerland

mail thibault.roch@alumni.epfl.ch

 [0000-0002-2495-8841](https://orcid.org/0000-0002-2495-8841)

Research interests

Heterogeneous fracture

- Physics of fast propagating cracks, Rupture nucleation on heterogeneous interfaces, Crack front deformations

Friction

- Analogy between friction and fracture, Frictional rupture modes, Rate and state friction, Energy budget of earthquakes, Statistical complexity

Computational Modeling

- Finite element method, Boundary integral method, High performance computing, Open source software

Education

- 2023 **Doctor of Philosophy (Ph.D.)**, *École Polytechnique Fédérale de Lausanne - Switzerland*
 - Doctoral program in civil and environmental engineering
 - Title : Friction and fracture: richness and complexity in dynamic rupture
 - Advisor : Prof. Jean-François Molinari
- 2017 **Master ès Science (M.Sc.)**, *École Polytechnique Fédérale de Lausanne - Switzerland*
 - Civil engineering
- 2014 **Bachelor ès Science (B.Sc.)**, *École Polytechnique Fédérale de Lausanne - Switzerland*
 - Civil engineering
- 2011 **Baccalauréat (High-school degree)**, *Lycée Anna de Noailles, Evian-les-Bains, France*
 - Baccalauréat scientifique, specialized in mathematics
 - With highest honour

Research experiences

Doctoral student, *École Polytechnique Fédérale de Lausanne, Switzerland*

- Study the behavior of fast propagating cracks and their interactions with material heterogeneities
- Coupling the finite element method with spectral boundary integral method
- Participation in the preparation and supervision of several courses
- Supervision of several student projects and master theses
- Three months visit at Eran Bouchbinder's laboratory at the Weizmann Institute of Science, Rehovot, Israel

Master project, with *David S. Kammer, Cornell University, United States of America*

- Master project in Cornell University during 6 months. Study the fracture behavior of composite laminates

Scientific collaborations

- with Mathias Lebihain, École des Ponts ParisTech, Paris, France. Crack front deformations in heterogeneous cohesive materials
- with Mathias Lebihain, École des Ponts ParisTech, Paris, France and Marie Violay, École Polytechnique Fédérale de Lausanne, Switzerland. Nucleation of cracks for heterogeneous materials
- with Fabian Barras, University of Oslo, Norway and Eran Bouchbinder and Michael Aldam, Weizmann Institute of Science, Rehovot, Israel and Efim A. Brener, Forschungszentrum Jülich, Germany. Emergence of crack-like behavior of frictional rupture, stress drop, edge singularity, and energy balance
- with Eran Bouchbinder, Weizmann Institute of Science, Rehovot, Israel and Efim A. Brener, Forschungszentrum Jülich, Germany. Behavior of velocity-driven frictional sliding. Emergence of steady-state pulses and their characteristics. Statistical complexity in frictional systems.
- with Fabian Barras, University of Oslo, Norway and Philippe H. Geubelle, University of Illinois at Urbana-Champaign, United States of America. Development, release and maintenance of an Open Source implementation of the spectral boundary integral method: cRacklet
- with Tal Cohen, Massachusetts Institute of Technology, United States of America. Supervision of master projects. Peeling behavior of adhesives materials

Journal publications

- [1] **Thibault Roch**, Efim A. Brener, Jean-François Molinari, Eran Bouchbinder. [Velocity-driven frictional sliding: Coarsening and steady-state pulses](#), *Journal of the Mechanics and Physics of Solids*, vol. 158, 104607, 2022
- [2] **Thibault Roch**, Barras Fabian, Philippe H. Geubelle, Jean-François Molinari. [cRacklet: a spectral boundary integral method library for interfacial rupture simulation](#), *Journal of Open Source Software*, 67(69), 3724. 2022
- [3] **Thibault Roch**, Mathias Lebihain, Jean-François Molinari. [Dynamic crack front deformations in cohesive materials](#), *Under Review*, 2022
- [4] **Thibault Roch**, Jean-François Molinari. Coupling the finite element method and the spectral boundary integral method for dynamic rupture simulations, *In preparation*, 2023
- [5] **Thibault Roch**, Efim. A. Brener, Eran Bouchbinder, Jean-François Molinari. Statistical and dynamical complexity in a driven physical system without disorder., *In preparation*, 2023
- [6] Fabian Barras, Michael Aldam, **Thibault Roch**, Efim A. Brener, Eran Bouchbinder, Jean-François Molinari. [Emergence of Cracklike Behavior of Frictional Rupture: The Origin of Stress Drops](#), *Physical Review X*, 9, 041043 2019
- [7] Fabian Barras, Michael Aldam, **Thibault Roch**, Efim A. Brener, Eran Bouchbinder, Jean-François Molinari. [The emergence of crack-like behavior of frictional rupture: Edge singularity and energy balance](#), *Earth and Planetary Science Letters*, vol. 531, 115978, 2020

- [8] Evelyne Ringoot, **Thibault Roch**, Jean-François Molinari, Thierry J. Massart, Tal Cohen. [Stick-slip phenomena and Schallamach waves captured using reversible cohesive elements](#), *Journal of the Mechanics and Physics of Solids*, vol. 155, 104528, 2021
- [9] Mathias Lebihain, **Thibault Roch**, Marie Violay, Jean-François Molinari. [Earthquake Nucleation Along Faults With Heterogeneous Weakening Rate](#), *Geophysical Research Letters*, vol. 48, iss. 21, 2021
- [10] Mathias Lebihain, **Thibault Roch**, Jean-François Molinari. [Quasi-static crack front deformations in cohesive materials](#), *Journal of the Mechanics and Physics of Solids*, vol. 168, 105025, 2022

Conferences and workshop

- [1] **Thibault Roch**, Efim A. Brener, Eran Bouchbinder, Jean-François Molinari, Emergence of statistical complexity on homogeneous frictional fault, *Summer School on Earthquake Mechanics and Aseismic Slip, Zurich, Switzerland.*, 2022, Poster
- [2] **Thibault Roch**, Jean-François Molinari, Coupling Finite Element and Spectral Boundary Integral Method to model complex dynamic rupture problems, *11th European Solid Mechanics Conference (ESMC), Galway, Ireland*, 2022, Oral presentation
- [3] **Thibault Roch**, Efim A. Brener, Jean-François Molinari, Eran Bouchbinder, Velocity-Driven Frictional Sliding: Coarsening and Steady-State Pulses, *American Geophysical Union Fall Meeting (AGU21), New Orleans, United States of America*, 2021, Poster
- [4] **Thibault Roch**, Mathias Lebihain, Jean-François Molinari Dynamic crack front deformations The role of the process zone, *25th International Congress of Theoretical and Applied Mechanics (ICTAM 2020+1), Milano, Italy.*, 2021, Oral presentation
- [5] **Thibault Roch**, Jean-François Molinari, Crack front deformation during dynamic heterogeneous fracture, *3rd General Assembly of SWICCOMAS, Zurich, Switzerland.*, 2020, Poster
- [6] **Thibault Roch**, Jean-François Molinari, On the supershear transition in heterogeneous media, *Numerical Modeling of Earthquake Motions: Waves and Ruptures (NMEM), Smolenice Castle near Bratislava, Slovakia.*, 2019, Poster
- [7] **Thibault Roch**, Jean-François Molinari, Interplay between process zone and material heterogeneities for dynamic cracks, *6th International Conference on Computational Modeling of Fracture and Failure of Materials and Structures (CFRAC), Braunschweig, Germany.* Oral presentation, 2019, Oral presentation
- [8] **Thibault Roch**, Jean-François Molinari, Dynamic fracture in heterogeneous media, *Modeling Tribology: Friction and fracture across scales (CECAM) Lausanne, Switzerland.*, 2019, Poster

Seminars and talks

- [1] **Thibault Roch**, Richness and complexity of slip events at a frictional interface, *University Van Amsterdam, Van der Waals-Zeeman Institute, Group seminar, Amsterdam Netherlands*, Feb 06 2023, Invited seminar
- [2] Jean-François Molinari, **Thibault Roch**, Richness and complexity of slip events at a frictional interface, *Commissariat à l'énergie atomique, Direction des Applications Militaires, Departemental Seminar, Bruyères-le-Châtel France*, Dec 20 2022, Invited seminar
- [3] Gilles Dubochet, Jean-François Molinari, Guillaume Anciaux, Nicolas Richart, **Thibault Roch**, What makes an open software successful?, *Open Science Summer School, École Polytechnique Fédérale de Lausanne, Lausanne Switzerland*, June 30 2022, Pannel disuccsion
- [4] **Thibault Roch**, Quasi-static and dynamic crack front deformations in cohesive materials, *MEchanics GAttering Seminar Series (MEGA.Seminar), École Polytechnique Fédérale de Lausanne, Lausanne Switzerland*, June 02 2022

- [5] **Thibault Roch**, Understanding the dynamics of frictional rupture front with fracture mechanics, *Physics of Complex Systems Laboratory, École Polytechnique Fédérale de Lausanne, Lausanne Switzerland* , Dec 10 2020, Invited seminar

Peer review

Journal of the Mechanics and Physics of Solids

Earth and Planetary Science Letters

Tribology Letters

Teaching experiences

- 2019,2020,2021 **Numerical Modeling of solids and structures**, by *Prof. Jean-François Molinari*
- Introductory class of finite-element modeling at the Bachelor level.
 - 14 weeks, in charge of 2 hours per week of exercise session and mini-projects supervision. 60 students
- 2018,2020 **Selected Topics of Solids and Structures**, by *Prof. Jean-François Molinari*
- Advanced class of fracture mechanics and elastodynamics for Master and PhD students
 - 14 weeks, in charge of 1 hour per week of exercise session. 20 students
- Fall 2019 **Scientific programming for Engineers**, by *Dr. Guillaume Anciaux*
- Doctoral class about scientific programming,
 - 14 weeks, in charge of 2 hours per week of exercise session and mini-projects supervision. 40 students
- Spring 2016 **Design of Steel Structures** , by *Prof. Alain Nussbaumer*
- Conception and design of steel structures at the Bachelor level
 - 14 weeks, in charge of 2 hours per week of exercise session. 80 students
- Fall 2013 **Structural Mechanics** , by *Dr. Eric Davalle*
- Introductory class of structural mechanics at the Bachelor level
 - 14 weeks, in charge of 2 hours per week of exercise session. 80 students

Advised master theses - With Prof. J.-F. Molinari and Prof. Tal Cohen

- 2019-2020 **Evelyne Ringoot**, *Stick-Slip in Peeling of Soft Adhesives: a Finite Element Model Using Reversible Cohesive Elements*, with Prof. Thierry Massart
- 2021-2022 **Thibault Ghesquière-Diéricks**, *Detachment Dynamics of Heterogeneous Adhesive Pads*

Advised semester projects - With Prof. J.-F. Molinari

- Fall 2018 **Olivier Schöpfer**, *Modelling the deformation of an X-ray micro-CT based 3D structure*
- Spring 2019 **Evelyne Ringoot**, *Dynamic fracture in heterogeneous medium: cascading cracks in brittle rods*
- Fall 2020 **Xavier Vingerhoets**, *Dynamic rupture in plexiglass*
- Spring 2021 **Thomas Poulain**, *Improving the frictional resistance of a micro-architected interface*, with Dr. Mathias Lebihain

Open Source Software

- [cRacklet](#) **Spectral boundary integral method library**, *Active developer*
- [Akantu](#) **Finite element method library**, *Active developer, Community Manager*

Awards and distinctions

- 2022 **SNFS Scientific Image Competition**, *Jury distinction in the category Object of Study*, [Mountains of friction](#)

Professional experience outside of academia

2017-2018 **Conseils Ingénierie Lémanique**, *Engineer*, Marin, France

- Design of steel structures: pedestrian bridge in St-Gingolph, France
- Design of retaining structures: stabilisation of St-Gingolph's docks, France
- On site work monitoring

2014-2015 **BG Ingénieurs Conseils SA**, *Intern*, Lausanne, Switzerland

- Design of underground structures
- On site work monitoring: Tunnel du Pinchat in Geneva, Switzerland
- Inspection of existing structures (bridges, retaining walls) on the Swiss highway

Voluntary work

2013-2014 **Travel GC**, *Sponsorship Manager*, Student association that plans and finances the study trip at the end of the Bachelor for the Civil Engineering students.